Fissuration par fatigue en mode mixte non proportionnel des rails de chemins de fer : De l'étude expérimentale à la mise en œuvre d'un modèle

Thomas Bonniot

université PARIS-SACLAY

NNT : 2019SACLX096

Thèse de doctorat

Fatigue crack growth under non-proportional mixed-mode loading in rail steel. From experiment to simulation.

Thèse de doctorat de l'Université Paris-Saclay
préparée à l'Ecole Polytechnique

École doctorale n°579 Sciences mécaniques et énergétiques, matériaux et géosciences (SMEMAG)
Spécialité de doctorat : Mécanique des matériaux

Thèse présentée et soutenue à Palaiseau, le 18/11/2019, par

THOMAS BONNIOT

Composition du Jury :

David Nowell Professeur, Imperial College London (Department of Mechanical Engineering)	Président
Stefano Beretta Professeur, Politecnico di Milano (Dipartimento di Meccanica)	Rapporteur
Julien Réthoré Directeur de recherche CNRS, Ecole Centrale de Nantes (GeM)	Rapporteur
Habibou Maitournam Professeur, ENSTA (IMSIA)	Examinateur
Sylvie Pommier Professeure, ENS Paris-Saclay (LMT)	Examinatrice
Véronique Doquet Directrice de recherche CNRS, Ecole Polytechnique (LMS)	Directrice de thèse
Si Hai Mai Encadrant industriel, SNCF	Invité

Remerciements

Cette thèse a été réalisée via un contrat CIFRE entre le Laboratoire de Mécanique des Solides de l'école Polytechnique et la SNCF, dans le cadre du partenariat scientifique IDR2 entre RATP, SNCF et British Steel. Je remercie la SNCF et le LMS d'avoir financé et porté ce projet de recherche.

Je remercie sincèrement David Nowell qui a accepté de présider je jury, Julien Réthoré et Stefano Beretta qui ont accepté de rapporter le manuscrit, ainsi que Sylvie Pommier et Habibou Maitournam qui ont accepté de faire partie de mon jury. Vous m'avez fait l'honneur de prendre le temps de juger ce travail, et ce malgré vos nombreuses obligations. Encore merci pour vos nombreuses remarques et échanges sur les aspects de corrélation d'images, d'usure... jusqu'aux voitures de collection.

Je n'aurais pas assez de ces quelques lignes pour remercier Véronique Doquet, ma directrice de thèse, pour son encadrement, son implication, et tout le temps, l'énergie, les brillantes idées, les commentaires qu'elle a su m'apporter. Un grand merci également à Si Hai Mai pour son encadrement, bien entendu sur le plan scientifique, mais également pour sa volonté d'aider à l'intégration dans l'entreprise et de former à plus que la recherche. Merci à Olivier Vo Van et Mac Lan Nguyen-Tajan, qui m'auront suivi durant les derniers mois de thèse (et qui ont donc eu la chance de relire le manuscrit ...).

Je remercie Nawfal Bouhout, qui m'a grandement aidé à développer des outils numériques lors de son stage de fin d'étude, et Xiqing Chang qui a réalisé les derniers essais alors que j'étais terré dans mon bureau pour rédiger ce manuscrit.

Un grand merci également aux nombreux ingénieurs et techniciens du LMS, Vincent de Greef, Jean-Christophe Eytard, Alexandre Tanguy, Simon Hallais, Eric Guimbretière, Hakim Gharbi, qui m'ont grandement aidé lors des essais et sans qui je n'aurais pu réaliser une telle campagne expérimentale. Merci encore à Eric et à Pascal, pour leur aide sur mes projets « hors thèse ». Merci au labo rail de SNCF de m'avoir accueilli pour les mesures de rugosité et l'ouverture de fissures dans des rails, à l'AEF de m'avoir permis de réaliser des mesures de contraintes résiduelles, et à Patrick Aimedieu du laboratoire Navier pour la tomographie.

Ce fut un réel plaisir de travailler au LMS (et il me semble que cela fait l'unanimité), tant les membres du laboratoire sont accueillants, abordables et enrichissants. La barre est placée très haut ! Je remercie tout particulièrement Alexandre & Alexandre, Simon, Clément, ainsi que Othmane, Yanis, Foucault, Jérémy, avec qui j'ai partagé l'intégralité de ces trois ans.

Je remercie également le personnel, les stagiaires et les prestataires de la Direction de l'Innovation et de la Recherche de SNCF, pour leur chaleureux accueil et la super ambiance.

Et pour finir, merci à mes parents, mes sœurs, mes amis, et bien sûr, à ma chère Sarah. Qu'il est bon d'être bien entouré !

Contents

Chapter 1

Introduction to the industrial problem

Contents

1.1 Introduction

Rails are submitted to Rolling Contact Fatigue (RCF) due to the repeated passages of train wheels. RCF cracks initiate on the rail surface, in the rail-wheel contact area, and propagate inside the rail. Due to the risks of rail failure, and potential accidents, such cracks are heavily monitored by SNCF. The associated maintenance policy is based on a damage tolerance approach.

In order to improve the understanding of the mechanisms responsible for the propagation of such cracks, and to optimize the maintenance rules, SNCF has developed a numerical tool to compute the local loading undergone by such cracks and their evolution [Trollé, 2014, Mai et al., 2017]. However, the modeling of the crack path and growth rate from the computed loading was simplified and not sufficiently predictive to simulate the crack propagation.

Those cracks undergo multiaxial loadings, including tension, compression and shear in variable proportions along the crack front and in time. Moreover, many factors may impact the loading amplitudes, such as the type of train and its dynamical behavior, the rail and wheel profiles, the track curvature, the rail stiffness, the meteorological conditions... making this a complex problem, as explained in the next sections.

Due to confidentiality reasons, some data have been removed from the manuscript.

1.2 Rails geometry, manufacturing and replacement

Three parts can be distinguished in a rail, as shown on figure 1.1.a. The top part, which is in contact with the wheel and from which Rolling Contact Fatigue (RCF) cracks initiate, is called the rail Head. It is linked to the foot through the web.

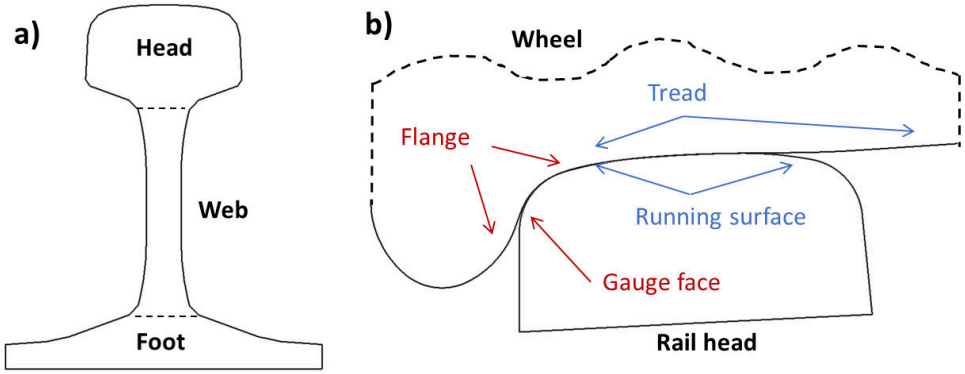

Figure 1.1: Rail nomenclature (a). Rail-wheel contact areas (b).

Those rails are made of low alloy steel, with various compositions and microstructures, depending on their usage and their manufacturing process. Pearlitic microstructures are the most commonly used, and the corresponding grades are denoted as R_{XXX} (for example $R260$), with XXX the Brinell hardness, which ranges from 200 to 370. In the case of heat treated rails, the suffix HT is added (for example $R350HT$). Harder rails have better tensile mechanical properties, but are not necessary better regarding RCF problems, as the wear induced by the passages of trains, which removes small defects, is less pronounced. Other microstructures can also be used, such as $B360$ steel, which is Bainitic.

Several profiles can be used, noted in European standard as ${}_{xx}E_{y}$ ($60E1$), where xx is the linear mass (for example 60 kg/m), and y a number used to differentiate rails with different shapes but similar linear mass. The higher the linear mass, the higher the bending stiffness, and the lower the bending stresses.

Rails are manufactured by a hot rolling process, following several steps, and then cooled down in ambient air, which induces some bending, due to a non uniform cooling (fig. 1.2.a). In order to correct this bending, the rails are straightened using a straightening machine (fig. 1.2.b) which induces some C-shaped residual stresses, as detailed later-on. The length of such rails can vary from a few meters to 108 m.

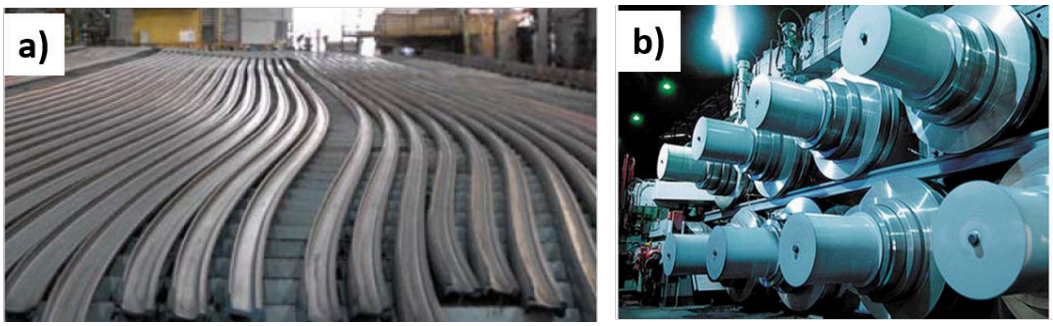

Figure 1.2: Manufacturing process: cooling (a) [SeverStal and Lucchini, 2009] and straightening (b) [C. Betegón Biempica et al., 2009].

Those rails pieces are then welded in the factory or on the field, using either alumino-thermic welding or flash welding. This induces microstructural changes in the Heat Affected Zone, but this is out of the scope of this study, which focuses only on plain rails. The on-field weldings are performed at a temperature $T \approx 20\ °C$. This is hot enough to avoid rail buckling due to a longitudinal compressive thermal stress when the operating temperature is higher, but not too hot, in order to limit the longitudinal tensile thermal stress when the operating temperature is lower, which is detrimental for the fatigue life (more details in section 1.3).

Rails are clipped on sleepers, which are usually laid on ballast, as shown in figure 1.3.a. The ballast consists of calibrated stones used -non exhaustively- to: hold the sleepers, distribute the load on the soil to avoid compaction, dissipate vibrations, drain water. Ballast and sleepers behave as springs regularly spaced under the rail in numerical simulations, as showed on 1.3.b. This stiffness has a large influence on the bending displacement of the rail, and thus on the stresses and crack growth rates.

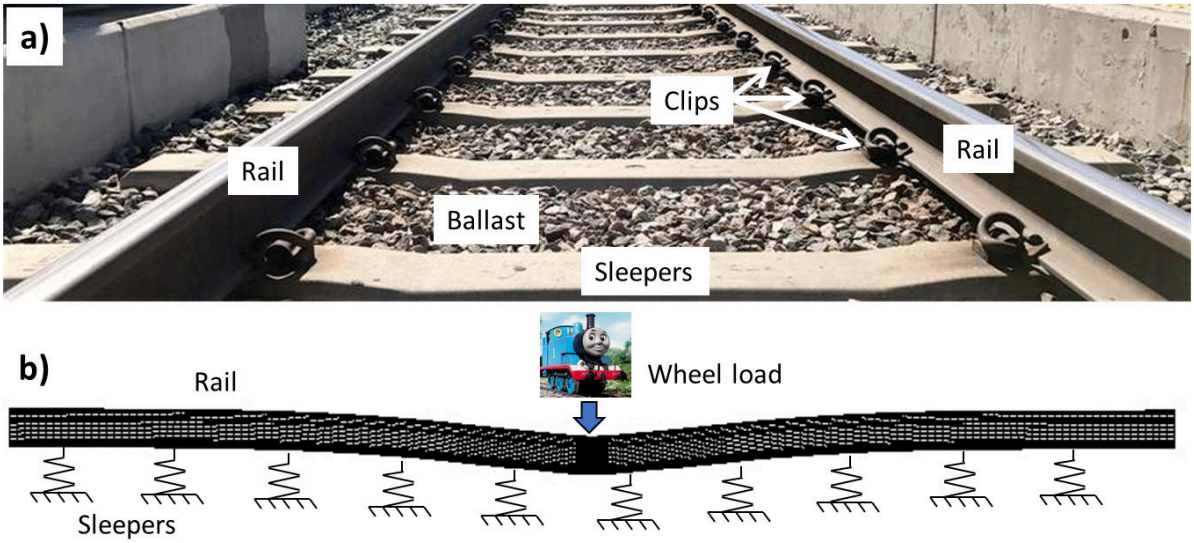

Figure 1.3: Track nomenclature (a). Equivalent Mechanical model (b).

Various types of trains (different masses and dynamic behavior) may circulate on the tracks, at various speeds. The wheel shape is described on figure 1.1.b. The tread is always in contact with the rail, while the flange is theoretically in contact with the rail only when in curves (due to the centrifugal force applied on the train).

Along with the various train loadings, rails may operate in very different external conditions: various temperatures, rain conditions, lubrication conditions, presence of salt or sand... More details on the induced loadings will be given in section 1.3.

If a rail portion is damaged (presence of cracks, excessive wear, excessive loss of material due to oxidation...), it can be replaced: the corresponding portion is cut (from a few meters to several hundreds of meters long), and an new portion is welded. At some point, the whole track is replaced, which can occur after only 5 years up to 80 years (on lines without passenger traffic), depending on the various parameters. Rails can usually sustain a few 500 MT of trains, meaning more than one million trains before being replaced.

1.3 Loadings

1.3.1 Train load

As explained earlier, the rail-wheel contact can occur on the rail running surface, but also on the gauge face of the external rail in curves, as shown on figure 1.4. This contact is often ideally modeled using Hertz's theory, where the contact stresses depends on the curvature of the two contacting surfaces. This contact area may vary: it is initially small, but it increases as plastic deformations and wear are generated at the rail surface.

The load per wheel axle can reach up to 23 tons, and is about $16 \sim 17$ tons for a TGV high speed train (the motor coach is usually heavier than the passenger coach). Such a TGV train has 10 cars, with 13 bogies, meaning that each train passage induces 26 loading cycles. In order to account for the variability in the type of trains, SNCF records the cumulative mega tons of passed trains.

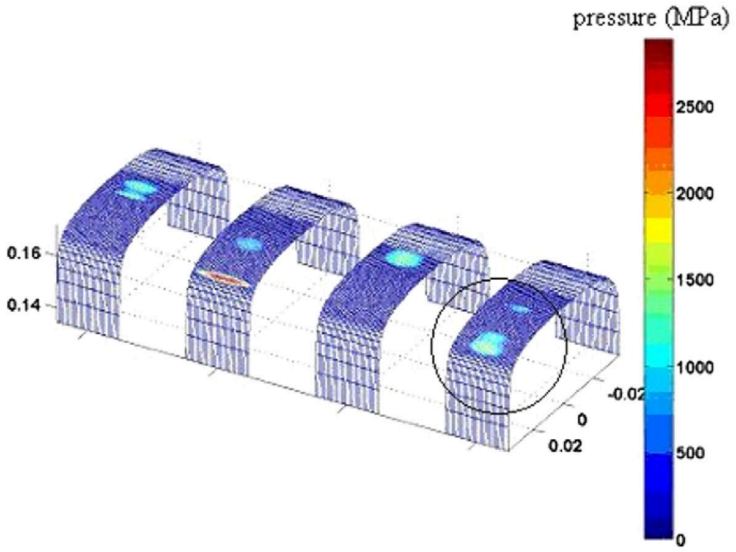

Figure 1.4: Contact area computed using VOCOLIN [Dang Van et al., 2009].

The contact load varies with the mass per wheel, but also with the track curvature, train type and train speed (train dynamic). Some defects in the rails can also induce additional dynamic forces, which can increase the vertical load by up to 60 % at 140 km/h [Zhao, 2012]. Defects in the wheel can also induce dynamic forces, as in Jonzac [BEATT, 2017], where a flattened wheel broke 13 cracks open.

1.3.2 Thermal stresses

As explained above, the rails are welded at a given temperature, and expand or contract depending on the outside temperature:

$$\underline{\underline{\epsilon}}_{th} = \underline{\underline{\underline{\underline{C}}}} * \underline{\underline{\sigma}}_{th} + \alpha * \Delta T * \underline{\underline{I}} \tag{1.1}$$

Since the rail length is fixed ($\epsilon_{th\ longitudinal} = 0$), longitudinal stresses will be induced, so that the rail will be under tension when the outside temperature is colder than the welding temperature, and under compression when it is warmer:

$$\sigma_{th\ longitudinal} = -E * \alpha * \Delta T \tag{1.2}$$

1.3.3 Residual stresses

As explained above, C-shaped residual stresses exist in rails due to the manufacturing process [Rodesch, 2013], following a distribution illustrated on figure 1.5. The repeated passage of train wheels induce high stresses in the contact area, leading to superficial compressive residual stresses ($\approx 5\ mm$ deep, see figure 1.5).

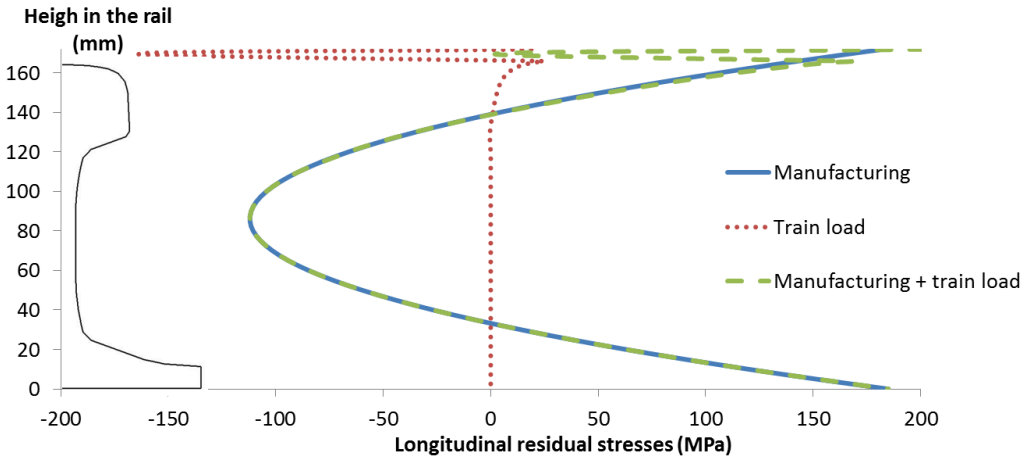

Figure 1.5: Evolution of the longitudinal residual stresses. Data from [Rodesch, 2013].

Due to those residual stresses, a crack on the top of the rail (but deeper than 5 mm) will remain open after the passage of a train.

1.3.4 Fluids

Fluids can be present on the track, such as water, or grease, which is used in curved sections to lower the wear induced by wheel sliding (the two contact areas, tread and flange, have different speeds, and sliding is thus unavoidable). Such fluids were shown to promote crack initiation [Kaneta and Murakami, 1987]. It is however unclear if they have an influence on the propagation of a long crack (more than 10 mm). The effects of fluids will be discussed in the following chapter.

1.4 Types of RCF cracks

Several type of RCF cracks can be observed on the field, outside of the heat affected zone near welded ends:

- Squats-type defects, which initiate from the running surface, and propagate quasi horizontally over a few *mm* to several *cm* before bifurcating at 70° relative to the horizontal axis, which can lead to a rail failure (figures 1.6.a & b).
- Head checks, which initiate from the gauge corner (in curves), propagate in the rail section and can lead to a rail failure (figure 1.6.c).
- Shelling, which is a network of cracks on the rail surface. It generally induces a loss of material but remains superficial (figure 1.6.d).

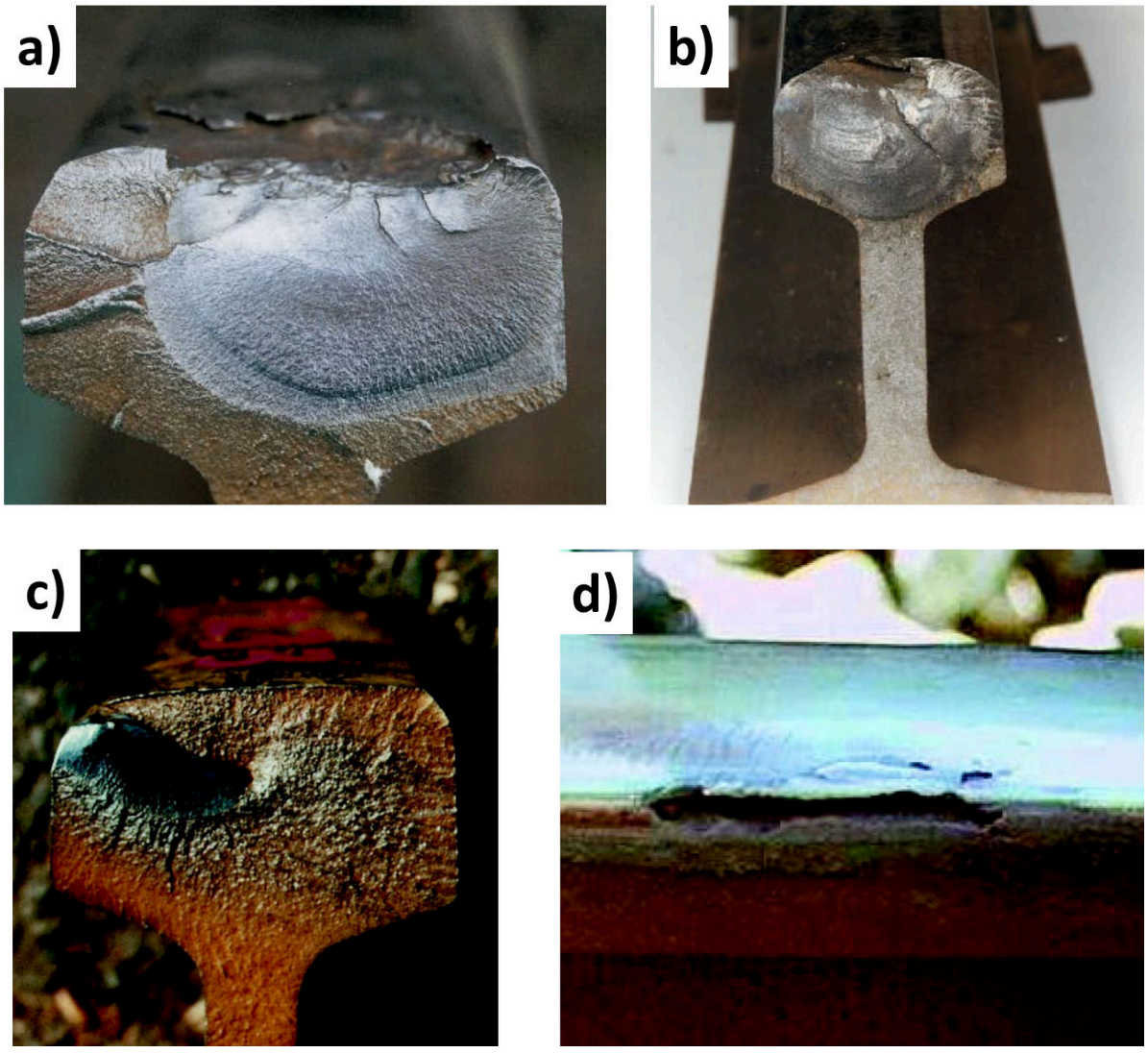

Figure 1.6: Main RCF defects (from [UIC, 2002], except fig. b.): Squat (a), Squat from Hatfield [ORR, 2006] (b), Head Check (c), Shelling (d).

This study will focus on Squat-type cracks, as it is the most frequent defect (especially in straight lines, where $R260$ rail steel is mostly used), responsible for more than 50% of the rail replacements.

1.5 Rails maintenance means and policy

Despite the monitoring and the maintenance repairs and replacements, a few hundreds of rail failures occurs each year in the French national network [BEATT, 2016] (see figure 1.7), among which a non negligible proportion of RCF defects.

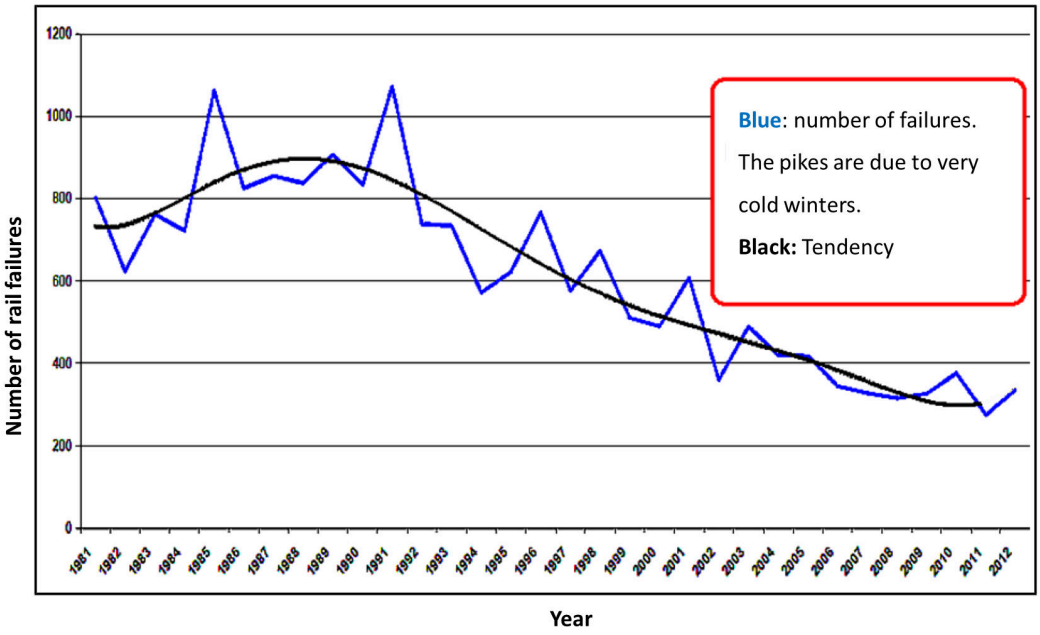

Figure 1.7: Evolution of the number of rail failure [BEATT, 2016] from every cause (not only RCF).

In most cases, rail failures are detected before any major incident occur. In some other cases, light material damage can occur, as in Carbonne in 2013 [BEATT, 2016], where a train went over 120 cm of missing rail due to a multiple fracture. Derailment did not occur thanks to the spacing between two wheels of a bogie ($\approx 2\ m$) being larger than 120 cm: three wheels were always on the rails.

In Saint flour, rail failure (not RCF) occurred on a welding in a curve and lead to a derailment without any casualties [BEATT, 2006].

The worst recent incident in Europe due to RCF occurred in Hatfield, UK, where multiple fracture led to 35 m of missing rails, a train derailment and 4 casualties [ORR, 2006].

Those cracks can be "naturally" removed by the wear induced by the rail-wheel contact. This supposes that the wear rate is sufficiently high relative to the crack growth rate.

When "natural" wear is not sufficient, rail grinding can be performed using specific grinding trains. This grinding aims at recovering the correct rail profile and remove small cracks. It can be performed over a depth of up to 0.5 mm.

The type of rail steel can also be chosen to limit certain defects. Indeed, some steels are more resistant to RCF than other depending on the configuration: harder steels ($R350HT$) perform better in curves (where Head-Checks appears), while regular railway steels ($R260$) perform better in straight lines (where Squats appear) [Innotrack, 2009]. New types of steels, such as bainitic steel, could be less prone to RCF cracking. They are currently tested by several railway infrastructure managers.

However, if those solutions can reduce the number of RCF cracks, none of them can totally avoid that RCF crack will propagate up to failure.

In order to avoid rail failure, a damage tolerance approach is used. Rails are inspected periodically using non destructive means, such as eddy currents or ultrasonic detection (as illustrated on figure 1.8).

Figure 1.8: Ultrasonic testing of a rail: a cart containing the transmitter and receptor is pushed manually over the track.

The inspection intervals have to be sufficiently frequent, so that a crack that was not detected during the previous inspection does not propagate up to failure before the next one. Since the detection means have a resolution of a few mm, it means that any crack smaller than a few mm should not be able to propagate up to failure in a given time.

To adjust the frequency of those inspection intervals, a way to predict the crack growth rate and path is thus needed.

1.6 Predicting RCF crack growth rate

Every crack detected on SNCF's network has been monitored and recorded into a database, called "DEFRAIL", for more than 20 years. From this database, it is possible to derive the average crack growth rate of a Squat depending on various parameters. The average crack growth rate of 10 mm deep Squats in TGV lines (obtained from 324 on-field measured values) is given in table 1.1.

Table 1.1: On-field measured crack growth rate of 10 mm deep Squats in TGV lines.

Average $(m/cycle)$	1^{st} decile $(m/cycle)$	9^{th} decile $(m/cycle)$
confidential	*confidential*	*confidential*

These data can be used for the damage tolerance approach. However, they do not give a physical understanding of the ongoing phenomena, which is key to find new solutions to control RCF defects. Moreover, the data are not sufficient to get a clear idea of the influence of every parameter, for example the temperature, which is known to

be important (most of the rail failures occur during winter). Finally, in the case of a change of some parameters (train masses, rail composition...), those data would be almost unusable.

In order to get a better understanding of RCF crack initiation and propagation, SNCF developed a multi-scale computations scheme, as illustrated on figure 1.9.

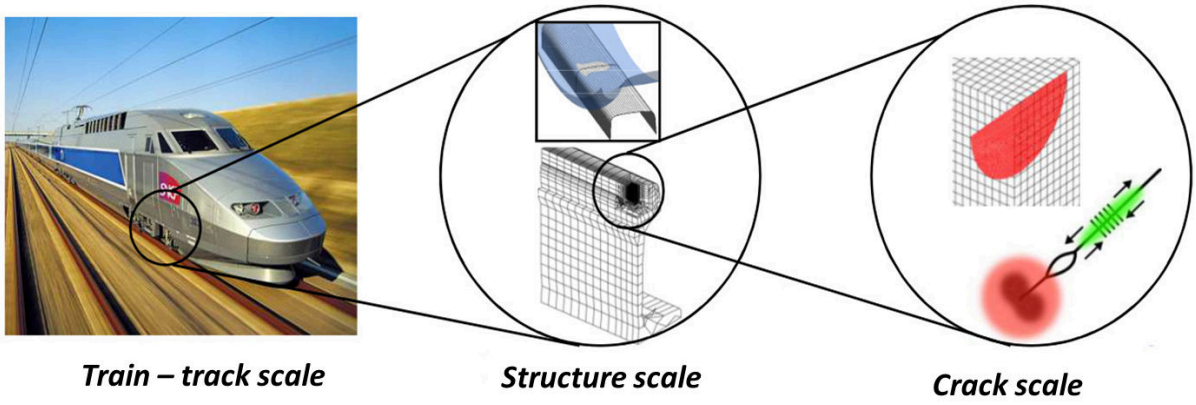

Figure 1.9: Multi-scale computation scheme [Trollé, 2014].

Multi-body simulations are performed at the train-track scale (using for example VOCOLIN software, from IFSTTAR) to compute the rail-wheel contact stresses (using Hertz & Kalker's theory [Kalker, 1979]). Using those stresses as an input, elastic-plastic computations are performed to find the stabilized cyclic state [Maouche et al., 1997] and evaluate the risk of crack initiation according to Dang Van's fatigue criterion [Dang Van, 1973]. More details on the numerical modeling are given in [Nguyen-Tajan and unfschilling, 2011].

Using the rail-wheel contact stresses, computations representing a wheel passing over a crack can also be performed in Cast3M [cas, 2019] FEM software. Those computations couple two very different scales: the rail, which is a few meters long, and the crack, which is a few mm long. The behavior of the crack is non linear, as friction and contact occur between the crack faces. In order to solve the problem in a reasonable time, an XFEM model taking into account the contact and friction between the crack faces was developed. The problem is solved iteratively using the LATIN method [Ladevèze, 1999] with a weak coupling between the structure and the contact/friction interface [Trollé, 2014].

From those computations, the evolution of all three stress intensity factors during one wheel passage can be derived. Some preliminary numerical results were obtained and presented in [Mai et al., 2017]. However, SNCF still lacks a physical model to predict more accurately the crack growth rate and direction which takes into account all the complexity of the loads, and is identified with an exhaustive set of material tests. This is the object of this work.

1.7 Summary

Rails are submitted to Rolling Contact Fatigue (RCF) due to the repeated passages of train wheels, coupled with other phenomena (residual stresses, thermal stresses...).
Several types of RCF defects can be induced, among which the Squat, which initiates at the top of the rail and propagates almost horizontally, before bifurcating towards a nearly vertical direction and growing up to failure. This study will mostly focus on this defect, as it is the mostly observed one, responsible for 50% of the rail replacements.
Such RCF defects need to be avoided for obvious safety reasons. In order to do so, a damage tolerance approach is applied, which requires the ability to predict the crack growth rate. A multi-scale computation scheme with XFEM computations was developed for this purpose, but a physical model to predict the crack path and growth rate is still needed, which is the object of this work.
$R260$ rail steel (pearlitic microstructure) will be studied, as it is the most commonly used in straight lines, where Squats occur.

Chapter 2

Bibliography

Contents

2.1 Squat-type cracks - Early stage

The repeated passage of train wheels induces high cumulated shear plastic strains at the top of the rail, below the running surface, by a ratcheting phenomenon. For $R260$ rail steel, such strains lead to microstructural evolutions at the very top of the rail (few tenth of μm), from pearlite to martensite due to carbon migration from cementite towards ferrite. This layer, called the White Etching Layer (WEL), is stiffer ($\approx 240\ GPa$ versus $\approx 200\ GPa$) and harder than the base metal, which might cause crack initiation in the WEL, or at the interface between the two layers, as proposed by Simon [Simon, 2014].

Below the WEL, the microstructure is still pearlitic, but the pearlite lamellae are reoriented along the shearing direction, and the grains are refined within a depth of a few mm (3 mm, as measured by Dylewski et al. [Dylewski et al., 2017] in $R260$), as shown on figures 2.1. In this layer, the crack propagates along the lamellae, at $\approx 20°$ relative to the rail axis.

Below a depth of a few mm (4 mm in [Dylewski et al., 2017]), the microstructure remains unchanged, and the crack bifurcates at $\approx 70°$ relative to the rail axis (fig. 2.1). It then continues to growth in this plane, up to rail failure at a depth of ≈ 25 to $50\ mm$.

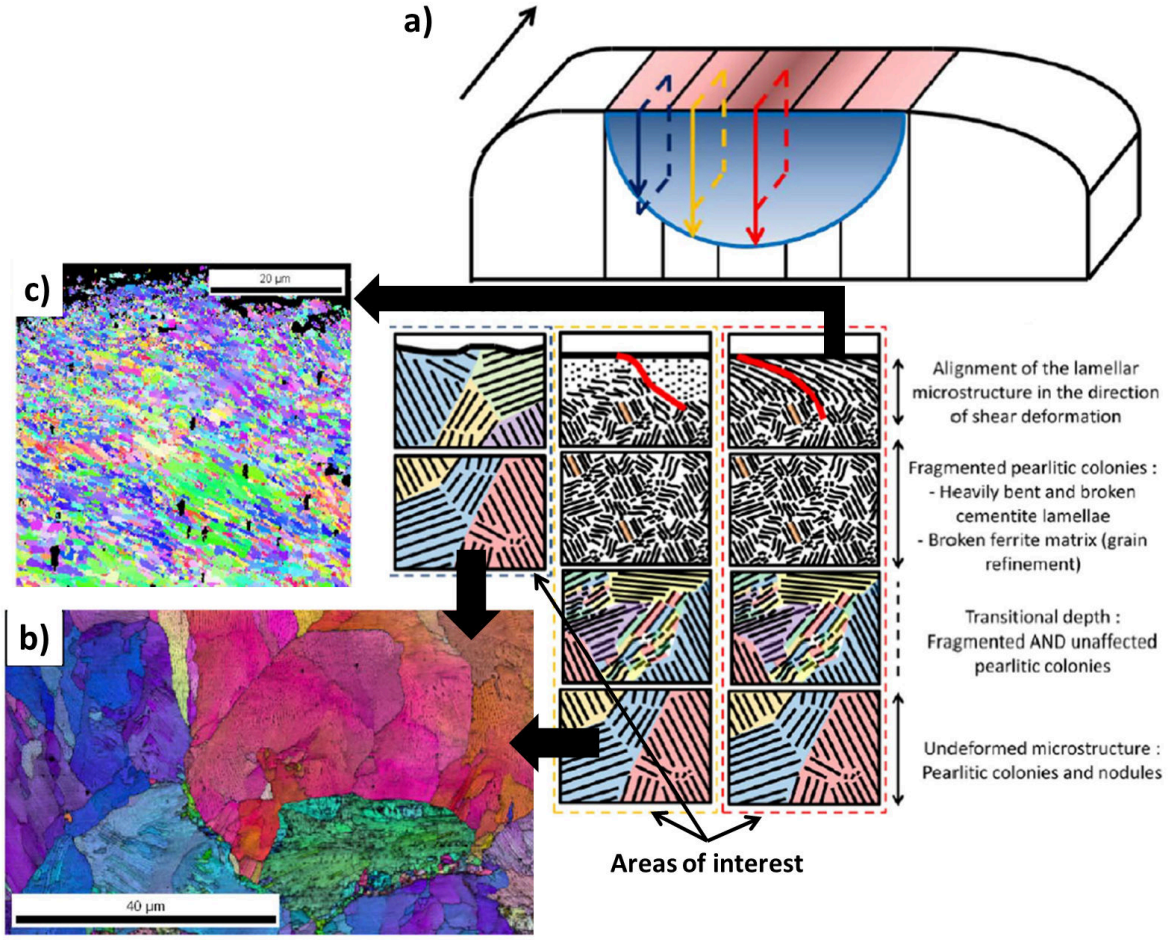

Figure 2.1: Schematic view of the gradient of microstructure at various positions relative to the running surface (a), along with EBSD (Electron Back Scattered Diffraction) images (b & c), from [Dylewski et al., 2017].

A model to predict the crack path and growth rate in this anisotropic layer was proposed by Larijani et al. [Larijani et al., 2014], using an anisotropic propagation threshold, as shown on figure 2.2. The larger this threshold in a given direction β, the "harder" the propagation in this direction. The non-propagation threshold surface evolves with the depth, until it becomes isotropic (circle in figure 2.2). Depending on the degree of anisotropy, Larijani et al. obtained very different crack paths, as illustrated in figure 2.3: some cracks are going down, as Squats do, and others are going up, which corresponds to flaking. Although the model allows interesting parametric studies, it is only 2D and no quantitative comparisons of its predictions with on-field observations was provided

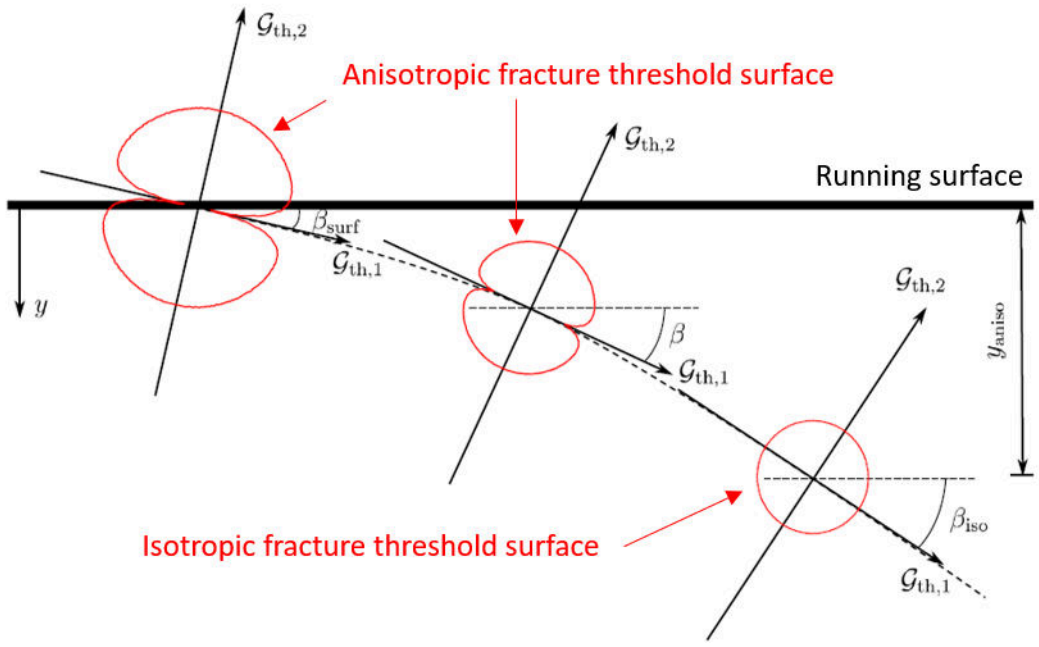

Figure 2.2: Evolution of the non-propagation threshold surface with the depth in the rail [Larijani et al., 2014].

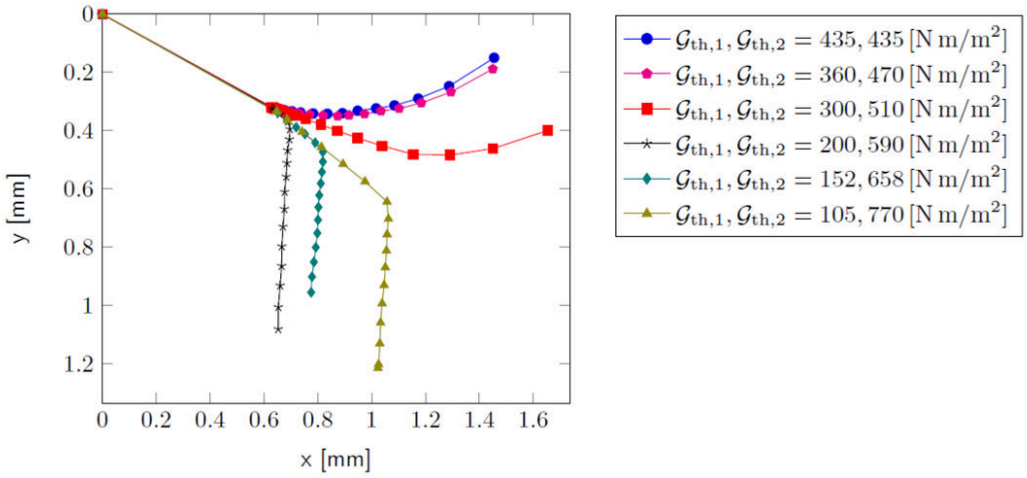

Figure 2.3: Predicted crack paths for different degrees of anisotropy [Larijani et al., 2014].

The shape of a Squat estimated by Simon et al. [Simon et al., 2013], using a succession of millings and measurements on the running surface, is represented on figure 2.4. The yellow surface corresponds to the quasi-horizontal

propagation in the highly plastified layer, while the green area corresponds to the bifurcation at $\approx 70°$ relative to the rail axis. Several branches initiate from this main crack, at various angle, as shown by Jessop et al. [Jessop et al., 2016] using X-ray tomography (see figure 2.5). Such branches may shield the main crack tip and reduce its growth rate.

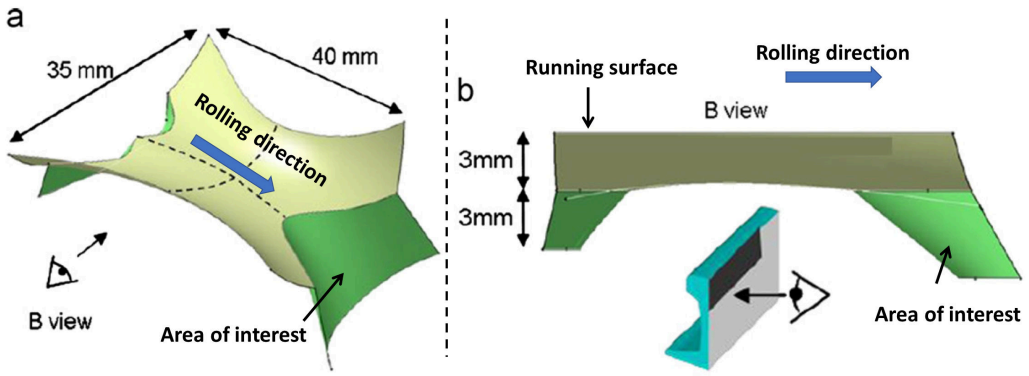

Figure 2.4: 3D Reconstruction of a Squat from [Simon et al., 2013]: isometric (a) and lateral (b) view.

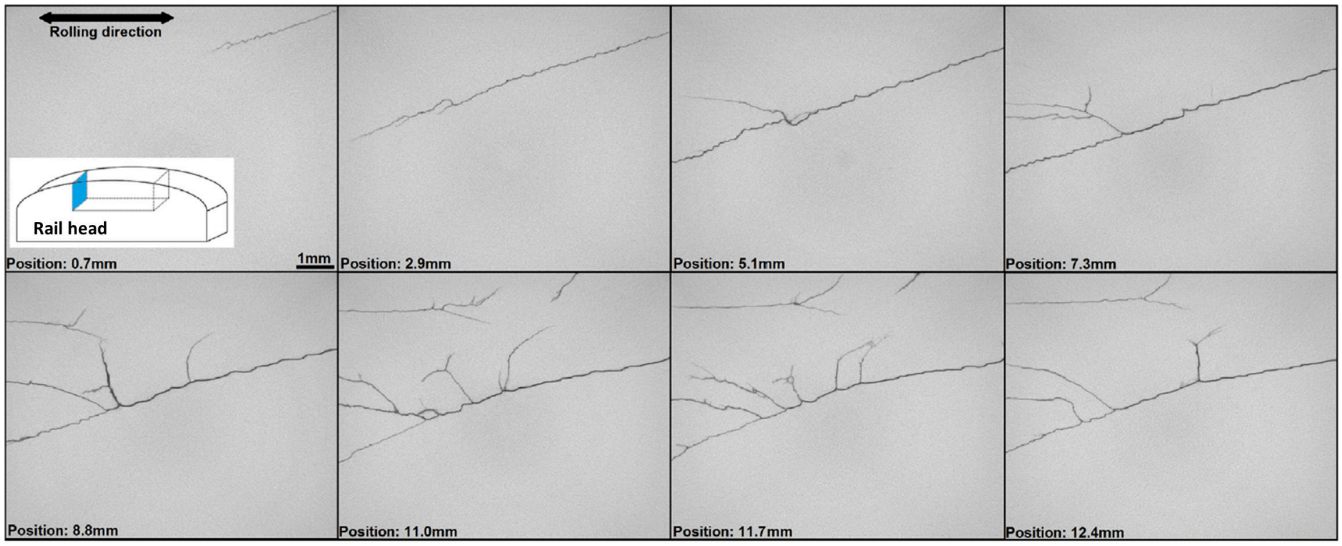

Figure 2.5: Sections of a Squat, at various positions transverse to the rolling direction [Jessop et al., 2016].

The wear induced by the wheel passage tends to remove such cracks, so that RCF and wear compete. Several attempts were made to model such competition, for example by Donzella et al. [Donzella et al., 2005]. However, the high anisotropy in the initiation area makes such modeling a challenge, as the evaluation of the crack propagation rate (which must be compared to the wear rate) is difficult. The effect of wear on the propagation of long Squats (already bifurcated) will be neglected in this study.

In the following, only Squats deeper than the plastified layer and already bifurcated will be considered. Indeed, for a damage tolerant approach, only cracks deeper than the detection threshold are relevant, which corresponds more or less to the depth of the plastified layer. Moreover, Squats really become dangerous once bifurcated towards the quasi vertical direction.

In order to study the fatigue-induced propagation of such long cracks in an isotropic, elastic material, Linear Elastic Fracture Mechanics (LEFM) is relevant, and its basic concepts will be presented next.

2.2 Linear Elastic Fracture Mechanics

2.2.1 Crack-tip stress field for a linear elastic medium

The presence of a crack in an elastic medium (as illustrated by fig 2.6) leads to singular stresses at the crack front. To account for such fields, the concept of stress intensity factors was proposed by Irwin. For a crack in a 2D plate (plane stress or plane strain) in an isotropic material, the crack tip stress field can be written (using Westergaard or Williams solutions) as:

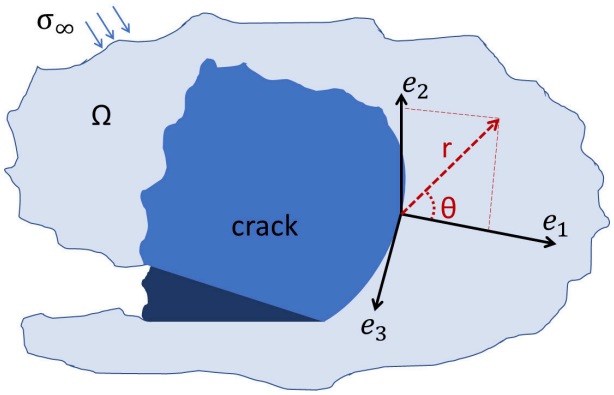

Figure 2.6: Schematic of a crack.

$$\underline{\underline{\sigma}} = \frac{K_I}{\sqrt{2\pi r}} * \underline{\underline{F}}^I(\theta) + \frac{K_{II}}{\sqrt{2\pi r}} * \underline{\underline{F}}^{II}(\theta) + \frac{K_{III}}{\sqrt{2\pi r}} * \underline{\underline{F}}^{III}(\theta) + O(\underline{\underline{1}}) \tag{2.1}$$

With K_I, K_{II}, K_{III} the mode I, II, III Stress Intensity Factors (SIFs) respectively, and $\underline{\underline{F}}^i$ some known functions, independent of the geometry. Close to the crack tip, in what is called the K-dominance zone, the stress field can be described solely by those SIFs. Each of those SIF corresponds to a different crack kinematics, as described on figure 2.7: mode I correspond to crack opening, mode II to in-plane shear and mode III to out-of-plane shear. This effect of each mode on the crack kinematics can be seen on the equation of the relative displacement jump between the crack faces (each SIFs induces a displacement along only one coordinate axis):

$$\underline{U}(r,\pi) - \underline{U}(r,-\pi) = [\underline{U}](r) = \frac{2(1+\nu)}{E}\sqrt{\frac{r}{2\pi}} * ((\kappa+1)K_I\underline{e}_2 + (\kappa+1)K_{II}\underline{e}_1 + 4K_{III}\underline{e}_3) \tag{2.2}$$

with $\kappa = \frac{3-\nu}{1+\nu}$ in plane stress or $\kappa = 3-4\nu$ in plane strain, E the Young's modulus and ν the Poisson's ratio.

If crack propagation is supposed to be driven by the stresses and strains infinitely close to the crack-tip, the higher order terms in $\underline{\underline{\sigma}}$ (equ. 2.1) become negligible, and propagation can be described solely by the knowledge of the three SIFs (as the Paris law and other models detailed later-on supposed). For example, the crack growth rate $\frac{da}{dN}$ can be predicted as:

$$\frac{da}{dN} = f(K_I, K_{II}, K_{III}) \tag{2.3}$$

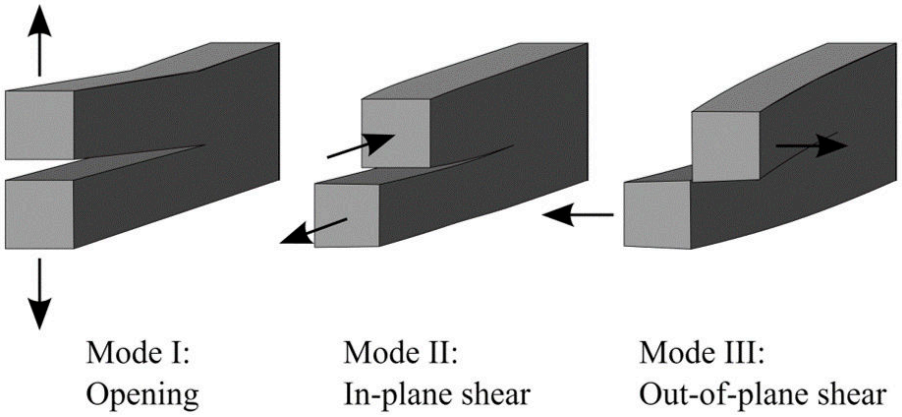

Figure 2.7: Displacements induced by the three modes.

However, if the crack propagation is supposed to be driven by the stresses and strains at a given distance to the crack-tip (or if the material is not elastic, as detailed later-on), higher order terms ($O(1)$ in equ. 2.1) might also play a role:

$$\frac{da}{dN} = f(K_I, K_{II}, K_{III}, \text{higher order terms}) \tag{2.4}$$

Those are called the non-singular stresses (as they do not go to infinity close to the tip). The most studied is the T-stress, that is along the e_1 direction, so that the stress fields writes:

$$\underline{\underline{\sigma}} = \frac{K_i}{\sqrt{2\pi r}} * \underline{\underline{F}}^i(\theta) + T\, \underline{e}_1 \otimes \underline{e}_1 + O(\underline{\underline{1}} - \underline{e}_1 \otimes \underline{e}_1) + O(r^{1/2} \underline{e}_1 \otimes \underline{e}_1) \tag{2.5}$$

Other non singular stresses can exist: compression/tension along $\underline{e}_3$ (σ_{33}), compression along $\underline{e}_2$ (closed crack, $\sigma_{22} < 0$) and shear along any plane when friction stresses exist along the crack.

The energy release rate and critical energy release rate are defined, respectively, as:

$$G = \frac{W_{ext}}{\Delta A} - \frac{\Delta U_{strain}}{\Delta A} \tag{2.6}$$

$$G_c = 2 * \gamma \tag{2.7}$$

Where A is the crack surface, γ a term linked to the energy dissipated in the decohesion mechanism, W_{ext} the external work and U_{strain} the strain energy. Unstable crack growth occurs when the energy released by the structure due to crack growth is equal to the energy required to propagate the crack:

$$G = G_c \tag{2.8}$$

For a straight, frictionless crack, Irwin has shown that G is related to the stress intensity factors by:

$$G = J = \frac{1}{E'}(K_I^2 + K_{II}^2) + \frac{1-\nu}{E} K_{III}^2 \tag{2.9}$$

with $E' = E$ in plane stress and $E' = E/(1-\nu)$ in plane strain. In fatigue, the amplitude $\Delta G = \max_{cycle} G - \min_{cycle} G$ is sometimes used.

2.2.2 Crack-path under monotonic loading

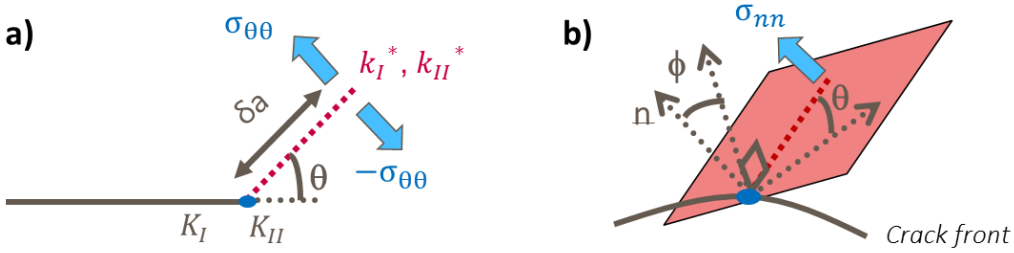

Figure 2.8: Principle of the MTS and max k_I^* criterion in 2D (a) and 3D (b).

The crack path under a monotonic loading can be predicted using LEFM-based criteria. Erdogan & Sih [Erdogan and Sih, 1963] proposed the Maximum Tangential Stress (MTS) criterion to predict the crack path: a crack propagates in the direction where the tangential stress ahead of the crack tip is maximum (see figure 2.8). In mixed-mode I & II, this writes:

$$\frac{\partial \sigma_{\theta\theta}}{\partial \theta} = 0 \text{ and } \frac{\partial^2 \sigma_{\theta\theta}}{\partial \theta^2} < 0 \tag{2.10}$$

and using equation 2.1:

$$\theta = 2arctan\left[\frac{1}{4}\left(\frac{K_I}{K_{II}} - sgn(K_{II})\sqrt{\left(\frac{K_I}{K_{II}}\right)^2 + 8}\right)\right] \tag{2.11}$$

While for mode III:

$$\phi = 2arctan\left(\frac{2K_{III}}{K_I(1-2\nu)}\right) \tag{2.12}$$

This criterion predicts a tilt at $-70.5°$ in pure mode II, and a twist at $45°$ in pure mode III.

The crack can also be supposed to propagate in the direction which maximizes K_I on an infinitesimal branch ahead of the crack tip, noted k_I^* (see figure 2.8):

$$\max_\theta k_I^*(\theta, K_I, K_{II}, K_{III}) \tag{2.13}$$

Where $k_I^*(\theta, K_I, K_{II})$ can be obtained using Amestoy's abacus [Amestoy et al., 1979]. In pure mode II, this criterion predicts a bifurcation at $-77.3°$, not so far from the $-70.5°$ predicted by the MTS criterion.

Similarly, the crack can be supposed to propagate in the direction for which k_{II}^* (K_{II} on an infinitesimal branch ahead of the crack tip) vanishes:

$$\theta \,|\, k_{II}^*(\theta, K_I, K_{II}, K_{III}) = 0 \tag{2.14}$$

Another criterion can be derived using the energy release rate G:

$$\max_\theta G^*(\theta, K_I, K_{II}, K_{III}) \tag{2.15}$$

which predicts bifurcation at $76.6°$ in pure mode II.

2.2.3 Crack tip plasticity

The previous formulae were obtained for elastic materials. However, metallic materials exhibit an elastic-plastic behavior and thus plastic deformation near the crack tip, where the stress level is high, forming the crack-tip plastic zone.

The shape of this plastic zone under plane stress/strain conditions is given on figure 2.9 using Von Mises criterion. In mode I, its extent ahead of the crack tip can be estimated roughly as:

$$r_p^I = \frac{1}{2\pi}\left(\frac{K_I}{\sigma_Y}\right)^2 \text{ in plane stress} \tag{2.16}$$

$$r_p^I = \frac{1}{2\pi}\left(\frac{K_I}{\sigma_Y}\right)^2 (1-\nu)^2 \text{ in plane strain} \tag{2.17}$$

And in mode II or III:

$$r_p^{II} = \frac{3}{2\pi}\left(\frac{K_{II}}{\sigma_Y}\right)^2 \text{ in plane stress or plane strain} \tag{2.18}$$

$$r_p^{III} = \frac{1}{\pi}\left(\frac{K_{III}}{\sigma_Y}\right)^2 \text{ in plane stress or plane strain} \tag{2.19}$$

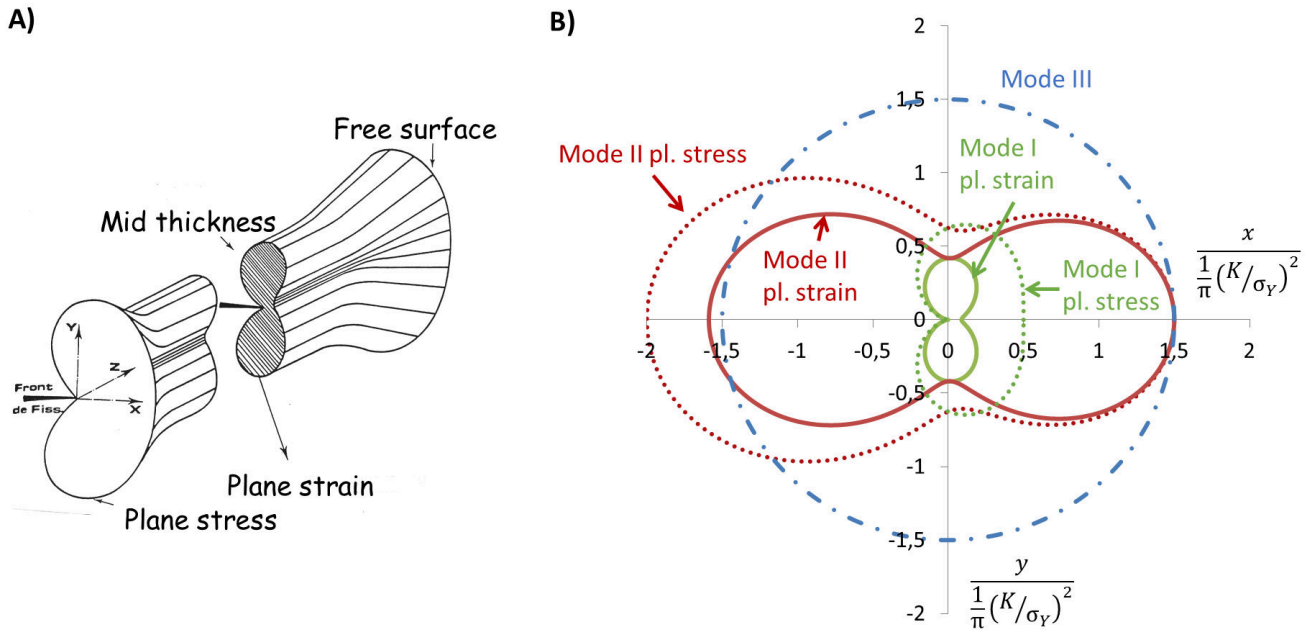

Figure 2.9: Shape of the monotonic plastic zone, under plane stress (in the bulk) or plane strain (on the surface) in mode I (A&B), mode II (B) and mode III (B). $\nu = 0.29$

These formulae do not take into account the plasticity-induced stress redistribution, and FEM computations are required to evaluate the real size and shape of the plastic zone. If σ_∞ approaches σ_Y, the plastic zone is much larger than what is predicted by this formula and restrictions on its size, compared to the crack size and all structural dimensions, have to be fulfilled for LEFM to be valid ([Lemaitre et al., 2009]). In this study, these conditions were always satisfied, except when otherwise mentioned.

Furthermore, these formulae estimate the size of the plastic zone after a monotonic loading on a structure in a virgin state (in terms of plastification). However, when several cycles are applied, residual stresses appear, the material adapts, leading to a reduction of the zone that undergoes cyclic plasticity (called cyclic plastic zone) relative to the monotonic plastic zone (see figure 2.10). The size and shape of this cyclic plastic zone depends on the amount and type of cyclic hardening: Isotropic or Kinematic.

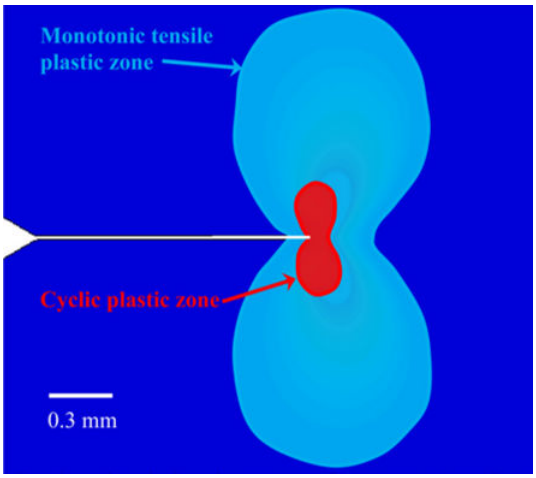

Figure 2.10: Shape of the monotonic and cyclic plastic zones, under plane strain conditions, in mode I, from [Paul and Tarafder, 2013].

2.2.4 3D effects in LEFM

The concept of SIFs, with the $1/\sqrt{r}$ singularity, is valid for points of the crack front located in the bulk of the structure. However, Bazant and Estenssoro [Bazant and Estenssoro, 1979] showed that at corner points, the singularity is not necessarily $1/\sqrt{r}$, but varies with the crack emergence angle (and the Poisson's ratio, ν).

In order to keep the $1/\sqrt{r}$ singularity, this angle has to be $> 90°$, and a rising function of ν in mode I, while in mode II & III, it has to be a decreasing function of ν and $< 90°$, as illustrated on figure 2.11. For a sample precracked in mode I and then loaded in cyclic mode II & III from [Doquet et al., 2010a], the emergence angle was $> 90°$ during the mode I part of the experiment, and $< 90°$ during the mode II & III part. It means that the crack front shape near the surface progressively adjusted until the $1/\sqrt{r}$ singularity was recovered.

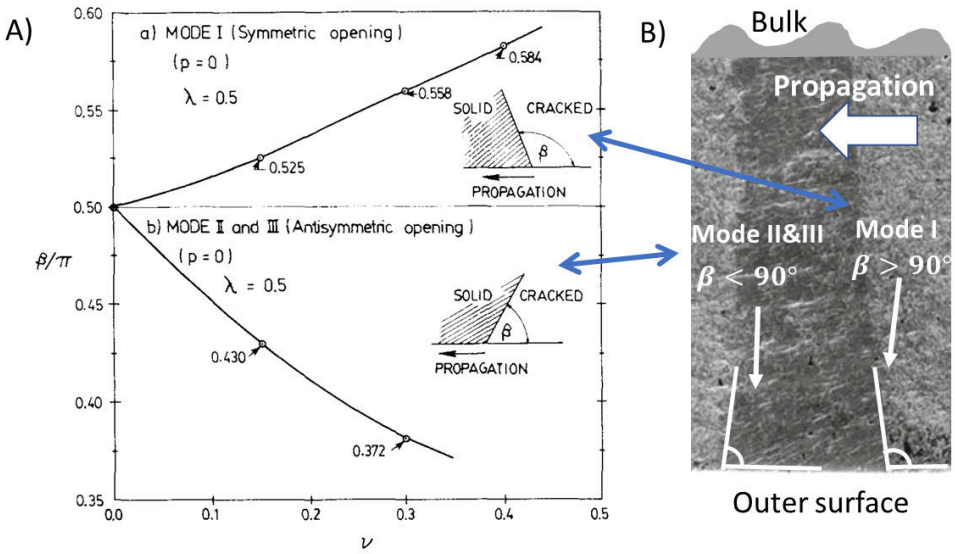

Figure 2.11: A) Evolution of the emergence angle leading to $\lambda = 0.5$ in mode I and mode II & III with the Poisson's ratio from [Bazant and Estenssoro, 1979]. B) Fracture surface after mode I precracking followed by mode II & III experiment from [Doquet et al., 2010a].

However, in mixed mode experiments, where mode I and mode II & III exist within each cycle, the emergence angle cannot allow a $1/\sqrt{r}$ singularity for each mode. LEFM is thus unable to describe crack propagation at corner points under combined opening and shear modes, as the SIFs do not represent the stresses and strains ahead of the crack tip for at least one of the modes.

Near those free surfaces, a mode II loading induces some mode III, due to the presence of a singular, skew symmetric stress parallel to the crack and to Poisson's effect, as explained on figure 2.12. Such a coupling between both shear modes is retrieved when the evolution of the SIFs along the front of a through crack is computed using the Finite Element method.

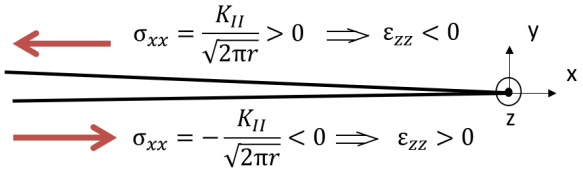

Figure 2.12: Mode II and Poisson's effect inducing expansion/contraction along z, leading to mode III.

Now that the basic concepts of LEFM have been introduced, it is possible to use it to analyze the mechanical loading on Squat-type cracks in relation with the external forces and thermal conditions.

2.3 Loading on Squat-type cracks

The time evolution of the SIFs during the passage of a train wheel over a Squat-type crack, as illustrated on figure 2.13, was evaluated by Bogdanski et al. and Mai et al. [Bogdanski et al., 1998, Mai et al., 2017]. Those studies showed that surface cracks are loaded in non proportional mixed mode I+II+III in variable proportions along their front, as illustrated on figure 2.14.

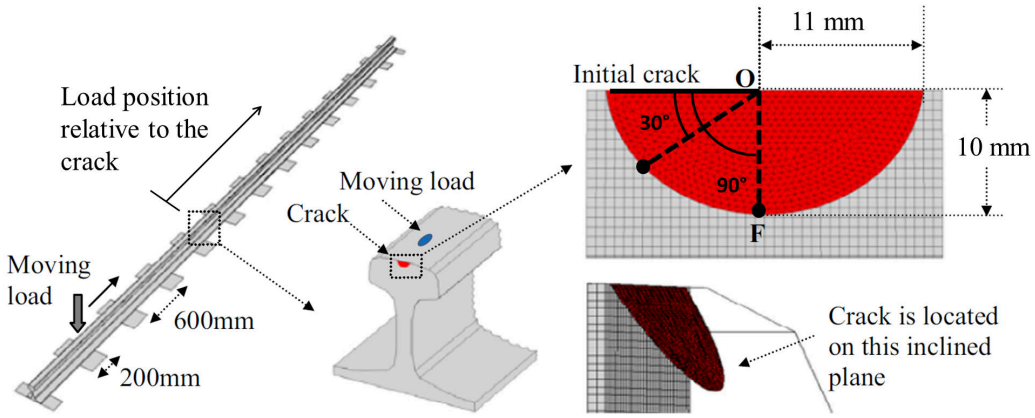

Figure 2.13: 3D rail model with one semi-elliptical Squat-type crack on the rail surface (figure taken & modified from [Mai et al., 2017])

Those SIFs evolutions were obtained from simulations using SNCF's computation scheme [Trollé, 2014, Mai et al., 2017], taking into account the manufacturing residual stresses, thermal stresses, rail bending and a frictionless crack. When the wheel is far away from the crack, the crack is opened due to thermal and residual stresses. As the wheel gets closer to the crack, the rail bends downwards, which closes and compresses the crack, which is sheared alternatively as the wheel passes.

At the deepest point of the crack (90° in the reference frame of 2.13), loading is nearly a sequence of mode I and mode II, as showed on figure 2.15, while at 30°, mode III is also present (fig. 2.14), and mode II is reduced: here, loading is a sequence of mode I and both shear modes. The amplitude ΔK_I is strongly dependent on the thermal stresses, as discussed later in chapter 4, and, if no fluid trapping and pressurization is considered, the crack is closed and under compression during the shearing stage of the loading cycle. This compression leads to friction between the crack faces, and thus a reduction of the shear mode singularities.

Those singularities vary with the parameters mentioned in 1.3, at very different frequencies: the temperature changes at a 24h period, while the train mass or train dynamic forces may vary between each train or even between each bogie. As discussed later, crack path and growth rate prediction under non-proportional mixed-mode loading with compression phases is a challenge in itself, which leads us to neglect the aspects of variable amplitude loading in the rest of the study.

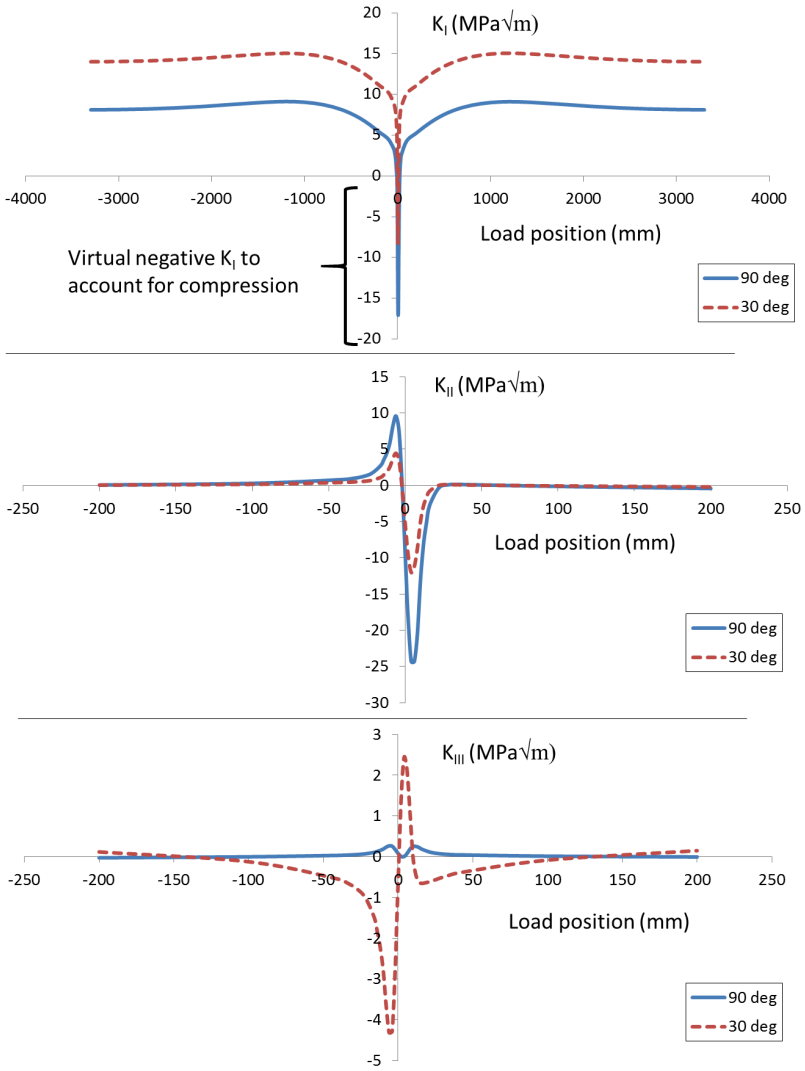

Figure 2.14: Evolution of the SIFs on two points at 30° and 90° on the crack front (see on fig. 2.13) versus the load position. TGV motor load (8.5 kN). 30 MPa longitudinal thermal stresses, corresponding to a 5° temperature. No friction between the crack faces. Residual stresses taken into account.

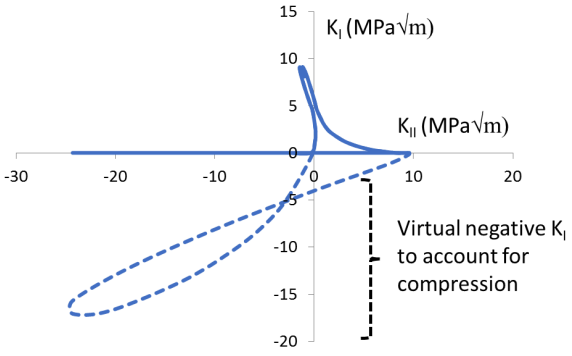

Figure 2.15: Loading path in $K_I - K_{II}$ space at the deepest point of the crack front (90°, see on fig. 2.13). TGV motor load (8.5 T). 30 MPa longitudinal thermal stresses, corresponding to a 5° temperature. No friction between the crack faces. Residual stresses taken into account.

Some authors suggested that fluids may play a role in the initiation and propagation of Squats. It has been shown experimentally [Kaneta and Murakami, 1987] that it favours the initiation and propagation of relatively short cracks (up to a few mm), due to penetration of the fluid inside the crack leading to: lubrication of the crack increasing the shear modes singularities, and fluid pressurization or entrapment, inducing an opening of the crack, as illustrated on fig. 2.16. Such phenomena have been modeled by many authors, such as [Kaneta and Murakami, 1987, Fletcher and Beynon, 1999, Bogdanski and Lewicki, 2008, Ancellotti et al., 2017]. However, few experiments have been performed for a Squat-type crack deeper than 5 mm, for which fluid penetration down to the crack tip might be difficult. Fletcher [Fletcher et al., 2007] had trains circulate over rails containing cracks and covered with a marking fluid. The cracks were broken open after several load cycles, and it appeared that the marking fluid did not penetrate down to the crack tip (but remained at 1-2 mm behind it). This contradicts the idea of crack tip opening due to fluid pressurization or entrapment. It is however still possible that such fluid lubricates the crack faces a few mm behind the tip, leading to an increase in the effective shear SIFs.

In the rest of the study, the effects of fluid pressurization or entrapment will thus be neglected.

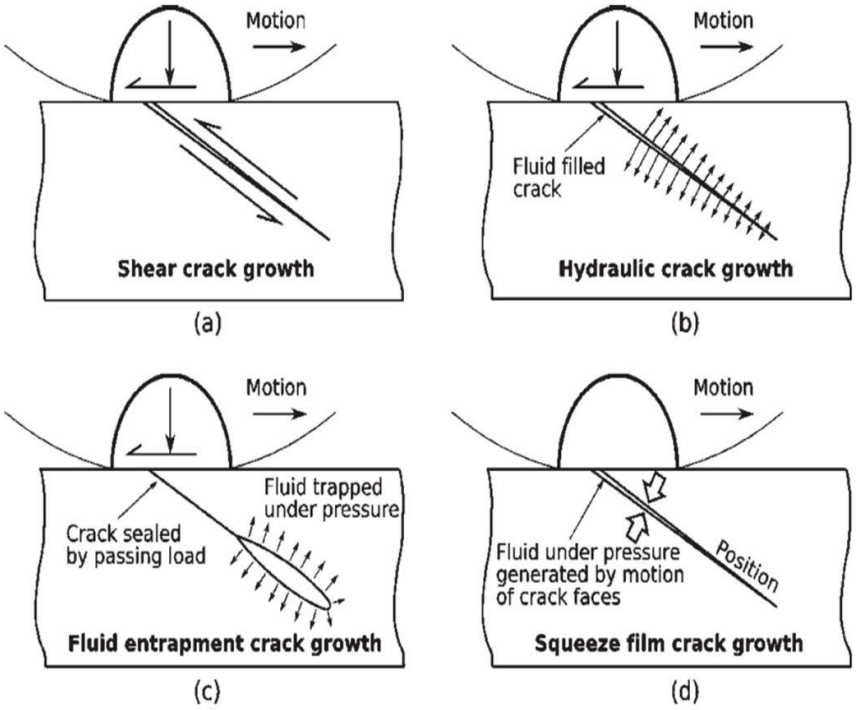

Figure 2.16: Illustration of the effects of entrapped water from [Fletcher et al., 2007].

The sequential loading undergone by Squat-type cracks includes a quasi pure mode I cycle, and one of the aims of this study is to determine if this loading alone might explain the crack growth in rails. Basic notions about mode I fatigue crack growth will thus be provided in the following paragraph.

2.4 Mode I fatigue crack growth

Fatigue cracks loaded in pure mode I exhibit a coplanar growth (at least at macro-scale), and their growth rate is usually predicted using:

$$\Delta K_I^{nominal} = \max_{cycle}(K_I) - \min_{cycle}(K_I; 0) \tag{2.20}$$

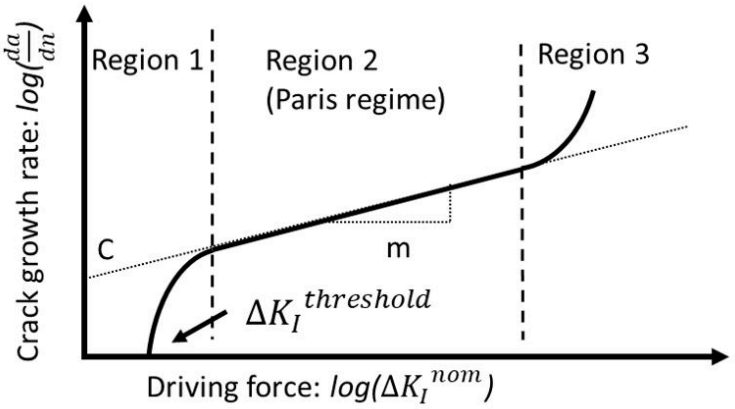

Figure 2.17: Typical mode I crack growth kinetics.

Where "nominal" means that ΔK_I is the theoretical one, obtained without accounting for closure effects, as discussed below. The values below zero are discarded, as the crack is closed and the singularity no longer exists (but there is a non singular compressive stress).

The crack growth rate evolves as described on figure 2.17, within three regimes. Region I corresponds to the near-threshold regime, where the crack growth is intermittent and very dependent on the microstructure, with rates of $\approx 10^{-10}$ $m/cycle$. Below $K_I^{Threshold}$, crack growth is hardly detectable. In region II, the crack growth rate can be predicted using Paris empirical law [Paris and Erdogan, 1963]:

$$\frac{da}{dN} = C(\Delta K_I^{nominal})^m \tag{2.21}$$

Where C and m are constants depending on the material but also the environment and other parameters, such as the load ratio:

$$R = \frac{F_{min}}{F_{max}} \tag{2.22}$$

With F the applied load.

Region III corresponds to the fast growth regime, where K_I approaches K_{IC}, the limit at which unstable fracture occurs. More sophisticated versions of the mode I crack growth kinetics exist to account for the other two regimes, such as Foreman's equation, where the driving force $\Delta K_I^{nominal}$ is modified, but the principle (that is: power law involving ΔK_I) remains similar to Paris law.

The dependence of mode I fatigue crack growth on the load ratio R can partly be explained by a premature contact between the crack faces while the applied load is still positive. Indeed, the effective amplitude of ΔK_I, called ΔK_I^{eff}, is reduced due to closure effects, as illustrated on figure 2.18, to:

$$\Delta K_I^{eff} = \max_{cycle}(K_I) - \min_{cycle}(K_I; K_{cl}) \tag{2.23}$$

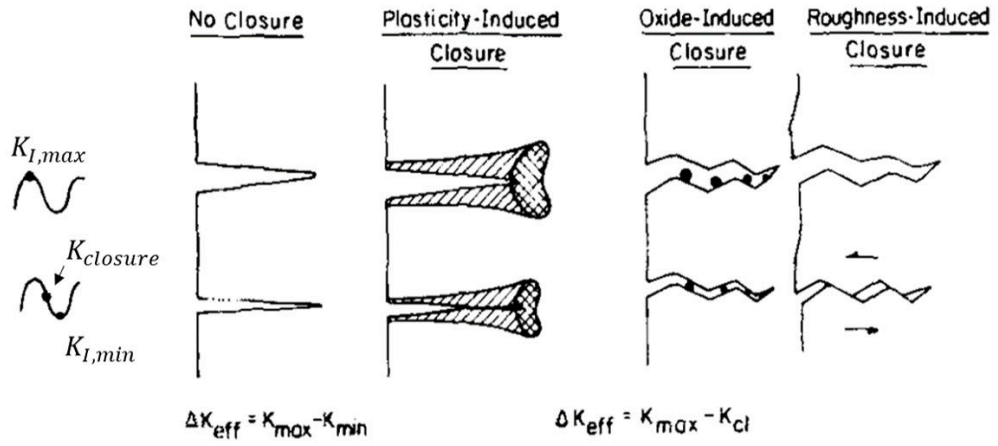

Figure 2.18: Illustration of the sources of closure effects, from [Suresh and Ritchie, 1982].

With K_{cl} the value below which the crack is closed at its tip. Some authors [Sehitoglu, 1985] differentiate the opening K_{op} and closing load K_{cl}, which we will assume to be equal for the rest of the study.

Compressive residual stresses ahead of the crack tip at unloading, as well as the residual stretch left behind as the crack propagates (the so-called "plastic wake"), lead to plasticity-induced closure. This effect can be modeled approximately using Newman's model [Newman, 1981] or more consistently using FEM elastic-plastic computations with node releasing, as performed by Pommier [Pommier et al., 1997] and de Matos & Nowell [de Matos and Nowell, 2007]. In particular, the type of material hardening (kinematic or isotropic), at similar yield stress and ultimate tensile stress, has a large influence on the amount of plasticity-induced closure [Pommier and Bompard, 2000].

At similar ΔK_I^{nom}, the crack growth rate can be lower for thin structures (plane stress conditions) than for thick structures (plane strain conditions), as discussed by de Matos & Nowell [de Matos and Nowell, 2009] or Branco et al. [Branco et al., 2008]. The plastic zone is larger under plane stress conditions than under plane strain (see figure 2.9), which leads to lower plasticity induced closure in the latter case (see fig. 2.19 A.&B.). For thick structures, this results in a slightly convex crack front shape (crack tunneling, see fig. 2.19 C.), as the crack growth rate is higher in the bulk than on the side surfaces (until the front becomes iso-ΔK_I^{eff}). The corner singularities effect discussed earlier (section 2.2.4) has little influence on plasticity induced closure on side surfaces, as shown by de Matos & Nowell [de Matos and Nowell, 2008], but will directly influence the crack emerging angle (see figure 2.11).

The formation of an oxide layer on the crack faces (often assisted by plasticity induced closure) leads to oxide-induced closure, as illustrated on figure 2.20 from Suresh et al. [Suresh et al., 1981]. Suresh performed mode I fatigue experiments on steel at $R = 0.05$ and $R = 0.75$, in moist air and dry helium. At $R = 0.05$ the non-propagation threshold is higher in air than in helium, due to the formation of a few 0.1 μm thick oxide layer on the crack faces, leading to premature contact upon unloading. At $R = 0.75$, $K_{I,\,min} > K_{cl}$, so that not closure effects occur and the crack growth kinetics and thresholds in both environments are similar.

Finally, the roughness of the crack, coupled with small permanent sliding displacements induced by shear-mode plasticity, induces a mismatch between the crack face asperities, which leads to their premature contact upon unloading and friction-induced locking. This roughness induced-closure explains some effects of the grains size on crack propagation. Gray [Gray et al., 1983] performed mode I fatigue experiments on a pearlitic rail steel, which was submitted to various heat treatments in order to change the grain size. At $R = 0.7$, the kinetic data for fine and coarse grains are superimposed (see figure 2.21), since no closure occurs, while at $R = 0.1$, the crack growth rate is lower for the coarse grained material, due to an increased crack face roughness and consequently an increased roughness-induced closure.

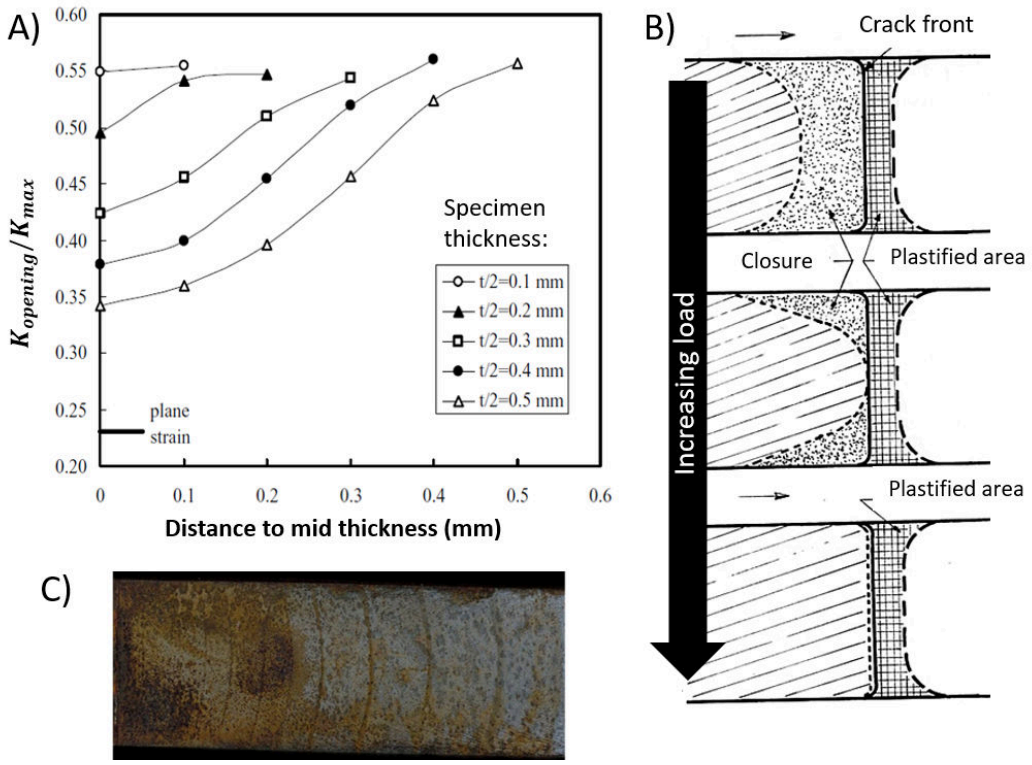

Figure 2.19: (A) Evolution of the opening load along the crack front for various specimen thicknesses, from [Branco et al., 2008]. (B) Illustration of the evolution of closure. (C) Crack front shape during a fatigue mode I experiment.

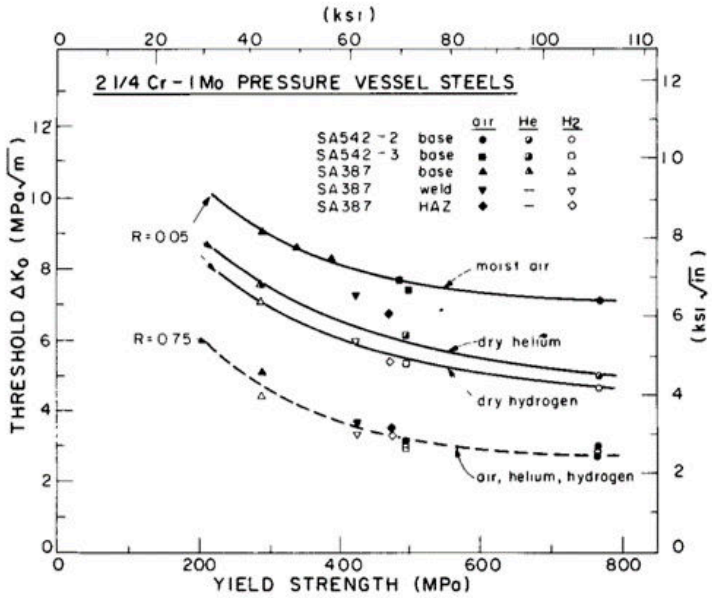

Fig. 6—Variation of threshold ΔK_o values for as-received 2¼ Cr-1 Mo pressure vessel steels with yield strength. Data for $R = 0.05$ and 0.75 in moist air, dry hydrogen and dry helium environments.

Figure 2.20: Effect of the environment and load ratio on the near-threshold fatigue crack growth from [Suresh et al., 1981].

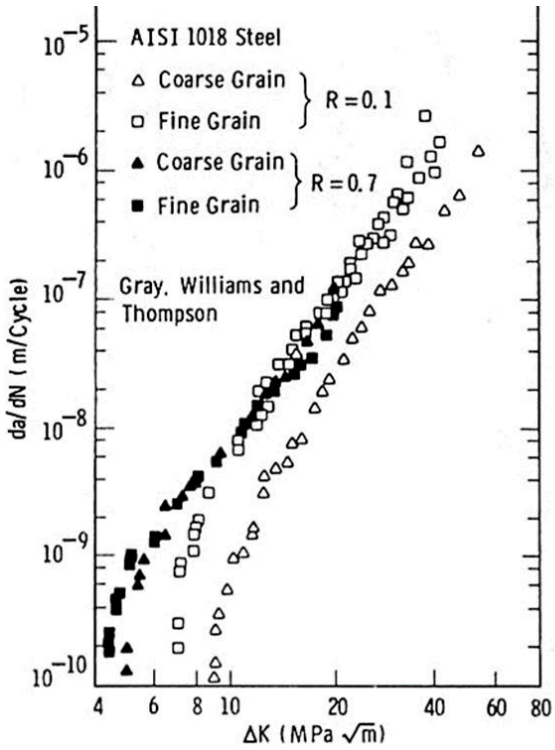

Figure 2.21: Effect of the grains size and load ratio on the near-threshold fatigue crack growth in a pearlitic steel, from [Gray et al., 1983].

Overloads (that is: cycles at higher amplitude than the current ones) temporarily increase the crack growth rate during the corresponding cycle, but slow down the propagation during subsequent cycles at normal (lower) amplitude, as observed by Topper & Yu [Topper and Yu, 1985]. Depending on the occurrence frequency of the overloads, it may increase of decrease the mean crack growth rate (if the higher growth rate during the overload cycle compensates the slower growth rate during the following cycles at normal amplitude). This question will however not be investigated in the present work.

As mentioned earlier, when a crack is closed, the stress singularity vanishes (although plastic blunting of the crack tip can keep it open), but a non-singular compressive stress is present. Some experiments at negative load ratios (crack under compression during a part of the cycle) have been reported [Carlson and Kardomateas, 1994] to yield higher growth rates than experiments at zero or positive load ratios, suggesting that the compressive part of the cycle may contribute to crack growth. This increase in growth rate can be explained by a decrease of plasticity-induced closure, which may even lead to a negative K_{cl}. The possibility of a saturation of this effect when the R ratio becomes more and more negative is yet unclear.

The load ratio R is often used to compare such data, but the peak compressive stress is probably a more relevant parameter, as suggested by [Zhang et al., 2007]. Indeed, as shown by [Pommier et al., 1997] and illustrated on figure 2.22, at a similar load ratio ($R = -1$), K_{cl} (or K_{op}) can be very different, depending on $\sigma_{compression}$. The higher the compression, the lower K_{cl}, which seems to be linked to kinematic hardening. Note that Newman's model is unable to predict the experimental data, as it does not allow crack closure for a negative load, while FEM computations with node releasing do.

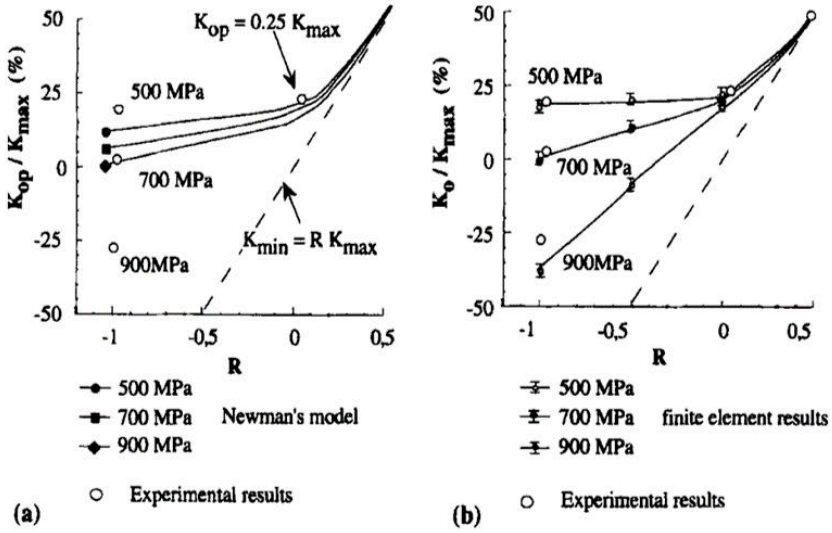

Figure 2.22: Effect of various loading amplitudes on the opening load K_{op} (which we assume to be equal to K_{cl}) from [Pommier et al., 1997].

Other authors, such as Pokorny, Vojtek et al. [Pokorný et al., 2017, Vojtek et al., 2019] reported a decrease of the crack growth rate at negative load ratios due to an increased oxidation of crack faces, and consequently an increased oxide-induced crack closure (OICC) in railway axle steel. Similar effects were observed by Maierhofer et al. [Maierhofer et al., 2018] on $25CrMo4$ steel. In this last study, oxide debris were found to be able to leave the crack near the side surfaces, thus reducing OICC. The overall influence of this local reduction of OICC near the side surfaces decreases as the specimen thickness rises, and it can be suppressed by applying an adhesive over the side surfaces to prevent the release of oxide debris

Mode I is responsible for crack propagation in most of the industrial problems. However, the sequential loading undergone by Squat-type cracks includes, aside from a mode I cycle, a quasi proportional mixed-mode II + III cycle.

2.5 Proportional mixed-mode and shear modes

For proportional cyclic mixed-mode loadings, the criteria proposed in section 2.2.2 for monotonic loading can be generalized to fatigue, using either peak values (for example, the MTS criterion becomes: $\max_\theta(\max_t \sigma_{\theta\theta})$) or ranges (for example, the MTSR criterion becomes: $\max_\theta \Delta\sigma_{\theta\theta}$), which is equivalent in terms of predictions, as long as the loading remains proportional (but may strongly diverge otherwise). Many studies showed that such criteria, coupled with Paris law, were able to predict crack growth for most proportional mixed-mode loadings.

In particular, in pure reversed mode II or pure reversed mode III, cracks have been reported to often tilt at $\pm \approx 70°$, or twist at $\pm 45°$ (forming a "factory roof" pattern, see fig. 2.23.a) respectively. These direction corresponds approximatively to those where the tangential stress ahead of the crack tip is maximum: the crack changes direction to be loaded in local mode I.

However, while the bifurcation criteria established for monotonic loading exclude the possibility of continued coplanar growth as soon as some mode mixity is present, several studies have shown that in some cases, (especially for zero or negative stress triaxiality ratios, and large ΔK_{II} & ΔK_{III}) macroscopic shear-mode propagation is possible in fatigue. In this case, the crack grows in a direction of maximum shear stress, instead of maximum tangential stress. The following section provides a short review on mode II and mode III fatigue crack growth (which bear many similarities), and introduces a fatigue-specific bifurcation criterion that can predict their occurrence.

2.5.1 Mode III

The possibility of a long coplanar crack growth in mode III, that the previous criteria cannot predict, has been reported by various authors, such as Tschegg [Tschegg, 1983b] or Brown et al. [Brown et al., 1985]. For a sufficiently high ΔK_{III}, a transverse circumferential crack in a notched bar loaded in reversed torsion (which induces a mode III loading) grew coplanar instead of bifurcating to form a "factory-roof" pattern (see figure 2.23).

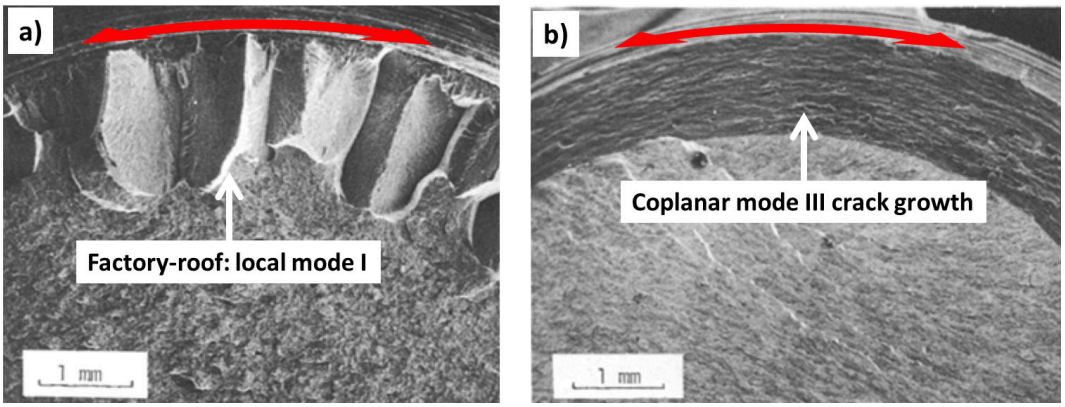

Figure 2.23: Factory roof type fracture surface (low ΔK_{III}) (a) and coplanar (high ΔK_{III}) (b) crack growth during a mode III experiment from [Tschegg, 1983b]. Loading direction indicated by the red arrow.

Such change in the crack path could be explained by the fact that the growth rate for a coplanar crack in mode III is lower than for mode I growth along a twisted facet at low ΔK, as shown on figure 2.24. However, at higher ΔK, the opening and shear mode growth kinetics intersect, and for high ΔK_{III}, coplanar mode III crack growth provides a higher growth rate than mode I. The crack grows in the direction and mode which maximize its growth rate: the maximum growth rate (MCGR) criterion initially proposed by Hourlier and Pineau assuming only mode I [Hourlier and Pineau, 1982] was thus generalized to take into account the possibility of both tension-driven and shear-driven mechanisms.

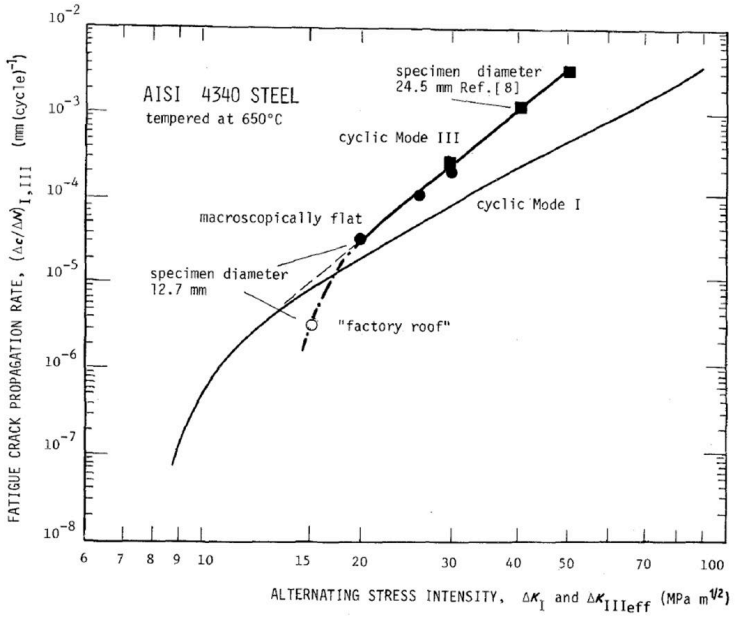

Figure 2.24: Comparison of fatigue crack growth rates in mode I and III as a function of ΔK_I and ΔK_{III}^{eff} in 4340 steel, from [Tschegg, 1983b].

As for mode I, the effective amplitude of the shear loading ΔK_{III}^{eff} is reduced, due to friction between the rough crack faces. Tschegg [Tschegg, 1983a] performed experiments at constant ΔK_{III}^{nom}, and observed that the deeper the crack, the smaller its growth rate (see figure 2.25 for $K_I = 0$). This effect was explained by a decrease of ΔK_{III}^{eff} due to the increase of the contact surfaces and thus of the energy dissipated by their friction. By comparing kinetic data at a given crack length to data at zero crack length, for which $\Delta K_{III}^{eff} = \Delta K_{III}^{nom}$, they estimated ΔK_{III}^{eff} for every crack length. The obtained load ratio, defined as:

$$U_{III} = \frac{\Delta K_{III}^{eff}}{\Delta K_{III}^{nom}} \tag{2.24}$$

decreased from 1 to 0.15 during crack growth, meaning that the effect of friction was not negligible. Brown et al. [Brown et al., 1985] and Tschegg & Stanzl [Tschegg and Stanzl, 1988] performed mode III experiments, with small compressive or tensile static axial loads to open the crack. The second led to higher growth rates due to a reduction of friction and an increase of ΔK_{III}^{eff}, while the former reduced the crack growth rate, as illustrated on figure 2.25.

From a limited number of experiments, it was concluded that contrary to mode I, mode III crack growth kinetics does not depend on the R ratio.

Pokluda & Pippan [Pokluda and Pippan, 2008] and Vojtek et al. [Vojtek et al., 2016a] who thoroughly investigated cyclic mode III, but in the near-threshold regime only, suggested that because it is associated with the coplanar emission of screw dislocations from the crack front, which does not create any new surface ahead of it, mode III is intrinsically unable to make a crack propagate. The growth of cracks loaded in cyclic mode III would rather be due to a local mode II component resulting from the in-plane tortuousity of the crack front. They provided convincing argument to support this idea for very low ΔK_{III}, which however might not hold in the high ΔK_{III} range investigated by Tschegg [Tschegg, 1983b] or Brown et al [Brown et al., 1985], where many other dislocation sources might be activated and profuse damage induced ahead of the front.

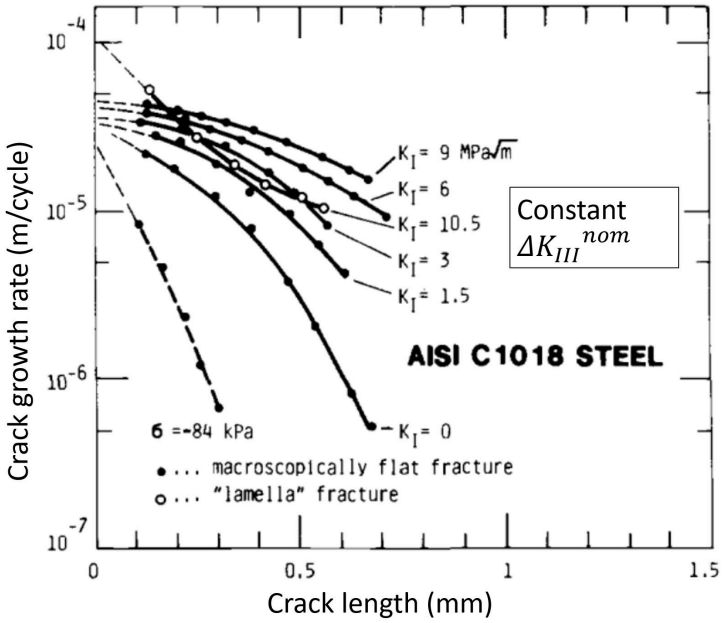

Figure 2.25: Crack growth rate versus crack length for cyclic mode III experiments, with or without a compressive or tensile static axial load ($K_I > 0$: tension), from [Tschegg and Stanzl, 1988].

2.5.2 Mode II

As for mode III, long coplanar growth was observed under mode II loading: above a certain ΔK_{II}, shear-driven coplanar crack growth becomes faster than mode I crack growth and is thus preferred (see for example [Smith and Smith, 1988] or [Pinna and Doquet, 1999]), as illustrated on figure 2.26. Like mode III, mode II crack growth kinetics was not found to depend on the R ratio.

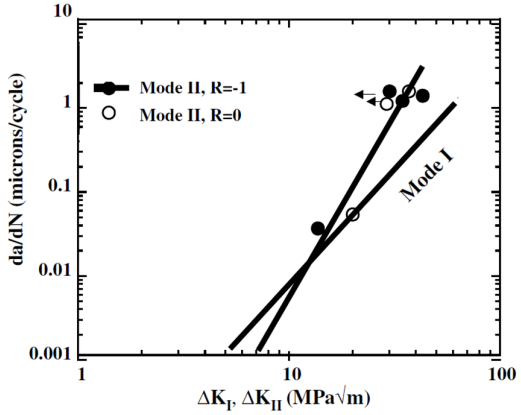

Figure 2.26: Intersection of mode I and mode II kinetics for ferritic–pearlitic steel, from [Doquet and Bertolino, 2008a].

Again, friction reduces ΔK_{II}^{eff}, and several direct or indirect measurements were made. Smith & Smith [Smith and Smith, 1988] estimated U_{II}, defined as:

$$U_{II} = \frac{\Delta K_{II}^{eff}}{\Delta K_{II}^{nom}} \tag{2.25}$$

They deduced U_{II} from the stiffness change detected on the load-sliding displacement loop (measured with a special extensometer straddling the crack), indicating a transition from locked to unlocked crack and vice-versa. Direct measurements of ΔK_{II}^{eff} were also made by comparing the relative displacement jump obtained from surface replicas to the theoretical one from 2.2, as illustrated on figure 2.27 (a).

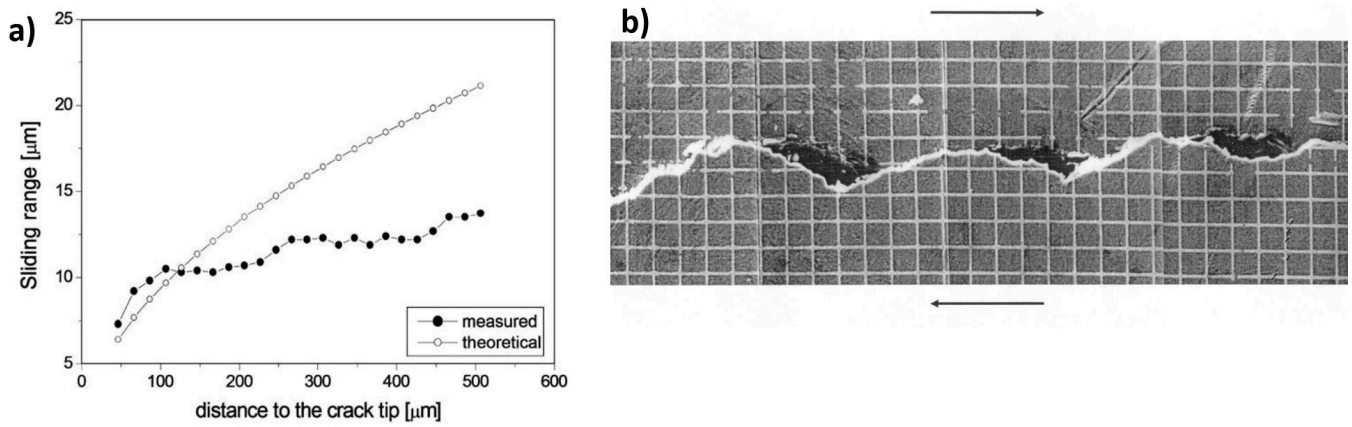

Figure 2.27: (a) comparison of measured in-plane sliding displacement jumps with LEFM predictions, from [Bertolino and Doquet, 2009], (b) *in situ* SEM (Scanning Electron Microscope) image of a crack under mode II loading from [Pinna and Doquet, 1999], 5 μm grid pitch..

Gross et al. [Gross et al., 1995] used a similar post-treatment on displacement fields obtained from electro-optic holographic interferometry, as shown on figure 2.28. Under pure mode II loading, they observed non zero ΔK_I (due to dilatancy: sliding leads to asperities climbing, and thus to an opening, as illustrated on figure 2.29), and ΔK_{III} (due to Poisson's effect, as mentioned in 2.2.4).

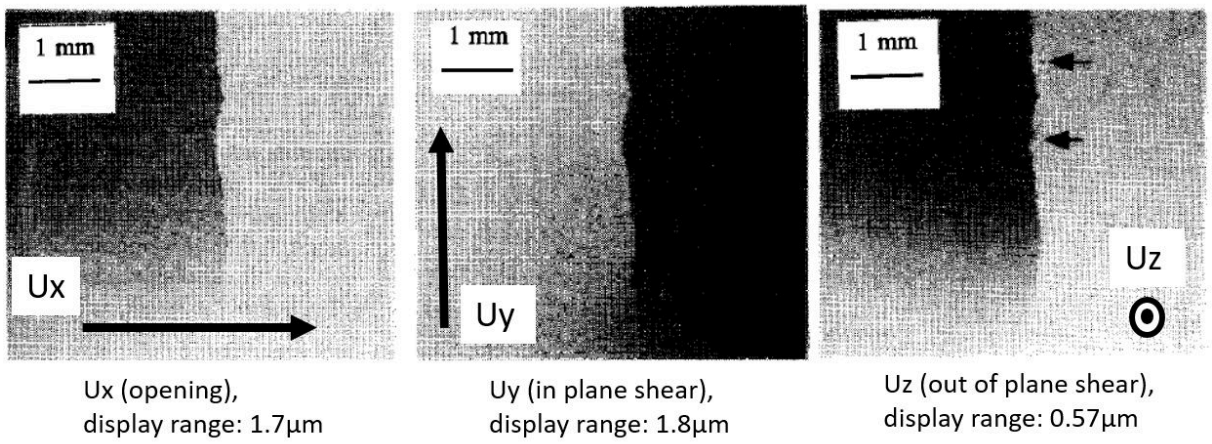

Figure 2.28: Displacements maps along the three directions, obtained by electro-optic holographic interferometry, for $\Delta K_{II}^{nom} \approx 5.6\ MPa\sqrt{m}$, from [Gross et al., 1995].

Several analytical models to account for friction and dilatancy effects in a rough crack (see figure 2.29) loaded in mode II or III were proposed by Gross and Mendelsohn [Gross and Mendelsohn, 1988, Gross and Mendelsohn, 1989], as well as by Tong, Yates et Brown [Tong et al., 1995a], Yu et al and others. In all those models, rigid asperities were considered, while experiments show clear evidence of plasticity and wear of the asperities.

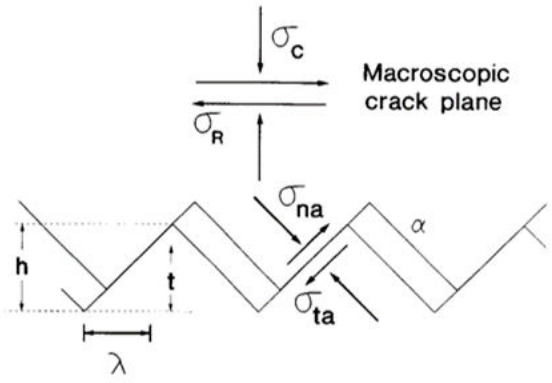

Figure 2.29: Schematic of idealized asperity profile under shear from [Gross and Mendelsohn, 1989]: friction and dilatancy effects.

In addition, the aforementioned experimental and modelling works did not take into account the influence of crack tip plasticity, which might artificially increase the estimated ΔK_{II}^{eff} as it increases the displacements relative to the LEFM ones. Smith et al for example reported some values of U_{II} larger than 1.

Bertolino and Doquet [Bertolino and Doquet, 2009] measured the relative crack face displacement jump under mode II loading using SEM *in situ* measurements with gold microgrids, as illustrated on 2.27 (b). An inverse approach, based on the comparison of the experimental displacement jump to that of elastic-plastic FEM computations with friction was used to determine the friction stress and ΔK_{II}^{eff}. Such method allows to decorrelate the two non linearities (friction and crack-tip plasticity).

2.5.3 Mixed-mode II & III

Only a few studies focused on mixed-mode II & III loading ([Pokluda et al., 2008, Vojtek et al., 2013, Pokluda et al., 2014, Vojtek et al., 2015b, Vojtek et al., 2015a, Vojtek et al., 2016b, Hellier et al., 1987, Merati et al., 2012, Doquet et al., 2010a]), which will be investigated and discussed more thoroughly in chapter 5.

As for pure mode II or mode III, shear-driven coplanar crack growth over long distances was observed for sufficiently high shear loads in maraging steel and Ti64 alloy, by Doquet et al. [Doquet et al., 2010a]. The crack growth rate could not be described only by ΔK_{II}^{eff} or ΔK_{III}^{eff}, but by a combination of the two:

$$\Delta K_{shear}^{eff} = \sqrt{\Delta K_{II}^{eff\,2} + \beta \Delta K_{III}^{eff\,2}} \tag{2.26}$$

where β is a fitted parameter. ΔK_{shear}^{eff} is proportional to the square root of the energy release rate ΔG (for plane strain conditions) if $\beta = \frac{1}{1-\nu}$. In this case, both modes contribute equally to crack growth. β was found to be equal to 1.2 for maraging steel and 0.9 for Ti-6Al-4V.

However, Squat-type cracks undergo non-proportional mixed-mode, which induces several difficulties compared to proportional mixed-mode.

2.6 Non proportional mixed modes

2.6.1 Generalization of classical approaches

During non-proportional mixed-mode loadings, as it is the case in rails (see figure 2.15), classical LEFM bifurcation criteria cannot be used in their original form, as the direction of the maximum tangential stress or maximum k_I^* keep varying during a cycle. Such bifurcations criteria can be extended, using either the absolute angular maximum of the peak value of the quantity of interest, for example for the MTS criterion:

$$\max_{\theta} \max_{t} \sigma_{\theta\theta} \tag{2.27}$$

or the angular maximum of the range of the quantity of interest, for example for the MTSR criterion (Maximum Tangential Stress Range):

$$\max_{\theta} \Delta\sigma^{+}_{\theta\theta} = \max_{\theta}(\max_{t} \sigma_{\theta\theta} - \max(0, \min_{t} \sigma_{\theta\theta})) \tag{2.28}$$

While under proportional loading, the two options are equivalent, their predictions under non-proportional loading can be drastically different. For example, according to the former version, a crack submitted to cyclic mode I plus static mode II should bifurcate, while according to the latter, it should continue its coplanar growth, since a static loading does not modify a range. Note that in either case, the crack cannot recover pure mode I loading, and that more generally, pure opening or pure shear loading do not exist whatever the crack path, under non-proportional loading.

Another approach, proposed by Highsmith [Highsmith and Woodruff, 2009], mixes a range and a maximum:

$$\max_{\theta} \overline{\Delta k_I} = \max_{\theta} \left[(\Delta k_I)^w (\max_{t} k_I)^{1-w} \right] \tag{2.29}$$

where k_I is an approximation of k_I^*, and w a fitting parameter. This approach gave satisfying crack path predictions for various loading paths, but with a specific w for each path: such LEFM approach is not sufficient to predict the crack path for any non-proportional mixed-mode loading.

The crack growth rate is often correlated to the range of the three SIFs by a Paris-like equation:

$$\frac{da}{dN} = C(\Delta K_{eq})^m = C(a_I(\Delta K_I)^{m_I} + a_{II}(\Delta K_{II})^{m_{II}} + a_{III}(\Delta K_{III})^{m_{III}})^m \tag{2.30}$$

Tanaka [Tanaka, 1974] proposed in particular:

$$\Delta K_{eq} = (\Delta K_I)^4 + 8(\Delta K_{II})^4 + 8/(1-\nu)(\Delta K_{III})^4)^{1/4} \tag{2.31}$$

Researchers often assume that the equivalent ΔK can be used in conjunction with the C and m parameters determined for pure mode I, which is questionable, because, as explained above, the opening and shear-mode crack growth kinetics generally have different exponents and different sensitivity to the R ratio.

The crack growth rate might also be predicted using a simple sum of the crack growth rates due to each mode:

$$\frac{da}{dN} = C_I(\Delta K_I)^{m_I} + C_{II}(\Delta K_{II})^{m_{II}} + C_{III}(\Delta K_{III})^{m_{III}} \tag{2.32}$$

Note that all those driving forces -which should be computed using effective SIFs, corrected for both closure and friction effects- depend only on their range, ignoring the influence of their time evolution (or the shape of the loading path), which, as detailed later-on, may be an error, due to crack tip plasticity couplings.

2.6.2 Couplings due to crack tip plasticity

Doquet and Pommier [Doquet and Pommier, 2004] performed sequential mixed-mode I+II (a mode I cycle followed by a mode II cycle) experiments on ferritic-pearlitic steel. The crack growth rate for this sequential loading was found to be larger than the simple sum of the the crack growth rate due to mode I and mode II alone: $da/dN > da/dN(\Delta K_I) + da/dN(\Delta K_{II})$. This effect was explained by synergistic effects between the two modes, due to crack-tip plasticity couplings, as illustrated on figure 2.30 for a material with kinematic hardening.

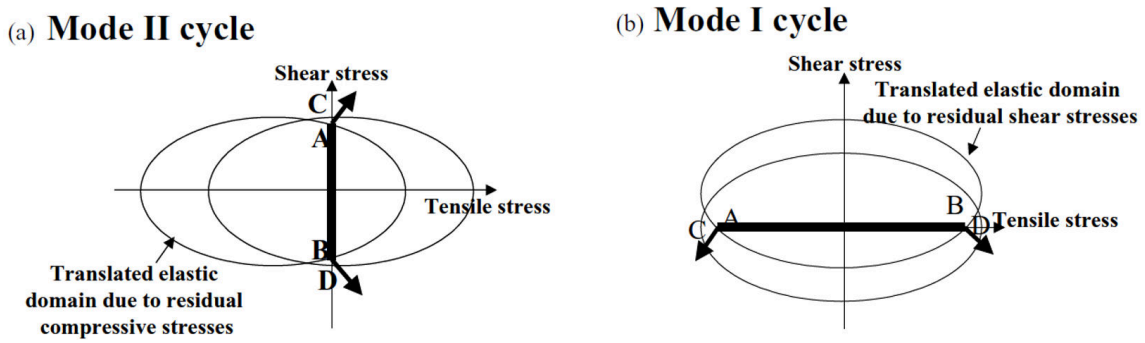

Figure 2.30: Schematic of plastic flow during the mode II (a) or mode I (b) part of a sequential mixed mode I+II test, from [Doquet and Pommier, 2004].

After the mode I part of the cycle, compressive residual stresses are left at the crack tip, so that, during the mode II part of the cycle, the plastic flow will occur earlier and in a different direction than in pure mode II. After the mode II part of the cycle, residual shear stresses are left, leading again to a change of the intensity and direction of the plastic flow during the mode I part of the cycle. Consequently, the plastic opening displacement at the crack tip ρ_I, which could be a potential crack driving-force, is lower for pure mode I than for sequential mixed-mode I+II (see figure 2.31).

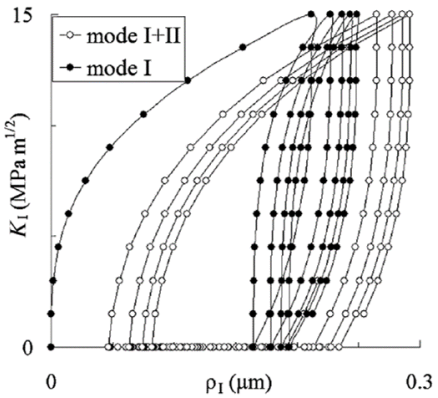

Figure 2.31: Evolution of the plastic opening displacement behind the crack tip ρ_I versus K_I for for pure mode I and sequential mixed-mode I+II, from [Doquet and Pommier, 2004].

These effects of crack tip plasticity couplings can also have an effect on the crack growth direction, as suggested by Dahlin & Olsson [Dahlin and Olsson, 2003], who proposed the MTS$_P$ criterion (a version of the MTS criterion taking into account crack-tip plasticity, detailed later in section 2.6.3), and showed (using the experimental data from [Plank and Kuhn, 1999]) that it was more suited than the MTS as it accounts for the stress redistribution due to crack tip-plasticity (see fig. 2.34 below), including the coupling between shear and tensile plastic flows.

Those couplings due to crack-tip plasticity could explain the loading path dependency of the crack growth rate observed by Fremy et al. [Fremy et al., 2014b]. Mixed-mode experiments were performed on 316L stainless steel with various loadings paths with the same ΔK, and with $R_I > 0.3$ in order to avoid contact and friction between the crack faces. Classical crack growth models involving ΔK (meaning: whatever combination of the range of the SIFs) would predict an identical growth rate for those loadings paths. However, different growth rates were obtained, as shown on figure 2.32, with differences of a factor up to 2.46.

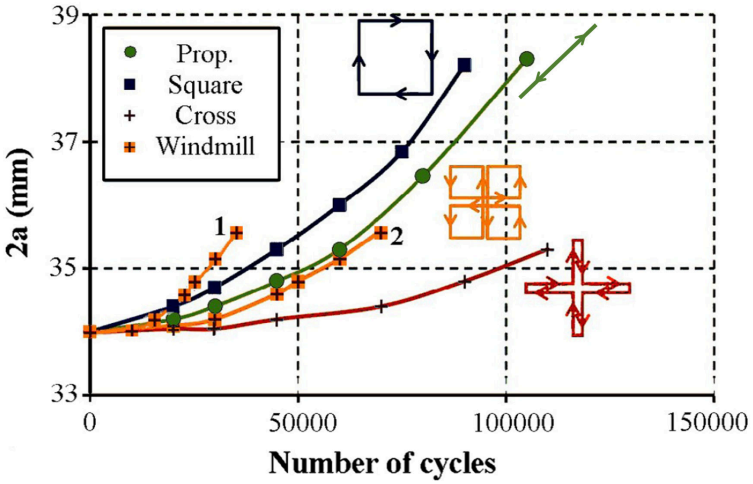

Figure 2.32: Evolutions of the crack lengths with the number of cycles for various loading path with the same ΔK 2.32.

These different loading paths induce different evolutions of the plastic blunting $\dot{\rho}$ (computed by FEM) [Fremy et al., 2014a], as shown on figure 2.33. The various loading paths are correctly sorted in terms of crack growth rate if $\dot{\rho}$ is supposed to be the crack driving force.

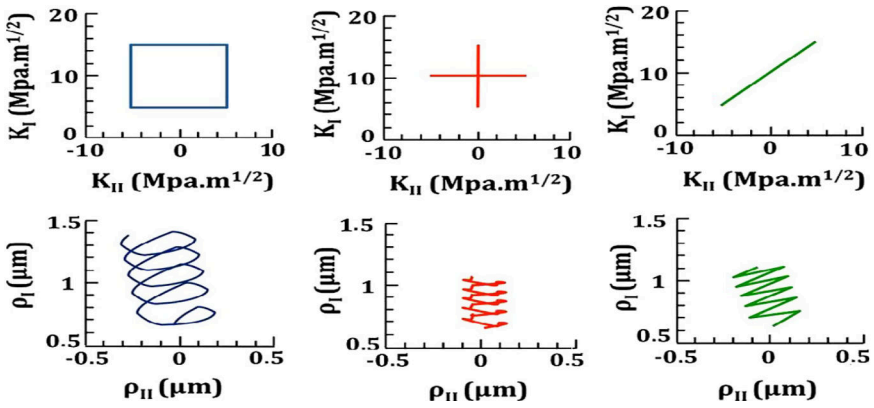

Figure 2.33: Evolutions of the plastic flow computed by FEM for various loading paths with the same ΔK [Fremy et al., 2014a].

2.6.3 Approaches accounting for crack tip-plasticity

In order to account for the stress redistributions and the couplings induced by crack tip-plasticity, Dahlin and Olsson [Dahlin and Olsson, 2003] proposed to use the MTS or MTSR criteria, not on LEFM fields, but on field computed using elastic plastic FEM computations. In this case, the criteria are denoted as MTS_p or $MTSR_p$

(p for plasticity). Those criteria were found to be more successful than their LEFM equivalents when applied to non-proportional mixed-mode loadings, as they account for the stress redistribution and couplings due to crack tip plasticity. An example is given on figure 2.34 for sequential mode I+II loading, where bifurcation is predicted by the elastic version of the criteria, while coplanar growth is predicted by their elastic-plastic version. However, these criteria can only be used to predict the crack path, but no the growth rate.

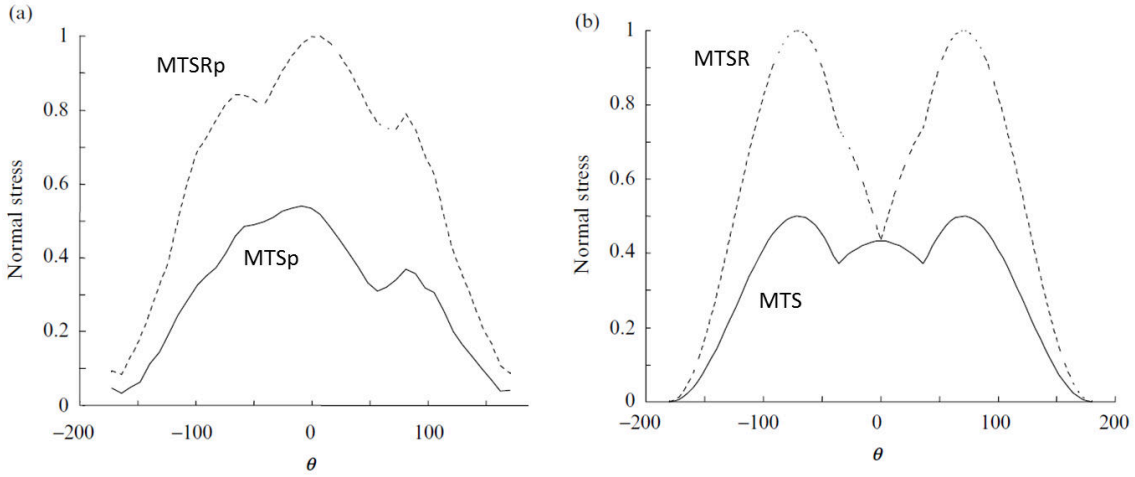

Figure 2.34: Angular evolution of the tangential peak stress and range of the tangential stress, (a) with or (b) without elastic-plastic behavior. Sequential mode I+II loading, from [Dahlin and Olsson, 2003].

Pommier & Hamam [Pommier and Hamam, 2007, Hamam et al., 2007b] proposed to use the crack tip plastic blunting ρ_I (see figure 2.35) as a crack driving force for mode I loading, which allowed to account for variable amplitude effects. Decreuse et al. [Decreuse et al., 2009], and Fremy et al. [Fremy et al., 2014a] then extended the approach to non-proportional mixed-mode, using the following equation (see figure 2.35):

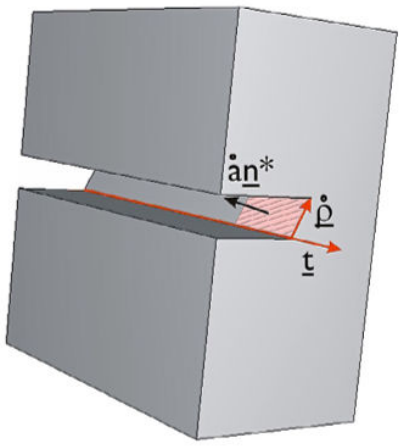

Figure 2.35: Schematics of the process of creation of new cracked area by crack tip plasticity, and illustration of $\underline{\dot{\rho}}$ from [Fremy et al., 2014a].

$$\dot{a} * \underline{n}^* = \alpha * (\underline{t} \wedge \underline{\dot{\rho}}) \tag{2.33}$$

In order to evaluate $\underline{\dot{\rho}}$, which is a 3 components vector with each component related to a loading mode, the

crack tip velocity field (time derivative of the displacement field) estimated from elastic-plastic FEM computations is divided into an elastic and a plastic part, which are proportional to the $\dot{K}_i$ and $\underline{\dot{\rho}}$ respectively. As discussed earlier, this approach accounts for the influence of the shape of the loading path on the crack growth rate when it is nearly coplanar. However, it cannot be considered as a bifurcation criterion, since it predicts no crack growth at all for pure mode III ($\underline{t} \wedge \underline{\dot{\rho}_{III}} = 0$), as well as for fully reversed mode II ($R_{II} = -1$): $\underline{t} \wedge \underline{\dot{\rho}_{II}}$ changes sign with the load, so that $\int_{cycle} \underline{t} \wedge \underline{\dot{\rho}_{II}} = 0$.

Doquet & Bertolino [Doquet and Bertolino, 2008b] proposed a local approach, based on the idea that fatigue damage ahead of the crack tip is responsible for crack propagation, and that two damage mechanisms are competing, one accounting for shear mode and the other for tensile mode. Two damage parameters are thus used. The first one, proposed by Smith, Watson and Topper accounts for tension-driven damage:

$$\beta_{Tension} = \beta_{SWT} = \Delta\epsilon_n * \sigma_{n,max} \tag{2.34}$$

The second one is a shear-driven damage function that can be either Findley's or Fatemi & Socie's damage function:

$$\beta_{Find} = \Delta\tau + k_{FI} * \sigma_{n,max} \tag{2.35}$$

$$\beta_{FS} = \Delta\gamma_{max}(1 + k_{FS}\frac{\sigma_{n,max}}{\sigma_y}) \tag{2.36}$$

$$\beta_{Shear} = \beta_{FS} \text{ or } \beta_{Find} \tag{2.37}$$

where k_{FI} and k_{FS} are dimensionless parameters.

Those two damage functions are evaluated after elastic-plastic FE simulations, and averaged over a small segment of length ΔL in every possible direction (characterized by a tilt angle θ and a twist angle ϕ) ahead of each node of the crack front (see fig. 2.36). The corresponding potential fatigue lives, $N_{f,\,tension}$ and $N_{f,\,shear}$, are deduced, using the equations fitted from low-cycle fatigue data, as explained in [Doquet and Bertolino, 2008b]. The minimum of those two values, $N_f = min(N_{f,\,tension}, N_{f,\,shear})$, as well as the associated direction are then extracted. The potential local crack propagation rate for each mechanism is evaluated as:

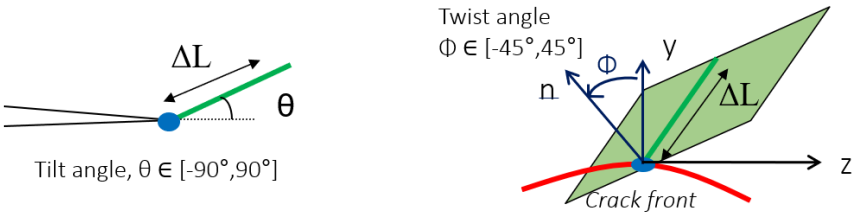

Figure 2.36: Evaluation of the damage functions in every possible direction over a length ΔL.

$$\frac{da}{dN} \approx \frac{\Delta L}{N_f} \tag{2.38}$$

In accordance with the MCGR criterion, the crack is assumed to propagate according to the mechanism which maximizes its growth rate, which gives both the propagation direction and the crack growth rate. This approach was able to predict the transition from tensile branching to shear driven coplanar under cyclic mode II, due to an intersection of the mode I and mode II kinetics, as shown on figure 2.37. It also gave reasonable predictions of the crack growth for mixed mode II & III loading [Doquet et al., 2010a].

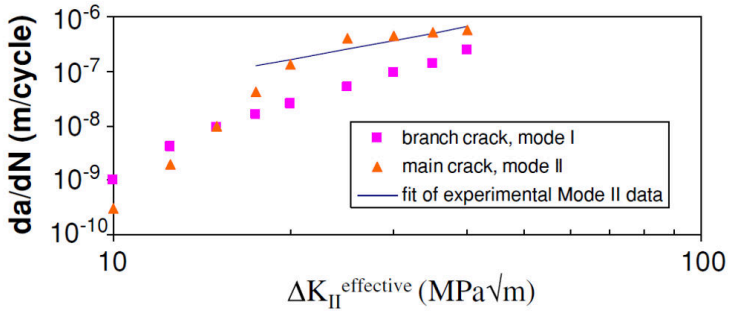

Figure 2.37: Potential crack growth rate for shear-driven coplanar growth or tensile branching under mode II loading, predicted using the local approach, from [Doquet et al., 2009].

All those approaches require elastic-plastic FEM computations, which are not yet compatible with the XFEM method, which does not incorporate cyclic plasticity (but just monotonic plasticity, using the HRR field). Furthermore, crack-tip plasticity is not the only source of couplings between shear and opening modes.

2.6.4 Couplings through closure effects, friction, asperities interlocking and wear

Coupling between opening and shear modes also exists due to crack face contact and friction. It is clear that a tension applied while shearing ($K_I > 0$) will reduce the friction and asperities interlocking, while a compression will enhance friction due to coulomb's law, thus changing K_{II}^{eff}. Conversely, the shear modes also have an influence on closure effects in mode I, or induce some dilatancy K_I.

Hourlier and Pineau [Hourlier and Pineau, 1982] superimposed static torsion (mode III) and cyclic tension (mode I) on cylindrical specimens with a circumferential notch and observed a reduction of the mode I crack growth rate, as well as an increase in the threshold ΔK_I^{th}, due to an increase of the asperity induced closure (mode III promoting crack twisting locally as well as a permanent shift of the asperities on each crack face), while an increased crack growth rate could have been expected from the crack-tip plasticity couplings. A similar effect was observed for a static mode II superimposed on cyclic mode I [Stanzl et al., 1989] and modeled by Doquet et al. [Doquet et al., 2009, Doquet et al., 2010b] using FE simulations on a rough crack (see figure 2.38.a) with Coulomb's friction. Such FEM model with rough crack allows to predict qualitatively the friction and dilatancy effects for cyclic mode II (fig. 2.38.b), as well as the early crack closure (and reduced ΔK_I^{eff}) induced by the superimposition of a static K_{II} to cyclic mode I (fig. 2.38.c).

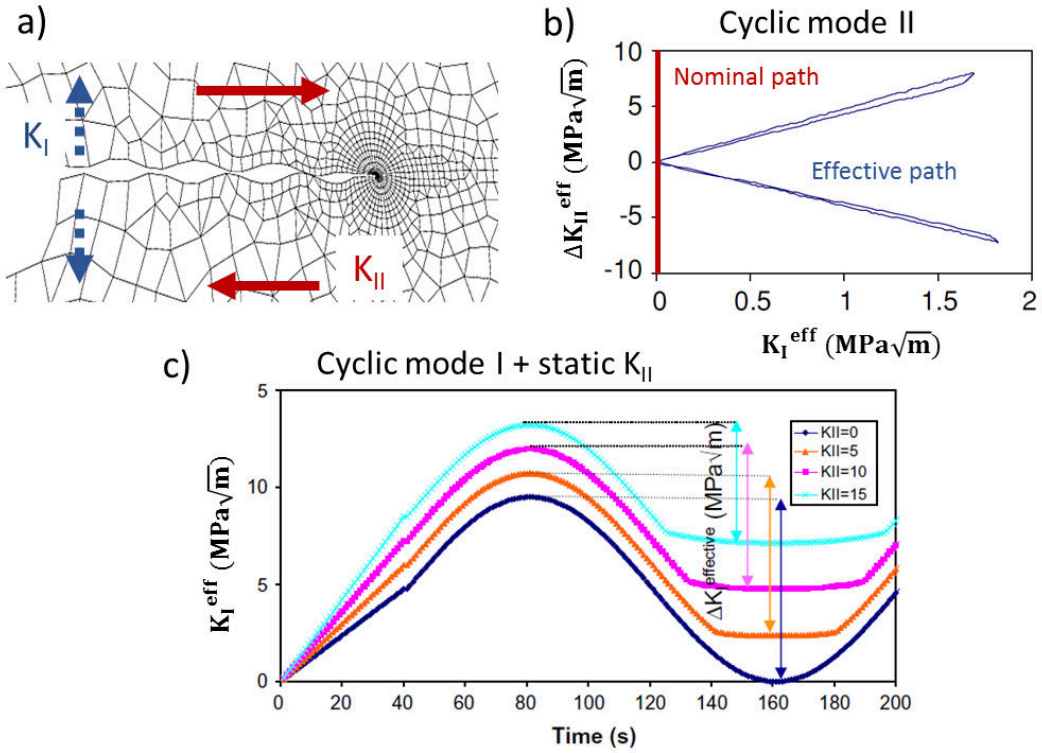

Figure 2.38: (a) mesh used for FEM computations with rough crack from [Doquet et al., 2009]. (b) Effective and nominal loading paths for a cyclic mode II loading, obtained from (a). (c) time evolution of K_I^{eff} for the superimposition of a static K_{II} to cyclic mode I, from [Doquet et al., 2010b] using (a).

A single shear mode overload can even reduce the mode I crack growth rate over a few mm, after which the crack recovers its initial growth rate (see figure 2.39), as shown by Dahlin & Olsson [Dahlin and Olsson, 2004]. This effect is explained by a permanent relative sliding displacement of the crack faces due to shear-mode plastic deformations. As the crack propagates, its influence will fade away.

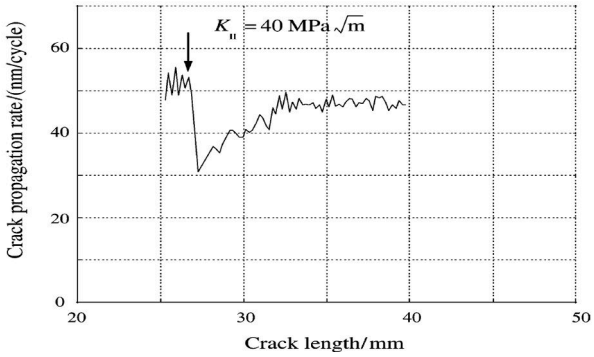

Figure 2.39: Evolution of the crack growth rate during a cyclic mode I experiment, after a mode II overload (2.39).

Jägg & Scholtes [Jägg and Scholtes, 2005] performed sequential experiments, and measured the residual stresses using X-ray diffraction. It appears that mode II does not induce compressive residual stresses, and that plasticity-induced crack closure is thus only induced by mode I. Sander and Richard [Sander and Richard, 2005] came to the same conclusions using node releasing FEM computations with Lemaitre and Chaboche's plasticity model. With the same type of approach, Doquet et al [Doquet et al., 2010b] even showed that a static mode II actually reduces plasticity-induced closure in mode I, which explains the acceleration of short cracks growth reported by Tschegg et al in presence of a static mode II.

Very few authors studied non-proportional loading with a compression phase while shearing, as it is the case in rails. Tarantino et al. [Tarantino et al., 2011, Tarantino, 2011] studied short crack growth ($< 1\ mm$) under out-of-phase cyclic compression + mode III in bearing steel. The experiments were performed on cylinders with a transverse micro notch, precracked in mode I at $R = -2$, and then loaded under combined cyclic tension/compression and torsion. The effective stress intensity factors were estimated using an analytical model derived from [Tong et al., 1995b], taking into account the real crack roughness obtained by SEM images processing.

Under 90° out-of-phase mode III + strong compression, with $R_I = -\infty$ and $R_{III} = -1$, coplanar cracks started to grow below the pure mode III threshold, and long stable coplanar growth was always observed, as shown on figure 2.40. This enhancement of shear driven-coplanar growth by compression was associated with severe rubbing of the crack faces, and with creation of wear debris coming out of the crack and leading to a residual "crack opening" (actually a loss of matter): paradoxically, the out-of-phase compression reduced friction and increased ΔK_{III}^{eff} by keeping the crack open.

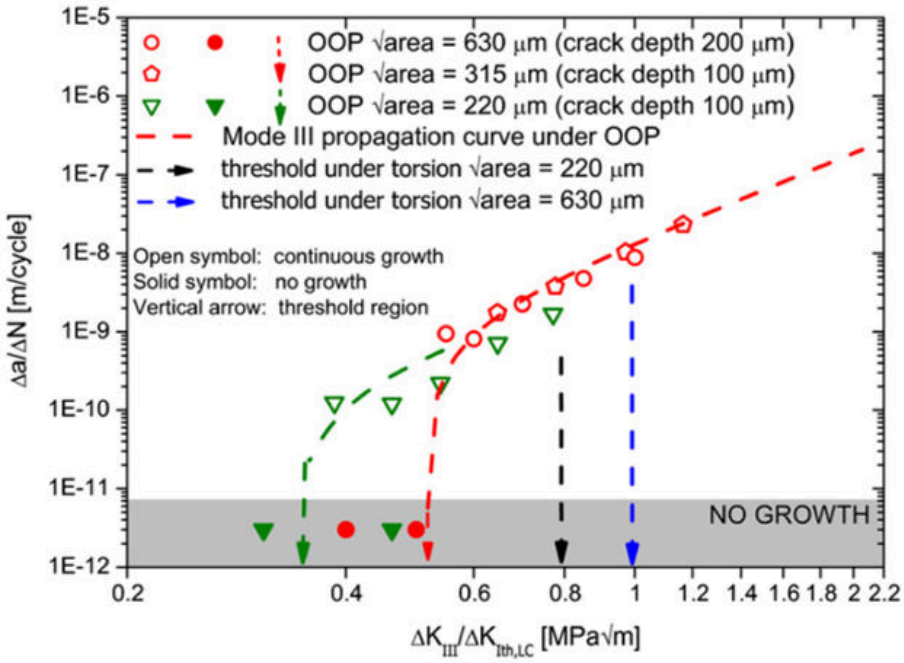

Figure 2.40: Crack growth rate as a function of ΔK_{III}^{nom} for pure mode III and 90° out-of-phase mode III + compression (noted "OOP"), with various notch sizes. "Continuous growth" means stable coplanar growth.

Similar results were obtained by Tarantino in [Tarantino, 2011] on railway steel, and by Beretta [Beretta et al., 2010] on SAE5135 gear steel. However, the residual opening due to wear was less pronounced in railway steel (close to $R260$) than in bearing steel.

2.7 Conclusions and structure of the manuscript

This study will focus on the propagation of Squats-type cracks below the layer that is repeatedly plastified and transformed by train passages. In this area, LEFM can be applied, and the loading is nearly a sequence of opening and shear modes, with a compression while shearing and various proportions of mode II and mode III along the crack front. Due to couplings between the three modes induced by crack-tip plasticity as well as contact, friction and wear between the crack faces, and a lack of widely accepted approach to deal with such a problem, the prediction of crack path and growth rate under such non-proportional mixed-mode loading is a challenge in itself. This leads us to neglect the effects of variable amplitude loading and water trapping/pressurization in the rest of the study. The manuscript is divided as follows:

First, the microstructure and mechanical properties or $R260$ rail steel will be presented. Then, some procedures common to the various crack growth experiments will be introduced.

Second, mode I fatigue crack growth in rail steel will be investigated, at various load ratios in order to get kinetic data, and study the influence of a compression. The possibility that mode I alone explains crack growth in rails will be discussed.

Third, mixed-mode II & III experiments will be presented, in order to asses the possibility of shear-driven coplanar crack growth in rails, and get kinetic data for various proportions of mode II and III.

Fourth, the results of non-proportional mixed-mode I+II experiments, with various loading paths, mode mixities, and compression phases will be discussed. Several approaches for crack growth prediction will be tested and compared to the experimental results. In all the aforementioned experiments, near-tip displacements will be measured and analyzed in order to measure the effective SIFs and estimate the effects of contact and friction between the crack faces.

Finally, an approach to predict the crack growth in rails will be proposed, and validated using non-proportional mixed-mode I + II & III experiments.

Chapter 3

Material characterization & procedures

Contents

3.1 Material

This section contains the material characterization along with the presentation of the observation means and testing machines. A large part of the work presented in this Material section was done during a 5 month master internship prior to the thesis.

3.1.1 Samples

The material for microstructural characterization, as well as all the samples used in the experiments were extracted from the head of 8 new rail 1-meter sections made of $R260$ low alloy rail steel, as shown in figure 3.1 and detailed in appendix A. Since the study focuses on crack propagation in the rail head, and the manufacturing process (rolling) might induce differences in microstructure and residual stresses in the rail section, it is preferable to extract the samples in this zone. The composition and tensile properties are given in tables 3.1 and 3.2 respectively. Spectrometry analysis (EDS in the SEM) gives a composition consistent with the nominal one.

Table 3.1: Mass % composition

C	Si	Mn	P	S
0.72	0.32	1.08	0.015	0.022

Table 3.2: Tensile properties

$Rp_{0,2}$ (MPa)	Rm (MPa)	A%
480	880	10

The loading direction might have an influence, since anisotropy between planes orthogonal to or containing the rolling direction can be induced by the rolling process. The samples for crack growth tests were thus machined so that the crack is always in a plane orthogonal to the rolling direction, as is it almost the case in rails.

6 Types of samples were manufactured, with a total of 72 samples, distributed as follow: 15 samples for tensile fatigue tests, 16 samples for shear & tensile fatigue tests, 8 samples for mode I crack growth tests, 18 samples for mixed mode II&III crack growth tests, 20 samples for non-proportional mixed mode I+II crack growth tests and 5 samples for *in situ* mixed mode I+II crack growth tests in a SEM.

3.1.2 Microstructure

Samples were extracted and cut in several directions, mechanically polished up to 1 μm with diamond paste and then ion-polished. Neither chemical etching, with various solutions, nor electropolishing gave satisfying results.

The $R260$ rail steel is a pearlitic steel (with a bit of proeutectoid ferrite at graind boundaries): lamellar structure, with ferrite and cementite, as shown figure 3.2. The inter-lamellar spacing is 50 to 80 nm, with lamellae length of a few microns and a pearlite colonies size of a few tens of microns. No flagrant anisotropy, neither in the grain shape nor in the lamellae orientation can be seen with SEM observations.

However, it contains manganese sulfide inclusions (MnS, confirmed by spectrometry analysis), with a ≈ 5 μm diameter and a ≈ 100 μm length, elongated in the rolling direction, as shown on figure 3.3). This shape is likely due to the rolling process.

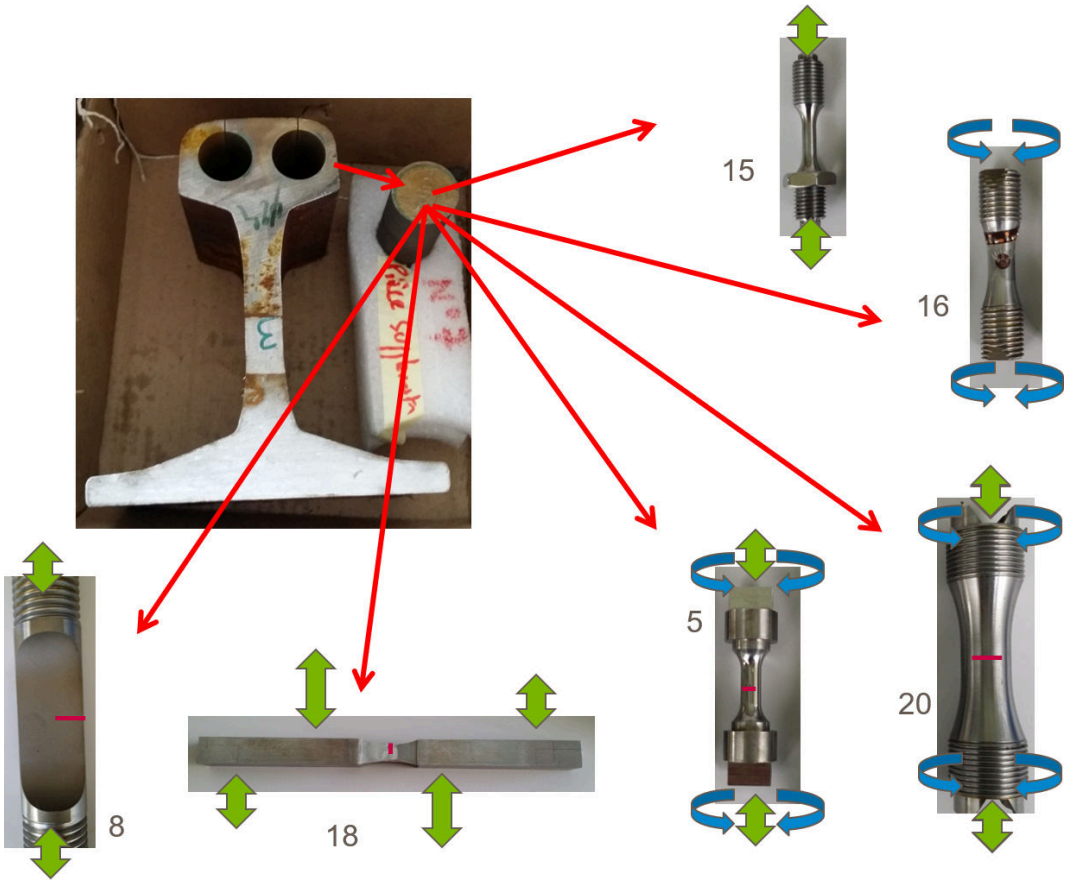

Figure 3.1: Cylinders extracted from the rail head and machined into 6 different samples. The number corresponds to the number of machined samples.

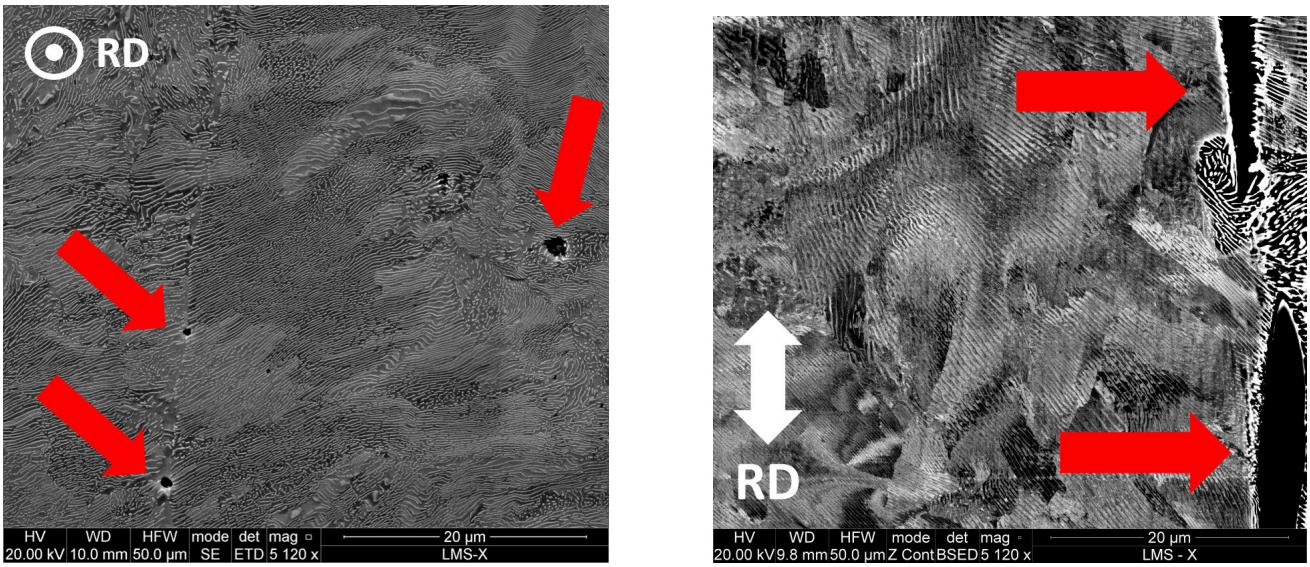

Figure 3.2: SEM observations of the lamellar structure in the plane orthogonal to the rolling direction RD (left), and in a plane containing the rolling direction (right). The red arrows point towards manganese sulfide inclusions.

EBSD analysis of nine images of $310 * 270\ \mu m^2$ (stitched image of $930 * 810\ \mu m^2$) with a 260 nm step shows a slight anisotropy (see figures 3.4 and 3.5). The texture index is 2.45.

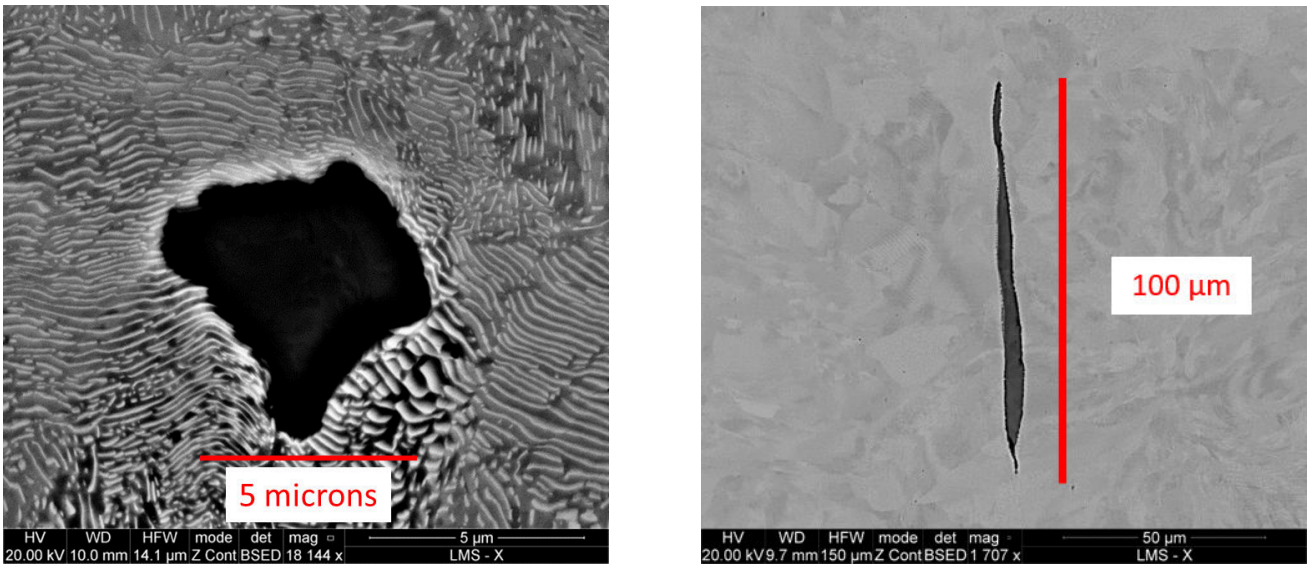

Figure 3.3: MnS inclusions in the transversal direction (left) and longitudinal direction (right)

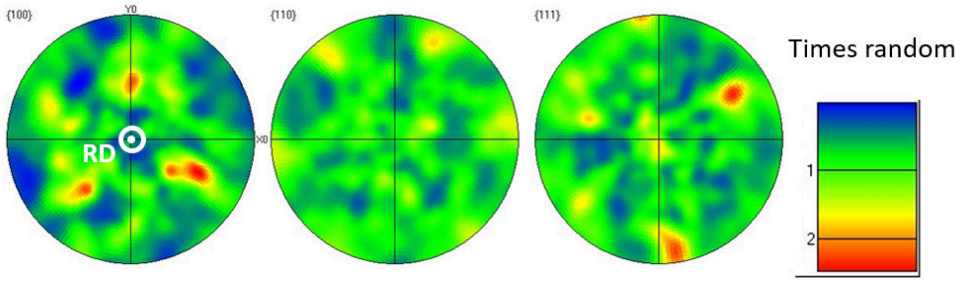

Figure 3.4: Pole figures on a $930 * 810$ μm^2 zone, with normalized scale, in the longitudinal direction.

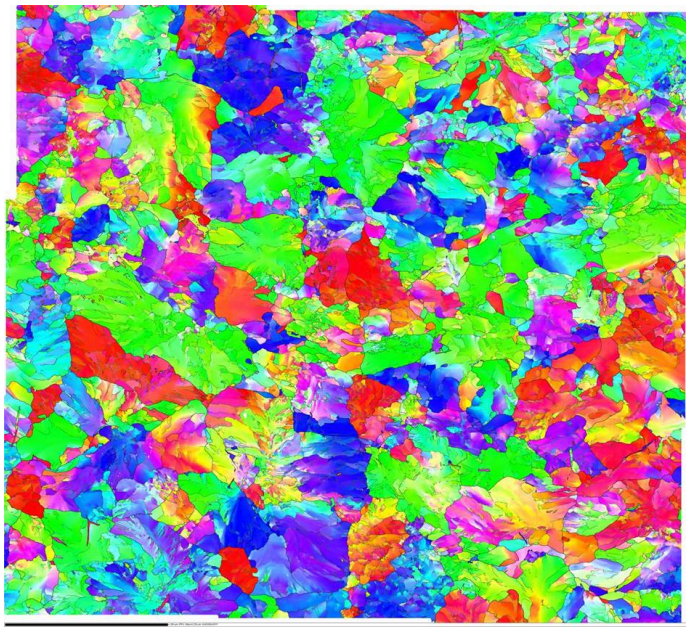

Figure 3.5: Orientations (Euler angles, IPF-X) obtained on a $930 * 810$ μm^2 zone normal to the rolling direction.

3.1.3 Monotonic tensile tests

A monotonic tensile test was performed in a 100 kN MTS hydraulic axial testing machine. The tests was displacement controlled, with an initial strain rate of $5 * 10^{-4}\ m/m * s^{-1}$. The ultimate elongation was measured at $A = 10$ % and the ultimate tensile strength at $R_m = 790\ MPa$, a bit lower than the 880 MPa theoretical value given table 3.2.

3.1.4 Cyclic tensile tests

In order to get the material constitutive equations along with a tension-driven fatigue damage model for the local approach [Doquet and Bertolino, 2008b], cyclic tensile tests were performed at various strain ranges and ratios, using the sample described on figure 3.6 and the aforementioned testing machine. Those samples had a diameter of 7 mm over a length of 15 mm, and a R_a of 0.2 μm in their central section. The experiments were strain controlled, using an extensometer, as shown on the left image of figure 3.6, all with the same plastic strain rate (≈ 0.15 %$/s$). Fracture was defined as a 5 % drop of the peak tensile stress. The test conditions and results of the 9 experiments are presented in table 3.3. At similar imposed strain range $\Delta\epsilon/2$, increasing $R = \epsilon_{max}/\epsilon_{min}$ decreases the number of cycles to failure. Since the material does not always exhibit a steady-state, but rather a slight continuous cyclic strain softening (see figure 3.7), the stresses reporter in the table were measured at mid-life.

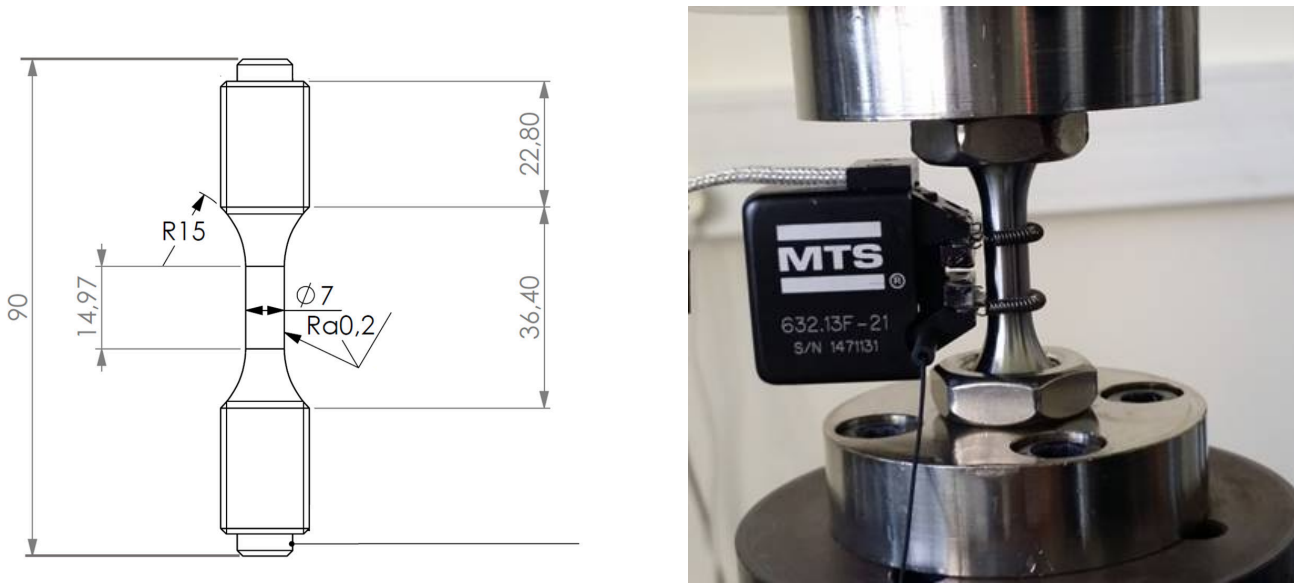

Figure 3.6: Cyclic tensile test specimens: drawing and experimental setup.

The low cycle fatigue life could be predicted using Manson-Coffin's law (left graph of figure 3.8):

$$N_f = a * \Delta\epsilon_{plastic}^{m} \tag{3.1}$$

Or slightly better using Smith, Watson & Topper's model [Smith et al., 1970], with a threshold to account for the possibility of infinite life (and non propagation in the local approach) (right graph of figure 3.8):

$$\beta_{SWT} = \Delta\epsilon_n * \sigma_{n,max} \tag{3.2}$$

$$N_f = a * (\beta_{SWT} - \beta_{Threshold})^m \tag{3.3}$$

Table 3.3: Test conditions and results of the cyclic tensile tests. Stresses measured at mid-life. $R = \epsilon_{max}/\epsilon_{min}$

$N°$	$\Delta\epsilon/2$ (%)	R	N_f (cycles)	$\Delta\epsilon_p$/cycle (%)	σ_{max} (MPa)	σ_{min} (MPa)
4	0.25	-1	*confidential*	0.28	360	-365
2	0.4	-1	*confidential*	0.69	445	-466
5	0.55	-1	*confidential*	1.2	497	-503
1	0.7	-1	*confidential*	1.70	537	-559
3	1	-1	*confidential*	2.75	619	-637
6	0.25	-0.5	*confidential*	0.26	369	-371
7	0.4	0	*confidential*	0.71	444	-450
8	0.25	0	*confidential*	0.24	396	-369
9	0.25	0.5	*confidential*	0.29	409	-300

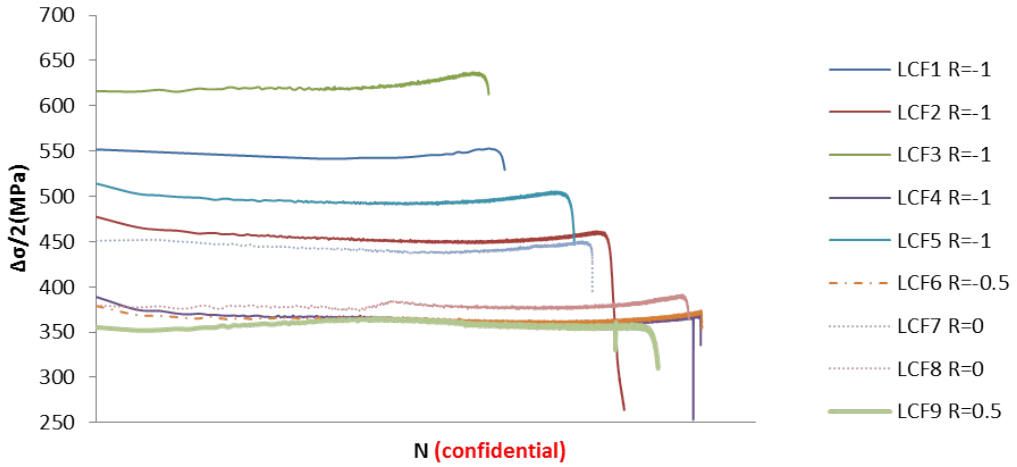

Figure 3.7: Evolution of the axial stress range during the experiments.

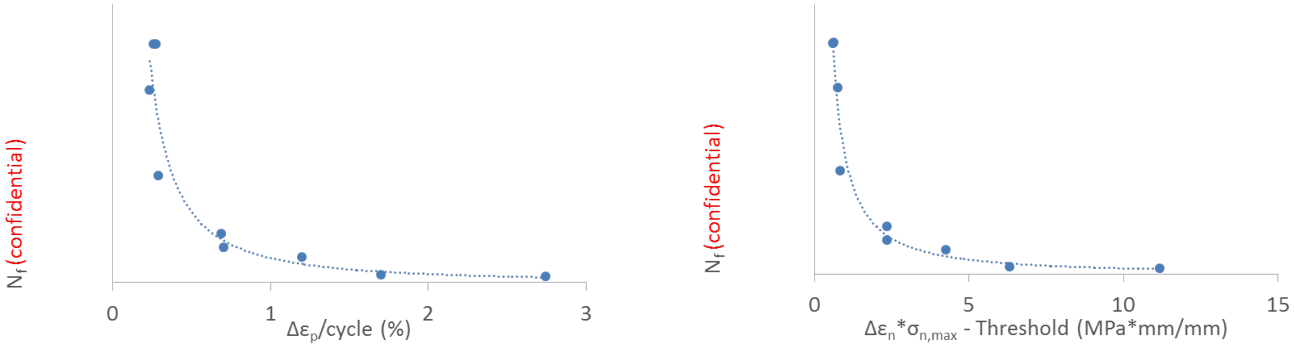

Figure 3.8: LCF life prediction: Manson-Coffin's law (Left), and Smith, Watson & Topper's model (right).

An initiation site for this tensile fatigue mechanism, along with some striations can be seen on figure 3.9.

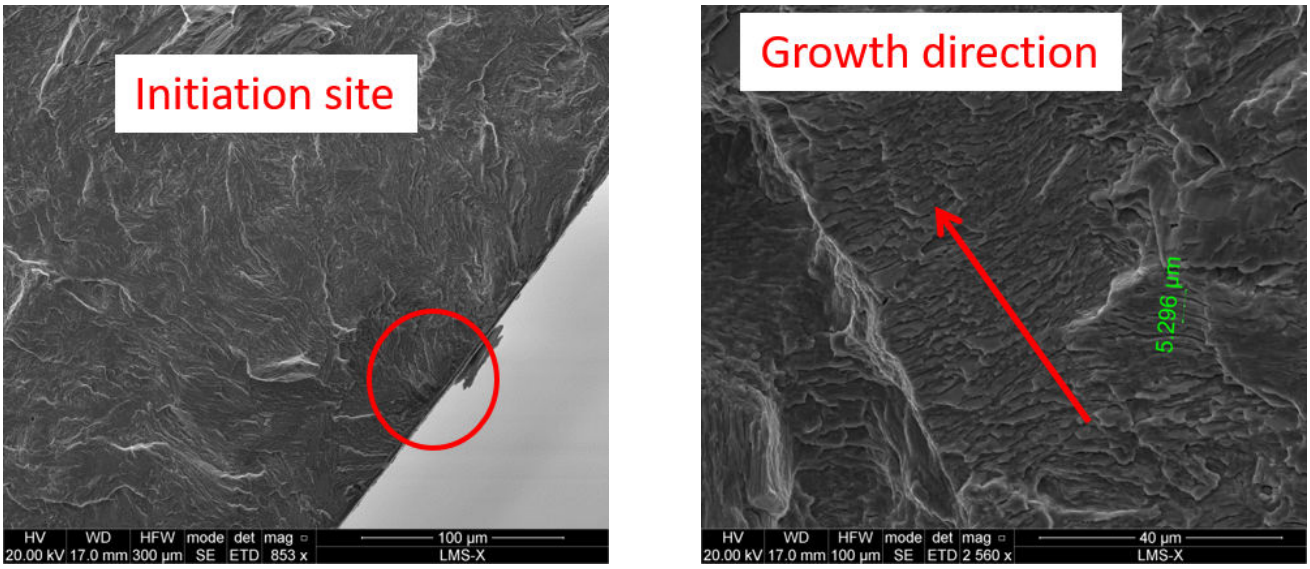

Figure 3.9: Initiation site and striations on sample N° 5

3.1.5 Cyclic shear tests, with or without a tensile static load

The previous experiments gave a tension-driven low cycle fatigue damage model for the local approach [Doquet and Bertolino, 2008b]. In order to get a shear-driven damage model, fully reversed torsional cyclic tests, at imposed torque and constant axial stress ($\sigma_{zz} = 0$, 90 or $150MPa$) were performed on a hydraulic triaxial testing machine, allowing tension/compression, torque and internal oil pressure ($\pm 100\ kN$, $\pm 600\ Nm$, $1500\ bar$). The tubular samples, described on the left image of figure 3.10, were equipped with biaxial strain gages (see right image of figure 3.10). As for the cyclic tensile tests, the plastic strain rate was kept at $\approx 0.15\ \%/s$. The strains could only be measured at the beginning, until the strain gages got unstuck from the sample, which fortunately generally occured after more or less steady-state stress-strain loop were recorded.

In the elastic domain, the shear strain and stress vary linearly with the radius:

$$\sigma_{r\theta} = \sigma_{r\theta}(r_e) * \frac{r}{r_e} \tag{3.4}$$

With r_e and r_i the outer and inner radius respectively. The shear stress on the outer surface writes as:

$$\sigma_{r\theta}(r_e) = \frac{C * 4 * r_e}{2 * \pi * (r_e^4 - r_i^4)} \tag{3.5}$$

If the gradient is neglected, this stress writes as:

$$\sigma_{r\theta}(r_e) = \frac{C * 3}{2 * \pi * (r_e^3 - r_i^3)} \tag{3.6}$$

Which gives a 6% difference. In the case of an elastic behaviour, this gradient has to be taken into account. However, FEM elastic-plastic computations with the constitutive equations described later on shows that the shear stress tends to become uniform as the material is plastified. Each of the hypothesis were thus considered depending on the torque amplitude.

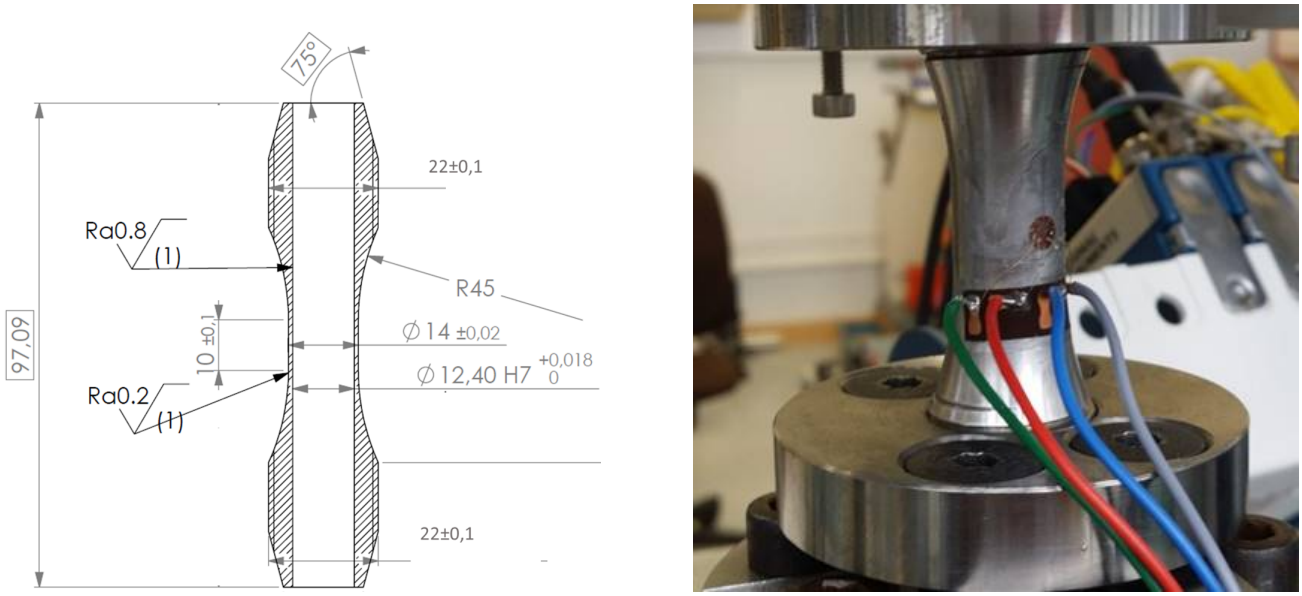

Figure 3.10: Cyclic shear test specimens: drawing and experimental setup.

The test conditions, resulting number of cycles to failure and fracture mechanism are presented in table 3.4. The tensile and longitudinal crack initiation directions should be equally probable for an isotropic material when the axial stress is equal to zero. However, in the R260 steel, crack initiations were always longitudinal, that is: parallel to the rail axis. This is probably due to the elongated MnS inclusions, whose elongated shape helps crack to initiate, as shown by the *in situ* experiments in the SEM (see appendix E). It is however possible to get a transversal initiation from a certain level of tensile stress, whose value seems to increase with the shear stress amplitude (90 MPa if $\Delta\tau = 502\ MPa$, 150 MPa if $\Delta\tau = 628\ MPa$).

The crack initiates in a maximum shear direction, and then sometimes bifurcates at ± 45 °, in a principal direction, as shown in figure 3.11. The higher the shear / normal stress, the longer the longitudinal / transversal crack. The preferential transversal initiation direction when a static tensile stress is applied is due to the resulting reduction in friction, which only exists in the transversal direction, while the axial directions only undergoes a positive T stress (non singular).

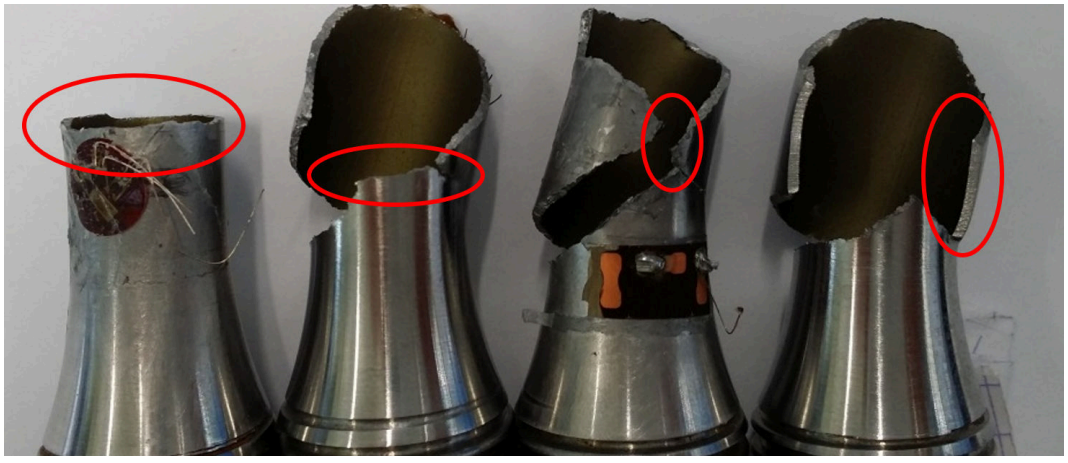

Figure 3.11: Various crack paths, from left to right: long transversal growth, short transversal growth, short longitudinal growth and long longitudinal growth.

Table 3.4: Test conditions and results of the cyclic shear tests. Strains measured at mid-life. L means longitudinal initiation and T transversal initiation.

$N°$	Tensile stress (Mpa)	Torque(Nm)	τ max (MPa)	τ mean (MPa)	N_f (Cycles)	$\Delta\gamma$ (%)	Initial Orientation of the main crack
2	0	± 52	± 251	± 237	*confidential*	0.86	L
4	0	± 56	± 270	± 255	*confidential*	1.38	L
3	0	± 60	± 290	± 274	*confidential*	1.85	L
6	0	± 62	± 299	± 283	*confidential*	1.71	L
5	0	± 65	± 314	± 296	*confidential*	2.25	L
1	0	± 70	± 338	± 319	*confidential*	2.51	L
12	0	± 85	± 410	388	*confidential*	5.14	L
13	0	± 95	± 458	433	*confidential*	7.69	L
10	90	± 52	± 251	± 237	*confidential*	1.21	T
7	90	± 65	± 314	± 296	*confidential*	2.28	L
9	150	± 52	± 251	± 237	*confidential*	1.26	T
8	150	± 65	± 314	± 296	*confidential*	1.88	T
11	250	± 52	± 251	± 237	*confidential*	1.23	T

In previous studies, [Doquet and Bertolino, 2008b, Doquet et al., 2009, Doquet et al., 2010a], Fatemi and Socie's damage function -homogeneous to a strain- was used, to account for shear-driven damage:

$$\beta_{FS} = \Delta\gamma_{max}(1 + k_{FS}\frac{\sigma_{n,max}}{\sigma_y}) \tag{3.7}$$

where $\sigma_{n,max}$ denotes the peak opening stress over a cycle on the facet which undergoes the maximum shear strain range, $\Delta\gamma$, and k_{FS} is a dimensionless coefficient.

Alternatively, Findley's damage function -which has the dimension of a stress- could also be used:

$$\beta_{Find} = \Delta\tau + k_{FI} * \sigma_{n,max} \tag{3.8}$$

where k_{FI} is a dimensionless parameter.

However, in the present study, a shear-driven damage function equal to the product of the two previous ones, -and which thus has the dimension of an energy, like the tension-driven damage function- was preferred:

$$\beta_{Shear} = \beta_{Find} * \beta_{FS} \tag{3.9}$$

The number of cycles to failure could then be predicted as:

$$N_f = a_{shear} * (\beta_{shear} - \beta_{shear,threshold})^{m_{shear}} \tag{3.10}$$

The resulting curve is plotted figure 3.12.

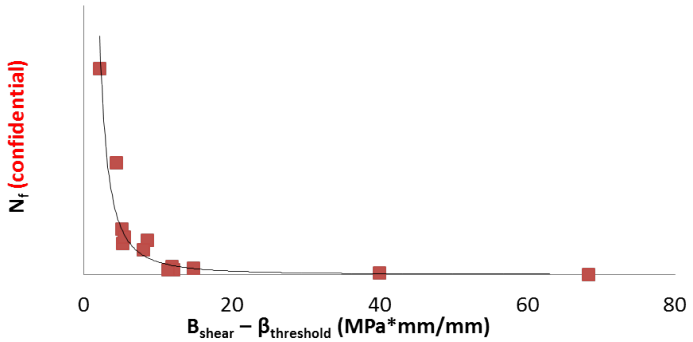

Figure 3.12: LCF life prediction for shear loading: Fatemi & Socie * Findley's damage function.

The fracture surfaces of 3 samples are presented here, as typical examples of the various fracture mechanisms: extended longitudinal crack growth, short longitudinal growth and transversal growth. In spite of the highly worn surfaces, the following elements can be noticed:

- Sample $N°3$ (figures 3.13 and 3.14): $\Delta\tau = 580\ MPa$, $\sigma_{nn} = 0\ MPa$, longitudinal growth, presence of MnS inclusions in the growth direction (a). Some marks of a transversally initiated crack (b) and marks of an aborted bifurcation (c).
- Sample $N°7$ (right image figure 3.14) : $\Delta\tau = 628\ MPa$, $\sigma_{nn} = 90\ MPa$ longitudinal growth, close to a transversal growth. Presence of transversal micro cracks (d): hesitation between the two directions.
- Sample $N°8$ (figure 3.15): $\Delta\tau = 628\ MPa$, $\sigma_{nn} = 150\ MPa$, transversal growth, some longitudinal micro cracks (e). Presence of detached inclusions in the longitudinal direction (f).

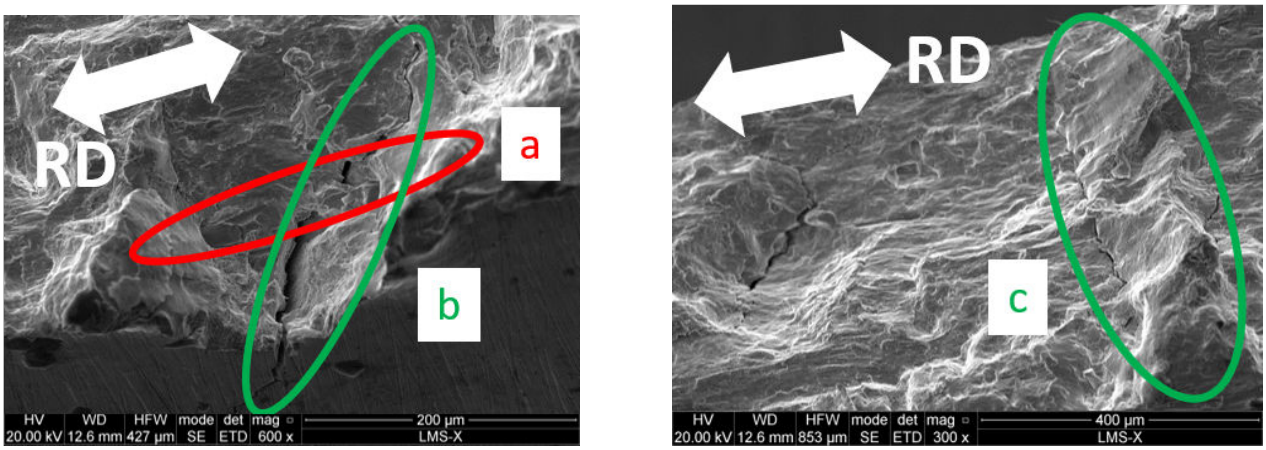

Figure 3.13: Crack initiation on an inclusion and branching on sample $N°3$, $\Delta\tau = 580MPa$ and $\sigma_n = 0$. RD (rolling direction) is parallel to the specimen axis.

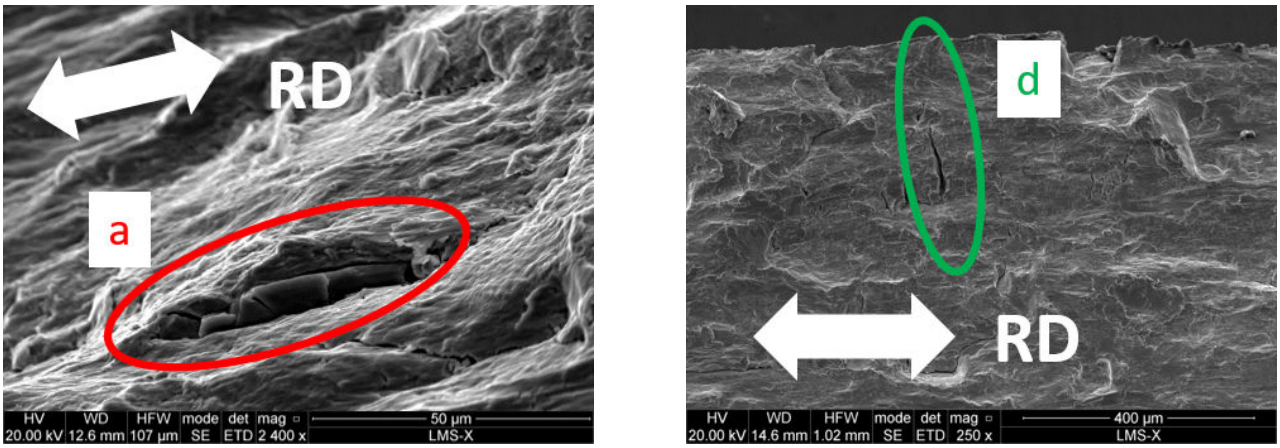

Figure 3.14: Left: broken inclusion in sample $N°3$, $\Delta\tau = 580MPa$and $\sigma_n = 0$. Right: transversal crack in sample $N°7$, $\Delta\tau = 628Pa$ and $\sigma_n = 90MPa$.

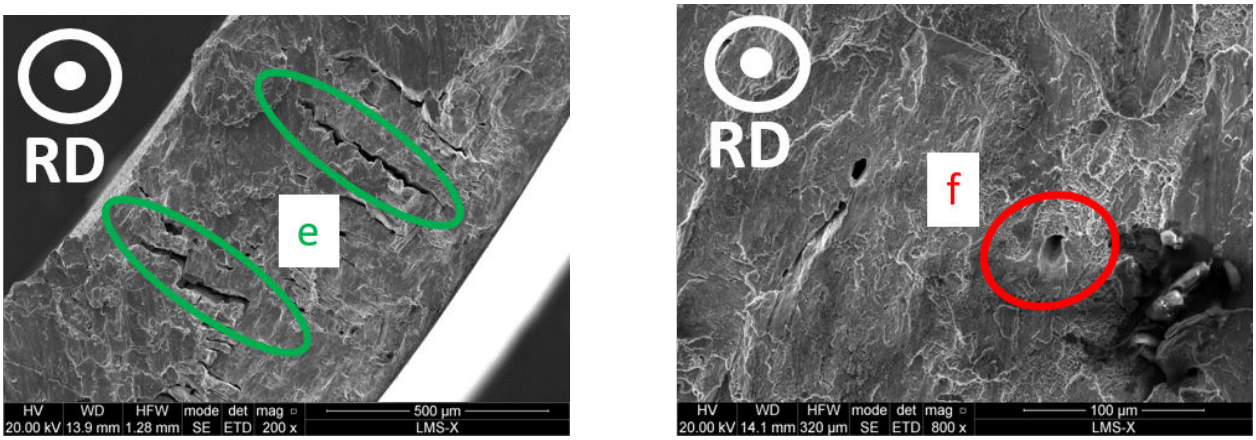

Figure 3.15: Left: longitudinal crack in sample $N°8$, $\Delta\tau = 628Pa$ and $\sigma_n = 150MPa$. Right: detached inclusion in sample $N°8$, $\Delta\tau = 628Pa$ and $\sigma_n = 150MPa$.

3.1.6 Constitutive equations

The stress-strain curves recorded during strain-controlled push-pull and cyclic torsion tests fed a Levenberg-Marquardt algorithm in order to fit constitutive equations using isotropic and one or two kinematic hardening variables, according to Lemaitre and Chaboche's model [Lemaitre and Chaboche, 1994], assuming that the behaviour is isotropic and can be described by Von Mises flow criterion:

$$f = J_2(\underline{\underline{\sigma}} - \underline{\underline{X_1}} - \underline{\underline{X_2}}) - R \tag{3.11}$$

$$d\underline{\underline{X_i}} = C_i * (\frac{2}{3} * A_i * d\underline{\underline{\epsilon_p}} - \underline{\underline{X_i}} * dp) \tag{3.12}$$

$$R = R_0 + (R_M - R_0) * (1 - e^{-b*p}) \tag{3.13}$$

$$d\epsilon_p = d\lambda * \frac{\partial f}{\partial \underline{\underline{\sigma}}} \tag{3.14}$$

where f is the yield function, $\underline{\underline{X_1}}$ and $\underline{\underline{X_2}}$ are the kinematic hardening variables , R the isotropic hardening variable, p the accumulated plastic strain, λ the plastic multiplier, and C_1, C_2, A_1, A_2, R_0, R_M, and b are material coefficients.

The material shows nearly no isotropic hardening, and one kinematic variable is enough to get a relatively good prediction of the behavior for small loads, and a good prediction for high loads, and as shown on figures 3.16, 3.17, 3.18 and 3.19.

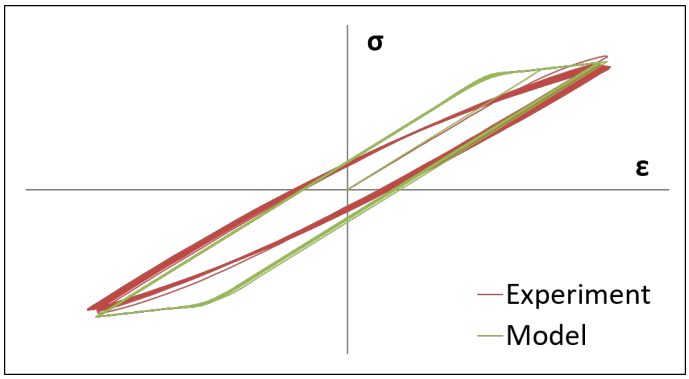

Figure 3.16: Experimental and fitted curve for a push-pull cyclic test, $R = 0$ and $\Delta\epsilon = 0.5$. *No data for confidentiality reasons.*

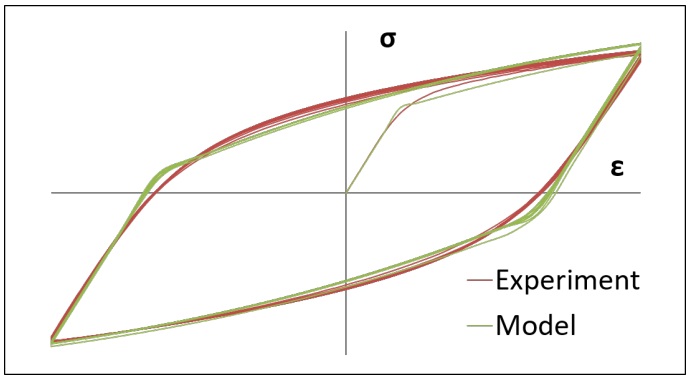

Figure 3.17: Experimental and fitted curve for a push-pull cyclic test, $R = 0$ and $\Delta\epsilon = 2$. *No data for confidentiality reasons.*

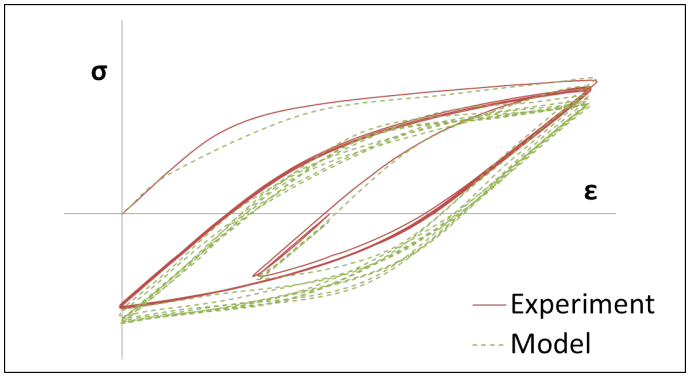

Figure 3.18: Experimental and fitted curve for a push-pull cyclic test, $R = 0$ and $\Delta\epsilon = 0.8$. *No data for confidentiality reasons.*

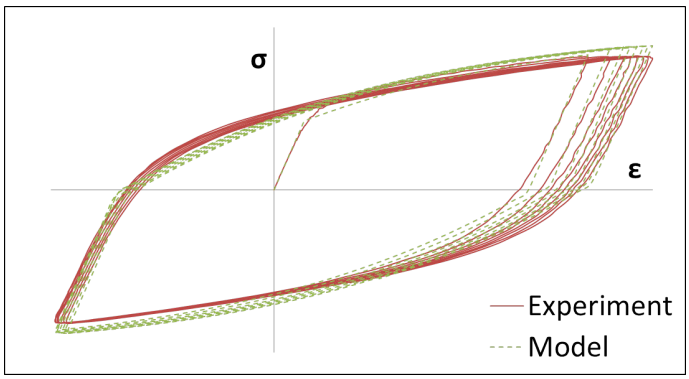

Figure 3.19: Experimental and fitted curve for a torsion cyclic test, $R = -1$ and $\Delta\tau = 820MPa$. *No data for confidentiality reasons.*

3.2 Procedures common to all fatigue crack growth tests

This section aims at giving general insights on how the crack tip was located and how the effective Stress Intensity Factors were determined from DIC fields in presence of contact stresses and plasticity. A part of this work has been published in [Bonniot et al., 2019]. The specific procedures for each type of experiments will be detailed in their corresponding section.

3.2.1 Introduction

As explained in section 2.3, rolling contact fatigue cracks in rails undergo non-proportional mixed-mode loading with compression phases [Bogdanski et al., 1998, Mai et al., 2017]. The mode I loading with various R ratios encountered at different points of the crack front or at different temperatures was reproduced in this work using SENT specimens described in chapter 4. In the (K_{II} - K_{III}) space, the loading path computed on squat cracks is almost proportional, and was reproduced using asymmetric four point bending tests on a bar detailed in chapter 5. Finally, in the (K_I - K_{II}) space, the computed loading paths is approximately sequential, with a static compression during the mode II cycle. Such loading paths were experimentally reproduced using transversally precracked thin tubes loaded in tension-compression and torsion, as detailed in chapter 6.

In each of those experiments, non-linearities were present, and DIC was used to monitor the crack growth and estimate the effective SIFs.

The principle of using an experimentally-determined displacement field to evaluate the SIFs was proposed by Barker et al. [Barker et al., 1985] in 1985, with a displacement field computed from the stress field obtained by photo-elasticity. The experimental displacement field was projected over a theoretical displacement field (obtained from Westergaard's equations), and the crack tip position was supposed to be known. The SIFs were computed from the resulting coefficients. A similar approach was then used by Abanto-Bueno & Lambros [Abanto-Bueno and Lambros, 2002] on a displacement field obtained by DIC, and has been used widely since then.

This approach based on a projection on William's series expansion (or another analytical displacement field, such as Westergaard's solutions) was used in [Barker et al., 1985, Abanto-Bueno and Lambros, 2002, Yates et al., 2010, Tong et al., 2018] with a crack tip position supposed to be known.

Others used this method to evaluate both the crack tip position and the SIFs, by seeking the position of the crack tip which minimizes the error between the DIC field and its projection on the theoretical field. Roux & Hild [Roux and Hild, 2006] used this principle, without giving further details on the method. Yoneyama et al. [Yoneyama et al., 2007] tried to optimize simultaneously the value of the SIFs and the crack tip position using a Newton-Raphson method, which as Zanganeh et al. [Zanganeh et al., 2013] pointed out, is very sensitive to the initial guess of the crack tip position. Zanganeh et al. [Zanganeh et al., 2013] used numerically generated or experimentally obtained displacement fields to perform a comparative study on various methods: two Newton-type methods, a simplex method, a genetic algorithm and a Pattern Search method. This last method was found to be satisfying, both in terms of accuracy and computational cost. Harilal et al. [Harilal et al., 2015] tried every possible position of the crack tip on a square grid, which has the advantage of avoiding convergence towards a local minima, but is not very efficient in terms of computational cost, especially since the grid pitch has to be small to get a precise estimation. Vormwald et al. [Vormwald et al., 2018] tried a similar approach, but with grids of varying size: a first estimation of the crack tip position is found using a coarse grid, then the process is repeated on a refined grid around the previously estimated crack tip. This process can be repeated as many times as necessary to get an accurate estimate of the crack tip position.

Some authors used a projection on a theoretical field, but with a different way to locate the crack tip, such

as Lopez-Crespo et al. [Lopez-Crespo et al., 2008, Lopez-Crespo et al., 2009] who applied a Sobel line detection algorithm to the DIC displacement field to locate the crack tip. Hamam et al. [Hamam et al., 2007a] as well as Mathieu et al. [Mathieu et al., 2012] added supersingular terms (terms of negative order) to William's series expansion. It was then possible to locate the crack tip by seeking the position where the -1 order term was equal to zero.

Other methods, not involving a projection over a theoretical field, were used by some authors. Réthoré et al. [Réthoré et al., 2005, Réthoré et al., 2007] used an interaction integral to evaluate the SIFs, but such method supposes stress-free crack faces. Roux et al. [Roux and Hild, 2006, Hamam et al., 2007a, Mathieu et al., 2012] used an integrated approach, where shape functions corresponding to a theoretical displacement field for an elastic cracked body were used in the image correlation process.

In all the aforementioned methods, only the displacements measured outside the crack tip plastic zone and the plastic wake were taken into account in the analysis, but crack tip plasticity was not taken into account in the analytical displacement fields used to determine the SIFs, except in [Hamam et al., 2007a, Mathieu et al., 2012] in a very simplified way.

Hos et al. [Hos et al., 2016] used the relative opening displacement measured between two points on each side of the crack (COD) and estimated crack closure using the stifness change method on the displacement jump - force loop. Vormwald et al. [Vormwald et al., 2018] used the same displacement jump measurements to get a direct estimate of the SIFs, knowing the analytical relationship between those two values. The same type of approach was used by Smith & Smith [Smith and Smith, 1988] using an extensometer to measure the crack sliding displacement, and by Wong et al. [Wong et al., 1996, Wong et al., 2000b] using surface replicas to measure the displacement jump. By contrast, Bertolino & Doquet [Bertolino and Doquet, 2009] compared the measured sliding displacement profiles to those issued from elastic-plastic simulations, with or without a uniform friction stress along the crack face.

Decreuse et al. [Decreuse et al., 2012] proposed a different approach, where the plasticity-free mode I and mode II displacement fields are not analytical, but obtained from DIC by correlating an image taken at maximum load and an image taken after a small, fully elastic unloading. A second displacement field, containing the influence of crack tip plasticity, can also be built by correlating images obtained during a monotonic loading and subtracting the elastic part obtained previously. The four fields (two for each mode) are then used in the same way as the analytical displacement fields in the previous projective approaches.

Bertolino & Doquet [Bertolino and Doquet, 2009], Doquet et al. [Doquet et al., 2010a] & Bonniot et al. [Bonniot et al., 2018] compared the measured in-plane or out-of-plane crack face relative sliding displacement profiles to those issued from elastic-plastic FEM computations run with various loading ranges, to find the loading range which gives the best fit of experimental data. The effective ΔK_{II} or ΔK_{III} were deduced from the corresponding loading range.

The experimental conditions of all those papers are summarized in table 3.5.

From this literature survey, it appears that except in [Hos et al., 2016, Vormwald et al., 2018], DIC analysis of fatigue crack growth was always applied for zero or positive mode I R ratios. For negative R ratios, it would be tempting to correlate the images captured at peak load and zero load, ignoring the compressive part of the cycle. However, crack closure sometimes occurs in compression and part of the compressive stage of the cycle sometimes contributes to crack growth [Pommier et al., 1997], so that a strategy for the post-treatment of DIC fields is needed in presence of a compressive stage. Furthermore, in mixed-mode, normal compression enhances contact and friction stresses along the crack and no theoretical expression of the displacement field is available in that case.

Table 3.5: Test conditions found in the literature. COD stands for the measurement of the displacement jump between two points. DJ stands for the measurement of the displacement jump between two lines. If the displacement field are not obtained from DIC, the method is given in parenthesis. I/II means proportional mixed mode and $I+II$ non-proportional mixed mode.

Authors	Material	Mode	R_I	Method for SIF measurement	Crack-tip plasticity modelling?
[Abanto-Bueno and Lambros, 2002]	polyethylene	I	(0, not fatigue)	Analytical full field	no
[Réthoré et al., 2005]	maraging steel	I/II	0	interaction integral	no
[Réthoré et al., 2007]	SiC	I	(0, not fatigue)	interaction integral	no
[Roux and Hild, 2006]	SiC	I	(0, not fatigue)	DIC integrated	no
[Roux and Hild, 2006]	SiC	I	(0, not fatigue)	Analytical full field	no
[Yoneyama et al., 2007]	PMMA	I/II	(0, not fatigue)	Analytical full field	no
[Hamam et al., 2007a]	Steel	I	0	Analytical full field	simplified
[Hamam et al., 2007a]	Steel	I	0	DIC integrated	no
[Lopez-Crespo et al., 2008, Lopez-Crespo et al., 2009]	7010 Al	I/II	0	Analytical full field	no
[Yates et al., 2010]	7010 Al	I	>0.15	Analytical full field	no
[Mathieu et al., 2012]	Ti35	I	0.1	Analytical full field	simplified
[Zanganeh et al., 2013]	Al (2 types)	I/II	0.1	Analytical full field	no
[Harilal et al., 2015]	2014-T6 Al	I/II	>0	Analytical full field	no
[Lachambre et al., 2015]	Iron	I	0.14	Analytical full field	no
[Hos et al., 2016]	S235	I+II	-1	COD	no
[Vormwald et al., 2018]	S235	I+II	-1	COD	no
[Vormwald et al., 2018]	S235	I+II	-1	Analytical full field	no
[Tong et al., 2018]	316L	I	0,1	Analytical full field	no
[Decreuse et al., 2012]	S355	I+II	>0	DIC basis	yes
[Bertolino and Doquet, 2009]	M250 & Ta6V	II	/	DJ (SEM insitu)	simplified
[Doquet et al., 2010a]	M250 & Ta6V	II/III	/	DJ (replicas)	yes
[Bonniot et al., 2018]	R260	II/III	/	DJ	yes
[Wong et al., 1996, Wong et al., 2000b]	Rail steel	I+II	0	COD (replicas)	no

3.2.2 Methodology

Several approaches were tested to evaluate the influence of non linearities on crack tip localization and estimation of the effective SIFs. For that purpose, displacement fields issued from finite element computations with contact/friction and/or elastic-plastic behavior, for which the exact crack-tip location and the effective SIFs are known were used. Those SIFs were computed using the relative crack face displacement jump, which allows a correct evaluation of the SIFs in the presence of contact and friction between the crack faces, contrary to classical J-integral methods. In the following, those effective SIFs will be referred to as ΔK^{FEM}. If plasticity is modeled in the computation, the SIFs are evaluated on a similar computation (loading & compression/friction), but with an elastic behavior.

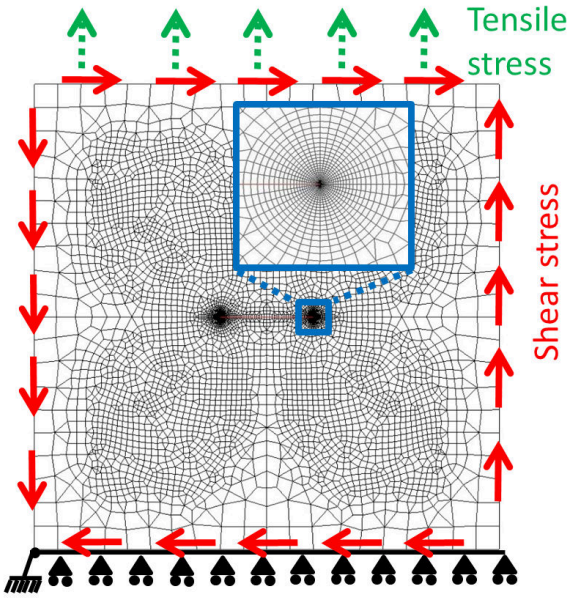

Figure 3.20: FEM mesh and boundary conditions. Plate size: $10 * 10\ mm^2$, crack length: $2a = 4\ mm$. Element size at the tip: $25\ \mu m$.

The mesh and boundary conditions are represented on figure 3.20. The crack length is $2a = 4\ mm$, and plane stress is assumed. The FEM-obtained displacement fields are projected on a square grid with a $20\ \mu m$ pitch, similar to the grid used for DIC.

For mode I, the load ratio R_I was either zero or negative, depending on the computations, but the displacement fields were always extracted at maximum and minimum loads, and their difference was used to compute ΔK_I^{FEM}.

Fully reversed mode II was simulated with or without a superimposed static normal compression. Again, the displacement fields were extracted at maximum and minimum shear loads and their difference was used to compute ΔK_{II}^{FEM}.

Using Von Mises criterion and Irwin's approach for perfectly plastic materials, the extensions of the cyclic plastic zone ahead of the crack tip in plane stress for mode I and mode II are approximately:

$$r_{p,I} = \frac{1}{2\pi}\left(\frac{\Delta K_I}{2\sigma_Y}\right)^2 \tag{3.15}$$

$$r_{p,II} = \frac{3}{2\pi}\left(\frac{\Delta K_{II}}{2\sigma_Y}\right)^2 \tag{3.16}$$

In order to allow a transposition of the results to other materials, the approximate size of the cyclic crack tip plastic zone, according to equations 3.15 and 3.16 will be specified for each mode I or mode II case analysed. But note that when real experimental mixed-mode displacement fields are analysed, due to friction stresses that reduce ΔK_{II}^{eff}, the effective size of the mode II plastic zone is not known a priori, and is often actually significantly smaller than predicted, inserting the nominal ΔK_{II} in eq. 3.16 [Vojtek et al., 2019].

Elastic frictionless computations were performed under mode I or mode II loading. Various elastic-plastic computations were performed using constitutive equations for $R260$ rail steel [Bonniot et al., 2018], to study the influence of crack-tip plasticity. In that case, two cycles were simulated, which was enough to get a stabilized cycle since the hardening is mostly kinematic. Elastic computations were performed under mode I or mode II with compression and friction ($\mu = 0.5$) in order to study the influence of contact stresses.

Other cases, combining both non linearities or both modes were investigated. For sequential and 90° out-of-phase mixed-mode loading (both with $R_I = 0$ and $R_{II} = -1$), the displacement fields extracted at maximum and minimum tensile load and shear load were used to determine ΔK_I^{FEM} and ΔK_{II}^{FEM}, respectively.

3.2.3 Compared approaches

Three approaches were evaluated: the first one is based on a projection of the displacement field over William's expansion, which is the most commonly used approach, the second one is based on a fit of the relative displacement between two rows of virtual extensometers, above and below the crack, for which an improvement is proposed to take into account contact stresses and crack tip plasticity, and the third one is based on a coupling between FEM computations and DIC.

3.2.4 William's expansion

This approach is based on the search for the crack tip position minimizing the error between the DIC field and its projection over William's expansion, which is the most common method. The algorithm used to locate the crack-tip is a pattern search algorithm [Zanganeh et al., 2013], with an initial guess chosen after testing all the positions on a coarse grid. This approach gives both the crack tip position, and an estimation of the effective SIFs.

The algorithm and its parameters are described in Appendix B. The results for various loading cases are given in tables 3.6 & 3.7.

In the elastic frictionless cases (LEFM hypothesis), the crack tip position and SIFs are predicted accurately for both modes.

In mode I, when crack-tip plasticity is present, the crack length is slightly overestimated and ΔK_I^{eff} as well, but the error, which rises with the applied loading range remains small: 3.6% for $\Delta K_I^{FEM} = 30\ MPa\sqrt{m}$ ($K_I^{FEM}/\sigma_Y = 0.063\ \sqrt{m}$). Adding a compression phase leads to an underestimation of the crack length, and an overestimation of ΔK_I^{eff}, because the displacement field for a closed crack under compression is not described by William's expansion.

Another solution could be to capture several images during one cycle and correlate them with the image at maximum force, allowing to plot ΔK_I measured with William's expansion versus the applied load, as in [Tong et al., 2018], and then seek for the change of slope (as in the force-displacement method). But this last method requires the capture of a lot of images and the post-treatment will be longer.

Table 3.6: Results obtained using William's expansion with PS algorithm in mode I. e stands for elastic behavior and $e-p$ for elastic-plastic behavior. Cyclic plastic zone r_p computed using eq. 3.15.

Material behavior	ΔK_I^{FEM} $(MPa\sqrt{m})$	r_p (μm)	Compressive stress	Error on crack tip location (μm)	estimated ΔK_I $(MPa\sqrt{m})$
e	10	/	0	0	10.1
e-p	10	17	0	7	10.1
e-p	20	69	0	33	20.3
e-p	30	155	0	74	31.1
e-p	30 + small unloading	155	0	-7	/
e	10	/	-50	-41	11.7
e	10	/	-100	-74	13.2
e	10	/	-150	-96	14.7
e	10	/	-150	Pre-determined tip	13.8

Table 3.7: Results obtained using William's expansion with PS algorithm in mode II. e stands for elastic behavior, $e-p$ for elastic-plastic behavior and $e-f$ for elastic with friction. Cyclic plastic zone r_p computed using eq. 3.16.

Material behavior	ΔK_{II}^{FEM}	r_p (μm)	Compressive stress	Error on crack tip location (μm)	estimated ΔK_{II} $(MPa\sqrt{m})$
e	10	/	0	-4	10.0
e-p	10	52	0	48	10.2
e-p	20	207	0	215	21.4
e-p	30	466	0	541	38.3
e-p	30	466	0	Pre-determined tip	48.0
e+f	6	/	-50	-78	7.8
e+f	1.9	/	-100	-278	5.3
e+f	2	/	-100	Pre-determined tip	5.0

For mode II, adding crack-tip plasticity leads to an overestimation of the crack length by up to 0.5 mm as well as an overestimation of ΔK_{II}^{eff} up to 28 %, due to the elongated shape of the mode II plastic zone ahead of the tip (see figure 2.9 in section 2.2.3). In mode II, the cyclic plastic zone is three times longer than in mode I for the same value of ΔK (see eq. 3.15 & 3.16), which explains the stronger effect of mode II crack tip plasticity on the crack tip localization and SIFs evaluation. Adding compression and friction leads to an underestimation of the crack length, and an overestimation of ΔK_{II}^{eff}, like for mode I.

From this first analysis, it appears that such an approach cannot be used to simultaneously locate the crack tip and determine the effective SIFs in the cases of high mode II loadings and high compression or friction between the crack faces. It can however be used to locate the crack tip in mode I if applied between two well chosen images: at maximum load, and after a small (elastic) unloading, as suggested by Decreuse et al. [Decreuse et al., 2012]. By doing so, the effects of crack-tip plasticity and contact forces between the crack faces (since the crack is always

opened) can be avoided, as shown in table 3.6.

The same approach but with a fixed crack tip (which can be determined using the aforementioned technique) was evaluated, but the same problems persisted: overestimation of ΔK_I^{eff} in the presence of compression, and overestimation of ΔK_{II}^{eff} in the presence of high friction or high ΔK_{II}^{eff}.

An attempt was made to change the size of the area close to the crack tip which is excluded from the analysis (see Appendix B) in order to avoid the plastic zone. This was done by changing the inner radius R_{int} and outer radius R_{ext} of the considered area (Appendix B, figure B.2). The results are given in table 3.8 for an elastic-plastic frictionless mode II computation with $\Delta K_{II}^{FEM} = 20\ MPa\sqrt{m}$. Increasing the inner or outer radius does no prevent an overestimation of the crack length nor an overestimation of the effective SIFs.

Table 3.8: Influence of the size of the excluded area (of radius R_{int}) around the crack tip for $\Delta K_{II}^{FEM} = 20\ MPa\sqrt{m}$ with elastic-plastic behavior. $r_p = 0.25\ mm$ computed using eq. 3.16

Rint (mm)	Rext location (μm)	Error on crack tip ΔK_{II} ($MPa\sqrt{m}$)	estimated
0.2	0.6	204	21.65
0.2	1.2	215	21.44
0.2	2	215	21.42
0.8	1.8	219	21.38

William's series expansion with additional terms

In order to try to capture the effects of friction and contact between the crack faces, an attempt was made to add the corresponding terms to William's series expansion and to perform the projection on this combined field.

In this case, the theoretical field writes as:

$$\underline{U}_{theoretical} = \underline{U}_{William's} + \underline{U}_{contact} + \underline{U}_{friction} \tag{3.17}$$

With:

$$\underline{U}_{contact} = \frac{\sigma_{yy,contact}}{E} * (y * \underline{u}_y - \nu * x * \underline{u}_x) \tag{3.18}$$

which is the displacement field in an uncracked plate submitted to an axial load $\sigma_{yy,contact}$, and

$$\underline{U}_{friction} = \frac{\sigma_{xy,friction}}{2 * G} * (x * \underline{u}_y + y * \underline{u}_x) \tag{3.19}$$

which is the displacement field in an uncracked plate submitted to a shear load $\sigma_{xy,friction}$. y corresponds to the vertical axis and x to the horizontal axis. The rest of the algorithm remains as described in Appendix B.

In mode I, the effects of crack tip plasticity remains: K_I and the crack length are a bit overestimated, as shown in table 3.9. However, the SIFs, crack tip position and contact stresses are correctly estimated in the case of an elastic behavior with compression phase, while the crack length is underestimated and the SIFs overestimated when using William's series expansion alone.

In mode II, the crack length and SIFs are still overestimated when plasticity is modeled, and the algorithm converged towards absurd values for $\Delta K_{II}^{FEM} = 30\ MPa\sqrt{m}$, as shown in table 3.10. In elastic cases with contact

Table 3.9: Results obtained using William's series expansion + additional terms with PS algorithm in mode I. e stands for elastic behavior and $e-p$ for elastic-plastic behavior.

Material behavior	ΔK_I^{FEM} $(MPa\sqrt{m})$	Compressive stress (MPa)	Error on crack tip location (μm)	estimated ΔK_I $(MPa\sqrt{m})$	Estimated contact stress (Mpa)
e	10	0	0	10.1	-1
e-p	10	0	7	10.1	-1
e-p	20	0	37	20.0	-7
e-p	30	0	78	30.8	-9
e	10	-50	0	10.0	-51
e	10	-100	0	10.0	-101
e	10	-150	0	10.0	-151
e-p	10	-100	26	10.2	-98

Table 3.10: Results obtained using William's expansion + additional terms with PS algorithm in mode II. e stands for elastic behavior, $e-p$ for elastic-plastic behavior and $e-f$ for elastic with friction.

Material behavior	ΔK_{II}^{FEM} $(MPa\sqrt{m})$	Compressive stress (MPa)	Error on crack tip location (μm)	estimated ΔK_{II} $(MPa\sqrt{m})$	Estimated frictionnal stress (Mpa)
e	10	0	0	10.0	-2
e-p	10	0	48	10.2	-1
e-p	20	0	222	21.1	-9
e-p	30	0	2867	-3.4	-664
e+f	6	-50	0	5.9	-51
e+f	1.9	-100	0	1.9	-100
e-p+f	1.9	-100	0	1.9	-100

& friction, the SIFs, crack tip position and frictional stresses are correctly estimated. Due to the strong influence of mode II crack tip plasticity, this method is not suitable for this type of loading.

3.2.5 Relative displacement jump

The second approach supposes that the crack tip position is known (for example thanks to the aforementioned elastic unloading approach). Here, only the amplitude of the relative displacement jump profile between two rows of virtual extensometers located above and below the crack (see figure 3.21) is used. The distance between the crack face and the extensometers lines is chosen as $\delta = 0.2\ mm$ (slightly larger than a DIC subset which is 0.15 mm) in order to avoid DIC subsets overlapping with the crack, which makes the correlation wrong.

The opening or sliding displacement jump profile behind the crack tip can fitted with:

$$[[U_i]] = a_i\sqrt{r} + b_i \ \ , \ \ i = x, y \tag{3.20}$$

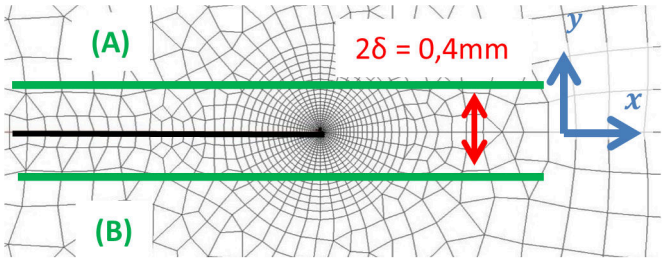

Figure 3.21: Lines above and below the crack between which the displacement jump is measured.

Where the offset b_i accounts for the fact that the displacements are not measured exactly along the crack faces, but at a distance δ. The effective SIFs can be deduced as:

$$\Delta K_I = a_y \frac{E\sqrt{2\pi}}{8} \ , \ \Delta K_{II} = a_x \frac{E\sqrt{2\pi}}{8} \tag{3.21}$$

In order to capture the influence of crack tip plasticity, it is possible to use a displacement jump profile obtained by elastic-plastic frictionless FEM computations and to apply an inverse method, as done in [Bertolino and Doquet, 2009, Doquet et al., 2010a, Bonniot et al., 2018]. Such computations are run at various loading ranges (each one corresponding to a certain ΔK), and by finding the loading range for which the computed displacement profile fits best the measured one, one can estimate $\Delta K^{effective}$:

$$[[U_y]] = [[U_y^{Plastic}]](\Delta K_I) \tag{3.22}$$

$$[[U_x]] = [[U_x^{Plastic}]](\Delta K_{II}) \tag{3.23}$$

This method however supposes that friction does not change the shape of the displacement jump profile, but only reduces its intensity, which may not be correct. The previous displacement jump can be improved by a constant term, which will account for the friction effects. If the crack is locked, the cracked plate will behave as a crack-free plate, and the displacement jump between the two lines will be constant:

$$[[U_y]] = [[U_y^{Plastic}]](\Delta K_I) + B_I \tag{3.24}$$

$$[[U_x]] = [[U_x^{Plastic}]](\Delta K_{II}) + B_{II} \tag{3.25}$$

By finding the combination of $[[U^{Plastic}]]$ and B which gives the best fit, one is able to estimate $\Delta K^{effective}$ in the same way as before.

The results of those three approaches are given in tables 3.11 & 3.12 .

When using eq. 3.20, the effective SIFs are alway underestimated, which is due to the fact that the lines between which the relative displacement is measured are too far away from the crack to use such form, as explained below. The inverse method taking into account crack tip plasticity (eq. 3.22-3.23) gives good estimations in the elastic plastic cases, but overestimates the SIFs when contact stresses are added. Eq. 3.24-3.25 taking into account both crack tip plasticity and contact stresses give good estimations in every cases.

Table 3.11: Results obtained using the displacement jump approaches in mode I. e stands for elastic behavior and $e-p$ for elastic-plastic behavior.

Material behavior	ΔK^{FEM} $(MPa\sqrt{m})$	Compressive stress	Estimated ΔK_I $(MPa\sqrt{m})$		
			Analytical displacement jump	Elastic plastic	Elastic plastic + offset
e	10.0	0	7.5	/	/
e-p	30.0	0	20.9	30.0	30.0
e	10.0	-150	7.5	/	/
e-p	10.0	-100	7.2	10.8	10.2

Table 3.12: Results obtained using the displacement jump approaches in mode II. e stands for elastic behavior, $e-p$ for elastic-plastic behavior, $e-f$ for elastic with friction and $e-p+f$ for elastic-plastic with friction.

Material behavior	ΔK^{FEM} $(MPa\sqrt{m})$	Compressive stress	Estimated ΔK_{II} $(MPa\sqrt{m})$		
			Analytical displacement jump	Elastic plastic	Elastic plastic + offset
e	10.0	0	6.3	/	/
e-p	30.0	0	15.1	30.0	30.0
e+f	6.0	-50	3.8	/	/
e-p+f	1.9	-100	1.2	3.5	1.9

The fact that the offset in eq. 3.24-3.25 improves the results in cases with friction/contact is due to the displacement induced by the stresses transmitted through the crack faces. The higher the distance between the two rows of extensometers (2δ), the higher these displacements, and the more necessary this offset is, as illustrated by table 3.13. Note that this offset also depends on the level of compression (or friction).

Table 3.13: Influence of the distance δ on the estimated SIF in mode I with 100 MPa compression and elastic-plastic behavior using no offset (eq. 3.22-3.23).

δ (mm)	0	0.05	0.1	0.2	0.5
estimated ΔK_I $(MPa\sqrt{m})$	10	10.4	10.6	10.8	11.7

Those approaches using the relative crack face displacement suppose that the crack tip position is known. For a 0.1 mm error on the crack tip position (either vertical or horizontal), the error on the estimated SIFs stays below 5%.

The approach giving the best results in pure mode I and mode II cases (eq. 3.24-3.25) was applied to non-proportional loading cases. In the case of a sequential loading path (table 3.14), the SIFs are evaluated accurately for $\Delta K_{I\&II} = 20\ MPa\sqrt{m}$, and are still acceptable at $\Delta K_{I\&II} = 30\ MPa\sqrt{m}$ (less than 10% error), even though the FEM-computed displacement jump profiles were obtained for pure mode I and pure mode II.

In the case of a 90° out-of-phase loading path with $R_I = 0$ and $R_{II} = -1$ (table 3.15), the results are acceptable

at $\Delta K_{I\&II} = 20\sqrt{m}$ (less than 10% error), but not at $\Delta K_{I\&II} = 30\ MPa\sqrt{m}$. In this case, the values of $\Delta K_{I\&II}$ are overestimated, and a high $\Delta K_{II} = 15.6\ MPa\sqrt{m}$ is measured (instead of $\Delta K_{II} = 0$) by correlation of the images taken at maximum/minimum tensile stress. This is due to the fact that the FEM-computed displacement jump are obtained for pure mode I or pure mode II, instead of the real loading path, for which the couplings between tensile and shear plastic flows at the crack tip [Doquet and Pommier, 2004] are not negligible at 0.2 mm from the crack tip for high loadings. For a material with kinematic hardening, a mode I loading applied before a mode II loading will translate the elastic domain along the tensile stress axis in the tensile-shear stress plane, so that the edge of the elastic domain will be reached faster and the plastic flow direction will be changed during the mode II loading, as illustrated on figure 3.22. In the same way, the presence of the mode II load changes the crack tip plasticity during the mode I part of the cycle.

Table 3.14: Results with eq. 3.24-3.25 for sequential loadings with $R_I = 0$ and $R_{II} = -1$.

$\Delta K^{FEM}_{I\&II}$ $(MPa\sqrt{m})$	part of the cycle	Estimated ΔK_I $(MPa\sqrt{m})$	Estimated ΔK_{II} $(MPa\sqrt{m})$
20	mode I	20	0.5
	mode II	0.1	20.3
30	mode I	33	1.5
	mode II	1.2	30.4

Table 3.15: Results with eq. 3.24-3.25 for 90° out-of-phase loadings with $R_I = 0$ and $R_{II} = -1$.

$\Delta K^{FEM}_{I\&II}$ $(MPa\sqrt{m})$	correlated images	Estimated $\Delta K_I\ MPa\sqrt{m}$	Estimated $\Delta K_{II}\ MPa\sqrt{m}$
20	tensile min/max	20	2.2
	shear min/max	0.4	20.1
30	tensile min/max	32.7	15.6
	shear min/max	6.1	30.1

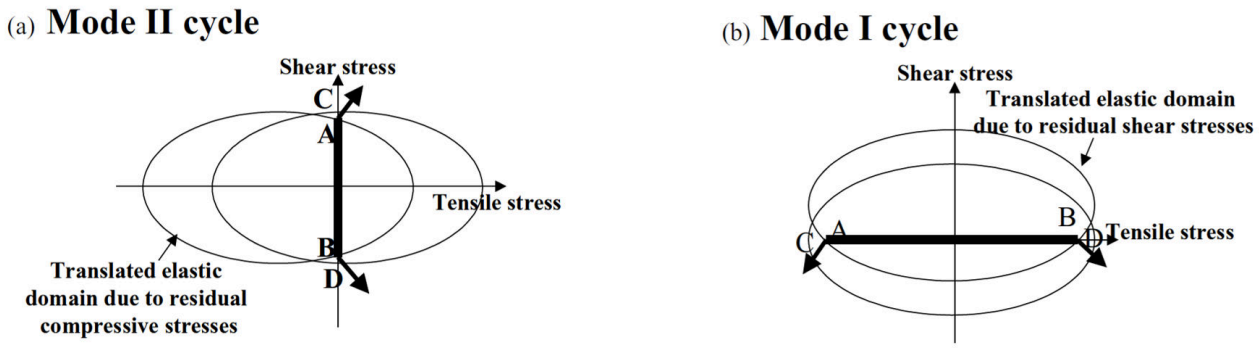

Figure 3.22: Coupling between shear and tensile plastic flows at the crack tip during a sequential experiment. Image from [Doquet and Pommier, 2004].

3.2.6 DIC-FEM coupling

The previous approach provides an estimate of the effective SIFs, but no information on the friction and contact forces along the crack faces.

An approach, coupling FEM computations and DIC is proposed in order to estimate both the effective SIFs and the distribution of the contact and friction stresses along the crack faces. The crack tip and path have to be determined beforehand using another approach.

Nawfal Bouhout, a student from Ecole des Ponts, helped with the development of this method during a 6 month internship.

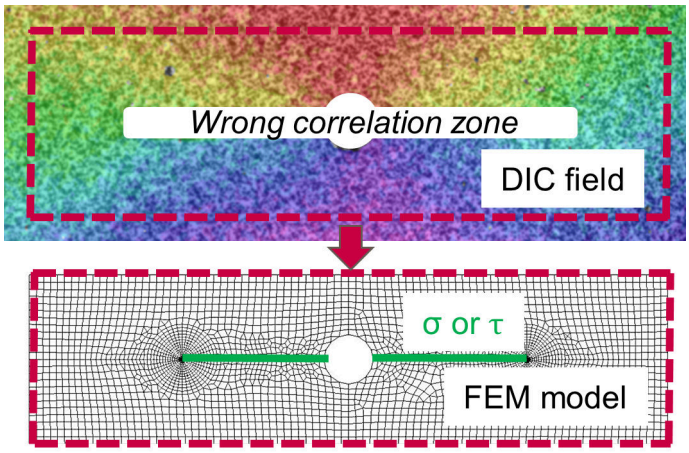

Figure 3.23: Principle of the DIC-FEM coupling.

The displacement is extracted on a closed contour (containing the crack) on the DIC field, as shown in figure 3.23, and linearly interpolated (without any noise filtering) and imposed on the nodes along the contour of the FEM model, similarly to what is done in [Hosdez et al., 2019] or [Lin et al., 2019] (no interpolation in the later). The displacement field obtained by solving the FEM problem is then compared with the DIC field. If contact stresses are present between the crack faces in the experiment, and if the FEM model does not consider the possibility of friction and contact between the crack faces, those two displacement will be equal close to the contour (where the displacement is imposed), but will be different close to the crack, as shown by figure 3.24 a.

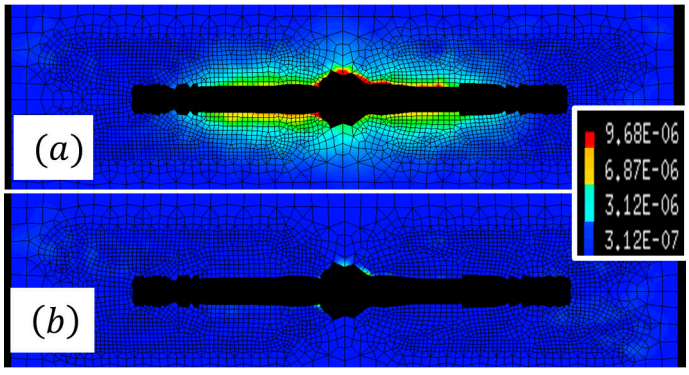

Figure 3.24: Quadratic error on total displacement without (a) and with (b) friction model with elastic modeling. DIC displacement field obtained experimentally for mode II loading with compression.

Contact and friction stresses along the crack faces are added in the FEM model, and their values are optimized in order to reduce the error between the DIC field and the FEM computed field, giving the results shown on figure

3.24 b. This idea is quite similar to the approach that Réthoré et al. [Réthoré, 2010] [Réthoré et al., 2013] used in order to obtain several material parameters by performing a single tensile test with DIC on a plate with a hole, or to the approach used by Blaysat et al. [Blaysat et al., 2015] to identify the cohesive traction profile for interface debonding.

Those contact/friction forces are modeled as piecewise affine. The values on each regularly-spaced points (spacing of 1 mm) are optimized in order to minimize the quadratic error between the DIC field and the FEM field on an area excluding points that are too close to the crack faces (where the DIC field is wrong), as in figure 3.23. The problem can be written as:

$$\{\sigma_l\} = ArgMin\left(\sqrt{\int\int(\underline{\underline{U}}_{DIC} - \underline{\underline{U}}_{FEM}(\sigma_l))^2}\right) \tag{3.26}$$

Where σ_l is the contact and friction stresses profile along the crack faces. The material behavior can be elastic, or elastic plastic. In the elastic case, the principle of superposition can be used, and the FEM field can be written as:

$$\underline{\underline{U}}_{FEM}(\sigma_l, BC_{DIC}) = \underline{\underline{U}}_{FEM}(\sigma_l = 0, BC_{DIC}) + \sum_i \sigma_{l,i} * \underline{\underline{U}}_{FEM}(\sigma_{l,i} = 1, \sigma_{l,j\neq i} = 0, BC_{DIC} = 0) \tag{3.27}$$

Where $\sigma_{l,i}$ is the contact/friction stress at point i of the piecewise affine contact stresses profile, and BC_{DIC} denote the DIC-obtained Dirichlet boundary conditions. The solution of eq. 3.26 is then:

$$\{\sigma_l\} = [[B]^T[B]]^{-1}[B]^T\left(\underline{\underline{U}}_{DIC} - \underline{\underline{U}}_{FEM}(\sigma_l = 0, BC_{DIC})\right) \tag{3.28}$$

With:

$$[B] = [\underline{\underline{U}}_{FEM}(\sigma_{l,i} = 1, \sigma_{l,j\neq i} = 0, BC_{DIC} = 0)] \tag{3.29}$$

This method has been applied on displacements fields obtained from elastic-plastic computations, and the results are given in tables 3.16 & 3.17 column 'Elastic'. In mode I, this method gives an acceptable estimation of $\Delta K_I^{effective}$ for every loading. In mode II, $\Delta K_{II}^{effective}$ is estimated accurately below 10 $MPa\sqrt{m}$ and overestimated above this amplitude. A few computed contact/friction stresses profiles are plotted on figure 3.25. These profiles are well estimated in mode I & mode II below 10 $MPa\sqrt{m}$, but not above, due to the fact that the algorithm tries to compensate the influence of crack tip plasticity by changing the contact stress profile.

Table 3.16: Results obtained using the DIC-FEM approaches in mode I. All displacement fields are obtained from elastic plastic computations.

ΔK_I^{FEM} $(MPa\sqrt{m})$	Compressive stress (MPa)	Estimated ΔK_I $(MPa\sqrt{m})$		
		Elastic	Plastic Dirichlet	Plastic Neumann
10	0	10.1	9.9	9.8
10	100	10.5	10.3	10.3
30	0	33.2	31.4	26.6

In order to avoid this artefact, the same problem (eq 3.26) is iteratively solved with an elastic-plastic behaviour. Since the superposition principle cannot be used any more, the problem is solved using a Levenberg Marquardt's algorithm. The damping parameter is increased by a factor 5 / decreased by a factor 2 if the current step gives a

Table 3.17: Results obtained using DIC-FEM approaches in mode II. All displacement fields are obtained from elastic plastic computations.

ΔK_{II}^{FEM} $(MPa\sqrt{m})$	Compressive stress (MPa)	Estimated ΔK_{II} $(MPa\sqrt{m})$		
		Elastic	Plastic Dirichlet	Plastic Neumann
10	0	10.8	10.2	9.8
20	0	27.1	21.9	17.7
30	0	61.6	39.3	23.2
1.9	100	1.9	1.8	1.8

lower / higher residual than the previous.

Once the contact/friction stresses along the crack faces σ_l are known, the effective SIFs can be estimated with an elastic computation, using the relative opening and sliding displacement profiles (SIF procedure in CAST3M FE code). In this elastic computation, the boundary conditions on the outside contour can be either Dirichlet (extracted from DIC) or Neumann (stresses extracted from the elastic-plastic computations). Results are given in tables 3.16 & 3.17, columns 'Plastic Dirichlet' and 'Plastic Neumann'.

In mode I, $\Delta K_I^{effective}$ is estimated accurately. In mode II, $\Delta K_{II}^{effective}$ is estimated accurately below 20 $MPa\sqrt{m}$. Above this amplitude, it is overestimated when Dirichlet BC are used for the SIFs computation, while it is underestimated when Neumann's BC are used. This error is due to the fact that the crack-tip plastic zone is so elongated ahead of the crack tip that it extend beyond the model's contour.

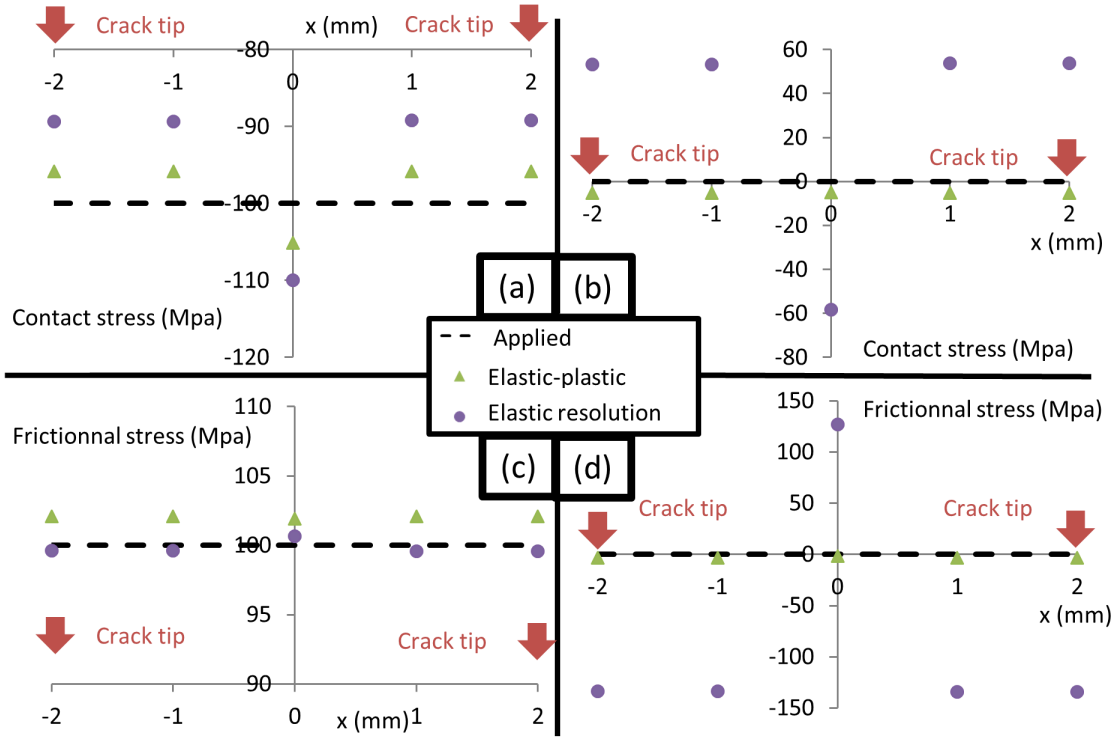

Figure 3.25: Estimated profile of the contact/friction stresses along the crack faces, for the hole-free model shown on figure 3.20. (a): Mode I $\Delta K_I^{FEM} = 10\ MPa\sqrt{m}$, 100 MPa compression. (b) Mode I, $\Delta K_I^{FEM} = 30\ MPa\sqrt{m}$, no compression. (c): Mode II $\Delta K_{II}^{FEM} = 1.9\ MPa\sqrt{m}$, 100 MPa friction. (d): Mode II $\Delta K_{II}^{FEM} = 20\ MPa\sqrt{m}$, no friction.

Taking into account the elastic-plastic behaviour improves the contact/friction stress profile estimation compared to the elastic resolution, as seen on figure 3.25. Even for $\Delta K_{II}^{effective} = 20\ MPa\sqrt{m}$, the error on the estimated frictional stress is below 7 MPa.

This contact/friction stress profile is quite sensitive to noise. Adding a white Gaussian noise with a Signal to Noise Ratio of 100 ($SNR = \Sigma U_{signal}^2 / \Sigma U_{noise}^2$) leads to a standard deviation of 16.8 MPa, with a maximum error of 37 MPa, as shown in table 3.18 for a discretization of contact stresses σ_l every 1 mm. A window average, similar to that induced by DIC (150 μm subset size) has no effects on the computed stress profile (less than 1 MPa difference with raw FEM field). This limited effect might be due to the large exclusion area (200 μm), outside of which the displacement gradient and thus the effect of the window average is lower. A finer discretization of contact stresses (every 0.5 mm, and thus an increase of the number of variables) increased the errors on the computed stresses. A compromise has thus to be found between resolution and noise sensitivity.

Table 3.18: Influence of noise (SNR = signal to noise ratio), window average of 150 μm (WA) and discretization of the piecewise affine function σ_l on the results of the 4 computations proposed in figure 3.25.

Noise / Window average	Discretization of σ_l (mm)	Max error on σ_l (MPa)	Standard deviation on σ_l (MPa)	Max error on ΔK^{eff} ($MPa\sqrt{m}$)	Standard deviation on ΔK^{eff} ($MPa\sqrt{m}$)
None	1	6.7	4.3	1.9	1.2
SNR 100	1	36.8	16.8	3.1	1.6
WA	1	7.3	4.5	1.9	1.2
None	0.5	14.9	5.9	2.0	1.2
SNR 100	0.5	54.9	22.7	3.6	1.9
WA	0.5	14.7	6.0	2.0	1.2

In the case of sequential and 90° out-of-phase loadings, the same type of problem as with the previous approach occurs: when the couplings between shear and tensile plastic flows at the crack tip becomes non negligible, some mode I is measured between images where only mode II should be present (and vice versa).

3.2.7 Application on experimental displacement fields

The previous approaches were applied on experimental data in order to estimate their robustness. A transversally precracked R260 rail steel tube was submitted to mode I cycles with a fixed maximum load of 10 kN (133 MPa) and various minimum loads, ranging from -5 kN to 8 kN. Images were captured periodically during those cycles.

Fully reversed mode II cycles with various amplitudes and various superimposed static tensile or compressive axial load were also run, with periodic image capture. Between two consecutive shear load amplitudes, the crack was opened by applying a 10 kN tensile load in order to eliminate any residual friction/asperities interlocking.

The crack tip was located using the projective approach with William's expansion between the images at 0 and 10 kN. The effective SIFs were then estimated using a fixed crack tip with a projection over William's expansion, the fit of the displacement jump profile with eq 3.24-3.25 and the DIC-FEM approach with elastic-plastic behavior and SIFs computed using Dirichlet boundary conditions.

$\Delta K_I^{effective}$ was estimated using those three approaches on DIC fields obtained between an image at maximum tensile force (10 kN) and images at lower forces. The results are given on figure 3.26. When the minimum tensile stress is larger than 27 MPa ($R > 0.2$), the three approaches gives the same results. Under this value, the crack closes and both the DIC-FEM and Displacement jump profile approaches gives the same $\Delta K_I^{effective}$, which remains constant as the crack goes into compression. As predicted from the tests on FEM computed fields, the $\Delta K_I^{effective}$ estimated using the projection over William's expansion increases when the crack is closed and under compression, and is thus overestimated. The same type of phenomena can be seen in figure 6.d. of [Vormwald et al., 2018] on a projective approach and a COD approach.

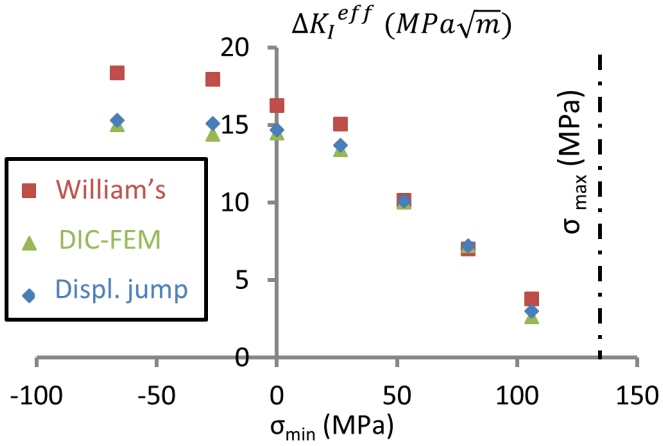

Figure 3.26: Estimated ΔK_I in pure mode I, at fixed σ_{max} (133 MPa) for various σ_{min}.

$\Delta K_{II}^{effective}$ was estimated using those three approaches on DIC fields obtained between images captured at maximum/minimum shear loads, for various loading ranges with a 66 MPa static compression. The results are given in figure 3.27. The DIC-FEM and displacement jump profile approaches give the same $\Delta K_{II}^{effective}$, while the projection over William's expansion gives a higher estimation of $\Delta K_{II}^{effective}$: as expected from the tests on FEM computed fields, this approach overestimates $\Delta K_{II}^{effective}$ in the presence of high friction between the crack faces. $\Delta K_{II}^{effective}$ was below 15 $MPa\sqrt{m}$ and the influence of crack tip plasticity on this last approach was thus negligible.

$\Delta K_{II}^{effective}$ was estimated using those three approaches on DIC fields obtained between images captured at maximum/minimum shear loads, at various crack lengths with a 53 MPa static tension so that the crack was opened and frictionless. The results are given in figure 3.28. When the crack is short, the three approaches give the

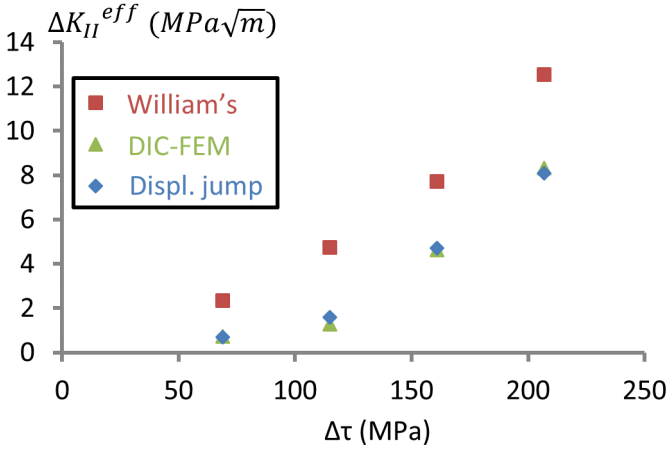

Figure 3.27: Estimated ΔK_{II} for various shear stress ranges and $-5\ kN$ $(-66\ MPa)$ static compression.

same $\Delta K_{II}^{effective}$ $(\approx 15\ MPa\sqrt{m})$. As the crack propagates, the SIFs increases and the projection over William's expansion gives a higher $\Delta K_{II}^{effective}$ than the other two approaches (which takes into account crack-tip plasticity), as predicted from the tests on FEM computed fields.

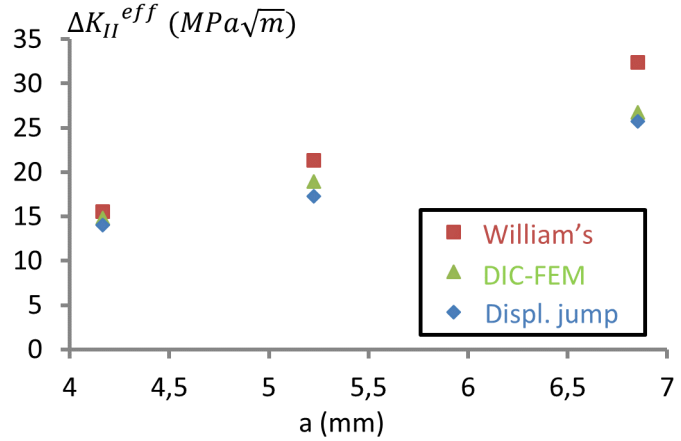

Figure 3.28: Estimated ΔK_{II} for various crack length at fixed $\Delta\tau = 115\ MPa$ with a $4\ kN$ $(53\ MPa)$ static tension.

The DIC-FEM coupling method with elastic-plastic computations was used to obtain the friction and contact stresses profiles along the crack faces (see figures 3.29 a&b). As expected, for mode II loading (figure 3.29.a), a static compression enhances crack face friction, which rises with the distance to the crack tip. The stress concentration due to the central hole does not seem to explain this tendency, because it drops much faster than the computed friction stress. Note that friction is still present without any far-field compression, and even when a slight opening stress is present $(K_I = 3.3\ MPa\sqrt{m})$, which is either due to crack face roughness or an artifact due to noise.

For mode I loading at negative R ratio (figure 3.29.b), the computed contact stresses are higher than the minimal far-field stress, and even for $R = 0$, contact stresses are still present, which is either due to closure effects or an artifact due to noise. The second interpretation seems more plausible, since slightly positive "contact stresses", which have no physical meaning, are obtained for a 27 MPa minimal tensile load $(R = 0.2)$.

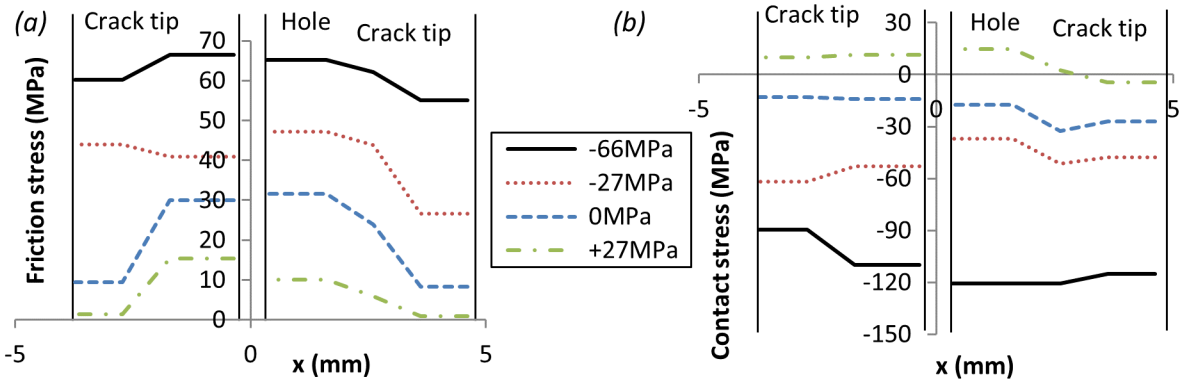

Figure 3.29: Estimated friction stress profile at fixed $\Delta\tau = 115\ MPa$ with various static tensile or compressive loads (a). Estimated contact stress profile in mode I at fixed σ_{max} (133 MPa) for various σ_{min} (b)

3.3 Conclusions on procedures common to all fatigue crack growth tests

The widely used method of projecting the DIC field over William's expansion, coupled with a grid search and a Pattern Search algorithm allows an accurate estimation of the crack tip position and effective SIFs when crack tip plasticity is limited and when no contact stresses are present along the crack faces. For high loading ranges, especially in mode II, the crack length is overestimated due to the elongated plastic zone ahead of the crack tip, while high contact stresses between the crack faces lead to an underestimation of the crack length. Both effects leads to an overestimation of the effective SIFs, even if the datapoints located in the plastic zone are excluded. This method can nonetheless still be used to locate the crack tip in mode I by applying it to images captured at maximum load and after a small elastic unloading.

An inverse analysis of the measured relative displacement jump profile compared to the profile obtained from an elastic-plastic computation plus an offset gives a better estimation of the effective SIFs when non linearities are present. It captures the effect of crack-tip plasticity as well as the effect of contact stresses between the crack faces for pure mode I, pure mode II and sequential loadings, which William's expansion cannot do. For 90° out-of-phase mixed-mode loading, it can be used until the coupling between shear and tensile plastic flows at the crack tip becomes non negligible.

An approach coupling DIC and FEM computations is proposed to evaluate the effective SIFs and the contact stresses along the crack faces. Although giving accurate results in terms of effective SIFs on FE-generated displacement fields, and providing estimates of the profile of contact and friction stresses along the crack faces, this method is much more sensitive to noise and time consuming (≈ 5 *hours*) than the aforementioned inverse approach (a few seconds).

Overall, the second approach provides the best compromise between accuracy and efficiency, at least until the FEM-DIC method has been improved to reduce its noise sensitivity.

From those results, the following methods will be used for the different experiments:

- Mode I with compression: William's series expansion + additional terms to locate the crack and to estimate the effective SIFs.
- Mixed mode II & III: direct localization of the crack tip on the images (since crack tip plasticity or friction is always present, it is not possible to get any images in LEFM conditions to use with William's series expansion), and SIFs estimation using the relative displacement jump from elastic-plastic FEM computations.
- Non-proportional mixed-mode I+II: localization of the crack tip using William's series expansion between well chosen images, and SIFs estimation using the relative displacement jump from elastic plastic FEM computations.

Chapter 4

Mode I experiments at various load ratios

Contents

4.1 Introduction

Squat-type crack undergo non-proportional mixed-mode loading, however, we can wonder if the mode I contribution alone can explain its growth. Even if it is not the case, mode I data would be useful to compare with non-proportional mixed-mode data and assess eventual synergistic effects.

4.1.1 Bibliography

Various effects influencing mode I fatigue crack growth were already discussed in chapter 2, and this part will focus on mode I fatigue crack growth experiments performed on rail steel. Such experiments were performed by many authors, such as [Gray et al., 1983, Kim and C.S., 2002, Maya-Johnson et al., 2015, Christodoulou et al., 2016], and their experimental conditions are reported in table 4.1.

Table 4.1: Some mode I FCG experiments on rail steels.

Article	Material	$Rp_{0,2}$ (MPa)	R_m (MPa)	CGR range $(m/cycle)$	R	Comments
[Gray et al., 1983]	AISI 1080	411 - 643	842 - 1024	$1.E^{-10}$ - few $1.E^{-6}$	0.1 - 0.7	Various heat treatment
[Kim and C.S., 2002]	/	481	887	$1.E^{-8}$ - $1.E^{-6}$	0.1 - 0.5	
[Tabatabaei, 2014]	$R260$	597	940	$1.E^{-8}$ - $1.E^{-7}$	0.1	Various extraction areas
[Tabatabaei, 2014]	$R350HT$	740	1278	$1.E^{-8}$ - $1.E^{-7}$	0.1	Various extraction areas
[Maya-Johnson et al., 2015]	$R260$	731	951	$1.E^{-10}$ - $1.E^{-6}$	0.1	Various extraction directions
[Maya-Johnson et al., 2015]	$R370HT$	767	1373	$1.E^{-10}$ - $1.E^{-6}$	0.1	Various extraction directions
[Christodoulou et al., 2016]	$900A$	533	924	$1.E^{-8}$ - few $1.E^{-7}$	0.1 - 0.5	
British steel	$R260$	480	880	few $1.E^{-8}$	0.5	

In all these studies, samples were extracted from a new rail, and it appears that the extraction area (Head, Web, Foot) has an influence on the fatigue crack growth kinetics [Tabatabaei, 2014], as well as the extraction direction for $R260$ steel [Maya-Johnson et al., 2015], while this effect was not seen for $R370HT$. Since this study focuses on rolling contact fatigue cracks, which develop in the head, it will only focus on this area, and the effects of the extraction direction will be neglected. Heat treatment also affects FCGR, as it changes the grain sizes and thus RICC: the larger the grains, the slower the growth [Gray et al., 1983]. Again, these effects will not be studied as this work focuses on $R260$.

Within these studies, two were performed on $R260$ steel [Tabatabaei, 2014, Maya-Johnson et al., 2015]. However, their tensile properties, reported in table 4.1, are quite different from those of the $R260$ steel of the present study ($Rp_{0,2} = 480\ MPa$, $\sigma_{UTS} = 880\ MPa$), and different fatigue crack growth properties can thus be expected. The only data available on a similar material are those from British steel, which were obtained by following the $NF - 13674 - 1$ norm, in a very small range of SIFs, and at $R = 0.5$.

All those studies were performed at a positive load ratio, which might not be very representative of the mode I loading experienced by RCF cracks in rails.

4.1.2 Mode I loading on Squat-type cracks

The mode I part of the loading is due to:

- The passage of the wheel (the secondary bending tends to open the crack, while the primary bending and hertz contact stress field tend to closes it).
- The thermal stresses (uniform along the section).
- The residual stresses inherited from the manufacturing process, which follow a "C" shaped evolution: the crack is under decreasing residual tension as it grows downwards.
- Entrapped and pressurized water (which is neglected here).

The maximum and minimum values of K_I were computed at the deepest point of a semi-elliptical squat crack inclined by 70° relative to the rail axis, loaded with a TGV train at 320 km/h in a straight line, at various operating temperatures. Without thermal stresses nor residual stresses, $\Delta K_I = K_I^{max} - max(K_I^{min}; 0) < 2\ MPa\sqrt{m}$. The crack is almost always closed and under compression, as showed on figure 4.1.

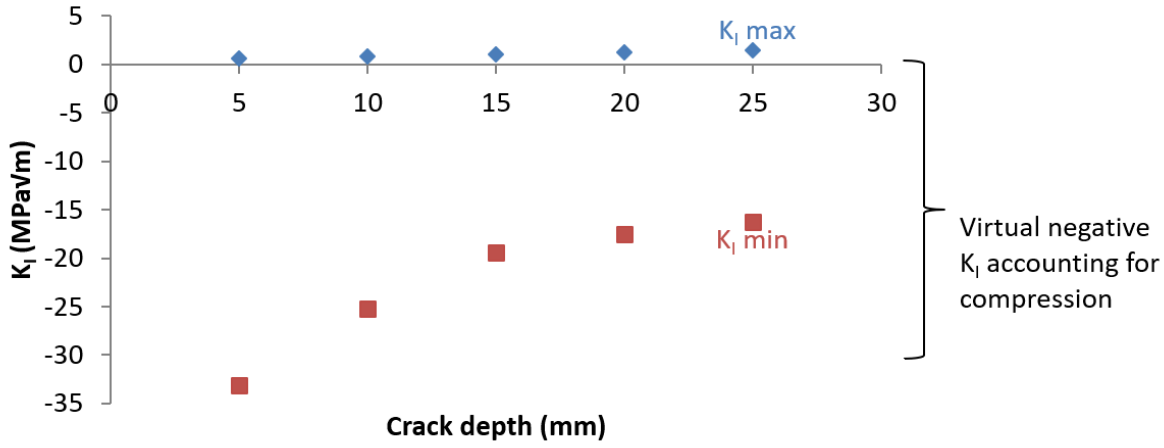

Figure 4.1: Evolution of K_I^{max} and K_I^{min} at the deepest point of a Squat-type crack, as a function of the crack depth, without residual nor thermal stresses.

When residual stresses are added, using the profile specified in section 1.3.3, K_I^{max} and K_I^{min} at the deepest point are shifted upwards, as showed on figure 4.2. In this case, ΔK_I reaches 5.9 $MPa\sqrt{m}$ for a 10 mm deep crack. Since those residual stresses have a "C" shape and thus decrease when going down in the rail head, the upward shift in K_I decreases as the crack grows downwards, until it goes to zero (the depth where the residual stresses goes through zero is around ≈ 25 mm). As the crack is elliptical, all its front is not at the same depth, and points which are on the side will not experience the same residual stresses as those on the deepest point. As a consequence, a gradient in ΔK_I and in R ratio is present along the crack front (see figure 4.3 for a 10 mm deep crack).

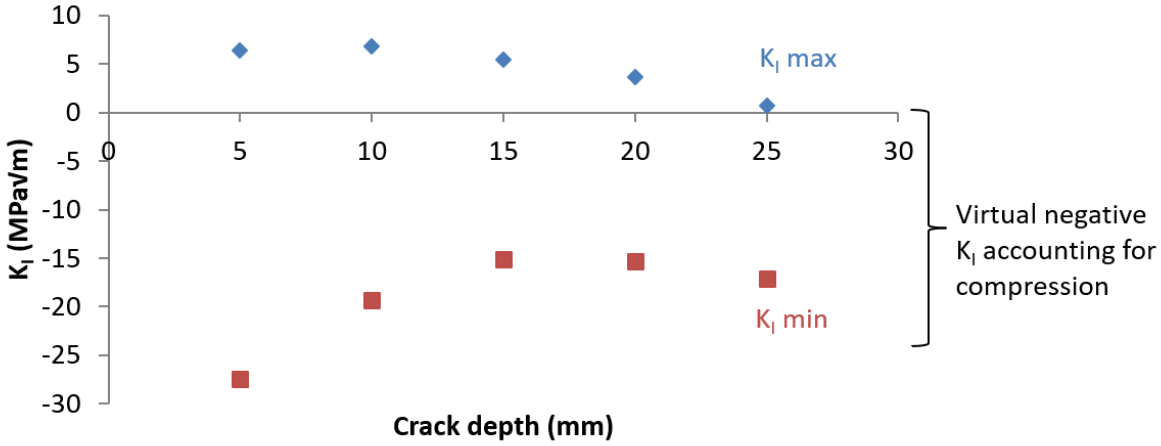

Figure 4.2: Evolution of K_I^{max} and K_I^{min} at the deepest point of a Squat-type crack, as a function of the crack depth, with residual stresses and no thermal stresses.

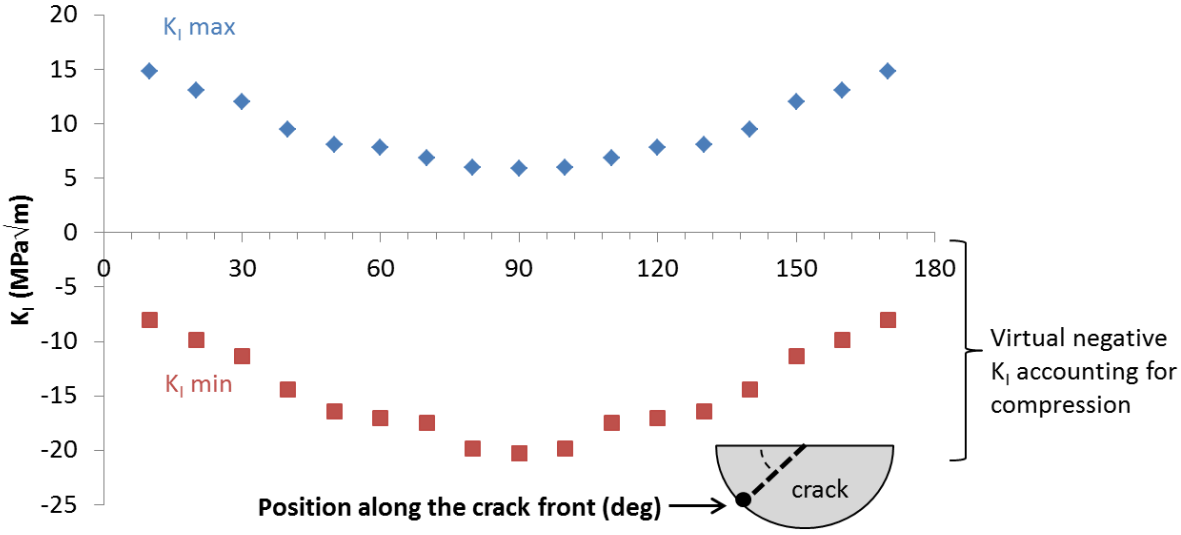

Figure 4.3: Evolution of K_I^{max} and K_I^{min} along the front of a 10 mm deep Squat-type crack, with residual stresses and no thermal stresses.

Contrary to the "C" shaped residual stresses, thermal stresses induce a uniform axial stress in the rail section, and thus a shift in K_I that will increase with the crack size ($\approx\propto \sqrt{depth}$). K_I^{max} and K_I^{min} at the deepest point are reported on figure 4.4 for various operating temperatures. For a 20 $°C$ reference temperature, a temperature of 5 $°C$ induces 30 MPa tension, while a temperature of -5 $°C$ will induces 50 MPa tension (see section 1.3.2), thus shifting K_I^{max} and K_I^{min} upwards. For a crack depth from 5 to 25 mm and temperatures from 20 $°C$ to -5 $°C$, ΔK_I varies from 1 to almost 13 $MPa\sqrt{m}$ and R from -24 to -0.5 at the deepest point. By making the approximation $K = \sigma\sqrt{\pi * a}$, compression at the deepest point can reach $\approx$ 200 MPa for a 5 mm deep crack, and is under $\approx$ 100 MPa for cracks deeper than 10 mm.

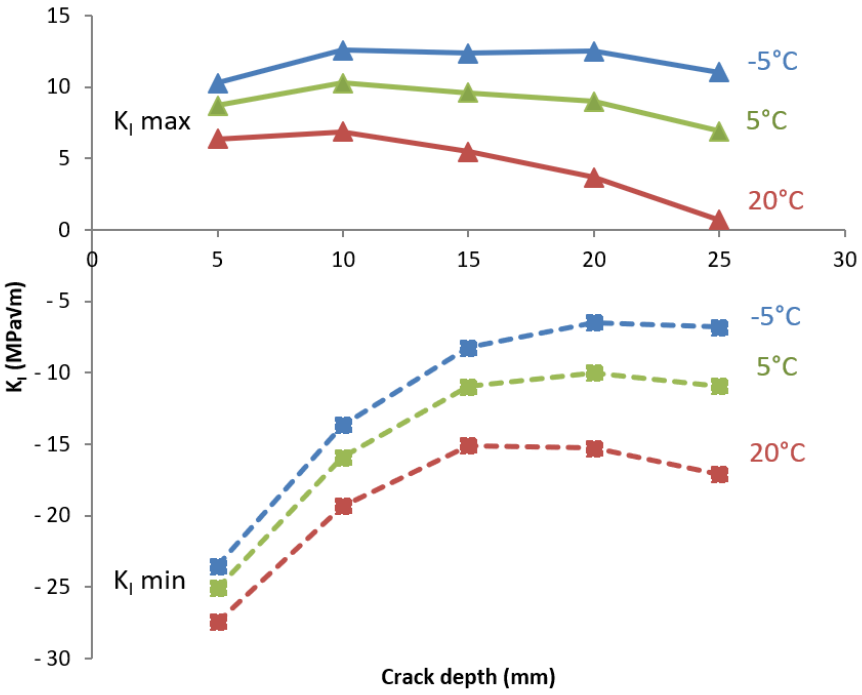

Figure 4.4: Evolution of K_I^{max} and K_I^{min} at the deepest point of a Squat-type crack, as a function of the crack depth, with residual stresses and for various operating temperature (20 $°C$ corresponding to the reference state)

This compression can have several effects, as discussed in chapter 2: it can lead to the formation of an oxide layer on the crack faces, leading to closure effects and reducing the crack growth rate, or accelerate the crack growth due to a reduction of RICC and a contribution of the part of the compressive stage during which the crack remains open.

Within the aforementioned studies on rail steel, no data for negative load ratios were found. Moreover, the existing data were obtained on steels with different properties (although their denomination is the same), or in very restricted SIFs ranges, which justifies to perform mode I experiments again.

4.2 Experimental and numerical procedures

4.2.1 Experimental setup

SENT specimens, with a 2.5 mm deep notch at mid height to initiate a crack, were extracted from the head of a new rail, as detailed in figure 4.5. X-ray diffraction measurements were performed on the side of a broken sample at the SNCF railway testing agency (Agence d'essais ferroviaires) on a 2 mm diameter area, over a depth of $5 \sim 10$ μm. The studied area was electro-chemically etched after each measurement, in order to evaluate the evolution of residual stresses with depth. Those measurements showed axial residual stresses of -420 ± 25 MPa on the surface, decreasing to -117 ± 25 MPa at a 50 μm depth and -20 ± 15 MPa at a 200 μm depth. Those residual stresses are certainly due to the milling process, and were not removed by annealing before the experiments as the thickness of the affected area (few hundred of μm) was small relative to the specimens thickness (7 mm). They can be responsible for some crack tunneling.

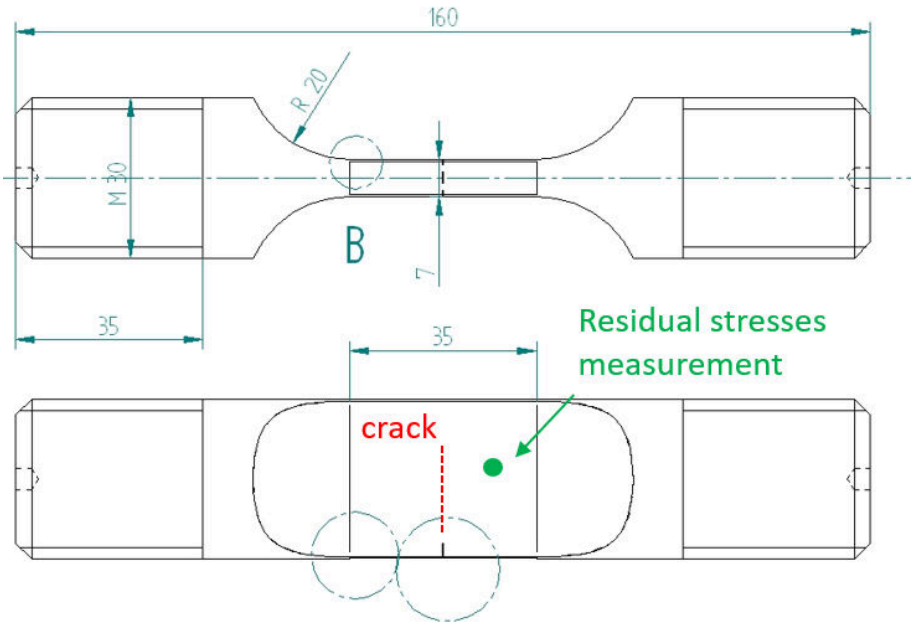

Figure 4.5: SENT specimen for mode I fatigue crack growth experiments.

The experimental setup is described on figure 4.6. The specimen is mounted in a MTS ± 100 kN uniaxial hydraulic testing machine, and cycled at 10 to 20 Hz. An extensometer is used to perform macroscopic closure measurement. The crack length is monitored using the DC potential-drop method, as well as direct observations on one of the specimens side surfaces with a QUESTAR traveling microscope (the specimens are polished up to 1 μm diamond paste in order to allow precise crack length measurements on the surface). The other side is covered with a speckle painting, consisting of a white layer, covered with a black spray-paint-induced speckle (15 to 320 μm). This speckle painting is used to perform DIC measurements, from which the SIFs are obtained using the approach detailed in 4.2.3.

The crack is initiated from the notch after 100 000 to 200 000 cycles at $\Delta\sigma = 133$ MPa and $R = 0$, and propagated over 1 mm at this loading (ΔK_I reaches 10 $MPa\sqrt{m}$). It is then propagated at a decreasing load until it stops propagating (less than 10 μm propagation after 100 000 cycles, meaning 10^{-10} $m/cycle$)). History effects due to the plastic zone of the previous larger loading step are avoided by allowing the crack to grow well beyond

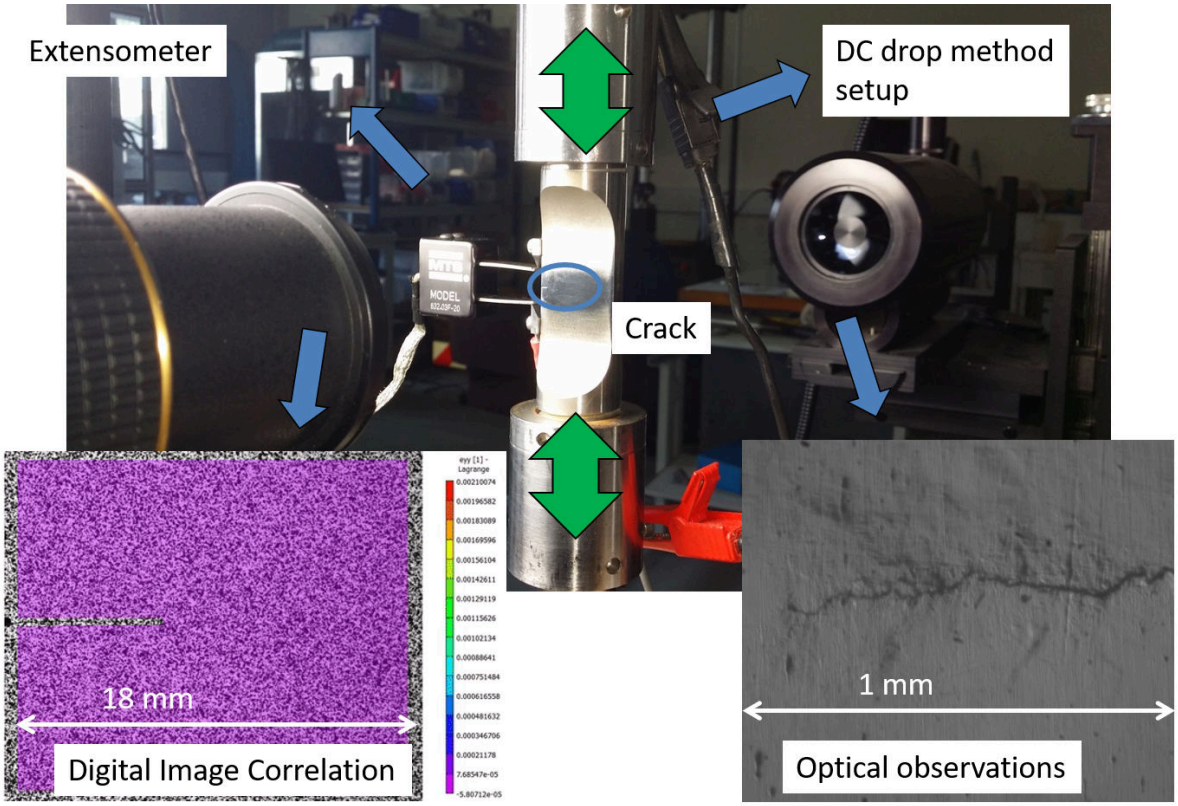

Figure 4.6: Experimental setup for mode I fatigue crack growth experiments.

that zone at each step.

Once the non-propagation threshold is obtained, the crack is propagated again at increasing load, up to $\sigma_{max} < 140\ MPa$ and $\Delta\sigma < 140\ MPa$. For each loading range, three loading blocks are applied, and the crack growth rate at this range is obtained by fitting a straight line on the three data points (thus reducing noise).

4.2.2 Nominal SIFs evaluation

The nominal SIFs for SENT specimens are given by Tada [Tada et al., 1973]:

$$K_I = \sigma\sqrt{\pi * a} * F(a/b) = \sigma\sqrt{\pi a} * \sqrt{\frac{2b}{\pi a}\tan\frac{\pi a}{2b}} * \frac{0.752 + 2.02(a/b) + 0.37(1 - \sin\frac{\pi a}{2b})^3}{\cos\frac{\pi a}{2b}} \tag{4.1}$$

With a the crack length, and b the specimen width (30 mm in our case). This formula is valid for any crack length if the applied stress is uniform (no bending moment).

Another formula is proposed by Gross [Gross et al., 1964] (which is used in $AFNOR\ A03-404$):

$$K_I = \sigma\sqrt{\pi * a} * F(a/b) = \sigma\sqrt{\pi a} * (1.122 - 0.231(a/b) + 10.55(a/b)^2 - 21.71(a/b)^3 + 30.382(a/b)^4) \tag{4.2}$$

Which is valid for $a/b < 0.6$ (0.5% precision is this case).

However, for high a/b, the sample will tend to bend due to the asymmetry induced by the crack (see figure 4.7.a). Since the clamping pieces have a non-negligible stiffness, this will induce a bending moment, and thus a non-uniform axial stress, and the aforementioned formula will not be valid anymore.

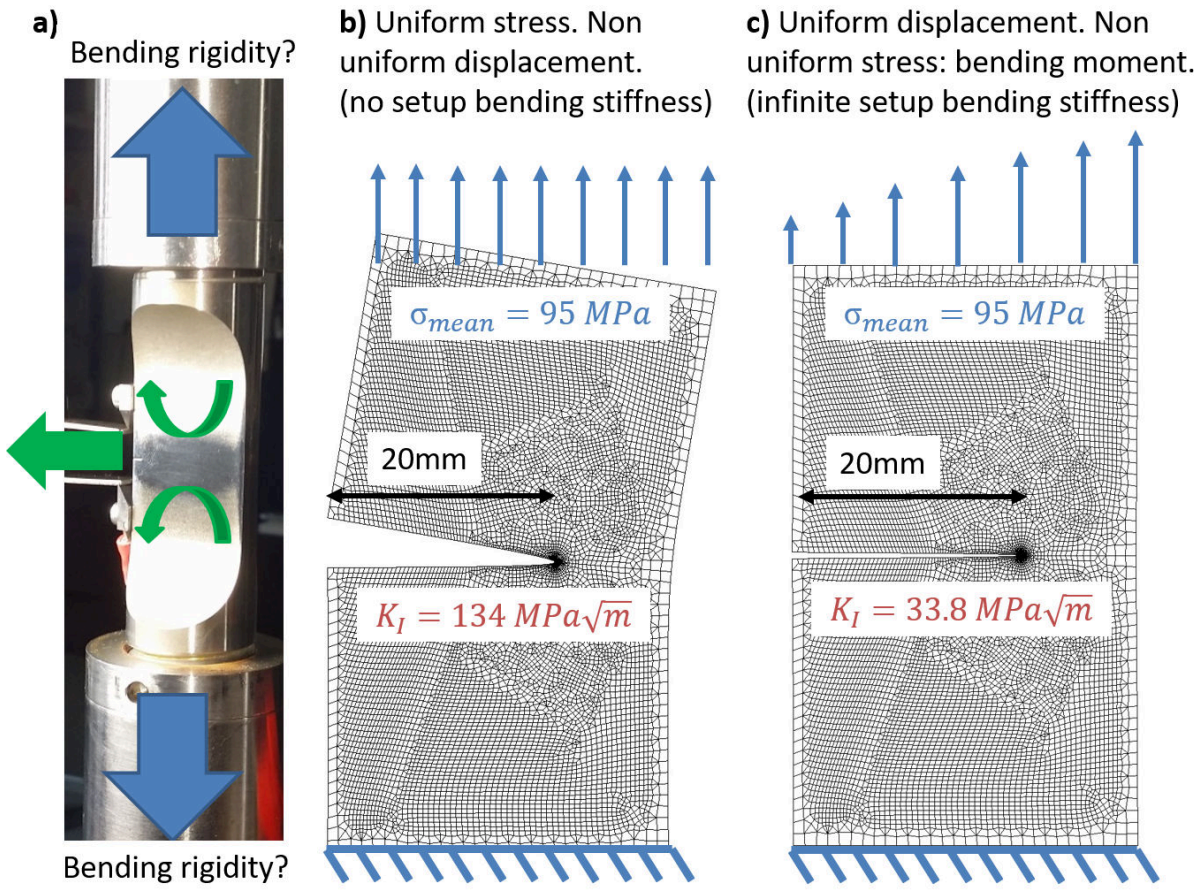

Figure 4.7: Influence of the setup bending stiffness (a). FEM computation with identical tensile force, but with a uniform tensile stress (b), and with a uniform vertical displacement (c).

Indeed, as shown on figure 4.7.b & c, two FEM computations (plane strain) performed with the same models and applied force, but with a uniform stress (no setup bending stiffness) or a uniform displacement (no rotation allowed, infinite bending stiffness) yield very different SIFs: $K_I = 134\ MPa\sqrt{m}$ & $K_I = 33.8\ MPa\sqrt{m}$ respectively (128.9 $MPa\sqrt{m}$ using Tada's formulae).

During the experiments, K_I up to 174 $MPa\sqrt{m}$ were obtained using Tada's formulae (for $a = 24\ mm$), while K_{IC} is supposed to be $\approx$ *confidential data* $MPa\sqrt{m}$, meaning that this bending problem is likely present in our case. One way to solve this problem could be to model the whole setup (sample + clamping device) using FEM, and build an abacus specific to these experiments. Such FEM model would be complex to create due to the complicated specimen and setup geometry, and might not be accurate due to the presence of screwed parts which might move during the loading.

In order to build this abacus specific to our experiments, the SIFs obtained from DIC using the projection over William's expansion between well chosen images were used (see 3.2.3). Images were recorded at F_{max} and $\alpha * F_{max}$ during two experiments, and then correlated and analyzed in order to get K_I^{nom}/F as:

$$K_I^{nom}/F = \frac{\Delta K_I^{DIC}(F, \alpha * F)}{(1-\alpha) * F} \tag{4.3}$$

α was set to 0.5 in order to avoid closure effects and minimize crack tip plasticity (so as to remain within the LEFM framework). A higher value was not chosen, in order to have sufficiently large displacements between the

two images so that the result is not too sensitive to the DIC noise.

The obtained evolution of $K_I^{nom}(a)$ for $F = 1\ kN$ is plotted on figure 4.8, along with K_I obtained from Tada's formula and from FEM computations as described in figure 4.7 b & c.

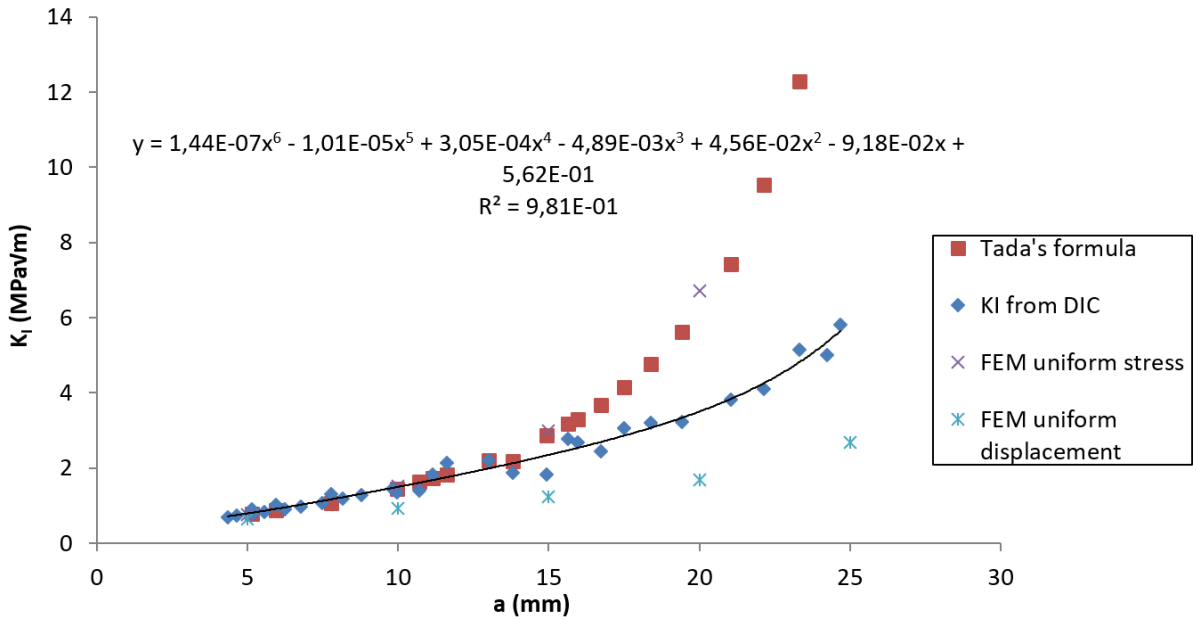

Figure 4.8: Influence of the setup bending stiffness (a). FEM computation with identical tensile force, but with a uniform tensile stress (b), and with a uniform vertical displacement (c).

Tada's formula and the FEM computation with uniform stress are almost superimposed, and overestimate K_I^{nom} for cracks longer than $\approx 10\ mm$ (by a factor of almost 2 for $a = 20\ mm$). Conversely, the FEM computation with uniform displacement underestimates K_I^{nom}, even for a crack length of 5 mm (factor of 0.8). This is consistent with the fact that the setup is neither infinitely rigid in rotation, nor infinitely soft, but in between.

For the rest of the study, K_I^{nom} will be estimated as:

$$K_I^{nom} = F * Polynomial(a) \tag{4.4}$$

Using the order 6 polynomial determined on figure 4.8 from DIC on two experiments. The length a corresponds to the length measured on the side surface with the QUESTAR optical microscope.

4.2.3 Effective SIFs estimation

ΔK_I^{eff} was estimated on the specimen side covered by the speckle painting using the relative crack face opening displacement on two 2 mm-long lines, spaced by $\pm 250\ \mu m$ above and below the crack tip:

$$[U_y] = \Delta K_I^{eff} * \sqrt{r} * \frac{8}{E * \sqrt{2\pi}} + \rho_I \tag{4.5}$$

The crack tip position was optimized to get the best fit.

An attempt was made to use the projection over William's expansion + additional terms 3.2.4, which was unsuccessful due to some aberrant values, and was thus abandoned.

For the cases with high load ratios ($R = 0.6$), the effective SIFs were also estimated using the projection over William's expansion (see appendix B). The results are given on figure 4.9. The error between the projection over William's expansion and the relative COD lines remains below 6 %. Those results are much better than those obtained with the same method in 3.2.3 as the considered length is much longer here.

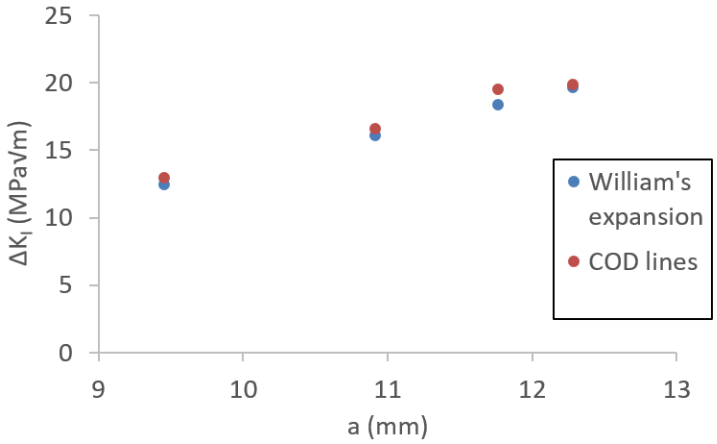

Figure 4.9: ΔK_I^{eff} estimated using two methods during an experiment with $R = 0.6$.

Those effective SIFs estimated from DIC correspond to surface measurement (plane stress conditions), and might be different from those in the bulk of the specimen (plane strain conditions, fewer plasticity induced closure than under plane stress conditions), as shown by de Matos & Nowell [de Matos and Nowell, 2009]. An attempt was made to estimate a global ΔK_I^{eff} (including the bulk) by using the change of slope on the force-displacement loop obtained from extensometer measurements. However, it did not prove to be reliable, as crack closure starting from the notch was observed in one experiment (see figure 4.10). In this case, closure would be detected, while the crack is not fully closed yet near the tip, thus leading to an underestimation of ΔK_I^{eff}. Such a strong effect was not seen in other experiments (even with identical load ratio), and could be due to an overload/underload: the data from the corresponding experiment were discarded.

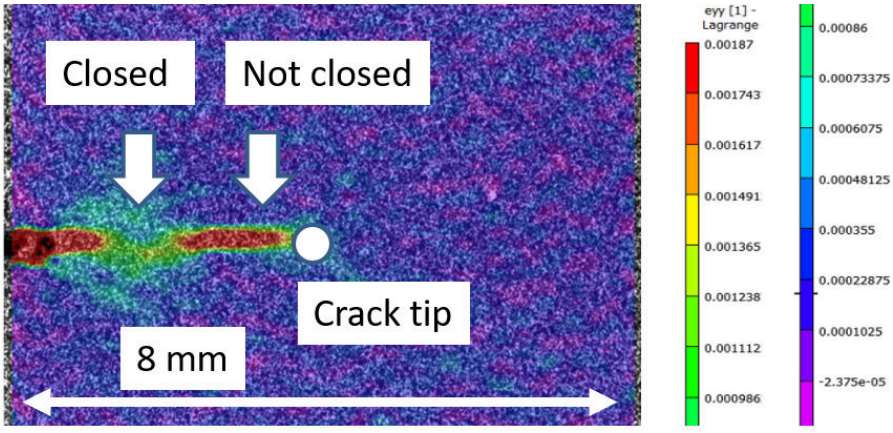

Figure 4.10: Crack closing from the notch: ϵ_{yy} obtained by DIC between images taken at $F = -5\ kN$ and $0\ kN$ during experiment $N°4$.

4.3 Results

Seven experiments were performed, at various load ratios: $R = 0.6$, 0.3, 0, -0.5, -1 and -2. For $R = -2$, $\sigma_{compression} = -95\ MPa$, which is close to the maximum compression experienced by a squat type crack deeper than 10 mm at 20 $°C$ (the compression is lower for lower temperatures and longer cracks). Two experiments were performed at $R = 0$, one experiment at $R = -0.5$ was discarded (see above), and one experiment was performed using two different load ratios: $R = 0$ and $R = -0.5$.

4.3.1 Crack growth rates versus nominal SIFs

The evolution of da/dN is plotted on figures 4.11 & 4.12 as a function of:

$$\Delta K_I^{nom} = K_I^{max} - \max(K_I^{min}; 0) \tag{4.6}$$

$$\Delta K_I^{total} = K_I^{max} - K_I^{min} \tag{4.7}$$

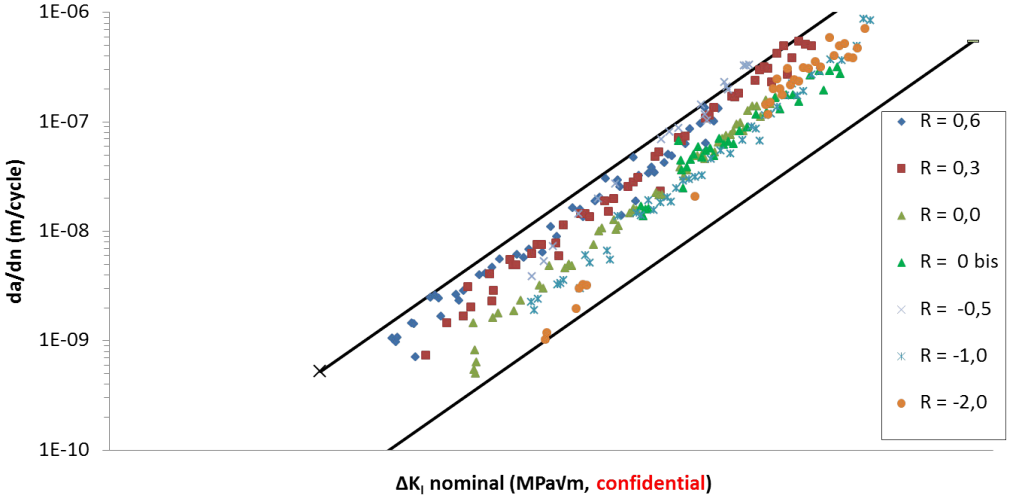

Figure 4.11: Crack growth rate versus ΔK_I^{nom} for various load ratios.

The datapoints on the da/dN - ΔK_I^{nom} curve are contained within an envelope of a factor 14.8 in growth rate, around the curve $da/dN =$ *confidential data* with $R^2 = 0.928$, when removing the experiment at $R = -0.5$ for which the crack was highly asymmetric (2 mm difference between the two side surfaces after precracking). The effect of the load ratio is quite limited, and tends to fade away as ΔK_I^{nom} increases: da/dN is ≈ 6.3 time lower for $R = -2$ than for $R = 0.3$ at $\Delta K_I^{nom} =$ *confidential data* $MPa\sqrt{m}$, but only ≈ 1.8 times slower at $\Delta K_I^{nom} =$ *confidential data* $MPa\sqrt{m}$.

Surprisingly, crack growth is slower at negative load ratio, while compression is usually acknowledged to accelerate it. Such effect was also observed by Pokorný et al. [Pokorný et al., 2017] on railway axle steel, and was explained by the formation of and oxide layer due to repeated contact under compression, leading to increased oxide-induced crack closure: the higher the compression, the thicker the oxide layer and the higher the closure effects. The threshold, which decreases as R increases, is $\approx$ *confidential data* $MPa\sqrt{m}$ at $R = -2$, and $\approx$ *confidential data* $MPa\sqrt{m}$ at $R = 0$.

The datapoints do not correlate with ΔK_I^{total}, as can be observed on figure 4.13: the negative part of K_I should not be added as a driving force. The datapoints at $R = 0.3$ and $R = 0.6$ are superimposed, suggesting that closure disappears above $R = 0.3$.

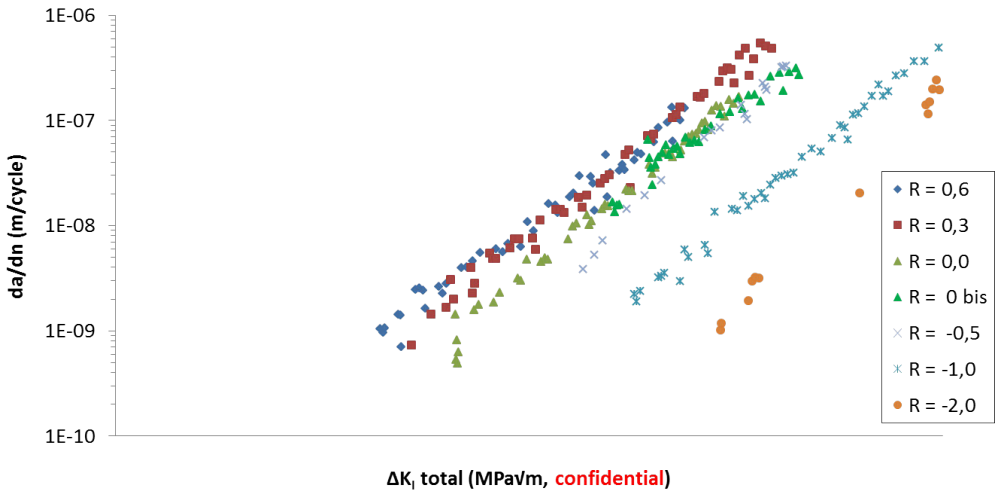

Figure 4.12: Crack growth rate versus ΔK_I^{tot} for various load ratios.

Adding an empirical threshold K^0 accounting for crack closure, in the form of:

$$\Delta K_I^{nom,\,0} = K_I^{max} - \max(K_I^{min}; K^0) \tag{4.8}$$

with $K^0 =$ *confidential data* $MPa\sqrt{m}$ can improve the results. All the datapoints (except one point at a low crack growth rate) are within an envelope of a factor 5.8 in growth rate, with $R^2 = 0.974$, when removing the experiment at $R = -0.5$ for which the crack was highly asymmetric (2 mm difference between the two side surfaces after precracking), as shown on figure 4.13.

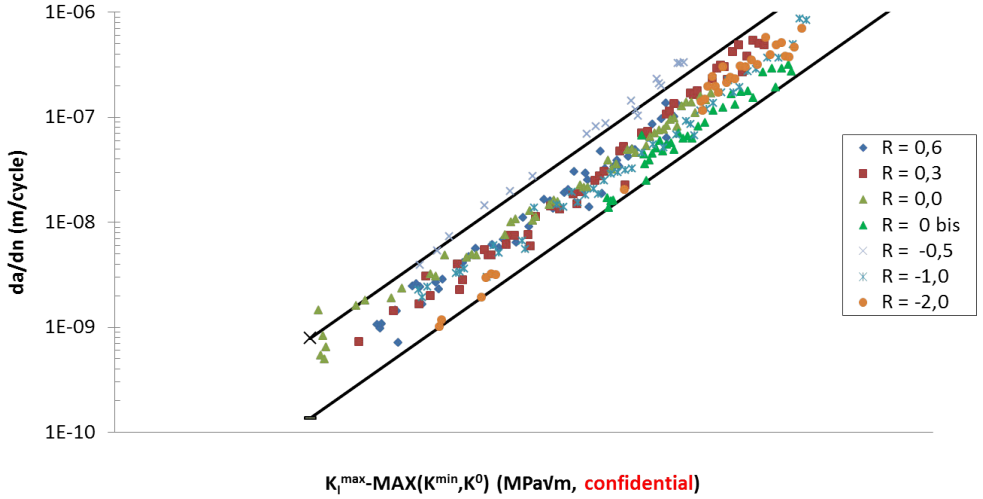

Figure 4.13: Crack growth rate versus $\Delta K_I^{nom,\,0} = K_I^{max} - \max(K_I^{min}; K^0)$ for various load ratios.

4.3.2 Fracture surface analysis

The fracture surfaces of samples tested at various R ratios, from $R = 0.6$ to $R = -2$, are reported on figures 4.14 to 4.22.

In each case, the final crack front is convex, which is typical of crack tunneling. Such tunneling is generally attributed to plasticity-induced closure [Branco and Antunes, 2003], which is more pronounced near the free surfaces than at mid-thickness. However, there is no clear evidence of an influence of the load ratio on the crack front shape: the crack front is more curved at $R = 0$ than at $R = -2$ and $R = 0.6$. Some samples had a very long crack (25 mm), close to the specimen width (30 mm), which might have an influence the shape of the crack-tip plastic zone and thus plasticity-induced closure. Tunneling might also partly be due to the compressive residual stresses that exist near the surfaces.

The microstructure (pearlite lamellae) can clearly be seen on the fracture surface for all the experiments, as illustrated on figure 4.15. Those lamellae are in random orientations (between different colonies), and should not be confused with striations, which are quite difficult to observe due to the microstructure. Striations could however be found in some areas, as shown on figure 4.16.

Whatever the load ratio, cleavage fracture areas (as on figure 4.14) can be found here and there, often close to the final crack front (and thus for $K_{I,\,max}$ close to K_{IC}). A positive load ratio does not seem to favor such cleavage: there is more cleavage areas at $R = -1$ (fig. 4.20) than at $R = 0.6$ (fig. 4.14), but less at $R = -2$ (fig. 4.22). More experiments would be necessary to draw a clear tendency. Such cleavage areas were also found in [Gray et al., 1983] during mode I experiments on rail steel, and a formation mechanism was proposed by Park and Bernstein [Park and Bernstein, 1979]. Those cleavage cracks propagate along {100} ferrite planes, and appear if a sufficiently large number of neighbouring pearlite colonies share a common {100} plane, leading to a sufficiently large "weak" area. Anyway, such cleavage areas are responsible for a local rise in crack roughness and thus of a potential, transient deceleration due to roughness-induced crack closure.

While for $R = 0.6$ and $R = 0.3$, no evidence of contact between the crack faces can be found, some mated areas appear at $R = 0$ (see figure 4.19) and below. This is consistent with the da/dN - ΔK_I^{nom} curves, which suggest an absence of closure for $R \geq 0.3$. At negative load ratio (figures 4.20 & 4.22), the mated areas are wider (figure 4.19 at $R = 0$ versus figure 4.21 at $R = -1$) and more frequent. Oxidized areas, in brown, can clearly be seen on the fracture surface (figure 4.22) of the sample tested at $R = -2$. The surface is more mated and oxidized near the crack stating point, which witnessed more cycles.

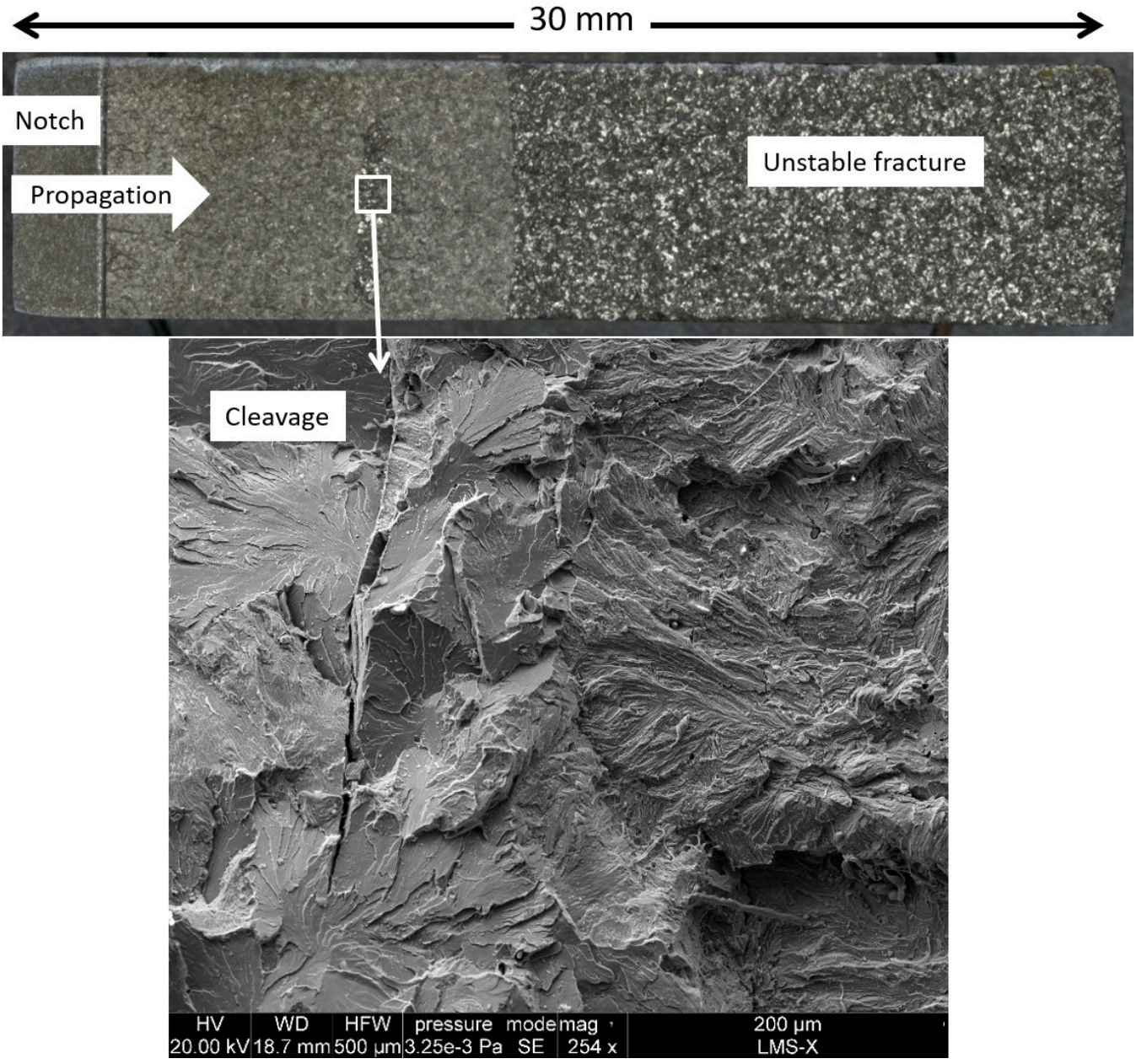

Figure 4.14: Fracture surface of a specimen tested at $R = 0.6$ captured with an optical microscope, and a cleavage area captured with SEM.

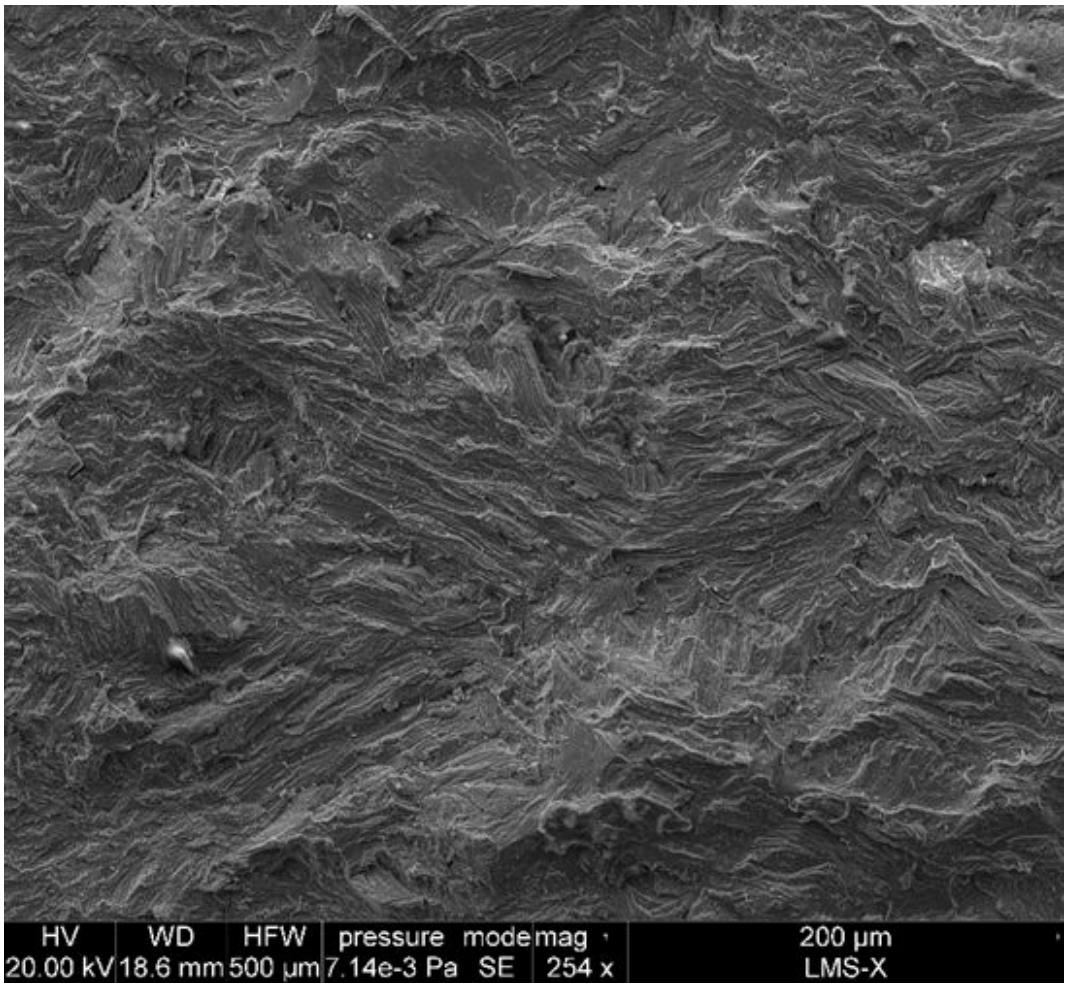

Figure 4.15: Fracture surface of a specimen tested at $R = 0.6$ captured with a SEM, at $\Delta K_I = 6.2\ MPa\sqrt{m}$.

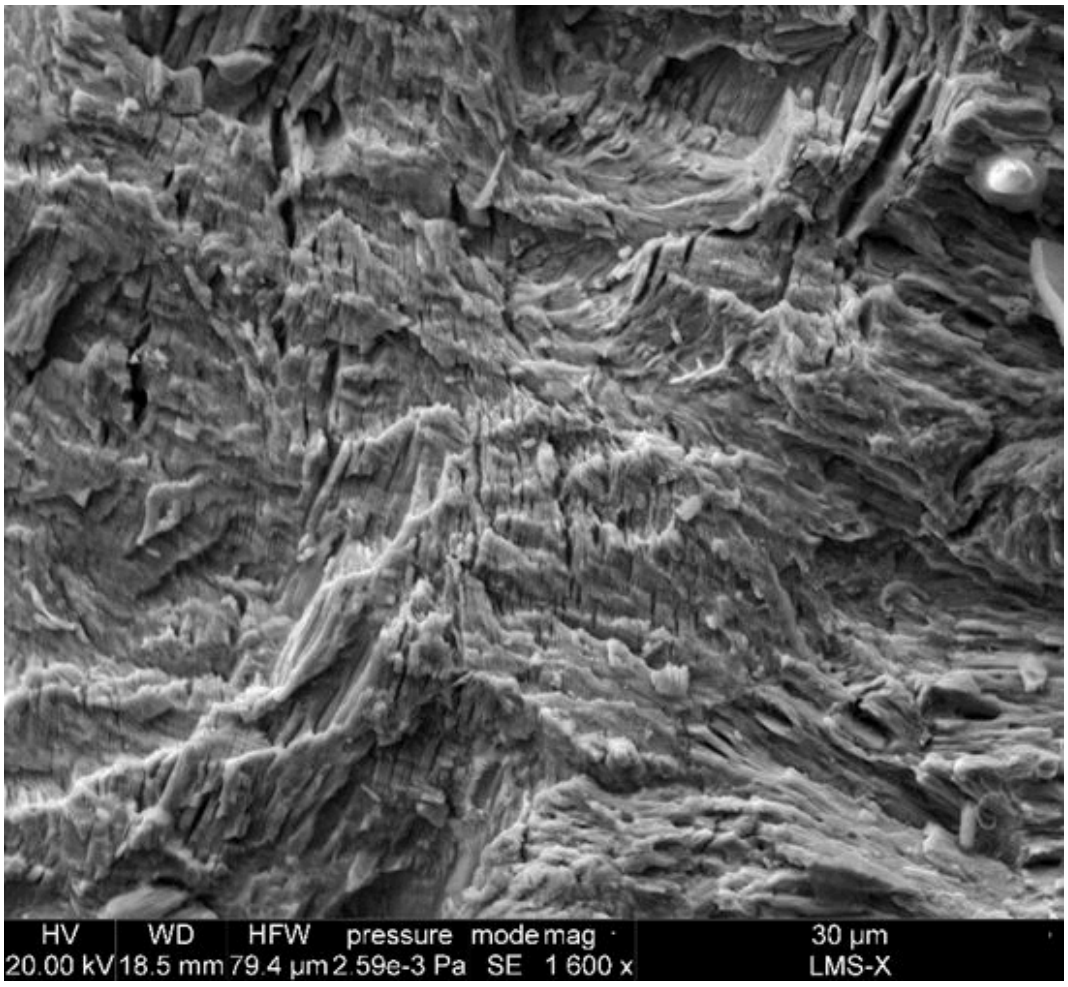

Figure 4.16: Striations on a specimen tested at $R = 0.6$ captured with a SEM, at $\Delta K_I = 20\ MPa\sqrt{m}$.

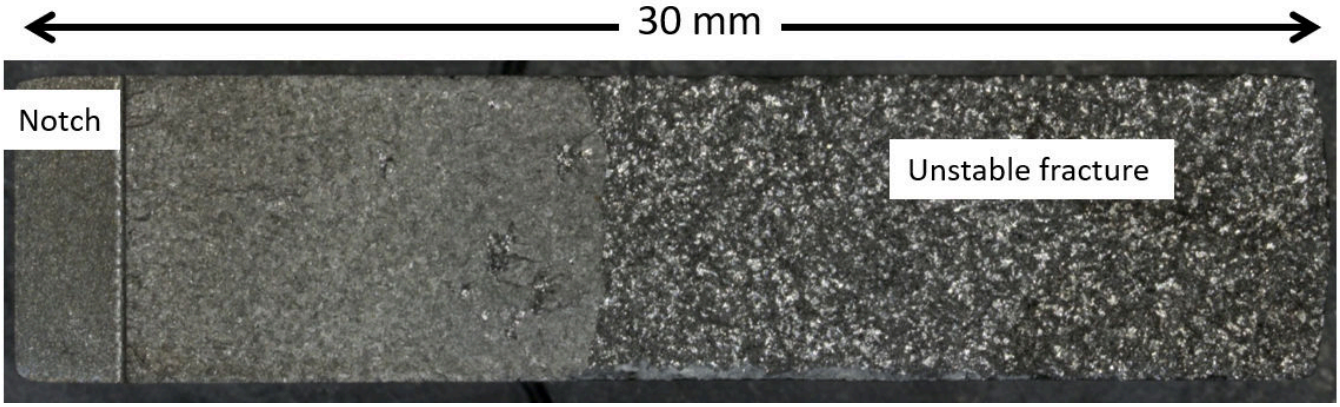

Figure 4.17: Fracture surface of a specimen tested at $R = 0.3$ captured with an optical microscope.

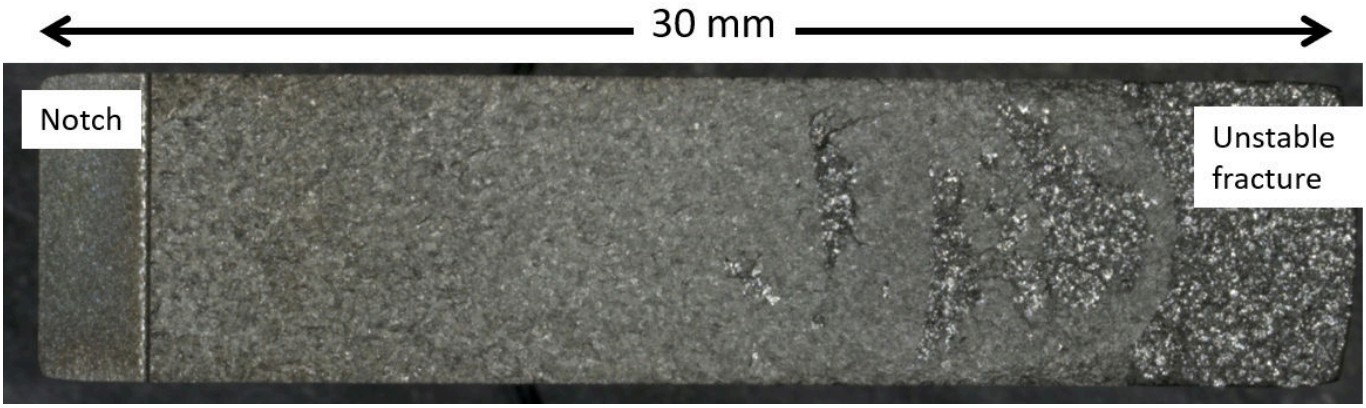

Figure 4.18: Fracture surface of a specimen tested at $R = 0$ captured with an optical microscope.

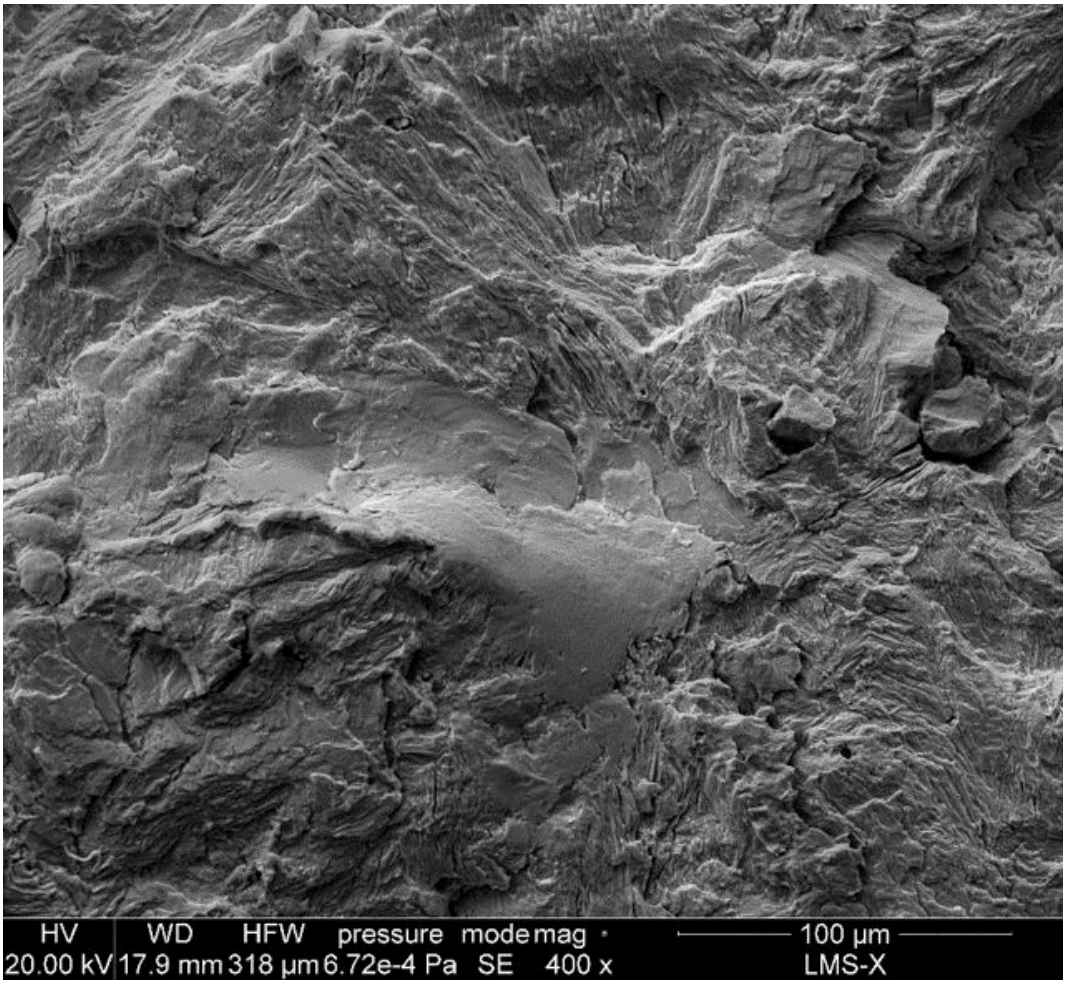

Figure 4.19: Mated fracture surface on a specimen tested at $R = 0$, captured with a SEM.

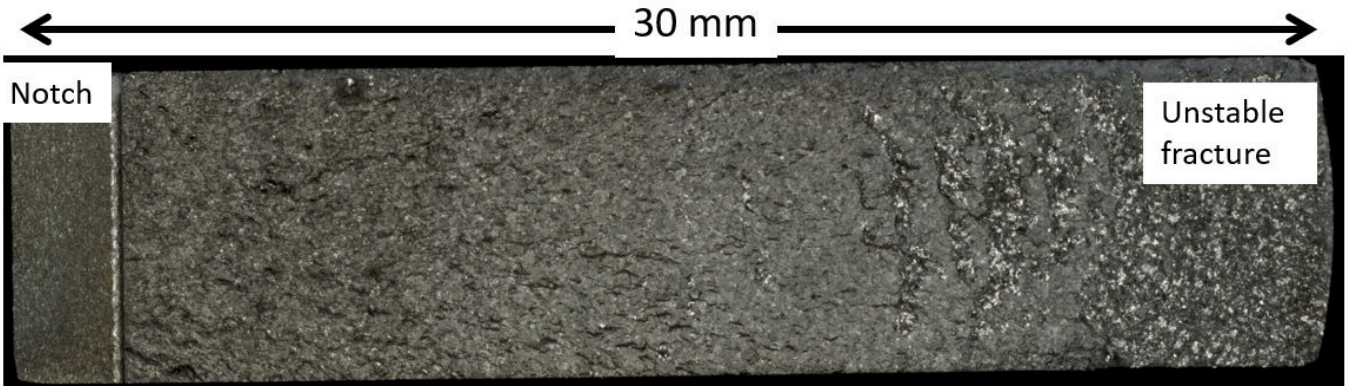

Figure 4.20: Fracture surface of a specimen tested at $R = -1$ captured with an optical microscope.

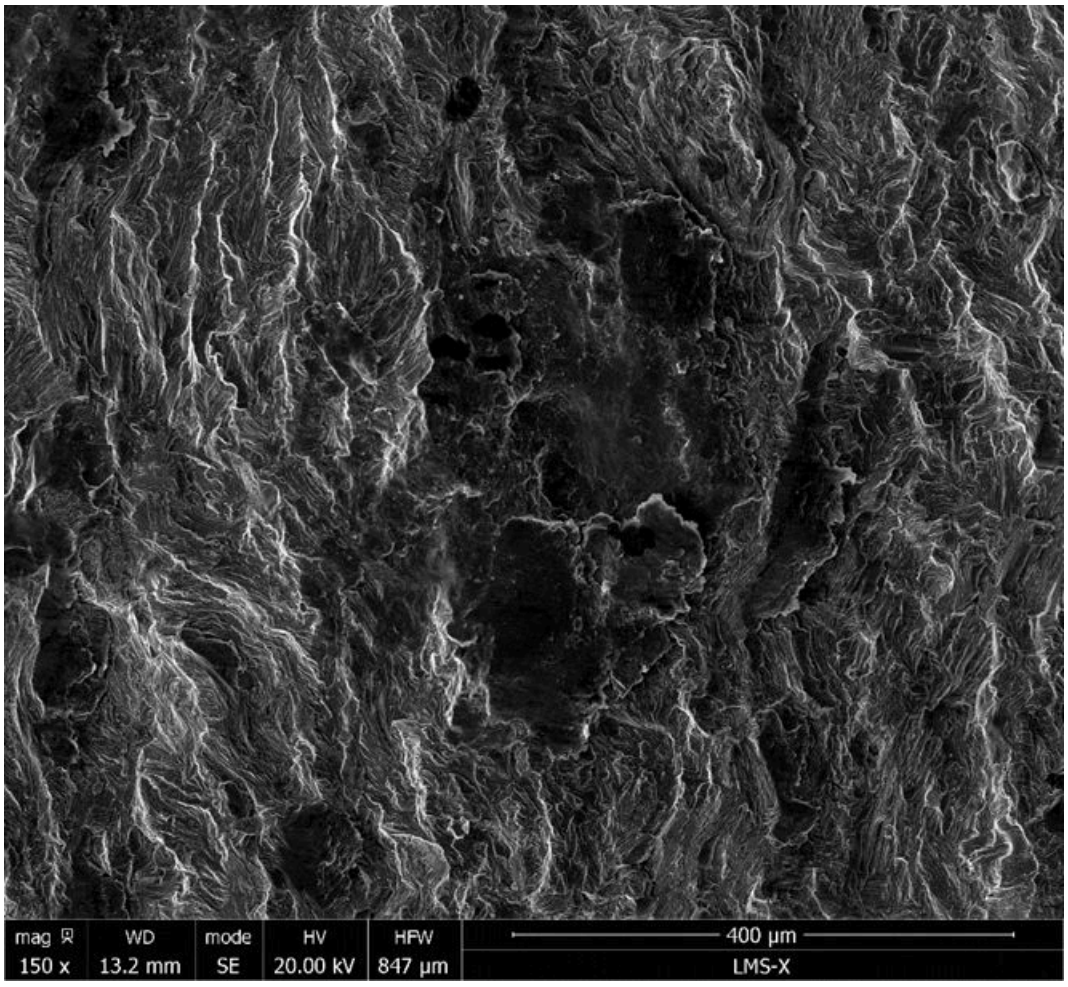

Figure 4.21: Highly mated and oxidized fracture surface on a specimen tested at $R = -1$, captured with a SEM.

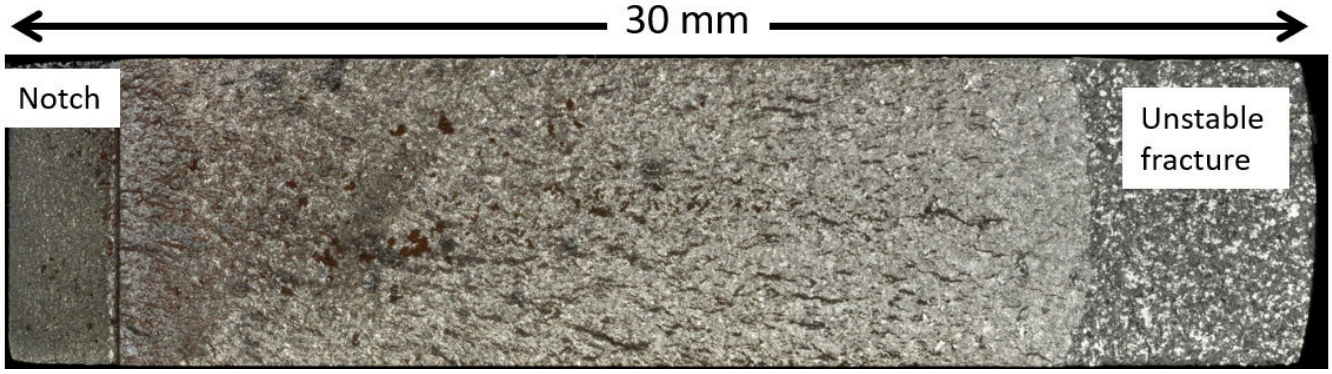

Figure 4.22: Fracture surface of a specimen tested at $R = -2$ captured with an optical microscope. Oxidation can be seen from this scale.

4.3.3 Effective load ratio

The evolution of the U_I ratio, defined as:

$$U_I = \frac{\Delta K_I^{eff}}{\Delta K_I^{nom}} \tag{4.9}$$

,where ΔK_I^{eff} is issued from DIC, is plotted on figure 4.23. No data are available at low ΔK for $R = 0$, as the first experiment at $R = 0$ was not equipped for DIC (which is used to compute U_I), and the second one was performed starting at a higher loading range (without seeking the non propagation threshold).

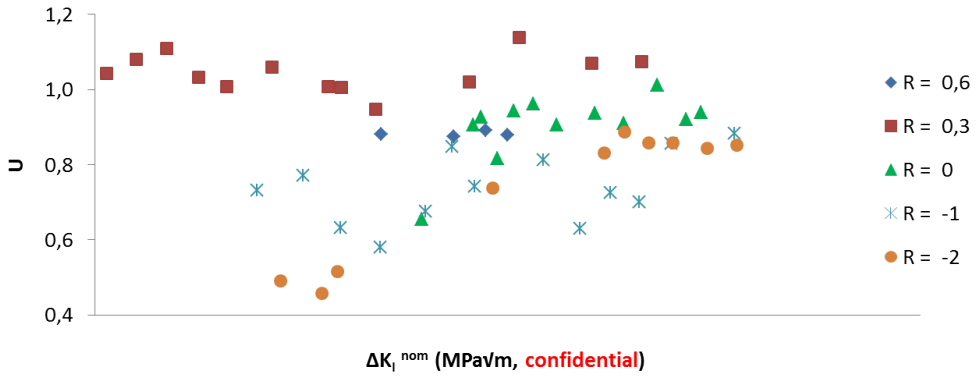

Figure 4.23: Evolution of U_I with ΔK_I^{nom} at various R ratios.

For $R = 0.6$ and $R = 0.3$, $U_I \approx 1$, whatever ΔK_I^{nom}, meaning that there are no closure effects, as suggested also by the da/dN - ΔK_I^{nom} curves. The ≈ 0.1 lower U_I for $R = 0.6$ than for $R = 0.3$, and the fact that U_I is sometimes larger than 1 for $R = 0.3$ can be due to more or less tunneling crack fronts (730 μm difference in crack length between the mid-thickness and the side surfaces for $R = 0.3$, versus 260 μm at $R = 0.6$), this leading to underestimated ΔK_I^{nom} and overestimated U_I at $R = 0.3$.

At $R = 0$, in the range of ΔK_I for which data are available, U_I is stable at ≈ 0.9.

At $R = -1$, and $R = -2$, $U_I \ll 1$ at low ΔK_I^{nom}, and this ratio tends to increase with ΔK_I^{nom}, up to $U_I \approx 0.85$. This means that the crack tip does not remain open during the compressive part of the cycle, in opposition to what was reported by some authors (see chapter 2). However, the ratio $\sigma_{compression}/Rp_{0.2}$ is below 0.2 here, while it was over 0.5 in most of the studies for which this occurred (or for which compression increased the growth rate).

This lower U_I ratio is consistent with the fractographic observations, showing highly oxidized surfaces at $R = -2$ (fig. 4.22), which will lead to oxide-induced closure effects. U_I is initially lower for $R = -2$ than $R = -1$, for which oxidation is less present. As mentioned above, such closure effects were also observed by Suresh et al. [Suresh et al., 1981], and the influence of compression was studied more thoroughly by Pokorný et al. on railway axle steel [Pokorný et al., 2017, Vojtek et al., 2019]: the lower the load ratio and the crack growth rate, the thicker the oxide layer and the higher the induced crack closure.

This evolution of U_I is also consistent with da/dN - ΔK_I^{nom} curves, which are initially shifted downwards for $R = -1$ & $R = -2$ compared to $R \geq 0.3$, but tends to get closer as ΔK_I^{nom} increases.

The mean value of $K_I^{closure} = \Delta K_I^{nom} - \Delta K_I^{eff}$ at the beginning of the experiments at $R \leq 0$ is $K_I^{closure,\ mean} =$ *confidential data* $MPa\sqrt{m}$, which is close to the empirical $K^0 =$ *confidential data* $MPa\sqrt{m}$. This K^0 tends to account for crack closure, and thus improves the da/dN predictions.

As shown on figure 4.22, the surface is more oxidized near the crack initiation site, where the crack growth rate was smaller and which witnessed more contact cycles. This is consistent with the observations made by Suresh et al. [Suresh et al., 1981]: the lower ΔK_I and thus the lower the crack growth rate, the higher the number of cycles, and the thicker the oxide layer. By contrast, when ΔK_I and da/dN are high, the oxide layer does not have time to grow sufficiently to have an influence on crack growth.

The oxidation on figure 4.22 seems more present in the center of the specimen, which can be explained by the fact that oxide debris can leave the crack near side surfaces, as shown by Maierhofer et al. [Maierhofer et al., 2018]. They observed that the evacuation of oxide debris led to a reduction of OICC. This effect of OICC reduction decreased as the specimen thickness increased, and it could be removed by applying a patch over the side surfaces in order to keep the oxide debris inside the crack.

These oxide debris will most likely remain trapped inside Squat-type cracks (thus leading to OICC), since those cracks grow downward, have a dimension of several centimeters, a complex crack path, and a crack mouth located at the very top of the rail.

4.3.4 Crack growth rates versus effective SIFs

The crack growth rate correlate well with ΔK_I^{eff}, as shown on figure 4.24 (again, the experiment at $R = -0.5$ is excluded, as the crack front was asymmetric). All the datapoints are within an envelope of a factor 5.6 in growth rate, around the mean curve $da/dN =$ *confidential data* with $R^2 = 0.964$. Considering the accuracy of the ΔK_I^{eff} estimated by DIC, along with the dispersion within the material (factor 2.2 scatter obtained by British Steel on 5 experiments at $R = 0.5$, fig. 4.25), this scatter is low and the measured ΔK_I^{eff} can be considered as representative of the crack driving force. No increase in growth rate is observed at high ΔK_I and high R ratio, meaning that having K_I close to K_{IC} does not accelerate the crack growth in a significant way.

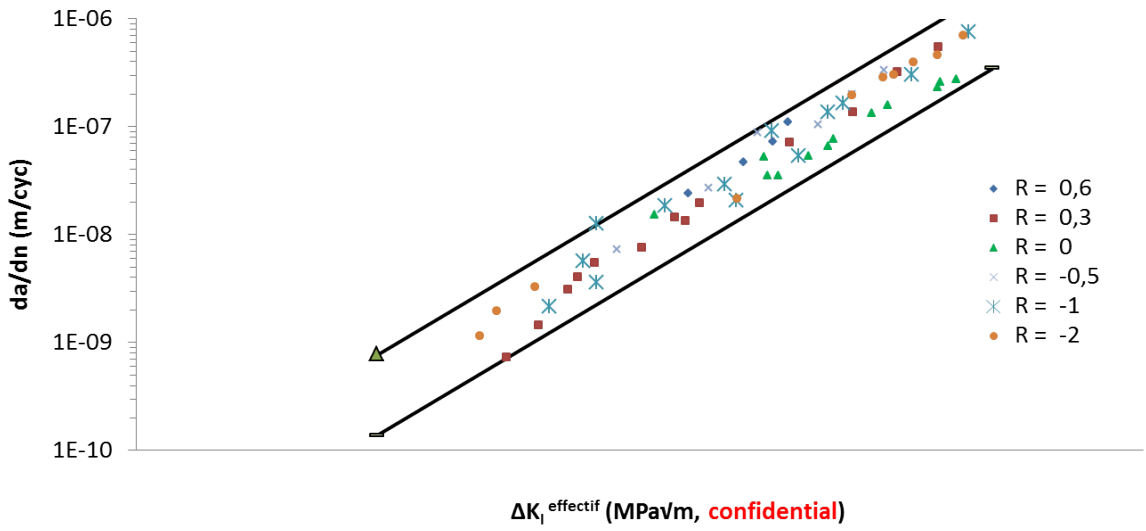

Figure 4.24: Crack growth rate versus ΔK_I^{eff} for various load ratios.

The C and m coefficients of Paris equation and the corresponding envelope and R^2 are given in table 4.2 for various driving forces. Both ΔK_I^{eff} and $\Delta K_I^{nom,0}$ (with $K^0 = \textit{confidential data}\ MPa\sqrt{m}$) give good results, and the second one can be used straightforward in FEM computations.

Table 4.2: Coefficients of various driving forces fitted to the data.

Driving force	C $(m/cycle)$	m	R^2	Enveloppe
ΔK_I^{nom}	*confidential*	*confidential*	0.928	14.4
ΔK_I^{eff}	*confidential*	*confidential*	0.964	5.6
$\Delta K_I^{nom,0} = K_I^{max} - \max(K_I^{min}; K^0)$	*confidential*	*confidential*	0.974	5.8

4.3.5 Comparison with other studies and on-field measured values

The best fit of da/dN - ΔK_I^{nom} obtained over all the data, as well as the datapoints for $R = 0.6$ alone are reported on figure 4.25, along with data of other studies on $R260$. The best fit over all the data is quite close to the results of [Tabatabaei, 2014], obtained at $R = 0.1$ for a $R260$ steel with different tensile properties. This fit over all the data is below the data obtained by British Steel at $R = 0.5$ (which is due to closure effects), while the data from the experiment at $R = 0.6$ are closer. The results presented in this study are consistent with those of British Steel (who provided the rails used to manufacture the test samples).

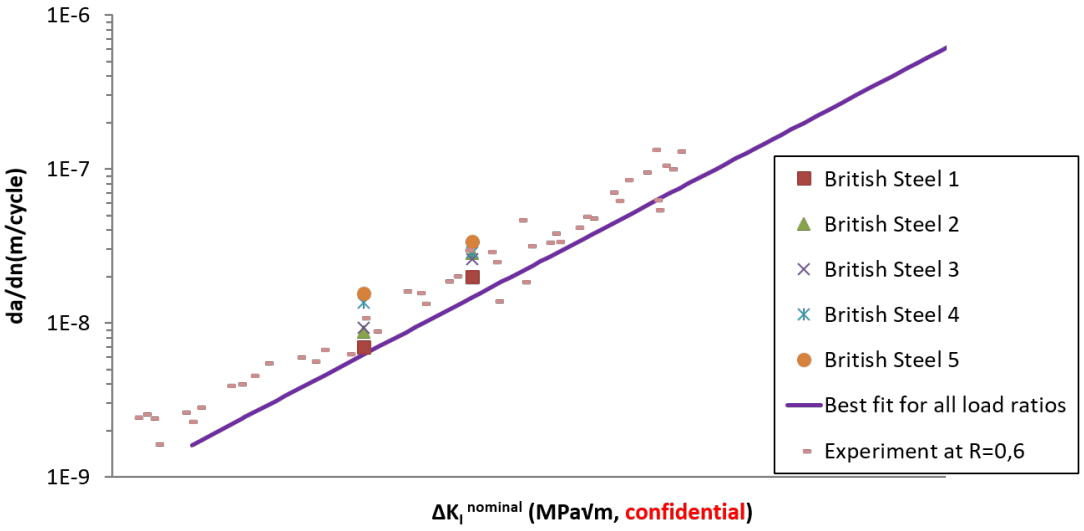

Figure 4.25: Crack growth rate versus ΔK_I^{eff} for various load ratios.

Using $\Delta K_I^{nom,0}$, the predicted crack growth rates at the deepest point of a 10 mm deep semi-elliptical Squat-type crack in a straight line, loaded with a TGV train would be *confidential data* $m/cycle$ at a $-5°C$ temperature, *confidential data* $m/cycle$ at $5°C$ and *confidential data* at a $20°C$. However, the mean crack growth rate obtained from 324 on-field measured values is *confidential data* $m/cycle$ (at the deepest point of a 10 mm deep Squat-type crack in a TGV line). The mean monthly temperatures in France distributes as described in table 4.3, leading to a predicted mean crack growth rate (over a year) of *confidential data* $m/cycle$. Considering the factor 5.8 scatter band, the predicted mean crack growth rate ranges from *confidential data* $m/cycle$ to *confidential data* $m/cycle$, which is still below the *confidential data* $m/cycle$ obtained from field data. If water trapping and pressurization is not considered, mode I alone cannot explain the crack growth in rails, as the predicted growth rates are too slow compared to the on-field measured values.

Table 4.3: Mean monthly temperatures in France (2014-2018) and predicted crack growth rate.

	Jan.	Fev.	March	April	May	June	July	Aug.	Sept.	Oct.	Nov.	Dec.
Mean temp. ($°C$)	6.4	6.4	9.2	12.4	15.6	19.9	21.9	21.2	18.1	14.1	9.8	7
Predicted da/dn ($m/cycle$)	*confidential data*											

4.4 Modelling

The capacity of the local approach introduced in chapter 2 to predict the mode I crack growth rate was investigated. Mode I coplanar crack growth is assumed to be controlled by tension-driven fatigue damage, and described by the Smith-Watson-Topper (SWT) damage function [Smith et al., 1970]:

$$\beta_{SWT} = \Delta\epsilon_n * \sigma_{n,max} \tag{4.10}$$

In the previous chapter, a relation between the fatigue life and the SWT parameter was deduced from push-pull experiments with various R ratios:

$$N_f = a_{SWT} * (\beta_{SWT} - \beta_{SWT,threshold})^{m_{SWT}} \tag{4.11}$$

The idea is to perform an elastic-plastic computation of the stress and strain evolutions ahead of a crack during a mode I cycle and then to estimate the crack growth rate form the fatigue life N_f of a coplanar segment of length ΔL over which β_{SWT} is averaged (in this study, ΔL was chosen as 40 μm):

$$\frac{da}{dN} = \frac{\Delta L}{N_f} \tag{4.12}$$

With a_{SWT}, m_{SWT} and $\beta_{SWT,threshold}$ obtained from LCF (see chapter 3.1) experiments.

The crack growth rate using this approach were estimated from 2D plane stress, or plane strain computations, as well as 3D FEM computations, with a 10 mm long crack. Three load cycles were simulated (the material behavior exhibits mostly kinematic hardening, so that the stress/strain loops stabilize in few cycles), and the stresses and strains during the last cycle were extracted. Several ΔK_I were simulated, at $R = 0$. The estimated crack growth rates are plotted on figure 4.26, and compared to the mean value of the da/dN - ΔK_I^{eff} data.

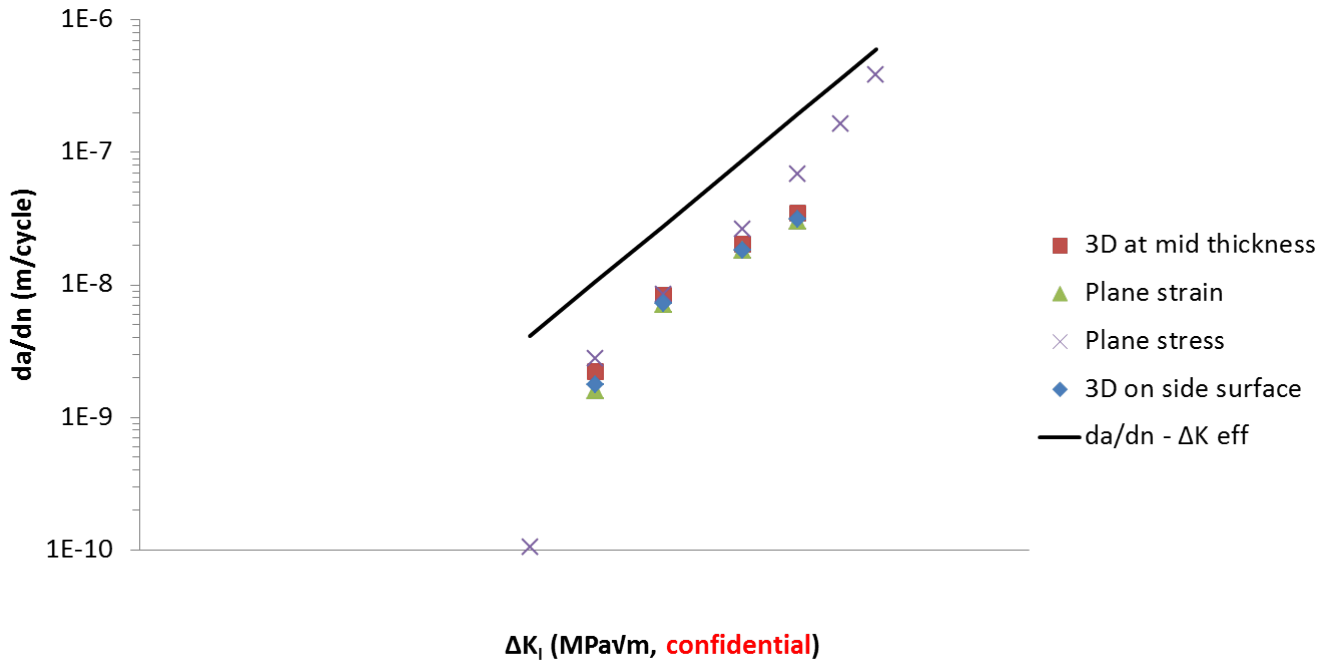

Figure 4.26: Crack growth rate estimated from the local approach versus ΔK_I for various hypothesis. Comparison with experimental data.

Whatever the hypothesis (2D plane stress/strain, 3D), the local approach underestimates the crack growth rate by a factor ≈ 4 in the *confidential data* range when using the coefficients of the damage function obtained from LCF experiments. However the slope is correctly predicted.

The underestimation of the crack growth rate might partly be due to the fact that the damage undergone by the segment of length ΔL before it touches the crack tip is not taken into account. Strictly speaking, a damage cumulation taking into account the progressive rise in stress and strain amplitudes when the crack approaches the segment should be performed. But this is beyond the scope of the present study, where a more pragmatic approach was adopted.

Another reason for such underestimation could be the different stress triaxiality between LCF experiments ($\sigma_h/\sigma_{VM} = 1/3$) and ahead of the crack tip ($\sigma_h/\sigma_{VM} = 0.75$ in plane stress, 2.5 in plane stress) during fatigue crack propagation.

This underestimation of the crack growth rate could also mean that at low da/dN (few 10^{-9} $m/cycles$), the crack driving mechanisms is not damage, contrary to LCF.

In order to improve the prediction of fatigue crack growth rates, the a_{SWT}, m_{SWT} and $\beta_{SWT,threshold}$ coefficients were adjusted in order to fit the da/dN - ΔK_I^{eff} curve (see figure 4.27), so that the approach could be used later to analyze the crack paths during mixed-mode experiments.

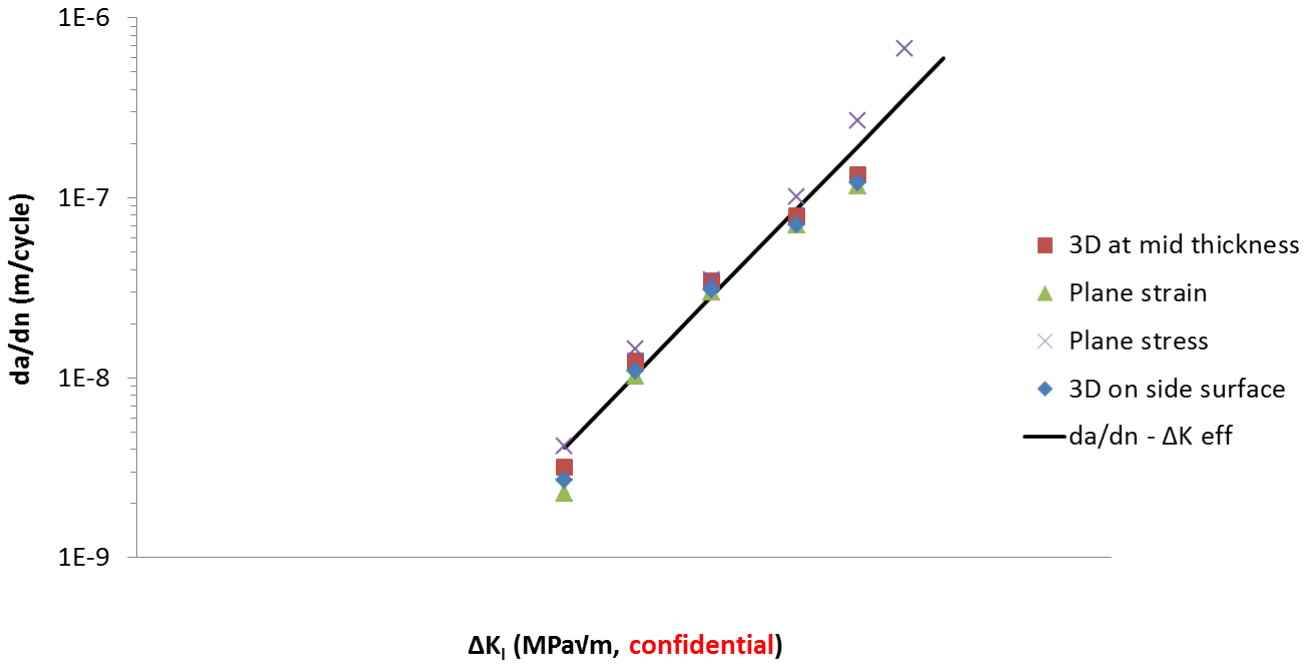

Figure 4.27: Crack growth rate estimated from the local approach with optimized coefficients versus ΔK_I for various hypothesis. Comparison with experimental data.

4.5 Conclusion

The mode I fatigue crack growth kinetics in $R260$ steel at $R = 0.6$, 0.3, 0, -0.5, -1 and -2 load ratio were obtained. The crack length was estimated using an optical microscope, while Digital Image Correlation was used to estimate both ΔK_I^{eff} and ΔK_I^{nom} since the analytical expressions of $\Delta K_I^{nom,\, SENT\, specimens}$ available in the literature do not account for the varying bending stiffness of the setup, which reduces ΔK_I^{nom} for long cracks. Those experiments led to the following results:

- A negative load ratio (with $\sigma_{min}/Rp_{02} < 0.2$) reduces the crack growth rate, especially at low ΔK_I, due to oxide induced closure. The lower the load ratio, the higher this effect. In Squat-type cracks, the oxide particles will remain trapped, which will certainly increase the amount of OICC [Maierhofer et al., 2018].
- Above $R \geq 0.3$, closure effects vanish.
- The measured crack growth rates correlate well with ΔK_I^{eff} or $\Delta K_I^{nom,\,0} = K_I^{max} - \max(K_I^{min}; K^0)$ (with $K^0 =$ *confidential data* $MPa\sqrt{m}$), which can be estimated directly in FEM computations.
- Mode I loading alone cannot explain crack growth in rails, as the crack growth rates predicted for a realistic ΔK_I range (neglecting water trapping/pressurization effect) are too small compared to the on-field measured values.
- The local approach using coefficients obtained from LCF experiments of a tension-driven damage model directly obtained from uniaxial LCF experiments correctly predicts the Paris exponent but underestimates the crack growth rate. This might be due to the absence of consideration of the damage cumulation at rising amplitude as the crack approaches and to the high triaxiality ahead of the crack tip. It is however possible to reproduce the mode I crack growth kinetics using modified coefficients in the damage model.

Chapter 5

Proportional mixed-mode II/III experiments

Contents

5.1 Introduction

Squat-type crack growth in rails could not be explained by mode I alone, as the crack growth rates measured for representative ΔK_I were too small compared to the on-field measured values. However, those cracks are not loaded under pure mode I but under non proportional mixed mode I+II+III in variable proportions along their front [Bogdanski et al., 1998, Mai et al., 2017], which might be the reason for this discrepancy.

As detailed in section 2.3 for Squat-type crack deeper than 5 mm, the amplitude of shear mode loadings (II & III), taking into account crack face friction using Coulomb's law, can be several times higher than that of mode I. However, while usual bifurcation criteria predict crack tilting at $\approx 70°$ for mode II and twisting at 45° for mode III [Erdogan and Sih, 1963], squat-type cracks do not bifurcate, but continue to grow along a highly sheared plane until failure. At a given point along their front, K_{II} and K_{III} exhibit more or less proportional time evolutions, but their proportions vary along the crack front. A necessary step in the experimental study of crack propagation in rails is thereby to perform proportional mixed mode II/III experiments in order to get kinetic data and thresholds for coplanar growth in shear modes or bifurcation, as predicted by usual criteria [Erdogan and Sih, 1963]. This work was published in [Bonniot et al., 2018].

Only a few studies focus on this type of loading (mixed-mode II & III). Pokluda, Vojtek et al. [Pokluda et al., 2008, Vojtek et al., 2013, Pokluda et al., 2014, Vojtek et al., 2015b, Vojtek et al., 2015a, Vojtek et al., 2016b] used cylindrical specimens with a circumferential notch (or two circumferential notches) on which a cyclic transverse shear force was applied. This device provides different mode mixity ratios K_{II}/K_{III} along the crack front, which allows comparisons of crack growth mechanisms and thresholds in mode II and mode III from one experiment. After the tests, the sample is broken in mode I, and the extent of shear-mode crack growth can be measured by SEM, but crack growth cannot be monitored during the experiment, and friction effects cannot be evaluated because crack face sliding displacement profiles cannot be measured. In [Pokluda et al., 2008, Vojtek et al., 2013, Pokluda et al., 2014, Vojtek et al., 2015b, Vojtek et al., 2015a, Vojtek et al., 2016b], crack face friction was prevented -but only for the early stage of crack growth- by compressive precracking, which induced some residual crack opening, and the studies focused on the thresholds, and near-threshold propagation mechanisms. Austenitic stainless steel, ARMCO iron, α-titanium, nickel and nobium were studied. For each of those materials, the measured mode II threshold was smaller than the mode III threshold (by a factor 1.7 for stainless steel, ARMCO iron, α-titanium and nickel [Pokluda et al., 2014]), and the crack growth rate was larger for mode II than for mode III. Near-threshold kinetic data were obtained for ARMCO iron and plotted versus a $\Delta K_{equivalent}$ [Vojtek et al., 2015b]. It appeared again that mode III was less efficient than mode II for crack growth. For nobium and titanium, cracks subjected to near-threshold mode III grew by local mode II, which explained the slower crack growth and higher threshold for mode III [Vojtek et al., 2016a].

Fremy, Pommier et al. [Fremy et al., 2014b] combined mode I, II and III on cruciform specimens made of 316L stainless steel, and loaded both in-plane and out-of-plane. They mostly focused on crack growth kinetics, depending on the loading path. Crack face friction was prevented by a positive K_I. Their experimental device allows a direct monitoring of crack growth, but a triaxial testing machine is needed, and the control of mode III, applied through a point contact on the surface of the specimen, is a challenge.

Hellier et al. [Hellier et al., 1987, Hellier et al., 1991, Hellier et al., 2011, Merati et al., 2012] developed an asymmetric four point bending device, and used beams, with a waisted central part and a straight central notch. By rotating the sample around its axis, one changes the orientation of the notch relative to the vertical shear force, hence changing the proportions of mode II and mode III. After the test, the specimens are broken in mode I in order to measure the extent of shear mode crack growth by SEM. In [Hellier et al., 1991], Hellier et al. performed tests on a rail steel (Australian standard 1085, slightly softer than $R260$: $Rp_{0,2} = 370 - 440\ MPa$, $\sigma_{UTS} = 770 - 880\ MPa$ versus $\sigma_Y = 480\ MPa$, $\sigma_{UTS} = 880\ MPa$, $A = 10\%$ for $R260$). No pre-cracking was performed, and the gradient

in mode mixity along the crack front was ignored. The reported thresholds were $\Delta K_{IIth} = 15 \pm 1.1 MPa\sqrt{m}$ and $\Delta K_{IIIth} = 18.8 \pm 2.0 MPa\sqrt{m}$. Again, the threshold for mode II was smaller than that for mode III. No coplanar growth was observed, but the cracks propagated at $\approx 70°$ relative to the notch in mode II, and exhibited a factory roof pattern at $\pm 45°$ in mode III, as predicted by the maximum tangential stress criterion [Erdogan and Sih, 1963].

Doquet et al. [Doquet et al., 2010a] performed mixed-mode II + III crack growth experiments on maraging steel and Ti-6Al-4V, using the same device as Hellier et al. 3D FEM computations [Doquet et al., 2010a] showed that for any position of the sample on the test rig, the mode mixity actually varies significantly along the crack front, which has to be taken into account in the analysis of experimental data. Crack growth was monitored on both side surfaces, and crack face sliding displacement profiles were measured, so as to evaluate the effective SIFs, allowance made for friction effects. Kinetic data were obtained for maraging steel and Ti-6Al-4V, and plotted versus a $\Delta K_{equivalent}$. It appeared that for both materials, mode III was less efficient than mode II for "stage III" coplanar shear mode crack growth.

In the present study, the same asymmetric 4 point bending device was used. Section 5.2 will introduce the experimental and numerical procedures, section 5.3 will summarize the results, and section 5.4 will show that the crack path and the extent of coplanar shear mode crack growth can actually be predicted by the local application, ahead of the crack front, of critical plane fatigue damage models, previously identified from biaxial fatigue tests, as detailed in appendix.

5.2 Experimental setup and numerical procedure

The experimental setup consists of a waisted bar with a central section of $10 * 10\ mm^2$ submitted to asymmetric bending (Fig. 5.1). This bar has a notch and a precrack in the middle of its length, where there is no bending moment, and thus no mode I, but a shear force, which induces shear modes on the crack. The sample can be rotated

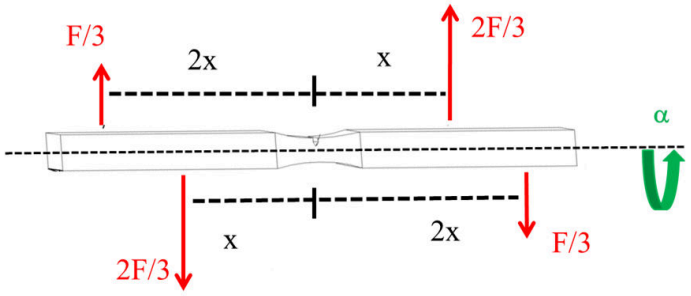

Figure 5.1: Asymmetric four point bending device.

around an horizontal axis by an angle α (Fig. 5.1), which changes the orientation of the crack front relative to the applied shearing force, thereby changing the mode mixity ratio K_{II}/K_{III}.

FEM computations with various crack front shapes were performed, using the same boundary conditions as in [Doquet et al., 2010a], in order to get the SIFs profiles along the crack front for different values of α. The sample was modeled using hexahedron elements of size $0.3 * 0.3 * 0.1\ mm^3$ near the crack front, and the crack plane was modeled using XFEM representation with quadrilateral elements of size $0.1 * 0.01\ mm^2$. SIFs were obtained using $G - Theta$ method [Destuynder et al., 1983]. The SIFs distributions along the crack front were fitted with a 6^{th} order polynomial, omitting the corner nodes, where the SIFs were extrapolated from the polynomial to avoid corner points singularities [Bazant and Estenssoro, 1979]. Examples for a straight crack front are presented on figure 5.2. Although mode II dominates for $\alpha = 0°$ and mode III dominates for $\alpha = 90°$, the other mode is still present and exhibits a skew symmetric distribution. Each test thus provides kinetic data for several mode mixities, depending

on the position along the crack front.

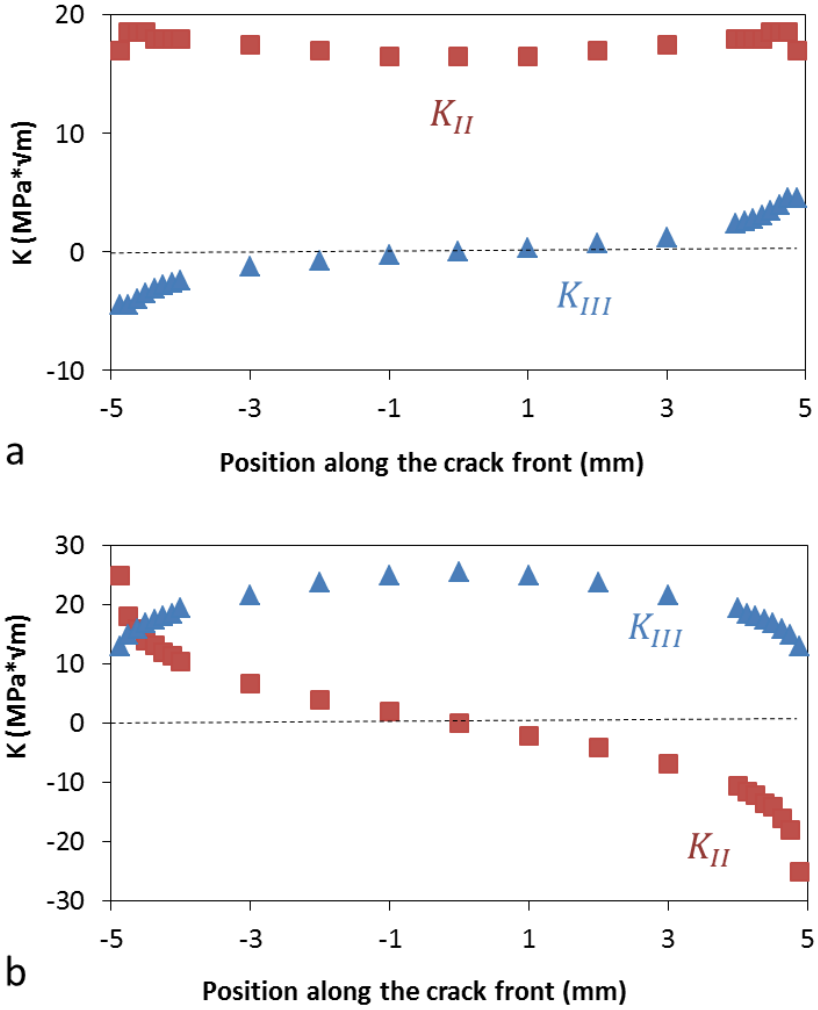

Figure 5.2: Stress intensity factors distribution for (a) $\alpha = 0°$ and (b) $\alpha = 90°$.

The specimens were pre-cracked at a constant $\Delta K_I = 16MPa\sqrt{m}$ and vacuum annealed for 4h at $450°C$ in order to remove -as far as possible- the pre-cracking residual stresses, without changing the microstructure. Then, a small number of shear mode cycles (from 50 to 2000, depending on the loading range) were applied, at a constant loading range, with a load ratio $R = -1$ and a frequency of 2 cycles per minute. Table 5.1 summarizes the test conditions. The tests were periodically interrupted in order to cast replicas of the crack along the side surfaces. After bifurcation or coplanar growth over a few hundreds of micrometers, the specimens were broken either by mode I cyclic loading, or using liquid nitrogen-induced brittle impact fracture. In cases when SEM observations of the fracture surfaces revealed some coplanar shear-mode crack growth, the positions and shapes of the initial, slightly tunneling precracking front, and final, rather concave, shear mode crack fronts were determined (Fig. 5.3).

Since the monitoring of crack length evolutions on side surfaces did not reveal significant acceleration or deceleration during the limited number of applied shear-mode cycles (denoted by N), a reasonable approximation of the local crack growth rate, at a given depth z is deduced from the increment of crack length $\Delta a(z)$ at the corresponding depth (Fig. 5.3) at the end of the test.

$$\frac{da}{dN}(a,z) \approx \frac{\Delta a(z)}{\Delta N} \tag{5.1}$$

Roughness measurements were performed on a few fracture surfaces, in two orthogonal directions, parallel or normal to the mean crack growth direction, using a mechanical profilometer Mitutoyo Surftest SJ-210.

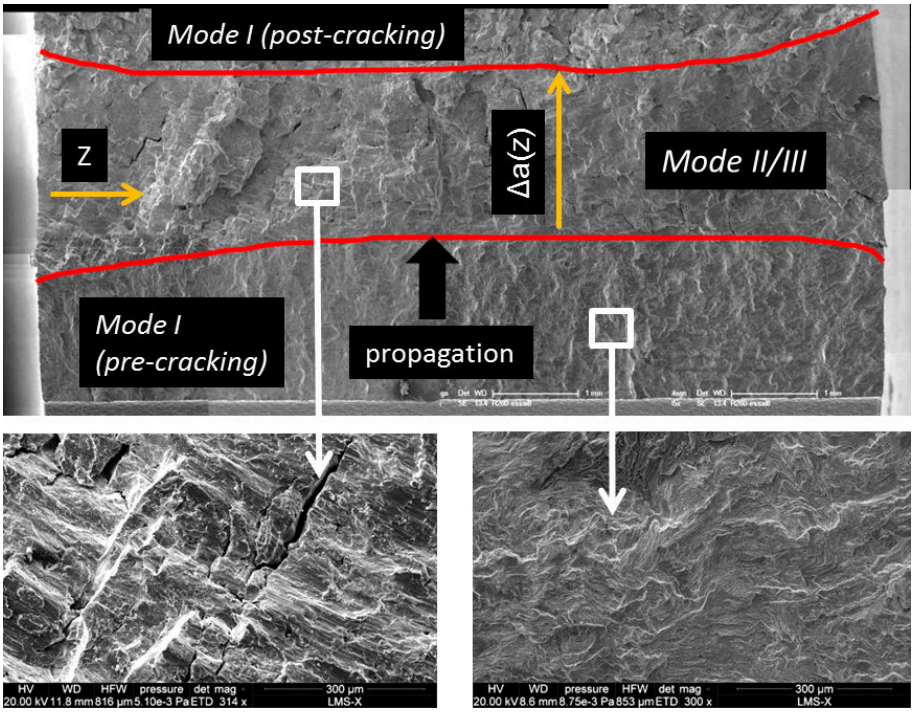

Figure 5.3: Initial and final shear mode crack fronts determined using SEM

In order to get Paris-like kinetic equations, it is necessary to determine the effective SIFs for each test, and each position along the crack front. Asperities interlocking and friction reduce the amplitude of crack face sliding displacements and the effective shear mode singularities at the crack front. The existence of such effects was confirmed here by the presence of wear debris on the fracture surfaces.

The determination of effective singularities relies on an inverse analysis of the crack opening and sliding displacement measured on the side surfaces, as detailed below. However, due to the position of the sample in the testing machine when the angle α is not equal to zero, the direct capture of images of both side surfaces is not feasible. Instead, plastic replicas are cast at maximum and minimum load, in order to get the sliding displacement range, but also at zero load, in order to measure the opening displacement range induced by the dilatancy effect. Due to crack face roughness, sliding of the crack leads to some opening, hence inducing two mode I sub-cycles inside one fully-reversed shear mode cycle [Doquet et al., 2009], as illustrated on figure 5.4. To analyze it, the images captured at maximum and minimum load have to be correlated with that captured at zero load.

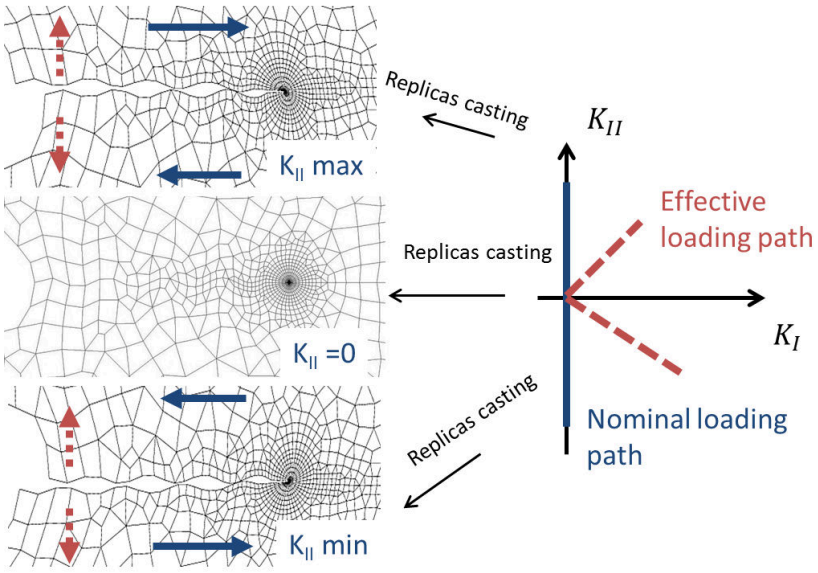

Figure 5.4: Nominal and effective path for a rough crack loaded in reversed mode II [Doquet et al., 2009].

DIC is used to measure the in-plane opening and sliding displacements. Since the painted speckle pattern generally used for DIC is incompatible with replicas, sand blasting (with sand particles diameters from 1 to 50μm) is used instead, in order to induce a topographic contrast on both side surfaces. A dense distribution of few micrometers wide craters form a pattern visible with an AFM or a digital optical microscope on the positive replicas cast from the plastic replicas. Two rows of virtual extensometers located 50 μm above and below the crack (Fig. 5.5) are used to measure the in-plane opening and sliding displacement jump profiles along the crack. The dilatancy ΔK_I is deduced from the slope of a plot (Fig. 5.6) of opening displacement range $[u_y](r)$ versus square-root distance to the crack tip, $\sqrt{r}$, using the relation given by Linear Elastic Fracture Mechanics for plane stress:

$$[u_y](r) = \frac{8\Delta K_I}{\sqrt{2\pi E}}\sqrt{r} \tag{5.2}$$

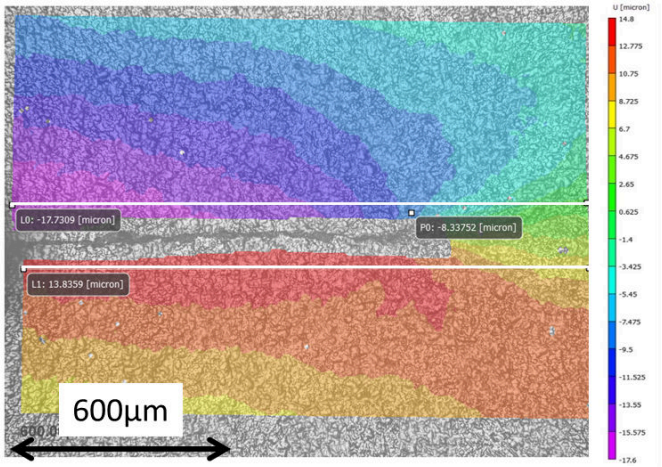

Figure 5.5: In-plane sliding displacement obtained by DIC (VIC2D). $ZOI = 35 * 35$ $pixels$, $1pixel = 1$ μm

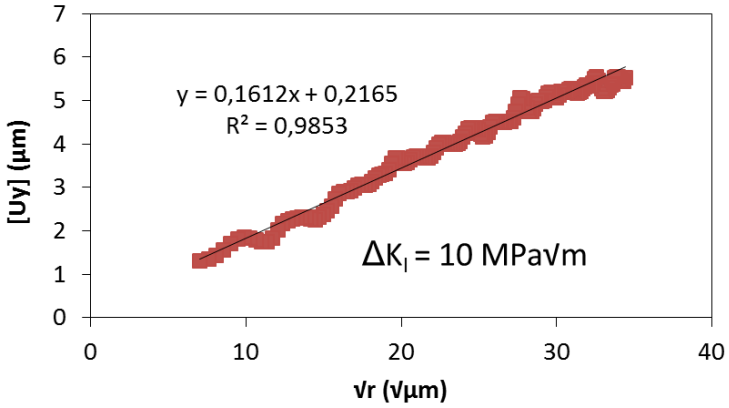

Figure 5.6: In-plane opening displacement versus $\sqrt{r}$. $\alpha = 90°$, $\pm 38\ kN$ loading range

The out-of-plane sliding displacement profiles along the crack are measured on the positive replicas, using an AFM (fig. 5.7 a) for displacement ranges under 10 μm. For greater displacement ranges, a topographic reconstruction is performed using a digital optical microscope (fig. 5.7 b). Again, two rows of virtual extensometers ± 50 μm above and below the crack are used to measure the out-of-plane displacement jump profile.

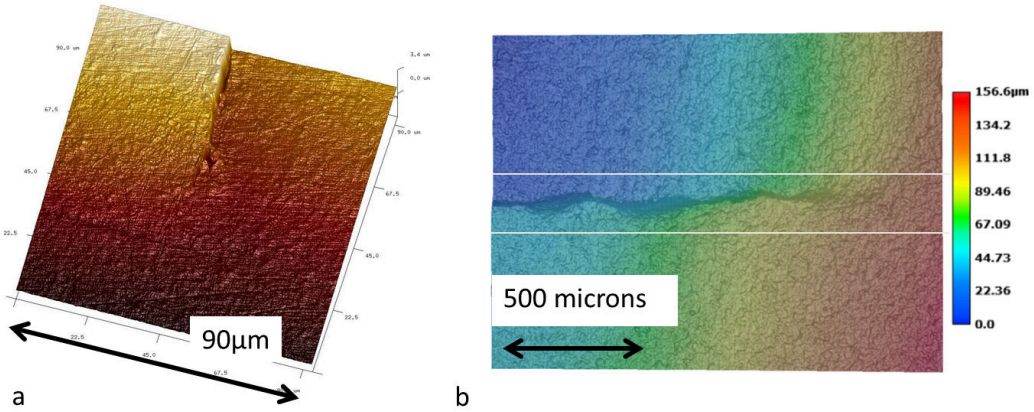

Figure 5.7: Out-of-plane sliding displacement obtained using an AFM (a), and topographic reconstruction with a digital optical microscope (b).

The effective fraction of the loading range is defined as:

$$U_i = \Delta K_i^{effective} / \Delta K_i^{nominal} \ , \ i = II, III \tag{5.3}$$

This effective loading range is determined by comparing the experimental in-plane (mode II) and out-of-plane (mode III) sliding displacement jump profiles to those computed using an elastic-plastic behavior, as detailed in chapter 3.2.5. Indeed, an elastic frictionless computation would neglect both the effects of crack tip plasticity, which increases the displacement jumps, and the effect of friction, which reduces it, and would not allow to separate those two effects. In order to measure the influence of friction, elastic-plastic frictionless computations are run with various loading ranges to find the loading range which gives the best fit of the experimental sliding displacement. The effective fraction of the loading range is then computed as:

$$U_i = \frac{\Delta F_i^{effective}}{\Delta F^{applied}} = \frac{\Delta K_i^{effective}}{\Delta K_i^{nominal}} \ , \ i = II, III \tag{5.4}$$

Within each test, the effective fraction of the loading range is found to be almost equal for both modes ($U_{II} \approx U_{III}$ with less than 15% difference) and on both side surfaces ($U_{side1} \approx U_{side2}$ with less than 10% difference). A mean U is thus computed for each test, and applied along the whole crack front, in order to get the effective SIFs from the nominal ones issued from FEM elastic, frictionless computations.

$$\Delta K_i^{eff}(z) = U_{mean} \Delta K_i^{nom}(z) \ , \ i = II, III \tag{5.5}$$

For the computation of nominal SIFs, the slightly tunneling pre-crack front shape, as well as the concave final shear-mode crack front shape measured on the fracture surface were taken into account in the F.E. mesh.

5.3 Experimental results

5.3.1 Crack paths

Table 5.1 indicates the test results in terms of crack path. For $\alpha = 90°$, almost immediate crack kinking/twisting was observed along the whole crack front for the smallest loading range. For intermediate loading ranges, coplanar shear mode crack growth was observed only near the side surfaces, over a few hundreds of micrometers, while for high loading ranges, for which small-scale yielding conditions were however still fulfilled, coplanar shear mode crack growth was observed, along the whole crack front, over distances larger than 2 mm. For $\alpha = 0°$, short coplanar growth was always observed, followed by bifurcation.

Table 5.1: Test conditions and results

α (°)	load (kN)	Number of cycles N	Distance of coplanar growth (surface 1) (μm)	Distance of coplanar growth (surface 2) (μm)	Distance of coplanar growth (mid thickness) (μm)
90	± 22	700	200	?	0
90	± 28	1000	580	700	340
90	± 34	700	1200	1000	700
90	± 38	180	2800	2700	2000
0	± 30	2000	220	290	?
0	± 35	500	500	250	85
0	± 39	600	350	300	190
0	± 42	120	405	485	135
0	± 45	300	330	400	?
0	± 47	50	335	320	170
0	± 50	90	420	110	200

During coplanar shear mode crack growth, branches orthogonal to the main crack line were observed on the replicas of the side surfaces, as illustrated on figure 5.8. Such secondary cracks leave traces more or less normal to the local crack growth direction on the fracture surfaces (Fig. 5.9a), and were also observed after mode II crack growth in austenitic steel by Pokluda et al (Fig. 7-10 in [Pokluda et al., 2008]) who attributed their nucleation to cyclic bending stresses on crack face asperities.

In mode II, a skew-symmetric singular stress parallel to the crack exists along the crack faces, so that after their nucleation, such orthogonal branches are loaded in cyclic mode I. The replicas cast at maximum (Fig. 5.8a),

zero (Fig. 5.8b) and minimum load (Fig. 5.8c) clearly show that the orthogonal branch behind the main crack tip undergoes cyclic opening/closure. Such a phenomenon was first underlined by Kfouri [Kfouri, 1999] and analyzed in detail by Doquet & Frelat [Doquet and Frelat, 2001]. In the latter study, the shielding effect of such branches on the main crack tip singularity was assessed, depending on their length and position behind the tip. For a fast propagating shear-mode crack, such a branch was predicted to grow in mode I at a decreasing rate, and to be left behind by the main crack, until it finally gets arrested, while for slower growth of the main crack in mode II, such a branch was predicted to develop faster than the main crack that stopped growing. These two cases can actually be observed on figure 5.8. In addition to the aborted orthogonal branch left behind the tip, a branch formed at an angle of 90° at the current tip above and below the main crack plane, and grew over approximately 100 μm, before kinking at 70°.

Branches were also formed in a plane normal to the crack front containing the local crack growth direction, as revealed by X-ray computed tomographic images (Fig. 5.10). The secondary cracks visible on the fracture surface in figure 5.9b and nearly parallel to the local crack growth direction correspond to the same kind of branch. Such secondary cracks were also observed after mode III crack growth in austenitic steel by Pokluda et al (Fig 11-15 in [Pokluda et al., 2008]), who attributed their formation to cyclic bending stresses on crack face asperities, or to the occasional presence of second phase particles. The position of the branches at the bottom of asperities on figure 5.10 tends to support the first explanation, even though in rail steel, the presence of elongated manganese sulfide inclusions normal to the crack growth plane might also play a role in the initiation of such branch cracks. But whatever their nucleation mechanism, these branches might grow either due to the cyclic shear stress induced by the mode III component: $\sigma_{xz} = K_{III}/\sqrt{2\pi r}$, or due to the cyclic opening stress associated with mode II, in plane strain: $\sigma_{zz} =$
$\nu K_{II}/\sqrt{2\pi r}$. Such branches probably also shield the main crack and may promote its bifurcation, although this deserves further analysis through 3D numerical simulation.

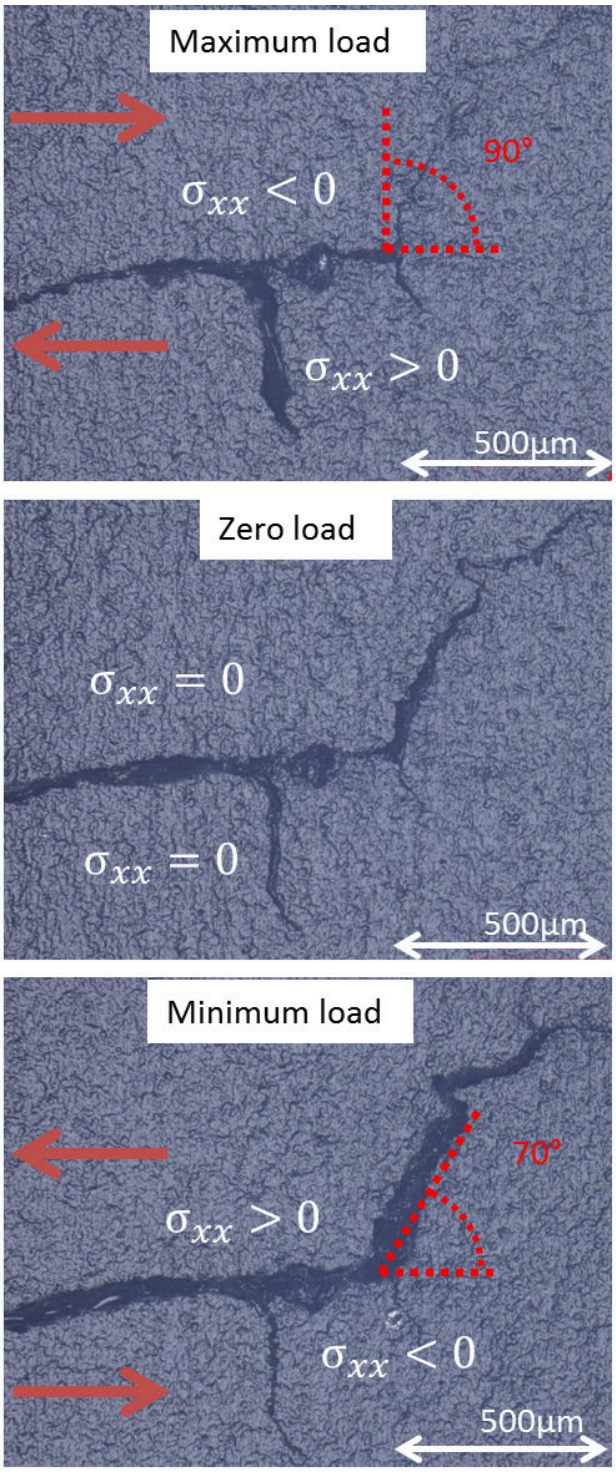

Figure 5.8: Replicas casted at maximum, zero and minimum load on a crack with branches, $\alpha = 0°$.

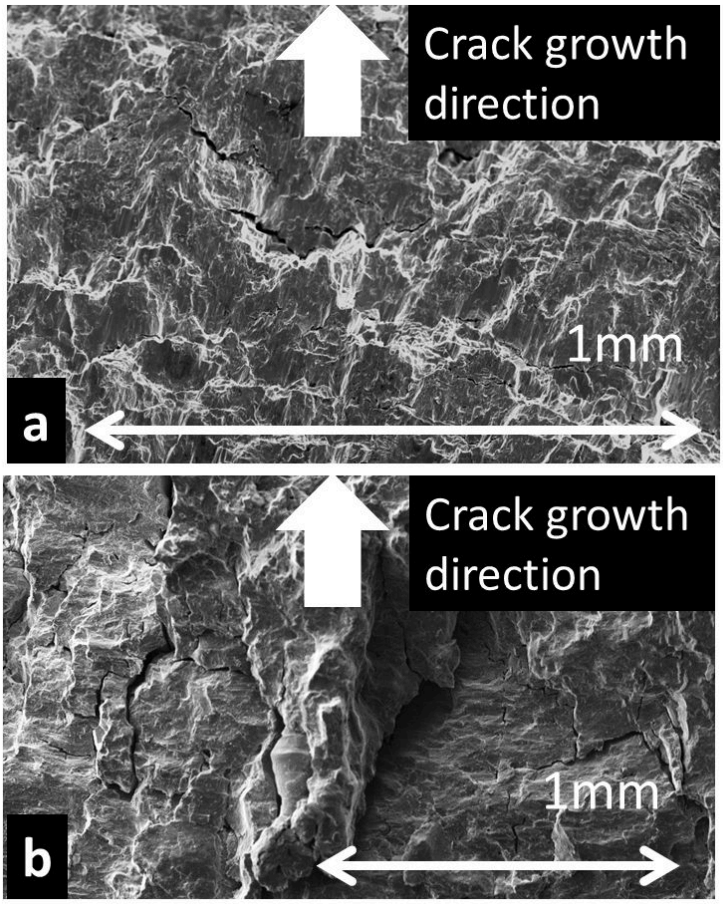

Figure 5.9: Secondary cracks on the fracture surfaces: a) nearly normal to the local crack growth direction where mode II dominates and b) nearly parallel to the local crack growth direction where mode III dominates.

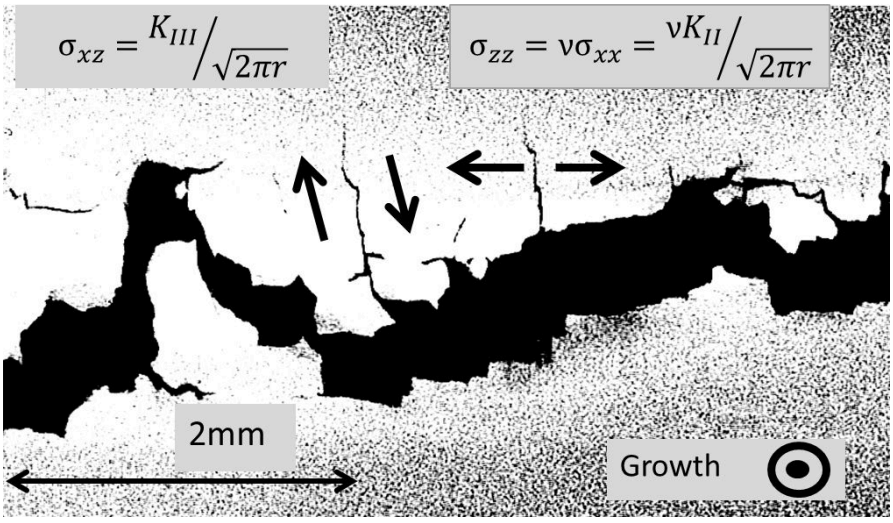

Figure 5.10: Branches in a plane normal to the crack front, $\alpha = 90°$. Tomographic image, resolution $5\mu m^3$. The crack growth direction is normal to the image plane.

5.3.2 Effective singularities

In plane strain, the energy release rate G is related to K_I, K_{II} and K_{III} by:

$$G = \frac{1+\nu}{E}[(1-\nu)({K_I}^2 + {K_{II}}^2) + {K_{III}}^2] \tag{5.6}$$

In the following, the contribution of shear-modes to the energy release rate ΔK_{shear} is defined as:

$$\Delta K_{shear} = \sqrt{{\Delta K_{II}}^2 + \frac{1}{1-\nu}{\Delta K_{III}}^2} \tag{5.7}$$

As mentioned above, the reversed sliding of rough crack face during one shear-mode cycle induces two mode I sub-cycles, which do not always have similar amplitudes (Fig. 5.4). The maximum amplitude of those two sub-cycles is denoted below as "dilatancy ΔK_I". The measured dilatancy ΔK_I divided by ΔK_{shear}^{eff} are plotted on figure 5.11a as a function of the effective ΔK_{shear}^{eff}. No systematic evolution appears, and the dilatancy ΔK_I lies between 22 and 31% of ΔK_{shear}^{eff} for $\alpha = 90°$ (predominant mode III) and between 8 and 27% for $\alpha = 0°$ (predominant mode II). The induced opening seems larger for predominant mode III. This is consistent with higher average roughness index Ra measured along series of lines parallel to the front ($< Ra >= 8.8\ \mu m$) than in the normal direction ($< Ra >= 5.9\ \mu m$). Higher asperities in the direction parallel to the front thus induce more crack opening when mode III dominates.

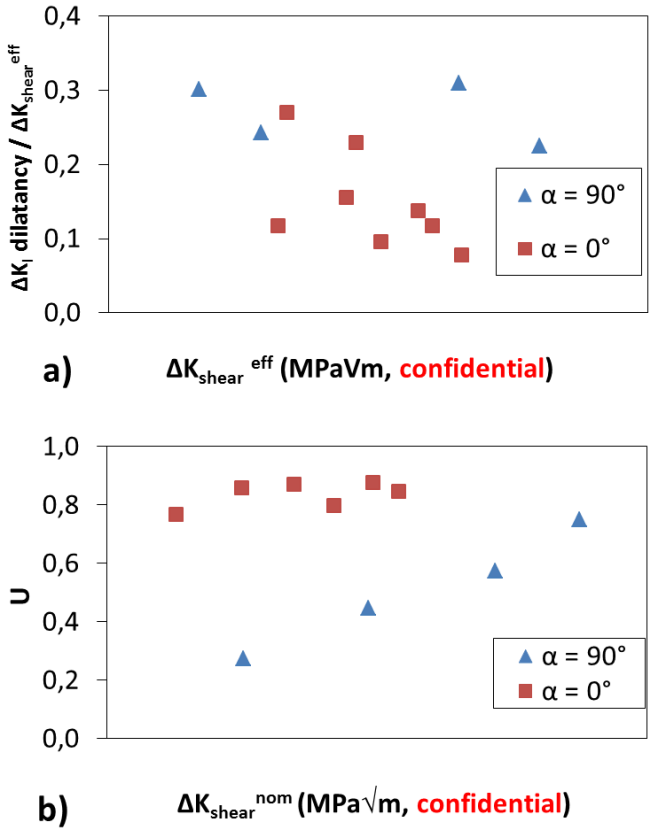

Figure 5.11: Evolution of $\Delta K_I/\Delta K_{shear}^{eff}$ versus ΔK_{shear}^{eff} (a) and U versus ΔK_{shear}^{nom} (b).

The effective fraction of the loading range, U, is plotted versus the nominal ΔK_{shear} on figure 5.11b. It lies between 0.3 and 0.9, which is comparable to the values measured on maraging steel and Ti-6Al-4V in [Doquet et al., 2010a] and on 65G steel in [Lenkovs'kyi, 2015]. This ratio is larger for $\alpha = 0°$ than for $\alpha = 90°$, which is consistent with the results on the dilatancy opening (Fig. 5.11a) and with the higher roughness measured in the direction parallel to the front. While U does not change much with ΔK_{shear} for $\alpha = 0°$, it increases with ΔK_{shear} for $\alpha = 90°$, meaning that the influence of friction tends to decrease as the loading range increases. This is consistent with the predictions of the model developed by Gross and Mendelsohn [Gross and Mendelsohn, 1989].

5.3.3 Shear-mode crack growth kinetics

The measured crack growth rates are plotted on figure 5.12 versus ΔG^{eff}_{shear} and ΔG^{eff} defined in equ.5.8 and 5.9, respectively.

$$\Delta G^{eff}_{shear} = \frac{1+\nu}{E}\left[(1-\nu)\Delta K^{eff\,2}_{II} + \Delta K^{eff\,2}_{III}\right] \tag{5.8}$$

$$\Delta G^{eff} = \frac{2*(1-\nu^2)}{E}\Delta K_I{}^2 + \Delta G^{eff}_{shear} \tag{5.9}$$

The dilatancy K_I is counted twice in equ.5.9 since there are two mode I sub-cycles within each reversed shear-mode cycle. Taking the induced opening into account does not increase the correlation coefficient R^2 when a power law is fitted.

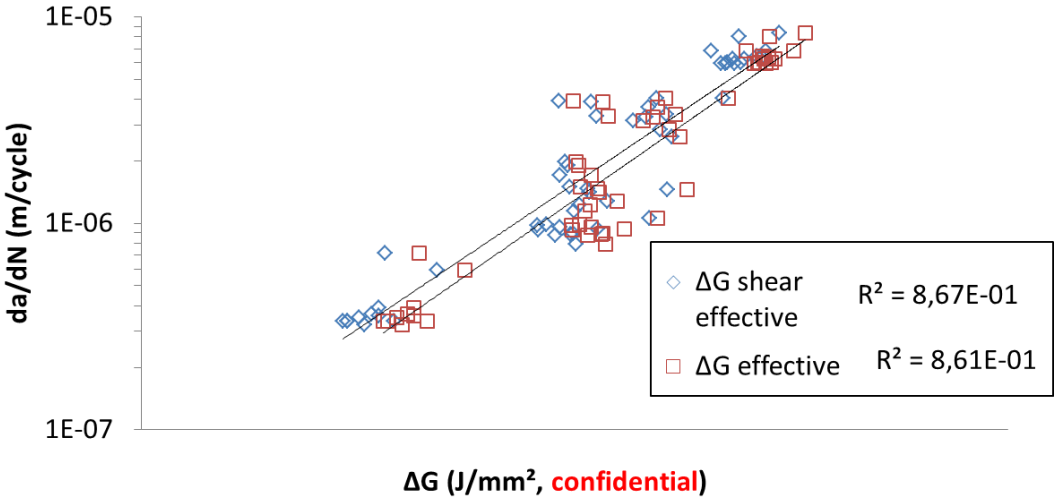

Figure 5.12: Crack growth rate as a function of $\Delta G^{effective}$ and $\Delta G^{dilatancy}$.

The influence of the dilatancy ΔK_I on crack growth kinetics was thus neglected in the following. An attempt to improve data correlation, by introducing an "equivalent" ΔK:

$$\Delta K^{eff}_{equivalent} = \sqrt{\Delta K^{eff\,2}_{II} + \beta \Delta K^{eff\,2}_{III}} \tag{5.10}$$

and searching for the weighting coefficient β corresponding to the highest correlation coefficient was made, as previously done in [Doquet et al., 2010a] and [Vojtek et al., 2015b]. The best fit for a power law ("Paris" like equation) was obtained for $\beta \approx 1.25$, with $R^2 = 0.871$ (Fig. 5.13), which is only marginally better than the fit obtained using $\Delta G^{effective}_{shear}$ ($R^2 = 0.867$). The latter assumes that mode II and III are equivalent driving forces, and corresponds to β equal to $1/(1-\nu) \approx 1.4$. The value of β found here suggests that mode III is slightly less

efficient than mode II for coplanar shear-mode crack growth. The best value of β found here is comparable to those found in [Doquet et al., 2010a] for Maraging steel ($\beta = 1.2$) and in [Vojtek et al., 2015b] for ARMCO iron for near threshold propagation ($\beta = 1.1$).

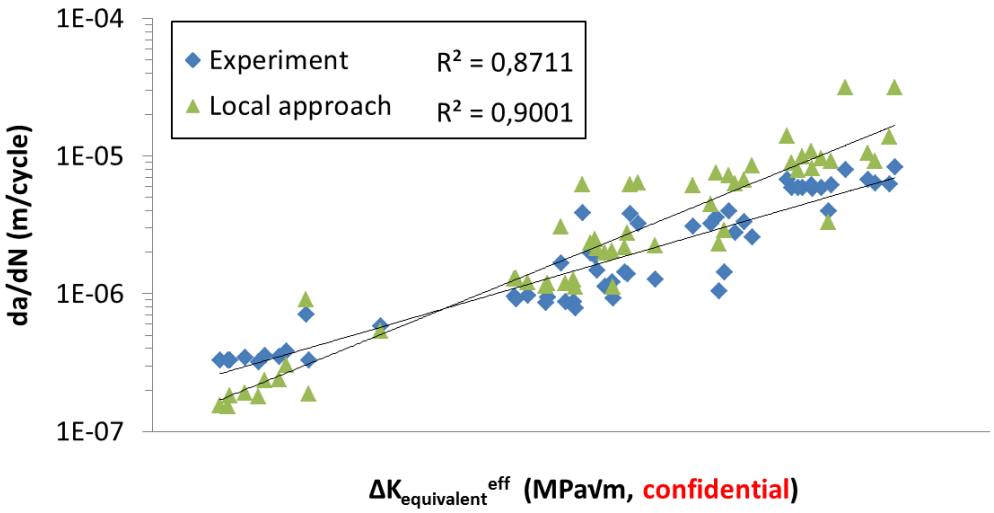

Figure 5.13: Experimental and predicted crack growth rate as a function of $\Delta K^{eff}_{equivalent}$, with $\beta = 1.25$.

As mentioned previously, using ΔK^{eff}_{equ} with an optimized β only marginally improves the results over $\Delta G^{effective}_{shear}$. As a consequence,

$$\Delta K^{eff}_{shear} = \sqrt{\Delta K^{eff\,2}_{II} + \frac{1}{1-\nu}\Delta K^{eff\,2}_{III}} = \sqrt{\frac{E}{(1-\nu^2)}\Delta G^{eff}_{shear}} \tag{5.11}$$

will be preferred as a driving force, due to its energetic meaning. The corresponding curve is given on figure 5.14 and as expected, using ΔK^{eff}_{equ} gives only marginally better results than ΔK^{eff}_{shear} ($R^2 = 0.871$ versus $R^2 = 0.865$). Note that $\Delta K^{eff}_{equ} = \Delta K^{eff}_{shear}$ for $\beta = 1/(1-\nu) = 1.40$.

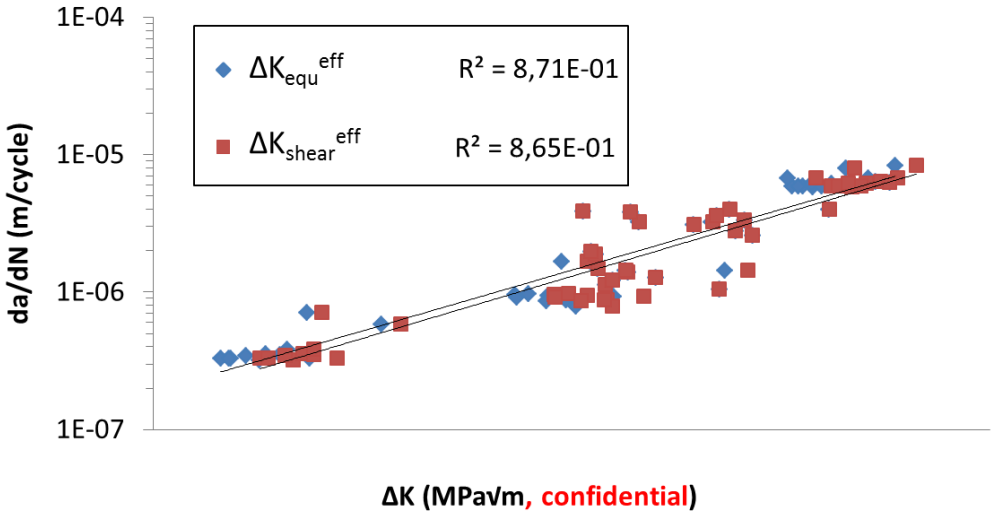

Figure 5.14: Experimental and predicted crack growth rate as a function of ΔK^{eff}_{shear} and $\Delta K^{eff}_{equivalent}$, with $\beta = 1.25$.

5.4 Modelling

5.4.1 Principle of the local approach

The above-mentioned approach based on Linear Elastic Fracture Mechanics and Paris-like equation allows satisfactory predictions of the crack growth rates in proportional mixed mode II & III, but may not be relevant in non proportional loading, as shown by Fremy and Pommier [Fremy et al., 2014b]. Since crack propagation in railways involves non-proportional mixed-mode I+II+III, another approach is needed. This approach should not only take into account the synergistic effects of the three loading modes -related to coupled crack tip plasticity- in terms of crack growth rate, such as the approach used in [Fremy et al., 2014a], but also account for the potential existence of two different propagation mechanisms (shear or tension driven), which the latter approach does not do.

A local approach was proposed by Doquet and Bertolino [Doquet and Bertolino, 2008b] in order to determine the crack growth rates and crack paths and is presented in section 2.6.3. This approach is based on the idea that fatigue damage ahead of the crack tip is responsible for crack propagation, and that two damage mechanisms are competing, one accounting for shear mode and the other for tensile mode. Two damage parameters are thus used. The first one , proposed by Smith, Watson and Topper [Smith et al., 1970], -homogeneous to an energy- accounts for tension-driven damage:

$$\beta_{SWT} = \Delta\epsilon_n * \sigma_{n,max} \tag{5.12}$$

This parameter was used to predict the crack growth rate in mode I, as detailed in chapter 4, and the coefficients of the power law linking β_{SWT} to N_f were modified to fit the experimental data.

In previous studies, [Doquet and Bertolino, 2008b, Doquet et al., 2009, Doquet et al., 2010a], Fatemi and Socie's damage function -homogeneous to a strain- was used, to account for shear-driven damage:

$$\beta_{FS} = \Delta\gamma_{max}(1 + k_{FS}\frac{\sigma_{n,max}}{\sigma_y}) \tag{5.13}$$

where $\sigma_{n,max}$ denotes the peak opening stress on the facet which undergoes the maximum shear strain range, $\Delta\gamma$, and k_{FS} is a dimensionless coefficient.

Alternatively, Findley's damage function -which has the dimension of a stress- could also be used:

$$\beta_{Find} = \Delta\tau + k_{FI} * \sigma_{n,max} \tag{5.14}$$

where k_{FI} is a dimensionless parameter.

However, in the present study, a shear-driven damage function equal to the product of the two previous ones, -and which thus has the dimension of an energy, like the tension-driven damage function- was preferred:

$$\beta_{Shear} = \beta_{Find} * \beta_{FS} \tag{5.15}$$

Those two damage functions are evaluated from elastic-plastic FE simulations, and averaged over a small segment of length ΔL in every possible direction (characterized by a tilt angle ϕ and a twist angle ψ) ahead of each node of the crack front. Contrary to the previous study on mixed-mode II+III [Doquet et al., 2010a] no assumption is thus made here on the crack path. The corresponding fatigue lives, $N_{f,tension}$ and $N_{f,shear}$, are deduced, using the equations fitted from low-cycle fatigue data, as explained in chapter 3.1. The minimum of those two values,

$N_f = min(N_{f,tension}, N_{f,shear})$, as well as the associated direction are then extracted. The potential local crack propagation rate is evaluated as:

$$\frac{da}{dN} \approx \frac{\Delta L}{N_f} \tag{5.16}$$

The crack is thus assumed to propagate according to the mechanism which maximizes its growth rate, which gives both the propagation direction and the crack growth rate.

This approach was applied on five of the experiments described above, which gave rise to some coplanar crack growth over the whole crack front. The effective loading range, corresponding to the measured sliding displacements, allowance made for friction effects, was applied in the F.E. computations, but the small mode I sub-cycles due to dilantancy were not simulated. When coplanar growth was predicted along the whole crack front, two FE computations were run: one with the initial, slightly tunneling crack front shape inherited from mode I precracking, and one with the final, slightly concave shear mode crack front measured on the fracture surfaces. The initial and final predicted crack growth rates were then averaged, and compared to the measured ones, which also correspond to a mean value over applied shear mode cycles.

The influence of the length ΔL, on the predicted crack growth rates was evaluated. For $\Delta L = 0.1\ mm$ the predicted crack growth rates were at most 30% higher than for $\Delta L = 0.04\ mm$. The influence of this parameter is thus relatively limited. A value of $\Delta L = 0.04\ mm$, which corresponds to the length of 2 elements ahead of the crack tip appeared to give the best predictions of the crack growth rates, and was thus adopted.

5.4.2 Predicted crack paths

Simulations were run for $\alpha = 0°$ and $\alpha = 90°$ with several loading ranges, in order to determine the effective threshold ΔK_{II} or ΔK_{III} below which no coplanar shear-mode crack growth is expected at mid-thickness, but rather crack tilting or twisting, respectively. The predicted threshold for coplanar growth at mid-thickness for $\alpha = 90°$ (mode III) is *confidential data* $MPa\sqrt{m}$, which is higher than the experimentally determined range *confidential data* $MPa\sqrt{m}$ (Table 5.2). For $\alpha = 0°$, the predicted threshold for coplanar growth at mid-thickness (mode II) is *confidential data* $MPa\sqrt{m}$, but available experimental data are not sufficient for an accurate determination of this threshold so that a comparison is not possible.

Table 5.2: Exprimental and computed thresholds

Mode	Experimental coplanar shear crack growth threshold ($MPa\sqrt{m}$)	Computed coplanar shear crack growth threshold ($MPa\sqrt{m}$)
II	*confidential*	*confidential*
III	*confidential*	*confidential*

For $\alpha = 90°$, no coplanar growth was observed for da/dn below $3*10^{-7}$ $m/cycle$ $m/cycle$. However, as discussed in 4.3.5, the mean crack growth rate measured at the deepest point of a 10 mm deep Squat-type crack in a TGV line (obtained from 324 on-field measured values) is *confidential data* $m/cycle$, with 90% of the data below *confidential data* $m/cycle$. The on-field measured crack growth rates are thus smaller by *confidential data* orders of magnitude than the smallest rate for coplanar shear-mode crack growth.

Moreover, even when coplanar shear mode crack growth was witnessed, branch cracks formed normal to the main crack plane and shielded its tip, thereby leading to its bifurcation, except for very high loadings ($da/dN \approx 6*10^{-6}$ $m/cycle$). In this case, there are *confidential data* orders of magnitude difference between the on-field measured crack growth rates and the rates required to get long coplanar shear-mode crack growth.

Shear modes loadings alone are thus unable to explain crack growth in rails, as the obtained crack path is not consistent with the one observed in rails.

5.4.3 Predicted crack growth rates

The predicted and measured coplanar crack growth rates profiles along the crack front are compared on fig. 5.15 for 3 tests run at an angle of $\alpha = 90°$, and on fig. 5.16 for 2 tests run at an angle $\alpha = 0°$. The crack growth rate is overestimated at the corner points by a factor up to 3.9, while at mid-thickness, the evaluated crack growth rates are within a factor 2 above or below the measured ones. Given the uncertainties on the local crack growth rates (the final shear mode crack fronts are sometimes difficult to locate accurately, especially near the side surfaces), as well as the uncertainties on the effective loading ranges, those predictions can be considered as successful. This is also illustrated by the comparison of the plot of predicted growth rates versus $\Delta K_{equivalent}$ with the experimental one, on fig. 5.13.

The local approach allow a prediction of the crack growth rate in mixed-mode II & III at high ΔK using only LCF data. This was not the case in mode I (see chapter 4.4), where the coefficients linking β_{SWT} to da/dN had to be modified in order to fit the $da/dN - \Delta K$ curve. These better results in shear modes can be due to the fact that the triaxiality ($\sigma_h/\sigma_{VM} = 0$) ahead of the crack tip was similar to that of torsional LCF experiments, which was not the case in mode I. It also suggests that coplanar shear mode crack growth at high ΔK is driven by damage.

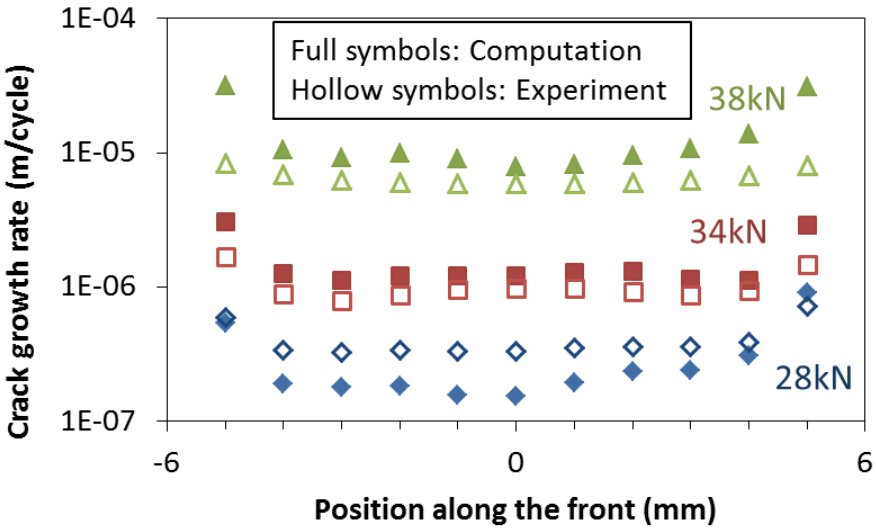

Figure 5.15: Experimental and computed crack growth rates along the crack front for $\alpha = 90°$.

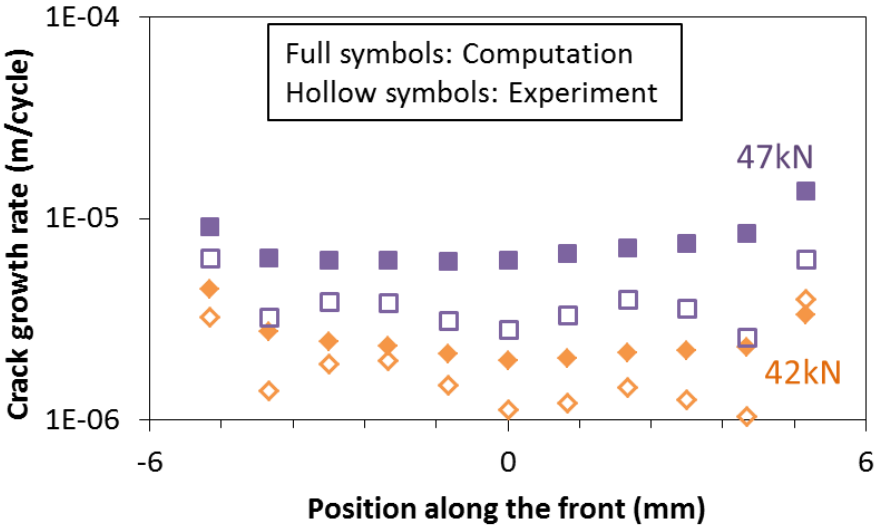

Figure 5.16: Experimental and computed crack growth rates along the crack front for $\alpha = 0°$.

5.5 Conclusions

Proportional mixed-mode II & III experiments were performed using an asymmetric four point bending device. The crack growth was monitored using casted replicas of the surface.

- Mode II & III coplanar fatigue crack growth was observed over distances up to 2.8 mm in R260 rail steel. For mode III, the effective threshold for coplanar shear-mode growth rather than bifurcation was *confidential data* $MPa\sqrt{m}$.
- Even when coplanar shear mode crack growth was witnessed, branch cracks formed normal to the main crack plane and shielded its tip, thereby leading to its bifurcation, except for very high loadings ($da/dN \approx 6 * 10^{-6}$ $m/cycle$).
- At crack growth rates similar to those observed in Squat-type cracks in rails (*confidential data* $m/cycle$), bifurcation is expected under mixed-mode II & III, while the cracks in rails grow coplanar: shear modes alone are thus unable to explain crack growth in rails, as the obtained crack path is not consistent with the one observed in rails.
- Due to crack faces interlocking and friction, the effective fraction of the loading range U was between 0.3 and 0.9.
- Sliding of rough crack faces induced two mode I sub-cycles within each reversed shear mode cycle. The resulting dilatancy ΔK_I was between 0.08 and 0.25 ΔK_{shear}.
- The best fit for a Paris-like equation was found for $\Delta K_{equ}^{eff} =$

$$\sqrt{\Delta K_{II}^{effective^2} + 1.25 \Delta K_{III}^{effective^2}}$$

  meaning that mode III is slightly less efficient than mode II for coplanar shear mode propagation.
- However, $\Delta K_{shear}^{eff} = \sqrt{E * \Delta G_{shear}^{eff}/(1-\nu^2)}$ was preferred over ΔK_{equ}^{eff} as a crack driving force due to its physical meaning, both giving similar results.
- Reasonable predictions of the shear-mode crack growth rates were obtained using a local approach. This approach is based on the local application, ahead of each node of the crack front -after elastic-plastic computations of local stress and strain ranges- of a shear-driven and a tension driven fatigue damage models. A 3D search for the direction in which failure of a small segment occurs first, by one mechanism or the other, is then performed to get the maximum crack growth rate and the associated direction.
- Sand blasting was shown to be a simple and effective surface marking technique for DIC.

Chapter 6

Non-proportional mixed-mode I + II experiments

Contents

6.1 Introduction

Mode I alone could not explain the crack growth in rails, as the crack growth rates measured for representative ΔK_I were too small compared to the on fields measured values. Neither could mixed mode II & III alone, as the SIFs needed to get a coplanar growth instead of bifurcation was too high ($\approx 0.37\ K_{IC}$ in mode III) compared to the computed values. The next step was thus to investigate the combination of shear and tensile modes, meaning non-proportional mixed-mode loading with compression phases, as it is the case in rails (see figure 2.14). Various open questions in non-proportional mixed-mode (couplings of opening and shear-induced crack tip plasticity, PICC, RICC, influence of a compression phase, crack front shape...) were already discussed in chapter 2. This section will focus on non-proportional mixed-mode experiments with a sequential loading and/or performed on rail steel.

Sequential mixed-mode loading has been studied by several teams, mostly on rail steel in order to get a better understanding of the rolling contact fatigue phenomena occurring in railways (and more specifically Squat-type defects).

Bold [Bold, 1990] performed experiments on a slightly softer rail steel ($\sigma_Y = 430\ MPa$, $\sigma_{UTS} = 795\ MPa$, $A = 22.2\%$ versus $\sigma_Y = 480\ MPa$, $\sigma_{UTS} = 880\ MPa$, $A = 10\%$ for $R260$). Proportional mixed-mode I + II experiments using an asymmetric 4 points bending device, as well as mode II experiments with a static mode I using a cruciform specimen in a biaxial testing machine led to crack bifurcation in the direction of maximum opening stress, after only 0.1 mm coplanar growth. By contrast, during sequential mode I + II experiments, long coplanar crack growth or bifurcation were obtained, depending on the loading conditions, and the results were successfully analyzed in terms of maximum growth rate criterion using the nominal strain intensity factors (see appendix 5. of [Bold, 1990]: using $\Delta K_{strain} = \Delta K_I / E_{secant}$, with $E_{secant} = \sigma_{VM}/\epsilon_{eq}$, supposedly improves the results for large scale yielding).

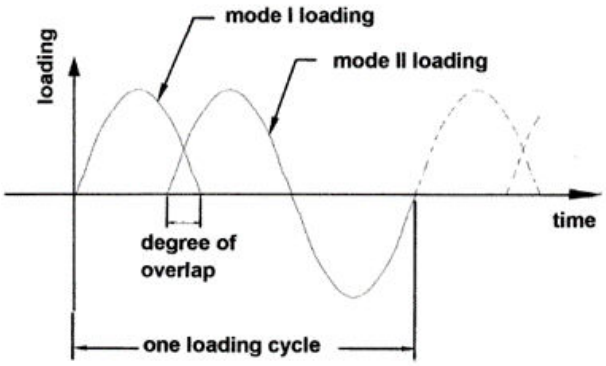

Figure 6.1: Sequential I + II loading with an overlap.

Wong et al. [Wong et al., 1996, Wong et al., 2000b, Wong et al., 2000a] continued this work, and performed sequential I + II experiments on cruciform specimens with an overlap between the mode I and mode II loadings, as shown in figure 6.1. Without the overlap, crack branching occurred when $\Delta K_{II}^{nom}/\Delta K_I^{nom} > 2$, but this criterion could not predict crack branching for overlaps different from zero. The effective SIFs were deduced from the measured crack face opening/sliding displacement using surface replicas or from a change of slope of load-displacement curves, and used to predict the crack growth rates, using three empirically-defined equivalent ΔK with a Paris-type equation:

$$\Delta K_{Wong,I}^{eff} = \Delta K_I^{eff} * (1 + (\frac{\Delta K_{II}^{eff}}{\Delta K_I^{eff}})^w) \tag{6.1}$$

$$\Delta K^{eff}_{Wong,II} = \Delta K^{eff}_{II} * (1 + (\frac{\Delta K^{eff}_{I}}{\Delta K^{eff}_{II}})^{w}) \tag{6.2}$$

$$\Delta K^{eff}_{equivalent} = \sqrt{(\Delta K^{eff}_{I})^2 + \Delta K^{eff}_{II})^2} \tag{6.3}$$

All three equivalent ΔK gave satisfying results, while ΔK^{eff}_{II} alone was unsuccessful at predicting the crack growth rate (see figure 6.2).

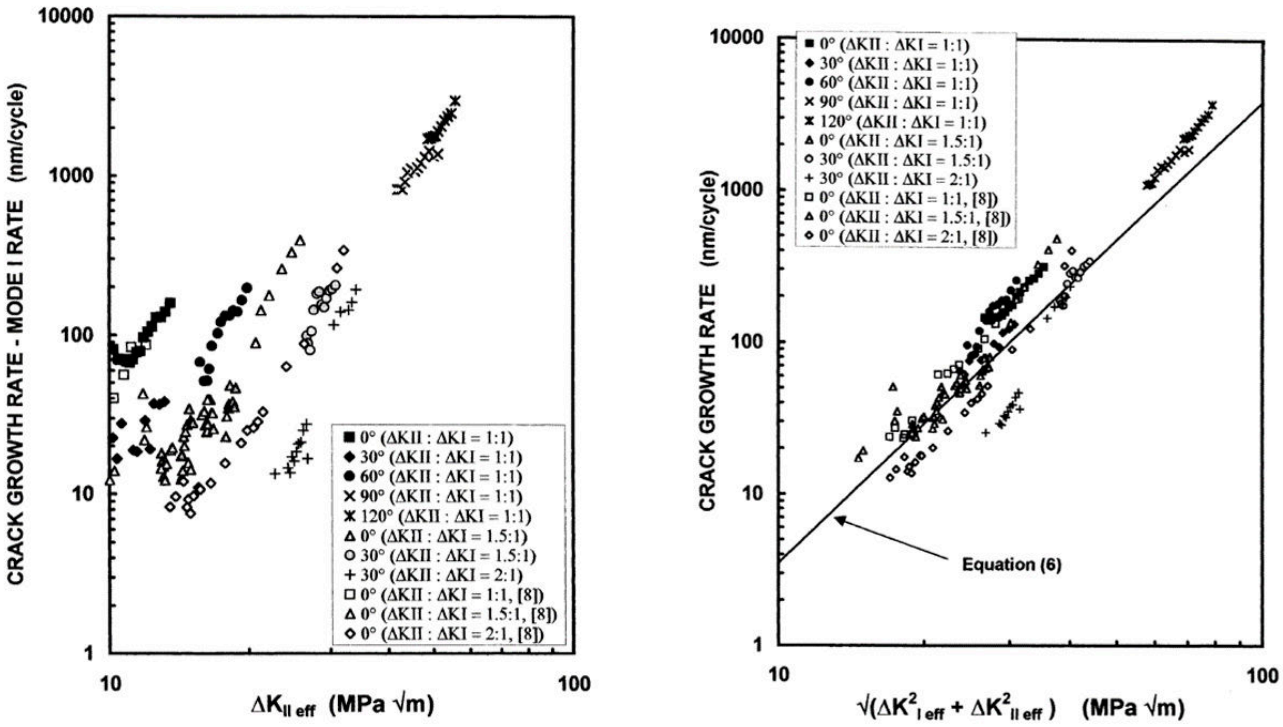

Figure 6.2: Crack growth rates from [Wong et al., 2000a], as a function of ΔK^{eff}_{II} (left) and $\Delta K^{eff}_{equivalent}$ (right).

The stable coplanar growth observed in sequential mixed mode I + II (at $R_{II} = -1$) for $\Delta K_{II}/\Delta K_I$ below a certain value can be explained in LEFM by extracting the peak value of $\sigma_{\theta\theta}(t)$: $max_t(\sigma_{\theta\theta}(t)) = \sigma_{\theta\theta,\,max(t)}$ and of $\Delta\tau$ at an angle θ ahead of the crack tip (see figure 6.3).

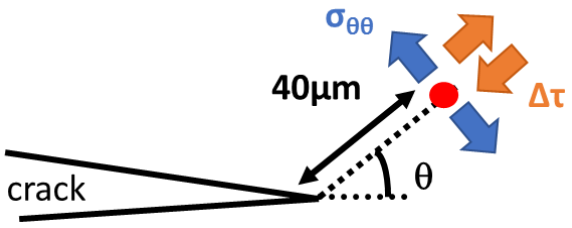

Figure 6.3: $\sigma_{\theta\theta}(t)$ and $\Delta\tau$ at an angle θ ahead of the crack tip.

For $\Delta K_{II}/\Delta K_I = 1$, $\sigma_{\theta\theta,\,max(t)}$ and $\Delta\tau$ are both maximum at 0°, as shown on figure 6.4.a, meaning that both the tensile driven and shear driven mechanisms tends to propagate the crack in a coplanar direction. However, when this ratio is over 1.73, $\sigma_{\theta\theta,\,max(t)}$ is not maximum at 0° but at ±70°, while $\Delta\tau$ is still maximum at 0° (see

figure 6.4.b, with $\Delta K_{II}/\Delta K_I = 2$): if the crack is tension-driven (MTS criterion), it will bifurcate.

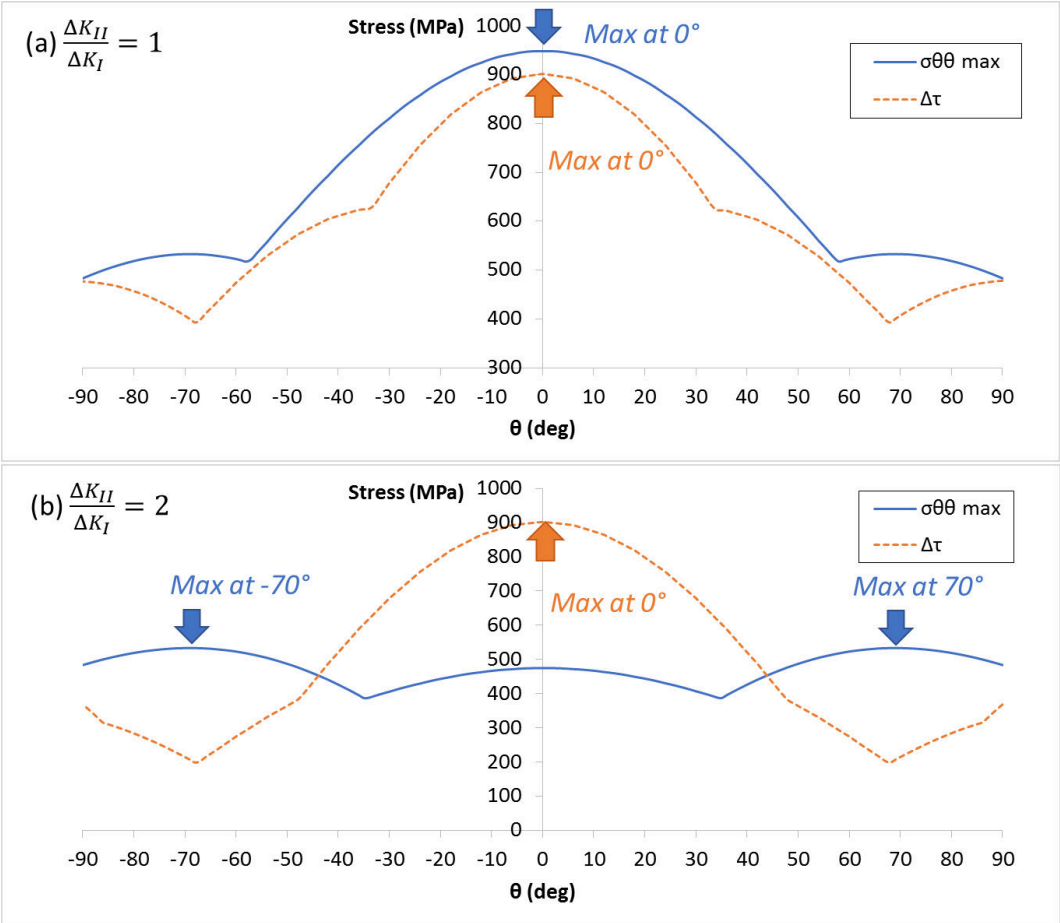

Figure 6.4: Evolution $\sigma_{\theta\theta}(t)$ and $\Delta\tau$ extracted at an angle θ ahead of the crack tip, for $\Delta K_{II}/\Delta K_I = 1$ (a) and $\Delta K_{II}/\Delta K_I = 2$ (b).

Those results were obtained with an elastic behavior. However, if we consider an elastic-plastic behavior (constitutive equations given in 3.1), and extract $\sigma_{\theta\theta,\,max(t)}$ (MTSp criterion, [Dahlin and Olsson, 2003]) at 40 μm from the tip for $\Delta K_{II}/\Delta K_I = 2$, the maximum of $\sigma_{\theta\theta,\,max(t)}$ is not at $\pm 70°$ anymore, but at 14°, as shown on figure 6.5. Crack-tip plasticity tends to reduce the height of the peaks at $\pm 70°$ and should increase the critical $\Delta K_{II}/\Delta K_I$ for bifurcation, which lies around ≈ 2 for $R260$ steel (and varies with the amount of plasticity, and thus increases with the loading amplitudes from 1.73 for $\Delta K_{II} -> 0$ to more than 2.1).

Sequential experiments with overlap were also performed by Akama [Akama, 2003] on rail steel, confirming Wong and Bold's results. The effective fraction of the opening and shear modes U_I and U_{II}, that they deduced from the relative crack face displacements measured on surface replicas, increased with the overlap, with some values above 1. This overestimation of the SIFs was certainly due to the effect of crack-tip plasticity that was not taken into account in their analysis of crack face displacements.

Akama and Kiuchi [Akama and Kiuchi, 2012] then performed sequential mode I + III experiments, with some overlap on cylindrical specimens with a circumferential notch. Depending on the conditions, coplanar crack growth or factory roof patterns (that is: bifurcation) were obtained. The crack growth rates could be described by an equivalent $\Delta K^{nom}_{equivalent} = \sqrt{(\Delta K^{nom}_I)^2 + \Delta K^{nom}_{III})^2}$ or just with ΔK^{nom}_{III}, as the influence of mode I on the crack growth rate was found to be low.

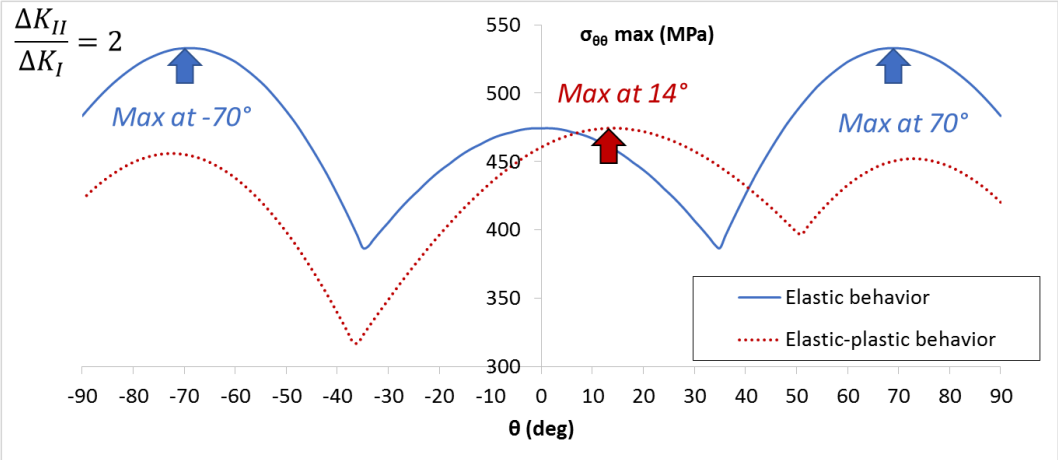

Figure 6.5: Evolution $\sigma_{\theta\theta}(t)$ extracted at an angle θ ahead of the crack tip, for $\Delta K_{II}/\Delta K_I = 2$, with an elastic or elastic-plastic behavior.

In those studies on railway steel, while the loading path (meaning the degree of overlap) was found to have an influence on the crack path, it did not have an influence on the crack growth rate (when considering the effective SIFs), contrary to what was observed on 316L stainless steel by Fremy et al. [Fremy et al., 2014b].

Doquet and Pommier [Doquet and Pommier, 2004] performed sequential mode I + II experiments on a ferritic-pearlitic steel (for railway applications, $\sigma_Y = 567\ MPa$, $\sigma_{UTS} = 898\ MPa$) tubes. *In situ* SEM measurements were performed periodically to measure the relative crack face displacement and evaluate the effective SIFs. Coplanar crack growth was obtained for $\Delta K_{II}^{nom} > /\Delta K_I^{nom}$ between 1 and 4, and the measured crack growth rate were found to be higher than the simple sum of the mode I and mode II growth rates, meaning that some synergistic effects occurred. This was explained by FEM elastic-plastic computations, showing that the amplitude of plastic blunting $\Delta\rho_I$ (which can be a driving force) is increased by the mode II cycles (four times higher when $\Delta K_I = 0.75\Delta K_{II}$ than in pure mode I).

The same type of synergetic effect was observed in [Doquet et al., 2009] for sequential loading on a maraging steel ($Rp_{0,2} = 1720\ MPa$). Coplanar crack growth was again observed for $\Delta K_{II}^{nom} > /\Delta K_I^{nom}$ between 1 and 4, as predicted by a local approach, and since this approach integrates both plastic and damage interactions between mode I and mode II (through the secondary contribution of the normal stress to shear-driven damage in Fatemi & Socie's criterion), it improved the prediction of crack growth rates, as compared to the simple superposition.

However, within these studies, while the influence of an overlap or other loading paths was assessed, the influence of the compression phase occurring in Squats during the shear-mode cycle was not evaluated. However, it has been shown by Tarantino, Beretta et al. [Tarantino, 2011, Tarantino et al., 2011, Beretta et al., 2010] that a 90° out-of-phase compression can favor shear-driven coplanar growth, reduce friction and increase ΔK_{III}^{eff} by keeping the crack open due to wear (which induces a loss of matter and a residual crack opening), as detailed in chapter 2. Sequential loading path was not considered, and residual crack opening of Squat-type cracks that grow downward would probably be reduced by trapping of the wear debris driven by gravity towards the bottom of the crack. Nonetheless, a compression certainly has an influence that might not be fully captured by Coulomb's friction and its effect on ΔK_{II}^{eff} and thus deserves to be investigated.

In the present study, an experimental setup consisting of a transversally precracked thin tube loaded in push-pull

and torsion was used to obtain non proportional mixed mode I + II loading, with an eventual compression during the mode II cycle (and some mode III, as discussed by [Vormwald et al., 2018]). A speckle painting was applied on the outer surface of the specimens to allow DIC measurements of the near-tip displacement field. Section 6.2 will detail the experimental and associated numerical means while section 6.3 will summarize and analyze the results.

6.2 Experimental and numerical procedures

6.2.1 Experimental setup

Thin tubes, with a through hole (0.7 mm in diameter) at mid height to initiate a crack were extracted from the head of a new rail, as detailed in figure 6.6. The samples were polished up to grain $P2400$ in order to remove the turning work striations. X-ray diffraction measurements were performed on four samples at the SNCF railway testing agency (Agence d'essais ferroviaires) on a 2 mm diameter area, over a depth of $5 \sim 10$ μm. Those measurements showed high levels of axial residual stress (≈ -350 MPa) at mid height on the outer surface of the gage length, with a constant level on the whole perimeter. In order to release as much as possible those residual stresses, without changing the microstructure, the samples were vacuum-annealed for 4 hours at 450 $°C$. The level of surface residual stresses dropped to ≈ -80 MPa. As for the mode I samples, those surface residual stresses relaxed during the experiments (20 ± 20 MPa measured on one broken sample).

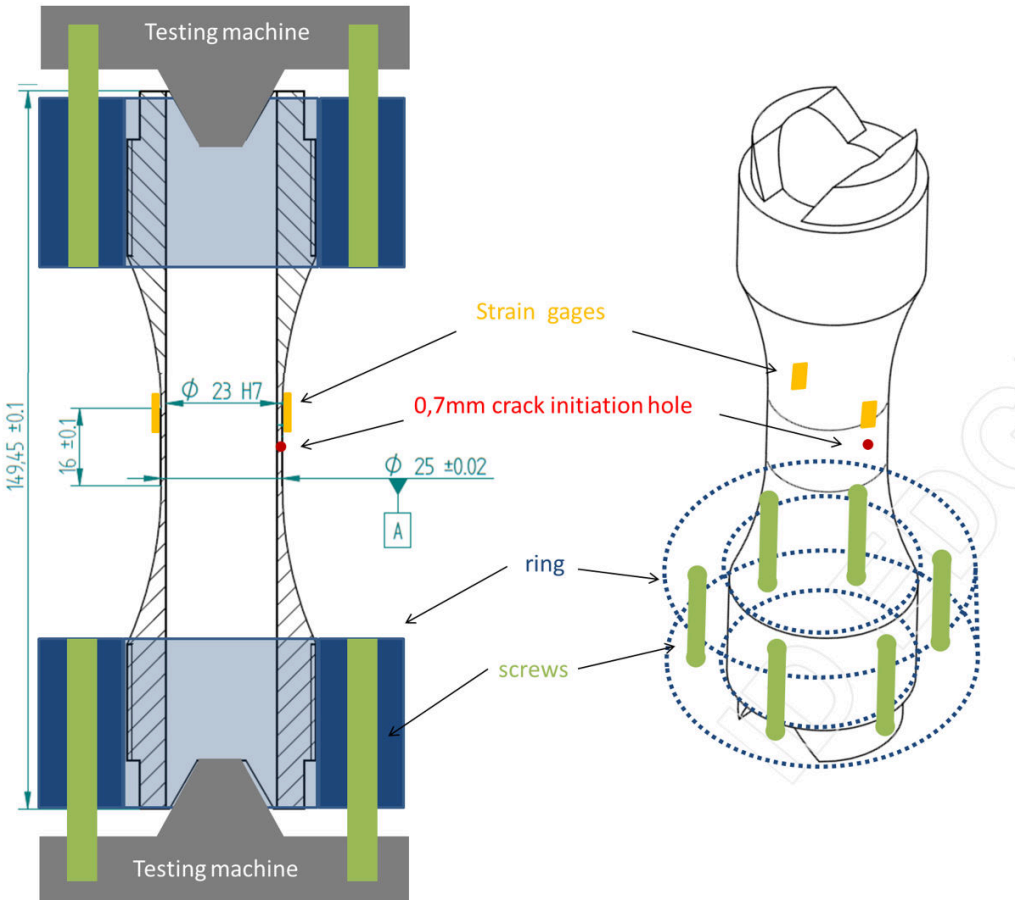

Figure 6.6: Sample and clamping device used for mixed mode I + II experiments.

This sample is mounted on the hydraulic triaxial testing machine presented in section 3.1, which allows frequency up to 1 Hz in non-proportional torsion & tension. For higher frequencies, it is difficult to get the correct loading paths due to retardation effects in the torque actuator.

A speckle pattern is applied on a $50 * 20$ mm^2 rectangular area around the crack initiation hole, using first a uniform white painting layer, followed by an airbrush induced black ink speckle pattern. The white paint is polished

with $P1200$ polishing paper in order to make it less glossy. The stains size ranges from 10 to 130 μm. This speckle painting is used for stereo digital image correlation measurements, using two $2452 * 2052$ $pixels$ pike cameras, with a pair of Tokina ATX-pro (100 mm focal length, aperture set at f/16) lenses. Those are set at approximatively 300 mm from the sample, and with a relative angle of approximatively 25 ° between the two cameras, as shown on figure 6.7. With this setup, the resolution is approximatively 7 μm per $pixel$. Lighting is provided by an annular light source.

Images pairs are recorded using the VICSnap software, using either a manual capture, a capture triggered by signals measured from the machine (torque or axial force), or a capture triggered by a signal sent by the test-driving software. The VIC3D software is then used to perform the stereo DIC, with a subset size of approximately 150 μm. Calibration of the setup is made automatically by processing a dozen pairs of images of a target ($6 * 5$ dots spaced by 2.5 mm) set at the future place of the sample and moved in various orientations.

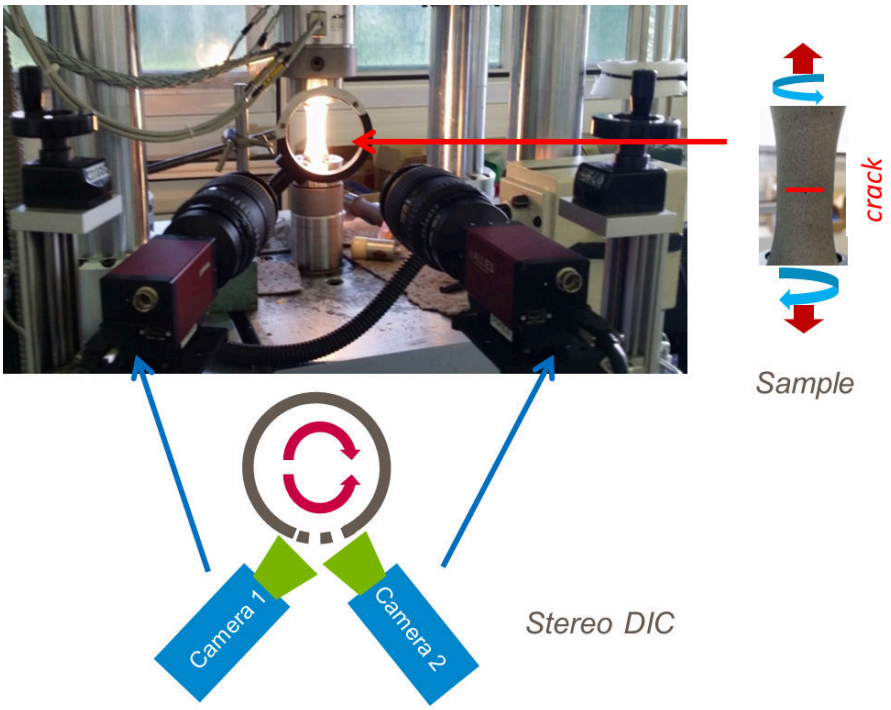

Figure 6.7: Experimental setup with the two cameras.

In order to maintain the sample in the testing machine, two rings are screwed on its top and bottom. Those rings are then attached to the machine using screws in order to lock the sample in translation. The V shaped specimens ends ensures rotary locking. The bottom and top rings are maintained by 6 and 8 screws respectively, which are screwed gradually in a star-shaped sequence in order to avoid an asymmetric locking of the sample. Such asymmetry can result in a bending of the sample, which can locally change the mode I load ratio R_I by adding a constant tensile/compressive force. On some samples, strain gages are placed 3 mm above the center hole, as well as on the opposite side of the sample in order to check that no bending is induced when tightening the screws. It appears that without these precautions, a non negligible bending can be induced, with a compressive stress on the crack up to ≈ 100 MPa (measured), and strain gages are thus necessary for this type of experimental setup.

The sample is first precracked in mode I by initially applying cyclic tension with a maximum tensile stress of 250 MPa ($\approx R_{p0.2}/2$) at $R = 0$ with a frequency of 20 Hz. Images are recorded every few 10000 cycles, and correlated

with VIC3D in order to measure the strain field and detect the crack initiation. Once the precrack is initiated, it is propagated at a decreasing ΔK_I to a length $a > 1.5\ mm$ and $\Delta K_I = 10\ MPa\sqrt{m}$. Once the crack is initiated, DIC fields are processed using the projection over William's expansion detailed in 3.2 in order to estimate the precrack length.

In order to reproduce specific loading paths computed on squat-type cracks (see figure 6.8 below), tilted precracks (as in figures 6.28 & 6.29) were also obtained along a tilted principal plane, by applying a suitable proportional combination of axial force and torque. Away from the hole, for plane stress, the first principal stress and the corresponding principal plane are, in the cylindrical coordinate system of the tube:

$$\sigma_1 = \frac{1}{2} * \sigma_{zz} + \sqrt{\frac{\sigma_{zz}^2}{4} + \sigma_{\theta z}^2} \tag{6.4}$$

In the direction:

$$\theta = \frac{1}{2} tan^{-1}(\frac{2\sigma_{\theta z}}{\sigma_{zz}}) \tag{6.5}$$

A setup was developed to perform experiments in water as detailed in appendix D. *In situ* mixed-mode I + II experiments were also performed in a SEM during a master internship prior to this study. Some results are given in appendix E.

6.2.2 Applied loading paths

As detailed in section 2.3, the squats-type cracks in rails undergo quasi pseudo sequential loading paths in $(K_I - K_{II})$ space, with compression phases. The amplitudes of ΔK_I ranges from 1 to 14 $MPa\sqrt{m}$, those of ΔK_{II} ranges from 4 to 35 $MPa\sqrt{m}$ and the compression can reach 85 MPa at the deepest point, depending on various parameters (train load, thermal load, crack length, friction coefficient). For a 10 mm deep semi-elliptical squat crack, loaded with a TGV train at 320 km/h in a straight line, at various operating temperatures, the loading ranges are given in table 6.1. Those values are used as references for the experiments, and the computations are performed with a frictionless crack, since those friction effects will already be present naturally in the experiments (by making computations with friction, the effects of friction would be counted twice).

Table 6.1: Loading amplitudes for a 10 mm deep squat crack, loaded with a TGV train in a straight line.

Temperature ($°C$)	ΔK_I ($MPa\sqrt{m}$)	ΔK_{II} ($MPa\sqrt{m}$)	$\frac{\Delta K_{II}}{\Delta K_I}$	σ_{compr} (MPa)
20	6.9	16.4	2.4	-62
5	10.4	16.4	1.6	-42
-5	12.7	16.4	1.3	-30

Most tests were run with pseudo sequential mixed-mode loading paths, close to those computed on squat-type cracks. As the loading frequency is limited to 1 Hz, and several experiments had to be performed, the crack growth rates had to be sufficiently large to avoid too long experiments (typically over 1 $nm/cycle$, which still needs more than 11 days to get a 1 mm propagation). Several amplitudes and load ratios $\frac{\Delta K_{II}}{\Delta K_I}$ had to be tested, along with an eventual compression, in order to understand the mechanism driving the crack (tensile, shear, both, other?), and to cover a loading range representative of the various conditions encountered in squat-type cracks (see table 6.1). The load ratio for mode II was kept equal to $R_{II} = -1$, since this parameter is known to have negligible influence in mode II. Examples are given in figures 6.8 a) & b), and test conditions in table 6.4. The applied loadings never exceeded $\sigma_{VonMises} = 320\ MPa$ (2/3 of Rp_{02}).

The computed loading paths are almost sequential, but a bit tilted with respect to K_I/K_{II} axes. In order to study this exact loading, pseudo-sequential experiments, tilted in the $K_I - K_{II}$ space had to be performed. Instead of using a complex driving of the machine, leading to very low frequencies (0.2 Hz), the sequential driving of the machine was kept (at 1 Hz), but with a tilted precrack, as in figures 6.28 & 6.29. An example of the loading path is given in figure 6.8 d), and test conditions are given table 6.5.

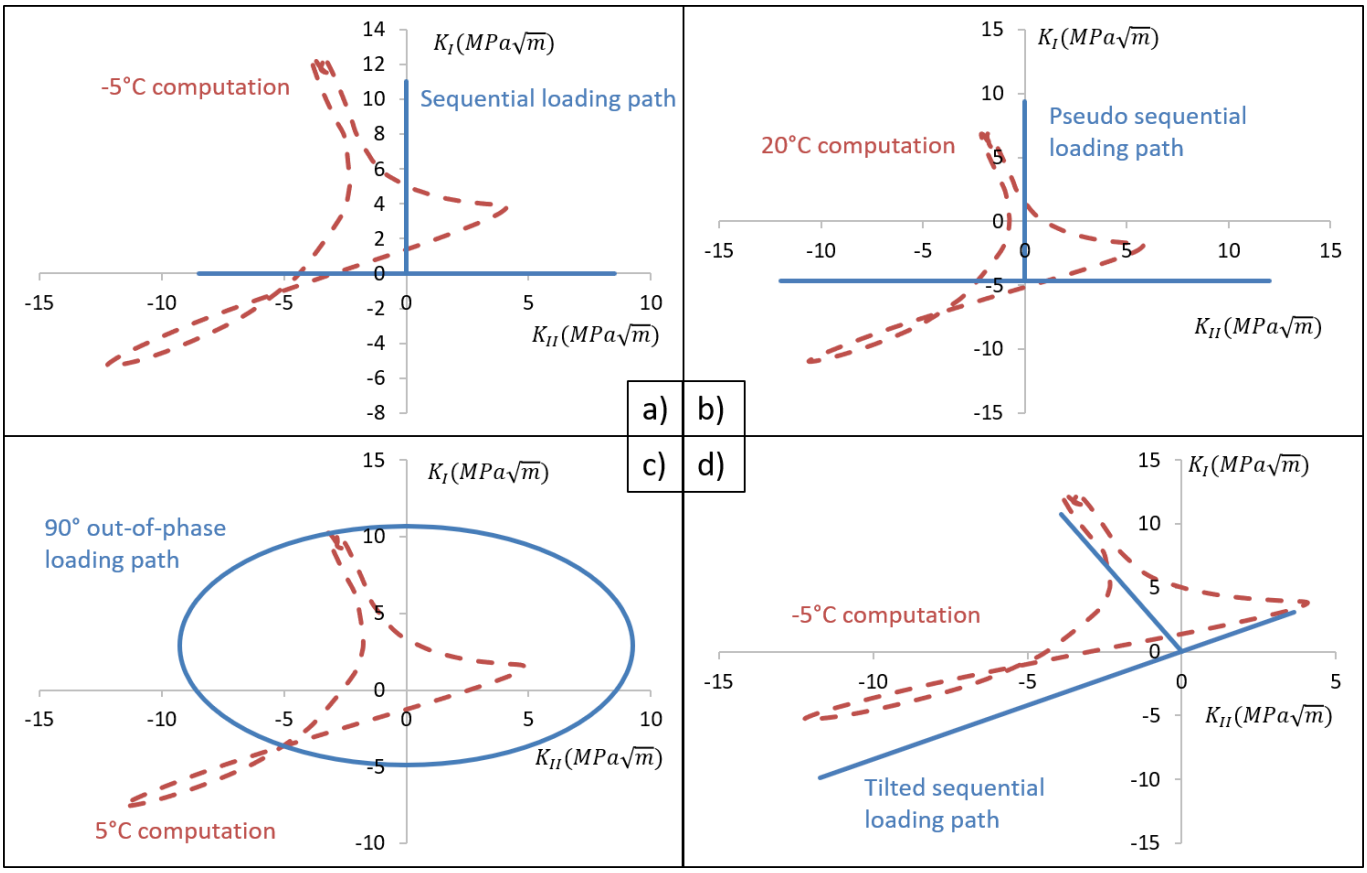

Figure 6.8: Examples of computed and tested loading paths. Computations at the deepest point of a 10 mm deep squat crack, loaded with a TGV train in a straight line, at various operating temperatures. *a*) sequential path applied to exp. 19. *b*) pseudo sequential path applied to exp. 6. *c*) 90 ° out-of-phase path applied to exp. 13. *d*) tilted sequential path applied to exp. 16. Negative values of K_I are plotted to account for compression.

To study the influence of the loading path on the crack growth rate and crack path, a few experiments were also performed with 90 ° out-of-phase tension and torsion, including a compression phase and with several amplitudes at $R_{II} = -1$. Some of those amplitudes were the same as that of pseudo-sequential experiments to allow a straightforward comparison. Since the loading frequency could only be 0.2 Hz, high loadings were chosen to get high growth rates and high couplings between shear an tensile plastic flows at the crack tip. An example of the loading path is given in figure 6.8 c), and test conditions in tables 6.6.

6.2.3 Nominal SIFs evaluation

In order to chose the appropriate axial load and torque evolutions to drive the testing machine and follow the desired loading path in (K_I, K_{II}) space, an abacus proposed in [Erdogan and Ratwani, 1972] for a crack in an infinitely long, thin tube (without a hole) linking the applied load/torque to the nominal SIFs and crack lengths was first used.

3D computations (see appendix C) were performed in order to verify that the hole could be neglected. For a 1.5 mm long crack, the error between the abacus and the computation is below 3%. The effect of a dissymmetry in the crack length on the two sides of the hole was also investigated and was found to have little influence.

The SIF values from this abacus are compared to SIFs deduced from DIC fields for which nonlinearities are very limited (very little plasticity, no contact between the crack faces, since $R_I = 0.4$, and small shear load amplitude) using William's expansion on figure 6.9. Both ΔK_I and ΔK_{II} diverge more and more as the crack becomes longer: Erdogan's abacus, which assumes an infinite tube length is not correct for long cracks in a finite length tube with rigid attaches.

To get more accurate values, XFEM computations of a finite length cracked tube were performed. The half specimen height was set to 30 mm, and a uniform σ_{zz} was applied at its end. The crack front was modeled as straight and normal to the inner and outer surfaces with 21 nodes regularly spaced by 50 μm across the thickness. The SIFs profiles along the front can show some significant gradients for shear modes, depending on the crack length (SIFs profile along the front are plotted later on, in figure 6.11, for other boundary conditions). This raises the question of which values of the SIFs to consider to control the experiments? The values at the mid-thickness, on the outer surface, or the mean values over the crack front? The means values of the SIFs, along with the values near the outer surface (50 μm from it, since corner points singularities [Bazant and Estenssoro, 1979] were avoided by discarding the values computed at the surface nodes) were estimated, and plotted on figure 6.9. The estimated K_{II} on the outer surface is closer to the values measured by DIC, but K_I is still very different. Erdogan's abacus seems to correspond to means values of the SIFs along the front.

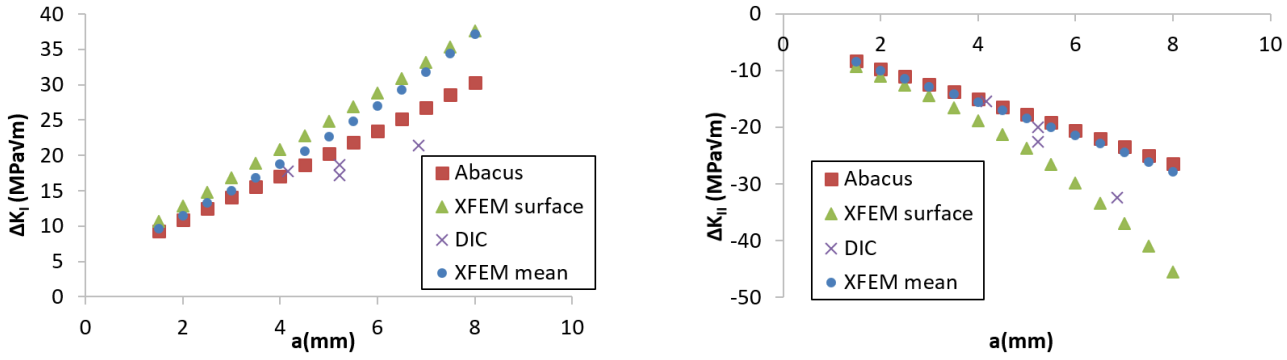

Figure 6.9: Left: K_I^{nom} estimated using DIC, Erdogan's abacus, and XFEM computations (mean and 50 μm from the outer surface value on the crack front) for a tensile load, as a fontion of the crack length. Right: K_{II}^{nom} estimated using DIC, Erdogan's abacus, and XFEM computations for a shear load, as a funtion of the crack length.

As for the mode I experiments, this increasing difference in K_I is probably due to the effects of bending. When the crack becomes long, its effect on the structure cannot be neglected any more, and if the experimental setup is too rigid, the applied σ_{zz} will not be uniform. Several XFEM computations were run, with an imposed uniform displacement instead of uniform σ_{zz}. Several height were tested, from a half height of 8 mm (height of the thinner part of the sample, see figure 6.6) to 75 mm (total height of the sample). The height for which the SIFs are closest to those issued from DIC was found to be 18 mm. The value of K_I, computed at 50 μm from the outer surface is plotted on the left graph of figure 6.10. This bending phenomena had little influence on K_{II}, but the position along the crack front did, as shown on figure 6.11. The value of K_{II} computed at 200 μm from the outer surface fits best that measured with DIC (see right graph of figure 6.10).

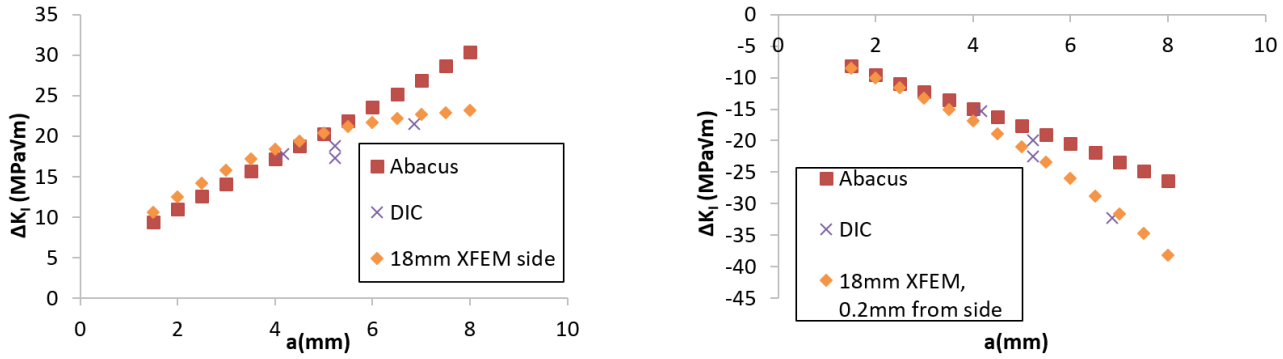

Figure 6.10: Left: K_I^{nom} estimated using DIC, Erdogan's abacus, and XFEM computations (uniform displacement of a 18 mm half height tube) for a tensile load, as a fiction of the crack length. Right: K_{II}^{nom} estimated using DIC, Erdogan's abacus, and XFEM computations for a shear load, as a fiction of the crack length.

For short cracks (below 4 mm), the profile of K_I & K_{II} along the crack front remains nearly uniform (see figure 6.11). For long cracks, the profile of K_I along the crack front remains nearly uniform, while K_{II} varies by up to 200 % from the inner to the outer surface (see figure 6.11 for a 8 mm long crack). The mean value of K_{III}, is 5 times lower than that of K_{II} for a 2 mm long crack, but becomes nearly as high as K_{II} for an 8 mm long crack. The evolution of the ratio K_{III}/K_{II} at mid-thickness is plotted on figure 6.12 as a function of the crack length.

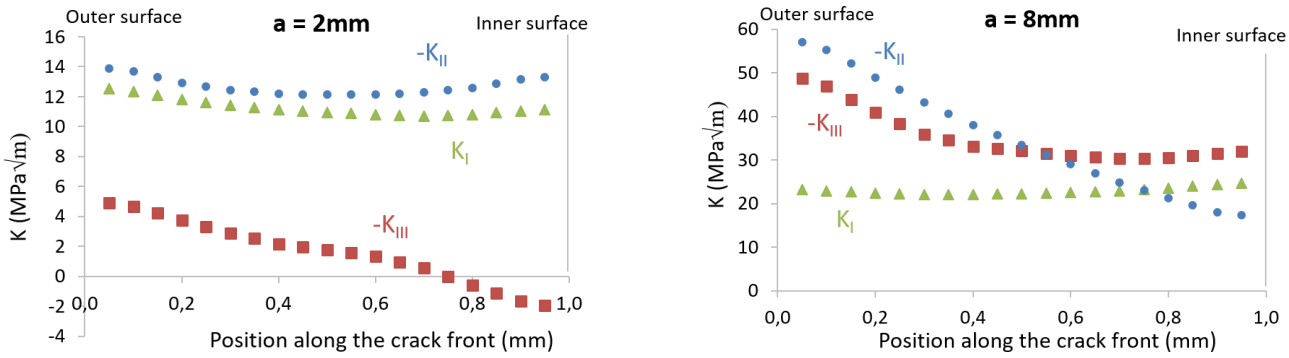

Figure 6.11: SIFs profiles along the crack front for two crack lengths

If the propagation is mostly tension-driven, the crack front will probably adopt and keep an iso effective ΔK_I shape, and should exhibit some tunneling [Branco and Antunes, 2003]. But if it is mostly shear driven, it will most likely change its shape to get an iso effective ΔK_{II} & ΔK_{III} profile, and the profile of ΔK_I will be non uniform.

Since the evolutions of K_{III} & K_{II} are influenced by too many parameters (friction, crack front shape) to be modeled confidently, the XFEM computed curves fitted on DIC measurements of figure 6.10 are used to build an abacus. This abacus writes as:

$$K_I(a,F,C) = F * (A_0^I + A_1^I * a + A_2^I * a^2 + A_3^I * a^3) \tag{6.6}$$

$$K_{II}(a,F,C) = C * (A_0^{II} + A_1^{II} * a + A_2^{II} * a^2 + A_3^{II} * a^3) \tag{6.7}$$

with the coefficients given in table 6.2.

Table 6.2: Coefficients for the abacus. a in mm, F in kN and C in Nm.

A_0^I	A_1^I	A_2^I	A_3^I	A_0^{II}	A_1^{II}	A_2^{II}	A_3^{II}
/	/	/	/	/	/	/	/

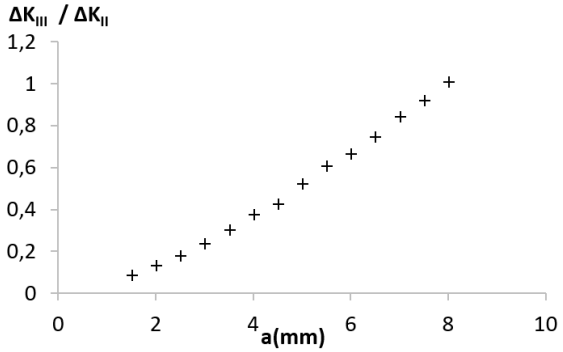

Figure 6.12: Evolution of K_{III}/K_{II} at mid-thickness

6.2.4 Crack tip localization and effective SIFs estimation

During the experiments, the crack tip is located using the projection over William's expansion with PS algorithm as described in 3.2. The displacement amplitude field on which the approach is applied is obtained from images captured at maximum tensile force and at zero load. This ensures that the contact stresses between the crack faces are low (only closure induced compression), and will not influence too much the crack tip position estimation, as explained in 3.2. As previously explained, mode I crack tip plasticity has little influence on the crack tip position estimation, and a full unloading can be used instead of a small elastic unloading. In sequential mixed-mode, it is important to correlate the image taken at maximum tensile force with an image taken after unloading and not before loading in order to release any residual asperities interlocking induced by the previous shear load.

The effective stress intensity factors for in plane modes (I&II) were measured using the projection of the relative displacement jump measured ± 0.2 mm above and below the crack over a field issued from elastic-plastic FEM computations plus an offset, as explained in 3.2.

As explained in 3.2, the estimated effective SIFs determined using this method can be overestimated for high amplitude mixed-mode loadings, due to the couplings between mode I and mode II-induced crack tip plasticity. In order to verify the validity of the measured SIFs regarding those plastic couplings, a few cycles of each experiments were analyzed, using the following method during some cycles of the experiments:

1. Estimation of the effective loading path $K_I^{DIC}(t) - K_{II}^{DIC}(t)$ from the DIC displacement fields.
2. Use of this effective loading path to perform elastic-plastic frictionless FEM simulations (detailed in section 6.3.5).
3. Estimation of the loading path $K_I^{FEM}(t) - K_{II}^{FEM}(t)$) from the FEM displacement fields (using the same approach as for 1)).
4. Comparison of $K_I^{DIC}(t) - K_{II}^{DIC}(t)$ and $K_I^{FEM}(t) - K_{II}^{FEM}(t)$:
   - If those paths are equals, plasticity couplings should be negligible and $K^{DIC}(t) = K^{eff}(t)$.

- If the FEM path is larger than the DIC estimated path, those couplings are not negligible and $K^{DIC}(t) \neq K^{eff}(t)$.

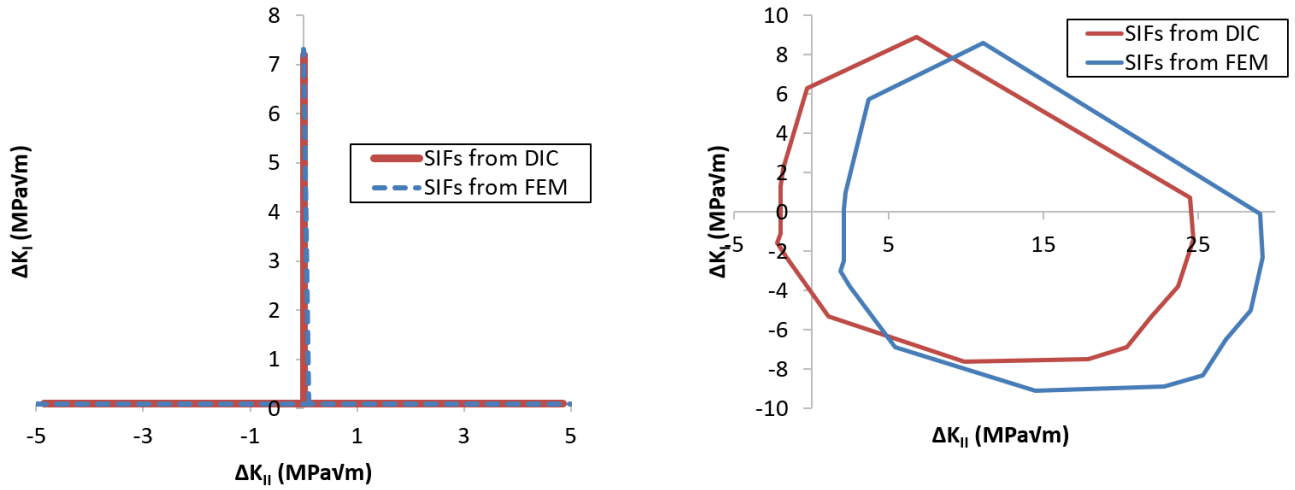

Figure 6.13: Effective loading path estimated from DIC displacement fields and from FEM (driven by the SIFs measured from DIC) displacement fields using the relative displacement jump method as explained in 3.2. (a) pseudo sequential experiment $N°6$, (b) 90° out-of-phase experiment $N°13$.

Illustrations of this method are given on figure 6.13 for two experiments. For a sequential experiment ($N°6$) with SIF ranges below 10 $MPa\sqrt{m}$, the loading path is well reproduced. However, for a 90° out-of-phase experiment ($N°13$), the loading path is shifted, with a K_I^{max} overestimated by 18%, which might influence the prediction of the crack path. However, the prediction of the SIFs ranges is still acceptable, as ΔK_I is overestimated by 2% and ΔK_{II} by 7%: the influence on the crack growth rate prediction which, as shown below, uses the range of the effective SIFs, is lower. In the rest of the document, we admit that $K^{eff} = K^{DIC}$ and only use the notation K^{eff}. Experiments for which $K^{eff} \neq K^{DIC}$ are pointed out.

For the (rough) estimation of ΔK_{III}^{eff}, the out-of-plane displacement jump $[U_R]$ was obtained using the stereo DIC and fitted using equ 6.8, which assumes that the crack front is normal to the outer surface:

$$[U_R] = \Delta K_{III}^{eff} * \sqrt{r} * \frac{8 * (1+\nu)}{E * \sqrt{2\pi}} \tag{6.8}$$

6.2.5 Bending correction

In order to quantify the influence of bending induced by an asymmetric tightening of the screws for the samples mounted without a strain gage, the $\Delta K_I^{effective}$ at the end of precracking were analyzed and compared to those obtained during experiment mounted with a strain gage.

The precrack tip position was estimated using the projection over William's expansion, and the SIFs were estimated using the relative crack face displacement method.

For each experiment with horizontal precracks, one cycle with similar $\Delta K_I^{effective}$ and for which the crack had propagated at the same loading range was analyzed, in order to have similar closure effects. The scatter in the $\Delta K_I^{nominal}$ - $\Delta K_I^{effective}$ curve plotted in figure 6.14 for experiments with and without a strain gage should be mostly due to bending. Some scatter is present for the experiments with a strain gage. This might be due to errors in the crack tip localization or in the effective SIFs estimation (the presence of the hole reduces the length of the lines along which the relative crack face displacement is analyzed).

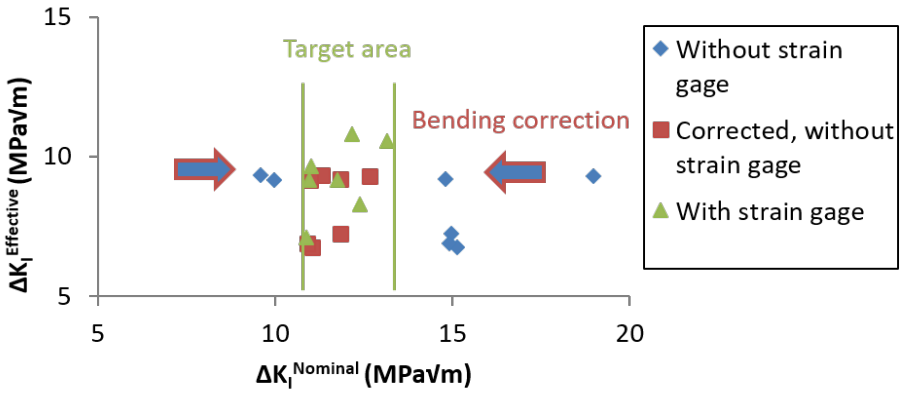

Figure 6.14: $\Delta K_I^{nominal}$ - $\Delta K_I^{effective}$ curve during precracking.

A corrective axial load was added to the experiments without a strain gage to shift the corresponding data points into the scatter-band of tests mounted with a strain gage (figure 6.14). The corrective loads are given in table 6.3.

Table 6.3: Corrective axial loads.

Experiment $N°$	4	5	6	7	8	9
Corrective load (kN)	2	-2.5	-3	-5	1	-3.5

6.3 Results and analysis

The amplitudes, number of cycles, and outcome in terms or coplanar propagation (mean value over the two sides) are described in tables 6.4, 6.5, 6.6 for the various loading types.

Table 6.4: Test conditions and resulting coplanar crack growth for **pseudo sequential** mixed mode I + II experiments. The loading range during experiments marked with a * were smaller during the first cycles, then increased to accelerate crack growth. Experiments marked with w were performed in water. The strain gage is used to avoid bending during screws tightening. The given number of cycles does not include the precracking stage. Values in parenthesis are corrected of screw tightening induced bending using the results of table 6.3

Exp. N°	Max / Min axial force (kN)	Torque (N.m)	Nominal $\frac{\Delta K_{II}}{\Delta K_I}$	Average coplanar growth (mm)	Total N of cycles at given load (at every load if $\neq$)	N of cycles of coplanar growth	Strain gage
9_a	10 / -5 (6.5/-8.5)	± 110	1.9 (2.9)	≈ 0.1	400 000	400 000	no
9_b *	10 / -5 (6.5/-8.5)	± 140	2.4 (3.7)	≈ 0.1	250 000 (1 050 000)	1 050 000	no
9 *	13 / 0 (9.5/-3.5)	± 90	1.2 (1.6)	>4.3	240 000 (1 640 000)	1 640 000	no
8	10/0 (11/1)	± 90	1.6 (1.6)	>4	75 000	70 000	no
19	10/0	± 90	1.6	>6	51 000	51 000	yes
18 w	10/0	± 90	1.6	>6	51 000	51 000	yes
4	7/0 (9/2)	± 110	2.7 (2.7)	1	235 000	180 000	no
7 *	12/5 (7/0)	± 110	2.7 (2.7)	0.6	110 000 (630 000)	600 000	no
5	10/0 (7.5/-2.5)	± 150	2.6 (3.5)	0.4	40 000	15 000	no
6	10/-5 (7/-8)	± 150	2.6 (3.7)	3.8	133 000	128 000	no
11	11/0	± 160	2.5	0.6	6 000	3 000	yes
10	11/-5	± 160	2.5	4.5	23 000	20 000	yes

Table 6.5: Test conditions and resulting coplanar crack growth for **90 ° out-of-phase** mixed mode I + II experiments. The strain gage is used to avoid bending during screws tightening. The given number of cycles does not include the precracking stage.

Exp. N°	Max / Min axial force (kN)	Torque (N.m)	Nominal $\frac{\Delta K_{II}}{\Delta K_I}$	Average coplanar growth (mm)	Total N of cycles	N of cycles of coplanar growth	Strain gage
12	11/-5	± 160	2.5	0.4	4000	500	yes
13	11/-5	± 110	1.7	0.6	23000	2000	yes
14	11/-5	± 70	1.1	0.3	105000	5000	yes

Table 6.6: Test conditions and resulting coplanar crack growth for **sequential** mixed mode I + II experiments on **tilted precracks**. The strain gage is used to avoid bending during screws tightening. The given number of cycles does not include the precracking stage.

Exp. N°	Max / Min axial force (kN)	Torque (N.m)	Nominal $\frac{\Delta K_{II}}{\Delta K_I}$	Average coplanar growth (mm)	Total N of cycles	N of cycles of coplanar growth	Strain gage
16	10/0	45/-145	1.6	0.4	136000	30000	yes
17	10/0	80/-160	2.1	0.3	44500	5000	yes

6.3.1 Crack paths

Extent of coplanar growth

The crack paths for the various non proportional mixed mode I + II experiments are reported in this section. Tables 6.4, 6.5, and 6.6 give the extent of coplanar growth before bifurcation for pseudo-sequential loading, 90° out-of-phase loading and pseudo-sequential loading on tilted precraks, respectively, while fig 6.15 to 6.29 show the crack paths on the outer surface of the tubes.

Most of the samples were broken open with the testing machine right after the experiment, and were then reassembled with more or less success to capture images, resulting in apparently huge crack opening. Some other samples were broken open after capturing images, using liquid nitrogen induced brittle impact fracture.

For sequential experiments without compression, the crack bifurcated after a short coplanar growth when $\Delta K_{II}^{nom}/\Delta K_{I}^{nom} > 2$, and grew coplanar when this ratio was below 2, as observed by [Wong et al., 1996]. However, when compression was added while shearing, a long coplanar growth was obtained even though $\Delta K_{II}^{nom}/\Delta K_{I}^{nom} > 2$. Experiments with the same shear loading ranges, but with or without compression while shearing (tests 5 & 6 and 10 & 11) led to different crack paths: compression substantially extended coplanar growth (3.8 mm for test $N°5$ with compression, instead of 0.4 mm for test $N°6$ without, 4.5 mm for test $N°10$ with compression, instead of 0.6 mm for test $N°11$ without). This result will be analyzed below, based on the effective mode-mixity ratios.

Experiment $N°18$, which is similar to experiment $N°19$, except that it was performed in water, led to similar crack path and growth rate (see appendix D), meaning that water did not increased the crack growth rate due to corrosion or entrapped water or a reduction of friction between the crack faces (which would increase ΔK_{II}^{eff}).

90 ° out-of-phase loadings led to much shorter coplanar growth than sequential ones, for similar loading ranges (only 0.4 mm for 90° out of-phase test $N°12$, as compared to 4.5 mm for pseudo sequential test $N°10$). The shape of the nominal loading path has thus a large influence on the crack path, and the ranges of the nominal SIFs are not sufficient to describe it.

The sequential tests run on tilted cracks -supposed to be more representative of squat-type cracks- led to bifurcation after a short growth in the precrack direction. This suggests that the computed loading paths might not perfectly mimic the real ones (inaccurate modeling of residual stresses in the computations?), which induce long coplanar growth.

Bifurcation

For the pseudo sequential loadings (figures 6.15 to 6.24), when bifurcation occurred, it occurred on both sides of the hole (except on the left side for experiment $N°6$ due to the shielding effect of a 45° branch initiated from the hole). On each side, two symmetric branches were usually formed from the same crack tip position, except for:

- Experiment $N°4$ (figure 6.15), on the right handside: a downward branch appeared, in competition with continued coplanar growth. This coplanar crack bifurcated upward later on.
- Experiment $N°6$ (figure 6.17), on the right handside: upward (a) & downward (b) branches appeared, in competition with continued coplanar growth (c). This coplanar crack bifurcated downwards (d) later on, with an attempt to branch back towards a coplanar direction (e). It seems that branches (a) & (d) "won" the kinetic competition, and continued growing while shielding the other branches.
- Experiment $N°7$ (figure 6.18), on the left handside: a double bifurcation (a), with the upward branch bifurcating back towards a coplanar direction (b). Along this coplanar branch, an aborted branch formed (c),

followed by a double bifurcation (d).

- Experiment $N°10$ (figure 6.21), on the right handside: an upward branch appeared (a), in competition with continued coplanar growth (b). A downward branch (c) appeared, at 90°, which then progressively kinked at $\approx 60°$. The coplanar crack (b) bifurcated upward and downward later on, at 90°. It seems that branches (a) & (c) "won" the kinetic competition, and continued growing while shielding the other branches. The long 90° bottom branch corresponds to liquid nitrogen-induced brittle impact fracture.

These bifurcation occurred during experiments with a high level of compression while shearing (induced either by the machine axial load, or some bending of the sample due to asymmetric screw tightening). This type of branching is very similar to those observed by Jessop [Jessop et al., 2016] using X-ray tomography on squat-type crack taken from the field (see figure 2.5), and to those observed during mixed mode II & III experiments (figures 5.8).

For the 90 ° out-of-phase experiments (see figures 6.25 to 6.27), when bifurcation occurred, two symmetric branches were formed on each side, one being faster than the other. The faster branches on each side had the same orientation and opened simultaneously.

During sequential experiments on tilted precracks (see figures 6.28, 6.29), the cracks bifurcated approximately to the horizontal direction (sometimes a bit tilted towards their initial direction), and continued in this direction.

The bifurcation angles, relative to the precrack direction, were measured on the outer surface using an optical microscope, and are reported in table 6.7. The branches considered for these measurements were of a few hundreds of micrometers long. Measurements were also made on the inner surface of some samples, and showed similar angles. These angles will be compared below to those predicted by various bifurcation criteria (section 6.3.5).

Table 6.7: Test conditions and resulting branch angles. Values in parenthesis correspond to smaller, slower branches.

Exp. N°	loading type	Max / Min axial force (kN)	Max / Min torque (N.m)	Nominal $\frac{\Delta K_{II}}{\Delta K_I}$	Left side bifurcation angles (°)	right side bifurcation angles (°)
4	Sequential	7/0	± 110	2.7	+59/-63	+57/-60
5	Sequential	10/0	± 150	2.6	+58/-52	+49/-63
6	Sequential	10/-5	± 150	2.6	0	+59/-62
7	Sequential*	12/5	± 110	1.6	+50/-50	45-56
8	Sequential	10/0	± 90	1.6	0	0
9	Sequential*	13/0	± 90	1.2	0	0
10	Sequential	11/-5	± 160	2.5	+60/-35	from +60 to -90
11	Sequential	11/0	± 160	2.5	+50/-50	+55/-65
19	Sequential	10/0	± 90	1.6	0	0
18	Sequential w	10/0	± 90	1.6	0	0
12	90 ° out-of-phase	11/-5	± 16	2.5	-40/(+40)	-40/(+40)
13	90 ° out-of-phase	11/-5	± 110	1.7	-50/(+50)	-50/(+50)
14	90 ° out-of-phase	11/-5	± 70	1.1	+40/(-40)	+40/(-40)
16	Tilted sequential	10/0	45/-145	0.8	12	20
17	Tilted sequential	10/0	80/-160	1.4	20	20

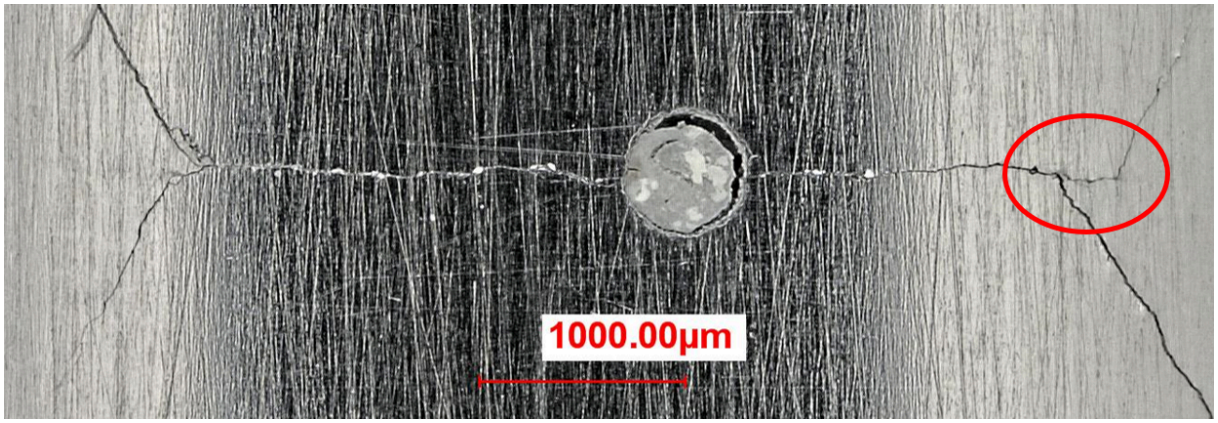

Figure 6.15: Crack path for pseudo sequential experiment $N°4$. $F = +7/0\ kN$, $C = \pm 110\ Nm$.

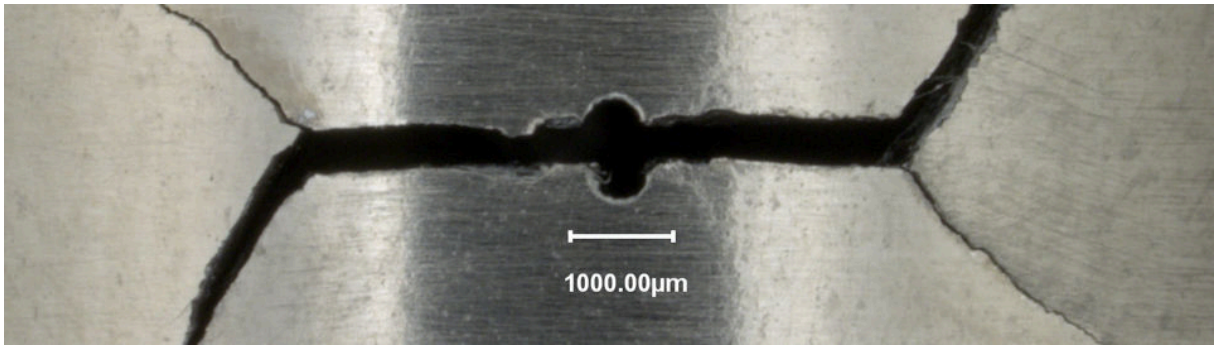

Figure 6.16: Crack path for pseudo sequential experiment $N°5$. $F = +10/0\ kN$, $C = \pm 150\ Nm$.

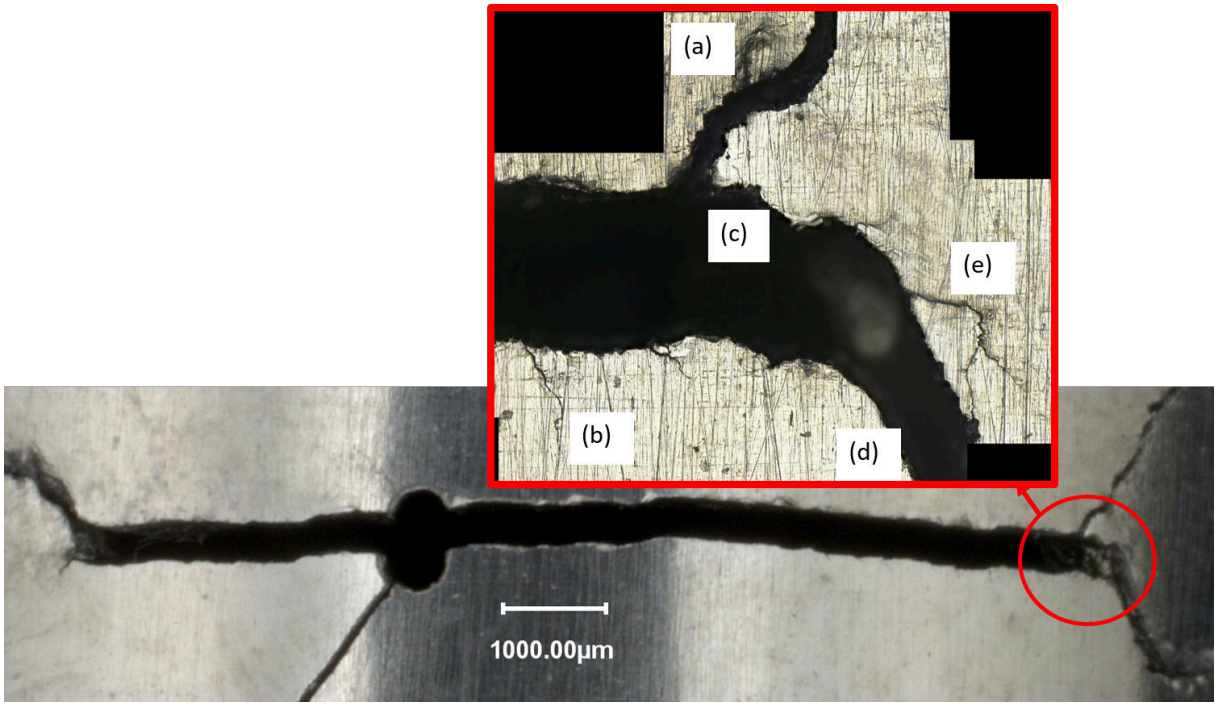

Figure 6.17: Crack path for pseudo sequential experiment $N°6$. $F = +10/-5\ kN$, $C = \pm 150\ Nm$.

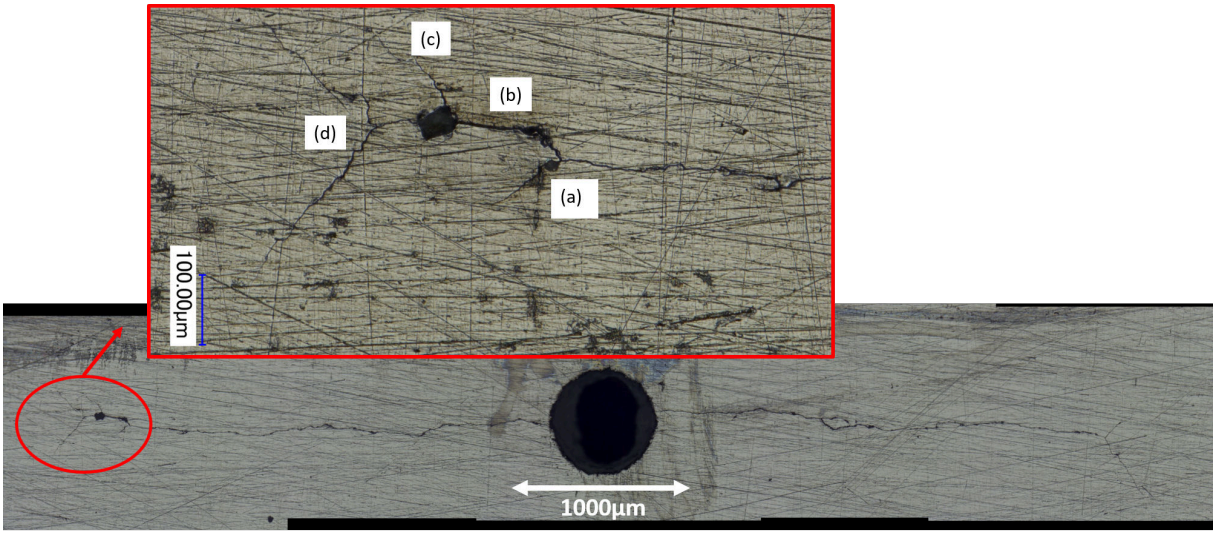

Figure 6.18: Crack path for pseudo sequential experiment $N°7$. $F = +12/+5\ kN$, $C = \pm 110\ Nm$.

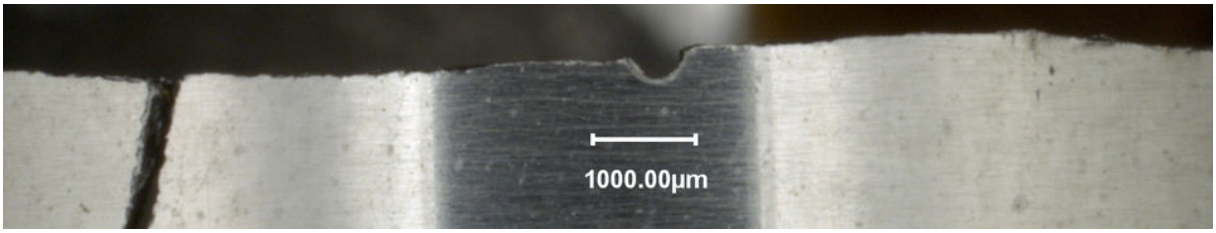

Figure 6.19: Crack path for pseudo sequential experiment $N°8$. $F = +10/0\ kN$, $C = \pm 90\ Nm$. Bifurcation due to a torque overload after a power shutdown.

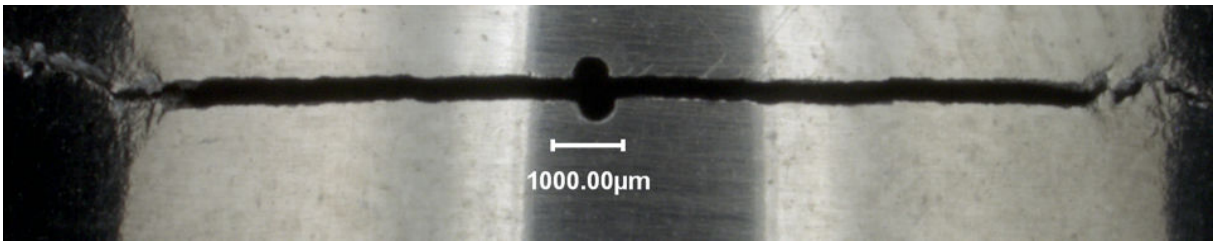

Figure 6.20: Crack path for pseudo sequential experiment $N°9$. $F = +13/0\ kN$, $C = \pm 90\ Nm$.

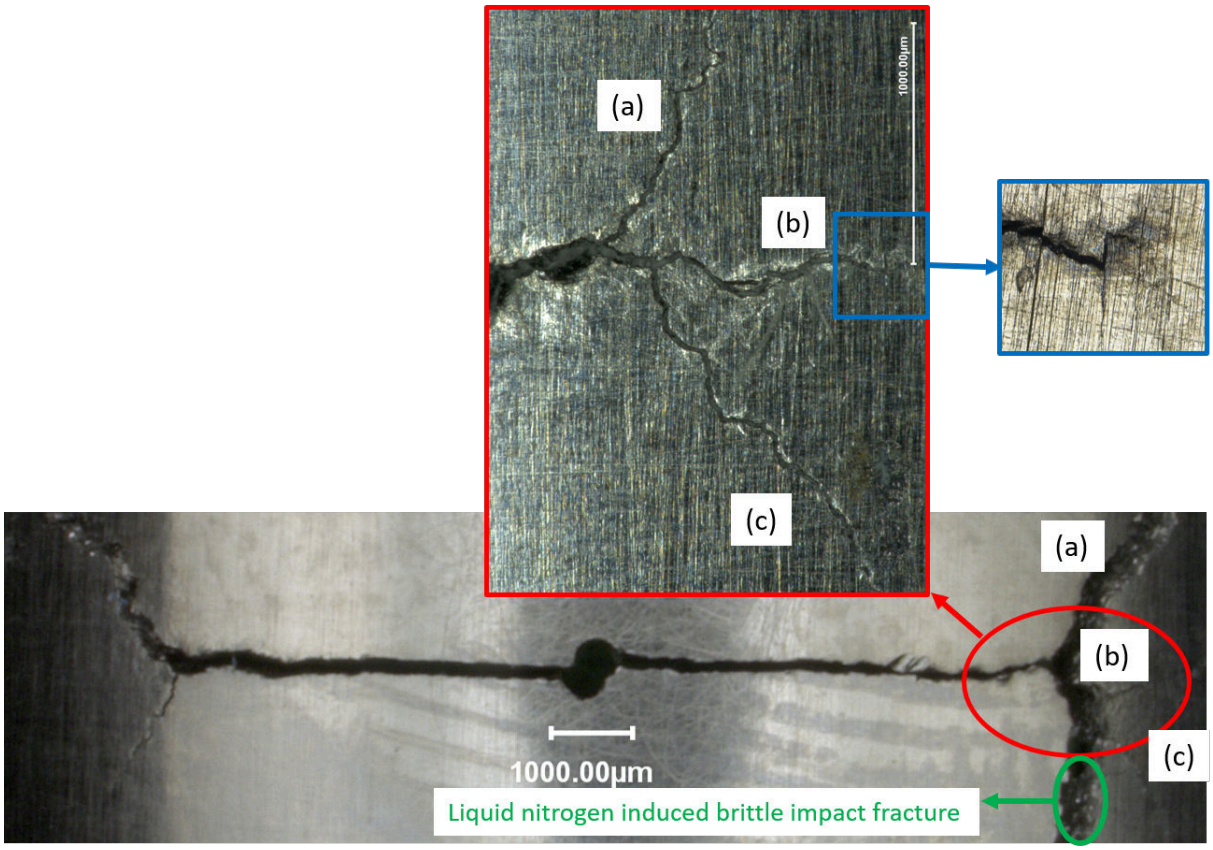

Figure 6.21: Crack path for pseudo sequential experiment $N°10$. $F = +11/-5\ kN$, $C = \pm 160\ Nm$.

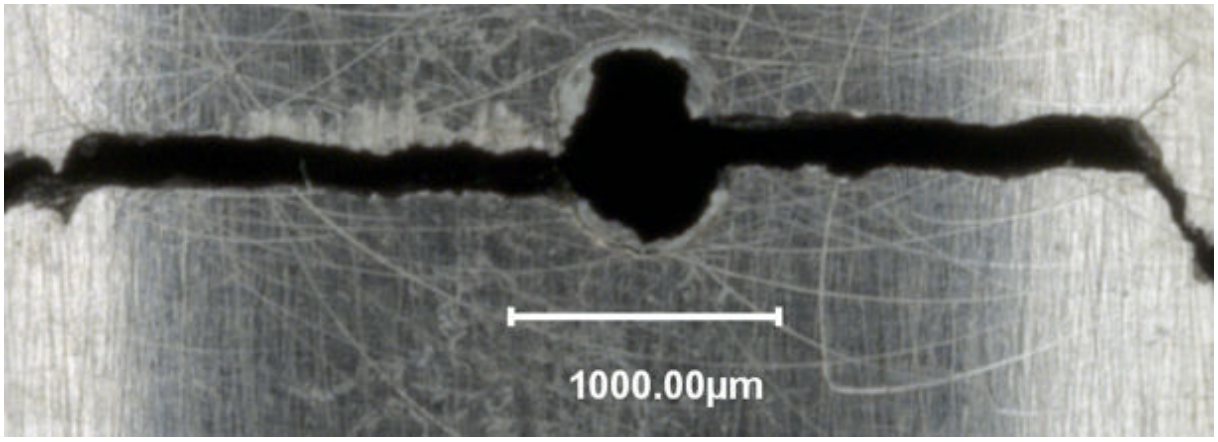

Figure 6.22: Crack path for pseudo sequential experiment $N°11$. $F = +11/0\ kN$, $C = \pm 160\ Nm$.

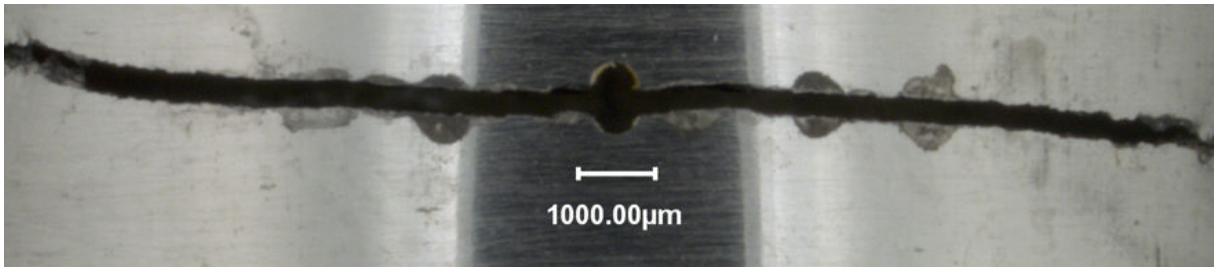

Figure 6.23: Crack path for pseudo sequential experiment $N°18$. $F = +10/0\ kN$, $C = \pm 90\ Nm$. This experiment was performed in water

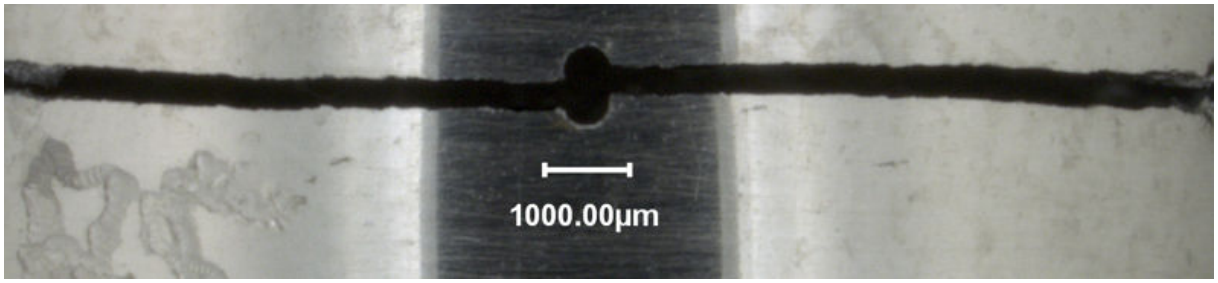

Figure 6.24: Crack path for pseudo sequential experiment $N°19$. $F = +10/0\ kN$, $C = \pm 90\ Nm$.

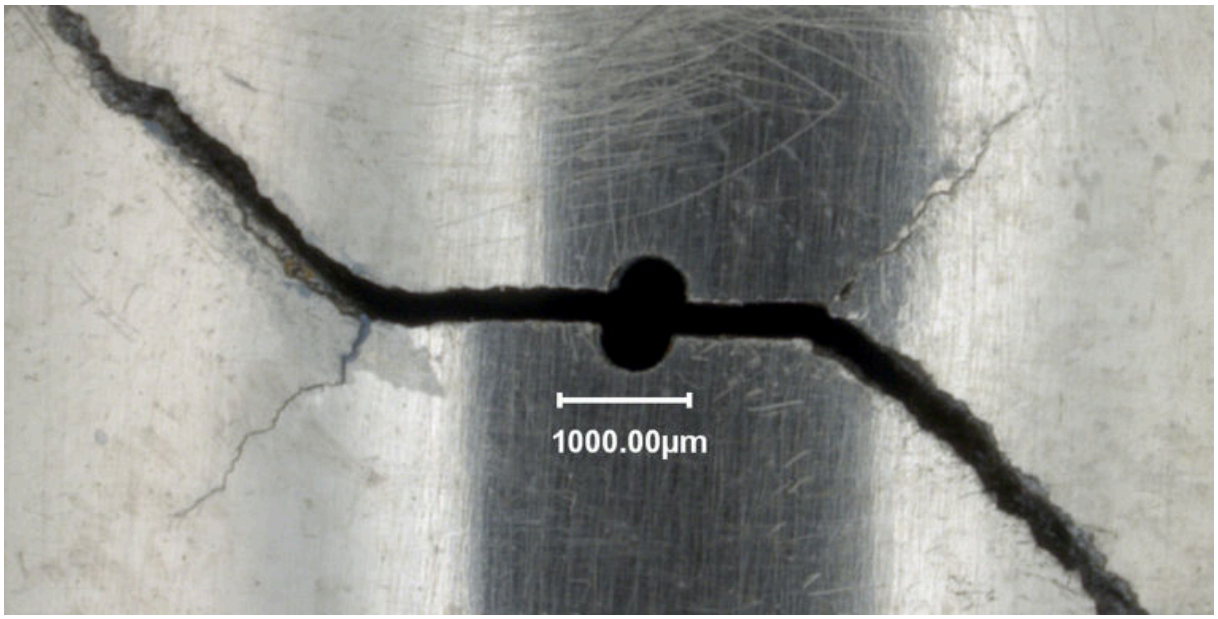

Figure 6.25: Crack path for pseudo 90 ° out-of-phase experiment $N°12$. $F = +11/-5\ kN$, $C = \pm 160\ Nm$.

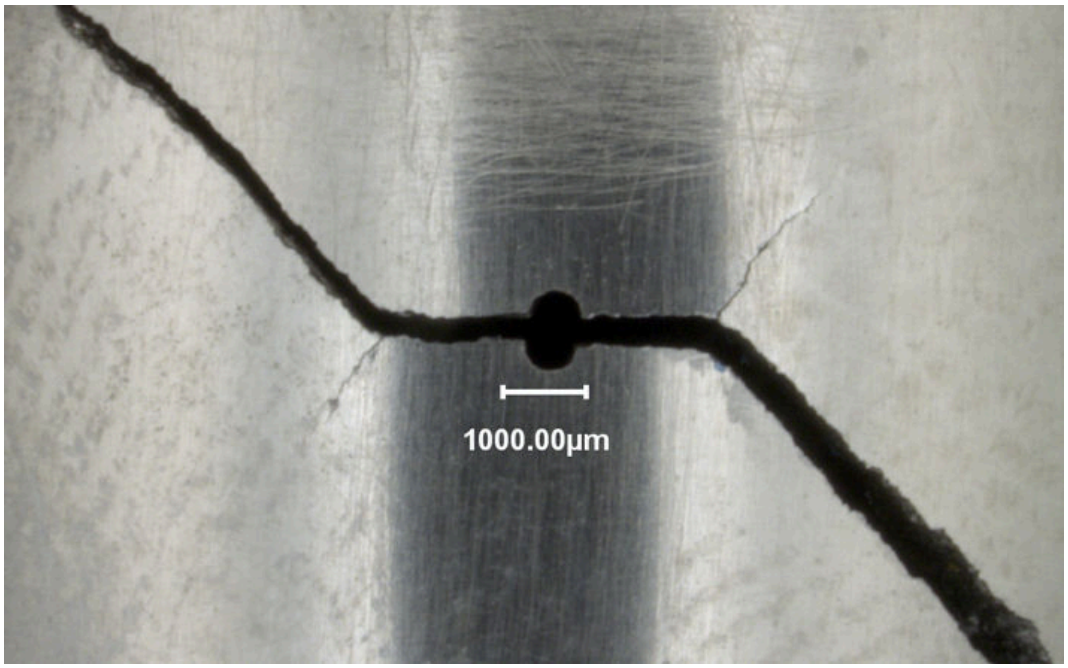

Figure 6.26: Crack path for 90 ° out-of-phase experiment $N°13$. $F = +11/-5\ kN$, $C = \pm 110\ Nm$.

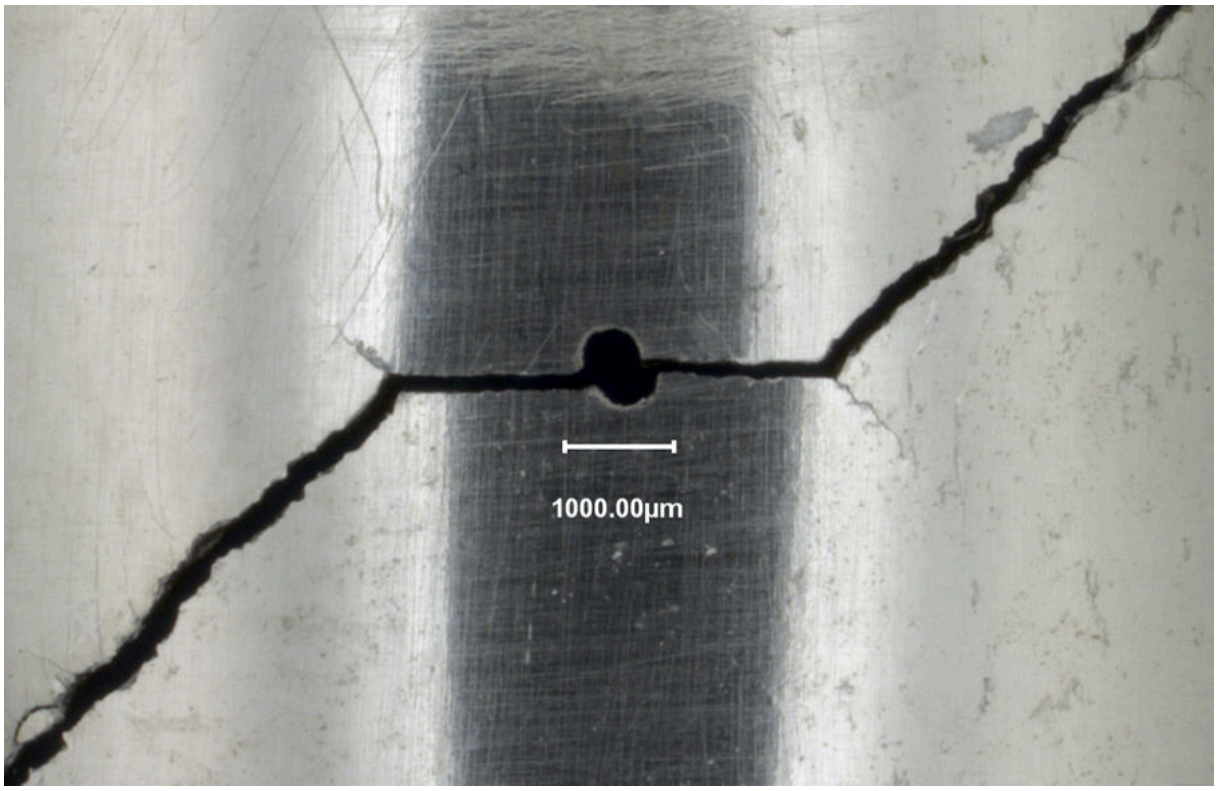

Figure 6.27: Crack path for 90 ° out-of-phase experiment $N°14$. $F = +11/-5\ kN$, $C = \pm 70\ Nm$.

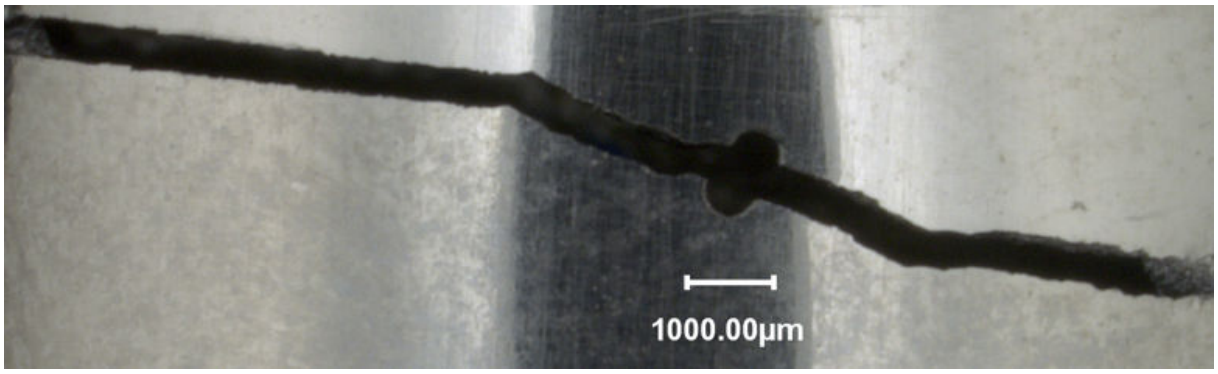

Figure 6.28: Crack path for sequential experiment $N°16$ on a tilted precrack. $F = +10/0\ kN$, $C = +45/-145$ Nm.

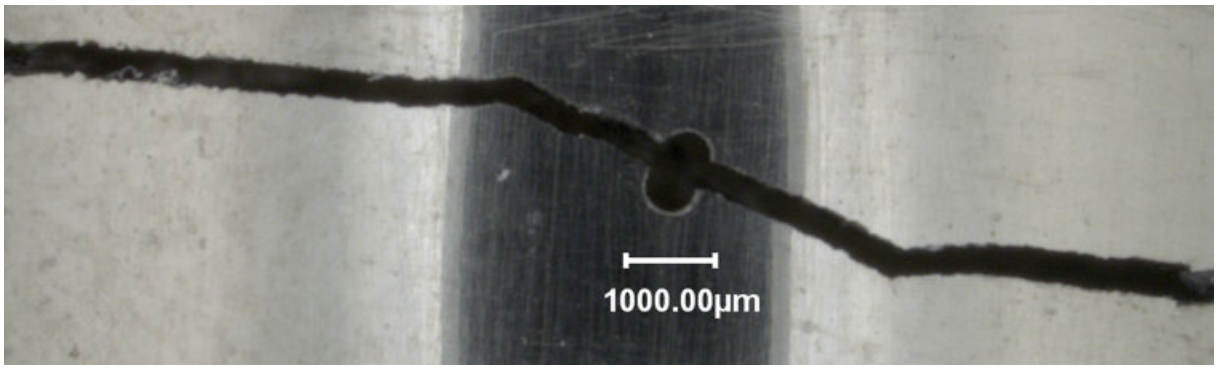

Figure 6.29: Crack path for sequential experiment $N°17$ on a tilted precrack. $F = +10/0\ kN$, $C = +80/-160$ Nm.

6.3.2 Effective loading paths

The effective and nominal loading paths during the 2000^{th} cycle of sequential experiments $N°10$ & 11, for which the crack lengths ($\approx 1.85\ mm$), shear loading range ($\pm 160\ Nm$) and peak tensile load ($11\ kN$) were the same, but F_{min} was -5 kN for test $N°10$, while it was 0 for test $N°10$, are plotted on figure 6.30a. The effective loading path are still approximately sequential in both cases, with zero or slightly negative K_I during compression. The U_I ratio, defied as:

$$U_I = \Delta K_I^{eff} / \Delta K_I^{nom} = \frac{\Delta K_I^{eff}}{K_{I,\,max}^{nom} - min(K_I^{nom}(t); 0)} \tag{6.9}$$

is smaller for $N°11$ without compression ($U_I = 0.75$) than for test $N°10$ ($U_I = 0.93$), which might be due to the enhanced asperities-induced closure associated with the higher ΔK_{II}^{eff} for test $N°11$, or due to more pronounced wear in presence of compression during the mode II cycle (test $N°10$) leading to a reduction of asperities-induced closure. As expected, the dilatancy (asperity induced) $\Delta K_I^{dilatancy}$ is higher without compression (higher $\Delta K_{II}^{effective}$), but the ratio $\Delta K_I^{dilatancy} / \Delta K_{II}^{effective}$ is similar (8 % for test $N°11$ and 7 % for test $N°10$), suggesting that the asperities profile is similar. Those values are slightly smaller than those measured during mixed mode II & III experiments (8 to 27%) and *in situ* SEM experiments ($\approx 16\%$). This difference can be due to the different setup rigidity.

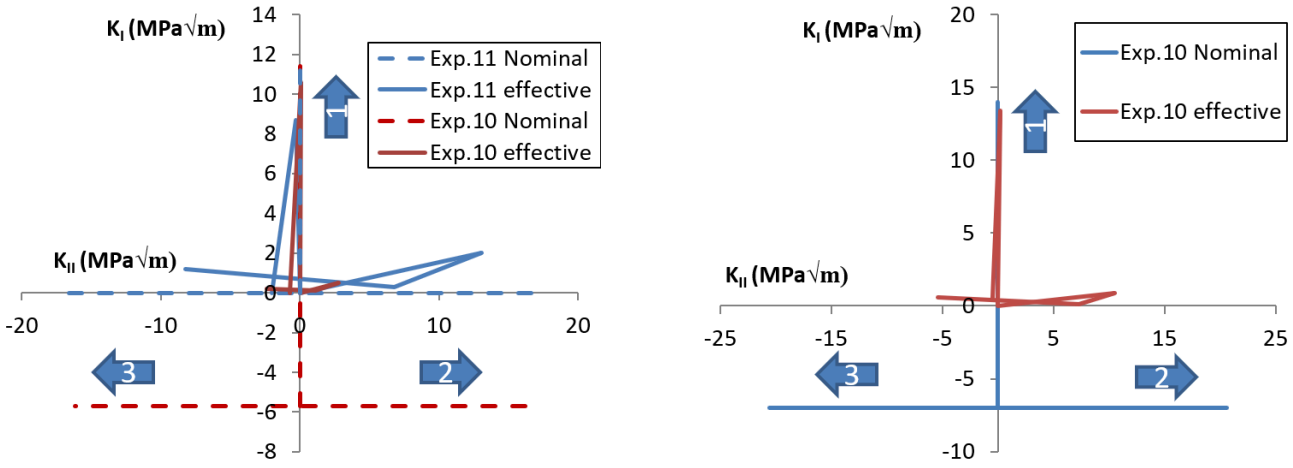

Figure 6.30: Nominal and effective loading paths for sequential experiment $N°10\&11$ ($F = +11/-5$ & $+11/0\ kN$, $C = \pm 160\ Nm$), a) at cycle 2000 for both experiments (similar crack lengths), and b) test $N°10$ at cycle 11000.

The U_{II} ratio is much smaller for test $N°10$ ($U_{II} = 0.16$) than for test $N°11$ ($U_{II} = 0.64$), due to compression-induced friction during the former. In both cases, the mode II load ratio is different from the nominal one ($R_{II}^{effective} = -0.86$ and -0.52 respectively, while $R_{II}^{nominal} = -1$). This change in the load ratio can be due to crack tip plasticity or asymmetric wear, with a higher K_{II}^{eff} in the direction of the first shear load. For those two tests, the higher ΔK_{II}^{eff}, the higher the asymmetry. In both cases, at the end of the mode II part of the cycle, the crack remains locked (at $K_{II}^{eff} = -0.7$ & $-2\ MPa\sqrt{m}$ respectively), and is then released as the crack is opened during the mode I part of the cycle.

The same graph is plotted at cycle 11 000 of experiment $N°10$ on figure 6.30b. The crack length is then $a = 2.6$ mm. The U_I ratio increased slightly relatively to cycle 2000 (from 0.93 to 0.96), while the dilatancy ΔK_I decreases ($\Delta K_I^{dilatancy} / \Delta K_{II}^{effective}$ from 7% to 5%), which remains negligible. The biggest change is on the U_{II} ratio, which

increased from 0.16 to 0.39 due to wear. The asymmetry in K_{II} increased, with a rise of $R_{II}^{effective}$ from -0.86 to -0.63: again, the higher ΔK_{II}^{eff}, the higher the asymmetry.

For sequential experiment $N°9$ ($F = +13/0\ kN$, $C = \pm 90\ Nm$), the apparent crack (seen by DIC) during the mode II part of the cycle was smaller than during the mode I part of the cycle, as showed on figure 6.31. It means that the crack tip remained locked during the mode II part of the cycle, and thus that $\Delta K_{II}^{eff} = 0$ and the effective loading was pure mode I. During experiment $N°9_a$ (same sample, different loading) performed at $F = 10/-5\ kN$ & $C = \pm 110\ Nm$, $\Delta K_{II}^{eff} \approx 0$, $\Delta K_{I}^{eff} \approx$ *confidential data* $MPa\sqrt{m}$ and $da/dn \approx 2 * 10^{-10}\ m/cycle$, which is similar to the $\approx 3 * 10^{-10}\ m/cycle$ obtained at $\Delta K_{I}^{eff} \approx$ *confidential data* $MPa\sqrt{m}$ during the mode I experiment at $R = -2$ ($\approx -100\ MPa$ compressive stress in both cases).

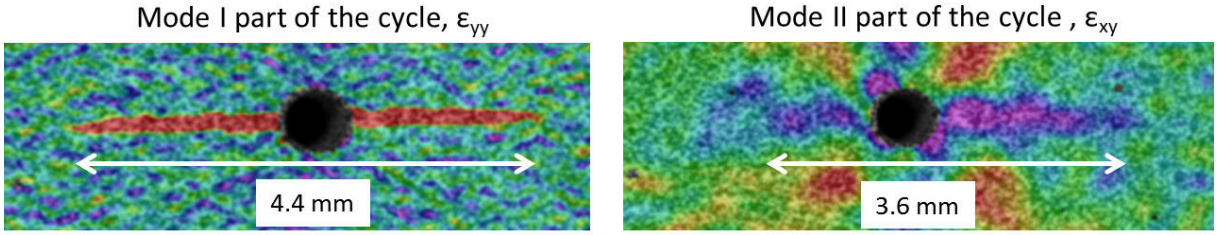

Figure 6.31: Sequential experiment $N°9$ ($F = +13/0\ kN$, $C = \pm 90\ Nm$): Smaller apparent crack during the mode II cycle than during the mode I cycle seen by DIC.

The nominal and effective loading paths during the 5000^{th} (before bifurcation) and 30000^{th} (after bifurcation) cycles of 90 ° out-of-phase experiment $N°14$ ($F = +11/-5\ kN$, $C = \pm 70\ Nm$) are plotted on figure 6.32. Before bifurcation, the effective loading path keeps an elliptic shape, with $U_I = 0.78$ in the same order of magnitude as in sequential experiments, and $U_{II} = 0.98$, much higher than during the sequential experiments due to the fact that the crack is opened while shearing. $R_{II}^{effective} = -1.04$, in this case, but it becomes smaller than -1 for higher shear ranges, as in the aforementioned sequential experiment. After bifurcation, at cycle 30 000, the loading path is rotated, and ΔK_{I}^{eff} is increased while ΔK_{II}^{eff} is reduced.

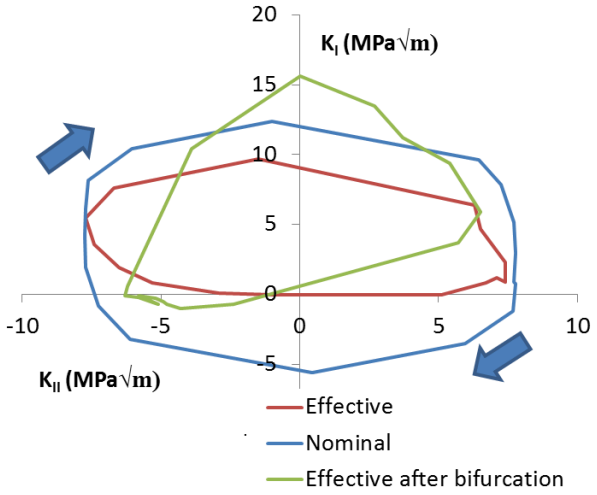

Figure 6.32: Loading paths for 90 ° out-of-phase experiment $N°14$ ($F = +11/-5\ kN$, $C = \pm 70\ Nm$), at cycle 5000 (before bifurcation) and 65000 (after bifurcation).

The nominal and effective loading paths during the 45000^{th} cycle of sequential experiment $N°16$ on a tilted crack

($F = +10/0\ kN$, $C = +45/-145\ Nm$) before bifurcation, at cycle 30000, and after bifurcation, at various cycles, are plotted on figure 6.33. Before bifurcation, the effective loading path is still tilted sequential, with $U_I = 0.64$ which is smaller than for the other loading paths, and $U_{II} = 0.42$. During the first loading segment, the effective loading path is aligned with the nominal one, while the opening is much smaller during the second segment, for which $K_I^{eff}/K_I^{nom} = 0.26$, and $K_{II}^{eff}/K_{II}^{nom} = 0.8$ which is higher than for sequential experiments because the crack is opened. During the third segment, the crack is closed & under compression, and $K_{II}^{eff}/K_{II}^{nom} = 0.08$, reduced by friction. Due to those effects, the mode II load ratio is changed from $R_{II}^{nom} = -3.2$ to $R_{II}^{eff} = -0.35$ when considering only parts 2&3 of the cycle ($R_{II}^{eff} = -0.8$ with part 1).

After bifurcation, the loading paths tends to become closer to a sequential path, but are still a bit tilted, in the opposite direction, and stay this way until the end of the experiments.

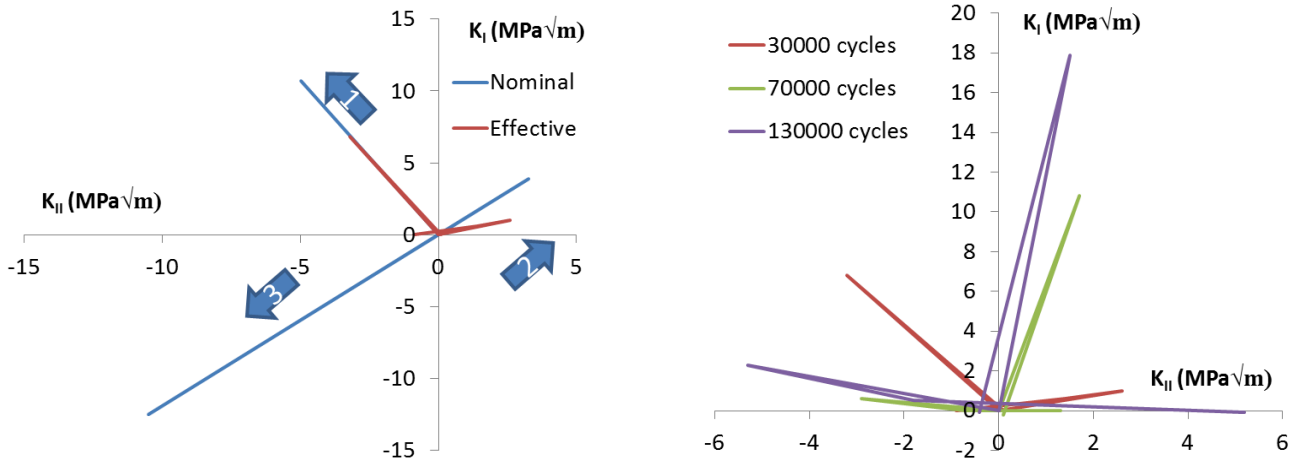

Figure 6.33: Loading paths for sequential experiment $N°16$ on a tilted precrack ($F = +10/0\ kN$, $C = +45/-145\ Nm$) before bifurcation, at cycle 30000 (left), and effective loading paths for various cycles (bifurcation occurred shortly after cycle 30000) (right).

The evolution of U_I as a function of the crack length for the pseudo sequential experiments is plotted on figures 6.34 & 6.35, with and without the bending correction respectively (experiment with a number over 10 included had a strain gage to avoid asymmetric screw tightening and resulting bending).

The correction clearly reduces the scatter in the data. For the experiments leading to bifurcation after a short coplanar growth (less than 1 mm), represented in line-made symbols, the U_I ratio deceases rapidly as the crack propagates, until bifurcation. Paradoxically, these tests ($N°4$, $N°5$, and $N°7$) correspond to mode I R ratios of 0, 0 and +0.42, respectively. For the experiments leading to long coplanar growth (3 to 7.5 mm) and ending with a bifurcation, among which two (tests $N°6$ and $N°10$) had mode I R ratios of -0.45 or -0.5 combined with a high shear range, this decrease in U_I before bifurcation is not present.

The experiments leading to long coplanar growth have a relatively stable or even slightly increasing $U_I = 0.8 \pm 0.2$ with bending correction (0.9 ± 0.1 for experiments with a strain gage), which is in the same order of magnitude as for mode I experiments on the SENT samples.

Experiments $N°10$ and $N°11$ have the same SIFs range (and a strain gage), but compression is added while shearing during the first one, and while both tests have the same initial U_I, its evolution is then very different: fast decrease for experiment $N°11$, and stable value for experiment $N°10$ (-5 kN compression while shearing). The same type difference seems to exist between experiments $N°5$ (no compression applied) & $N°6$ (-5 kN compression), but no strain gage was used so the results are less reliable. A compression-induced acceleration of crack face asperities

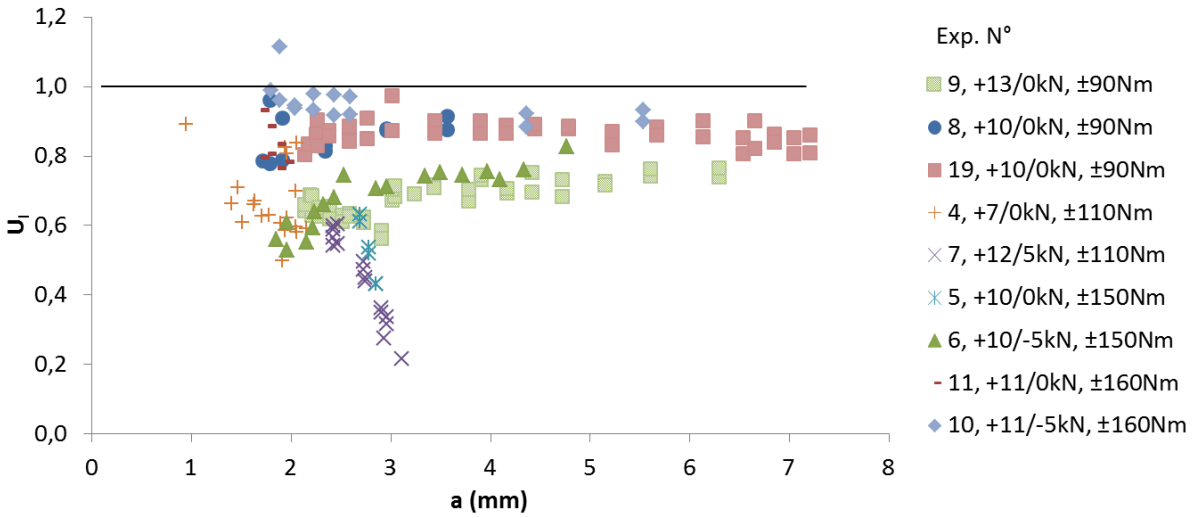

Figure 6.34: U_I as a function of the crack length for sequential experiments. Experiments leading to long coplanar growth are in full symbols, and the other in line-made symbols.

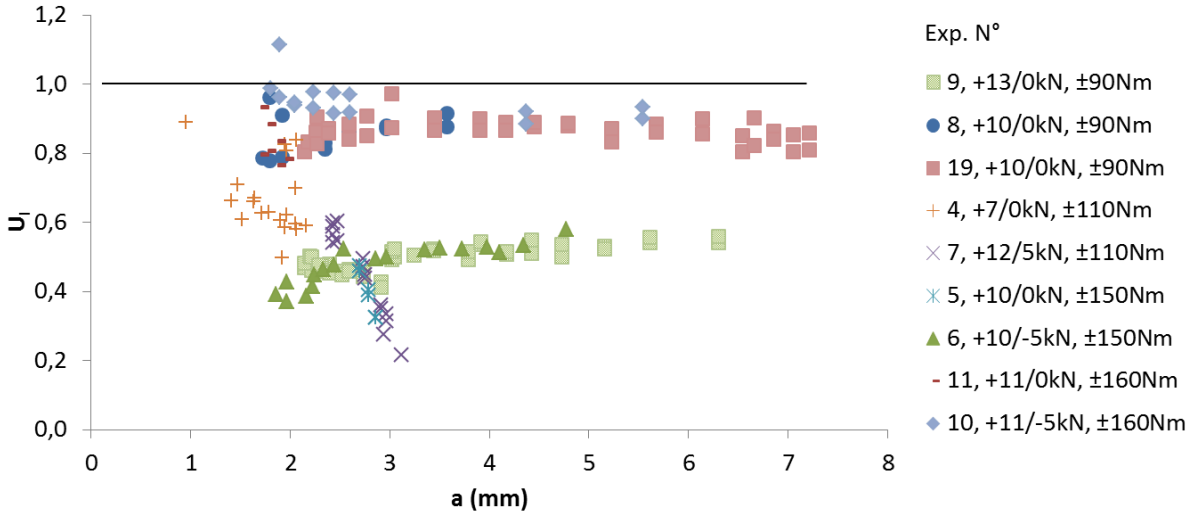

Figure 6.35: U_I as a function of the crack length for sequential experiments without bending correction. Experiments leading to long coplanar growth are in full symbols, and the other in line-made symbols.

wear might reduce asperities-induced closure effect and its enhancement by mode II loading.

An increase of roughness-induced closure with the shear singularity can be expected. However, U_I does not correlate with the effective mode mixity ratio $\Delta K_{II}^{effective}/\Delta K_I^{effective}$ for the sequential experiments, as shown on figure 6.36. The results may be different if shear is applied during the mode I part of the cycle.

For the sequential experiments giving rise to a long coplanar growth, and mounted with a strain gage to avoid bending, $\Delta K_I^{effective}$ can be predicted quite accurately as an affine function of ΔK_I^{nom}, with a slope of *confidential data* and a small offset close to *confidential data* $MPa\sqrt{m}$, as shown on figure 6.37. Those results are similar to those of pure mode I experiments, meaning that shear not did not induce any major increase roughness-induced closure during those experiments.

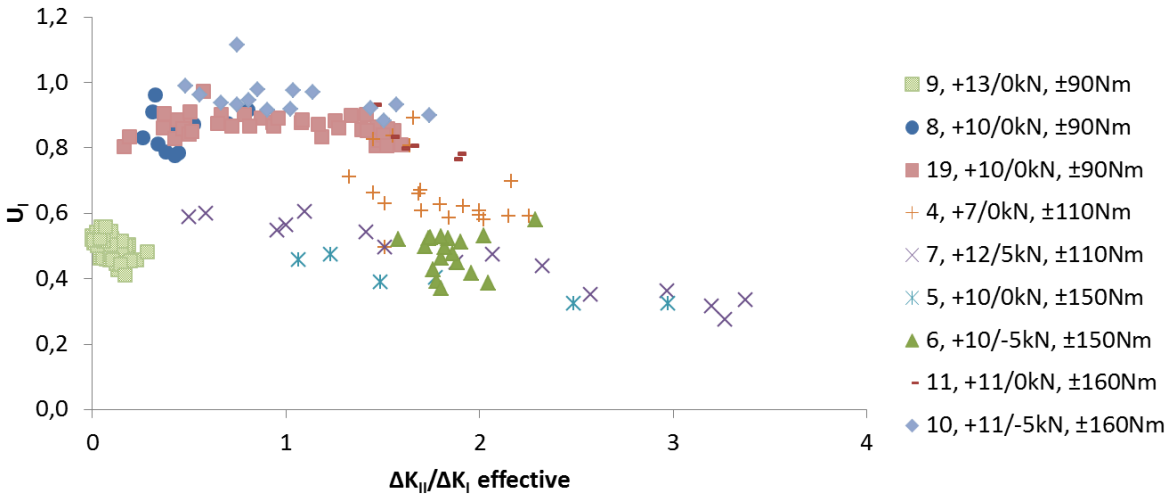

Figure 6.36: Evolution of U_I as a function of $\Delta K_{II}^{effective}/\Delta K_I^{effective}$ for sequential experiments, without bending correction.

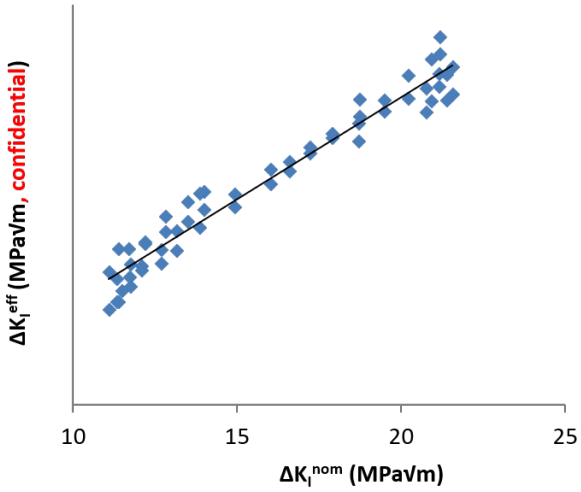

Figure 6.37: Evolution of $\Delta K_I^{effective}$ as a function of $\Delta K_I^{nominal}$ for long coplanar sequential experiments with a strain gage.

Figure 6.38 shows the evolution of the U_{II} ratio as a function of ΔK_{II}^{eff} for the pseudo sequential experiments. This ratio rises with ΔK_{II}^{eff} for all experiments, probably due to wear or because a large sliding displacement of rough crack surfaces wedges the crack open. U_{II} ranges from 0 to 0.5, which is lower than the ≈ 0.8 values obtained during mixed mode II & III experiments in predominant mode II, for which the loading ranges were higher (ΔK_{II}^{eff} from *confidential data* $MPa\sqrt{m}$). In addition, the roughness of a crack grown in pure mode II & III (for which the shear stress ahead of the tip peaks at 0°) might be smaller than that of a crack grown in sequential mode I + II (because the shear stress ahead of the tip during the mode I cycles peaks at ±70°). As expected, the datapoints of experiments $N°6$ & $N°10$, performed with compression while shearing, are a bit below the others, while those of experiments $N°4$ and $N°11$ (short coplanar growth) are a bit above. For experiments $N°19$ & $N°10$, for which the cracks grew over 7.2 and 5.5 mm, respectively, the U_{II} values are a bit uncertain due to the difficulties to estimate $\Delta K_{II}^{nominal}$ for a crack longer than 4 mm (see section 6.2.3). At the same ΔK_{II}^{eff}, a higher U_{II} was expected for experiments run during a higher number of cycles (and longer coplanar growth), due to wear, but is not observed.

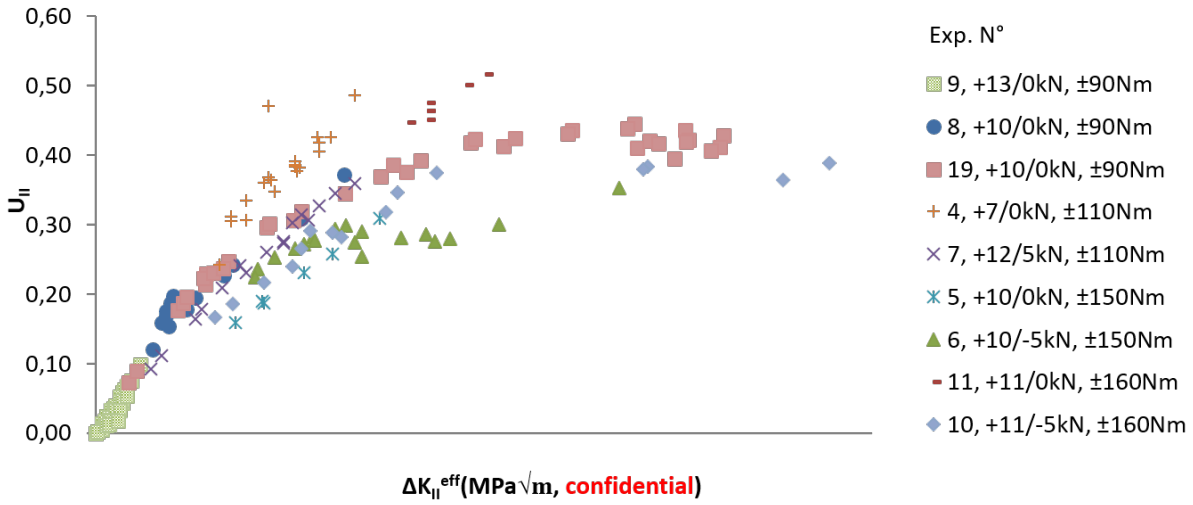

Figure 6.38: U_{II} as a function of $\Delta K_{II}^{effective}$ for sequential experiments. Experiments leading to long coplanar growth are in full symbols, and the others in line-made symbols.

As mentioned above, for pseudo sequential experiments, the U_I ratio decreases before bifurcation during short coplanar growth, while U_{II} increases due to wear. As a consequence, the ratio $\Delta K_{II}^{effective}/\Delta K_I^{effective}$ increases rapidly, as shown on figure 6.39. When the effective mode-mixity ratio exceeds a value around 2, the crack bifurcates (as indicated by circles). For long coplanar growths, the ratio increases slowly, until it eventually reaches ≈ 2 and the crack bifurcates (experiments $N°6$ & $N°10$). When this ratio stays below 2, the crack remains coplanar. Experiment $N°11$ & $N°10$ correspond to the same shear amplitude and peak tensile load, but with compression while shearing for the later. This compression leads to an initially smaller $\Delta K_{II}^{effective}/\Delta K_I^{effective}$ ratio, which also rises slower than for experiment $N°11$, leading to a longer coplanar growth.

Surprisingly, this ratio is initially smaller for test $N°5$ than for test $N°6$, although they had the same shear amplitude and peak tensile load, with compression while shearing during test $N°6$. This can be due to a longer precrack (2.6 mm) for test $N°5$ compared to 1.6 mm for test $N°$ 6. However, like for tests $N°10$ & $N°11$, this ratio increases slower for test $N°6$, with compression, than for test $N°5$, without, leading again to a longer coplanar growth.

The evolution of $\Delta K_{III}^{eff}/\Delta K_{II}^{eff}$ for experiments $N°10$ and 19 is plotted on figure 6.40 as a function of the crack length, and compared to the nominal ratio obtained by XFEM computations. As expected, the relative value of K_{III} increases with the crack length, but not as much as expected from the XFEM computations (maximum measured ratio of 0.35 versus 1 predicted). These differences could be due either to a change in the crack front shape, or to a poor estimation of ΔK_{III}^{eff} (due to an inaccurate out-of-plane displacement measurement by DIC, and a simplified method to estimate the mode III singularity). For cracks smaller than 4 mm, this ratio is below 0.2 and the influence of K_{III} can be neglected (especially in expressions of "equivalent" ΔK involving squared SIFs).

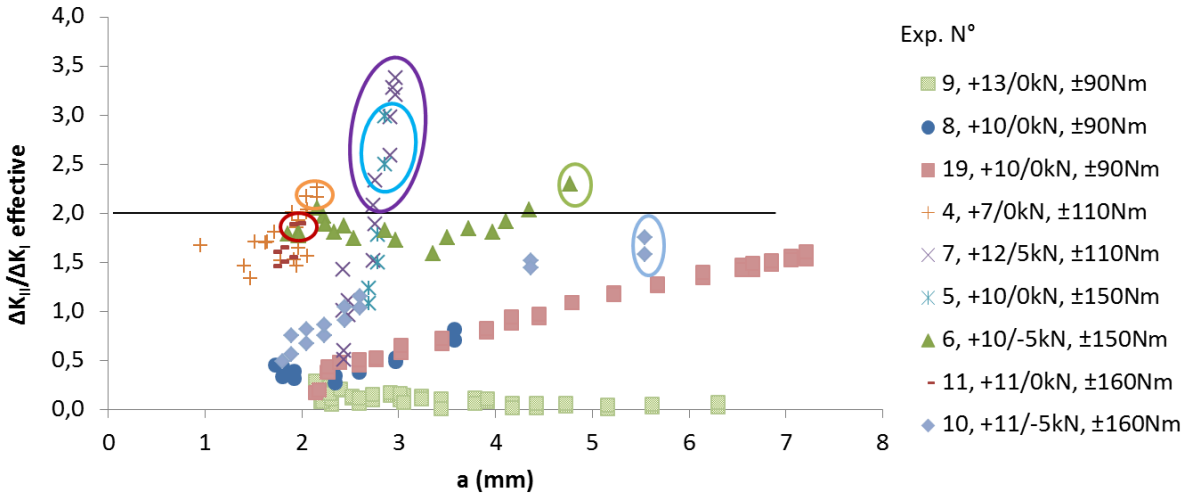

Figure 6.39: Evolution of $\Delta K_{II}^{effective}/\Delta K_{I}^{effective}$ as a function of the crack length. Bifurcations are marked by circles.

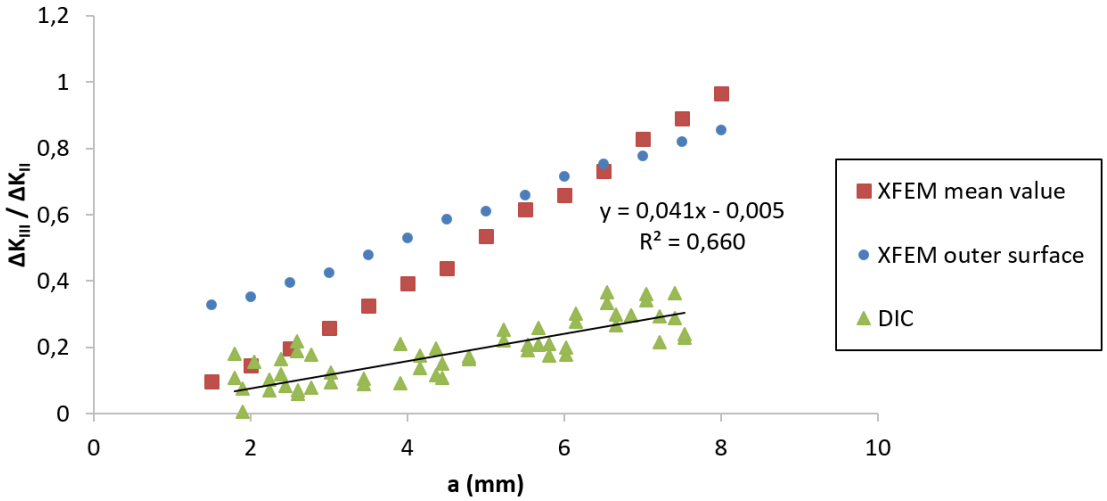

Figure 6.40: Evolution of $\Delta K_{III}/\Delta K_{II}$ as a function of the crack length, mean value along the front computed by XFEM, value on the outer surface computed by XFEM and value measure on the outer surface by DIC during experiments 10 and 19.

The evolution of $\Delta K_{II}^{effective}/\Delta K_{I}^{effective}$ is plotted on figure 6.41 for 90 ° out-of-phase and sequential experiments on tilted cracks. In those experiments, bifurcation did not correspond to any particular value of $\Delta K_{II}^{effective}/\Delta K_{I}^{effective}$. The mode mixity ratio is not sufficient to predict bifurcation for non-sequential experiments. Still, bifurcation leads to a decrease of this ratio, meaning that bifurcation tends to occur in a direction increasing the proportion of mode I relative to mode II.

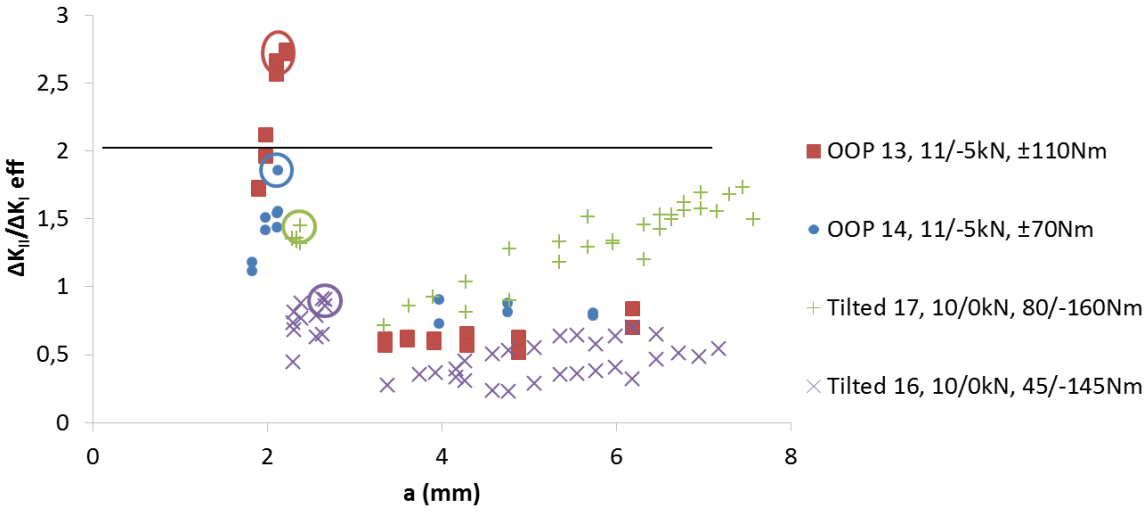

Figure 6.41: Evolution of $\Delta K_{II}^{effective}/\Delta K_{I}^{effective}$ as a function of the crack length for 90 ° out-of-phase (OOP) and sequential experiments on tilted precracks. Bifurcations are marked by circles.

6.3.3 Fracture surface analysis

The fracture surfaces of sequential experiment $N°9$, with lowest torque amplitude ($F = +13/0\ kN$, $C = \pm 90\ Nm$), are shown on figures 6.42,6.43 & 6.44.

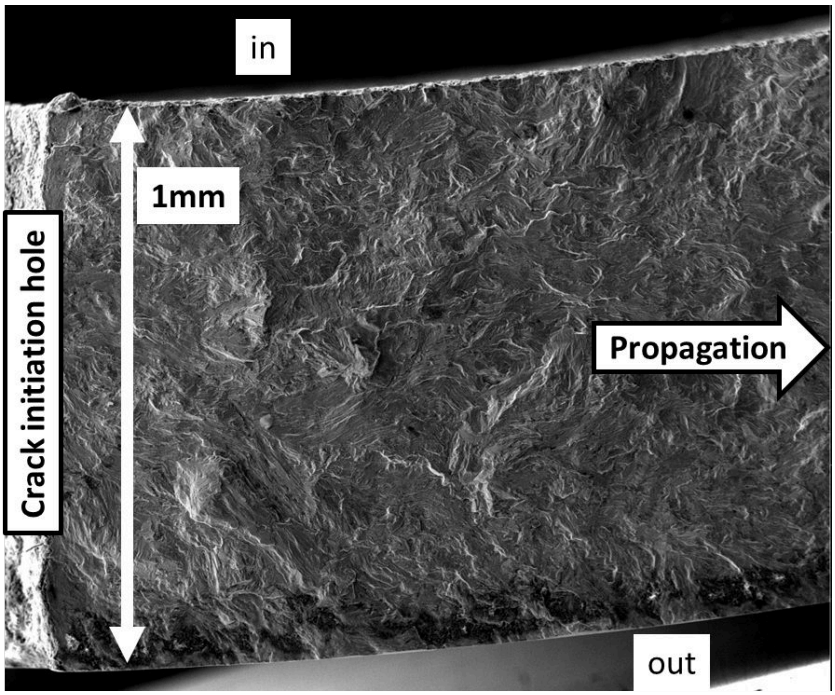

Figure 6.42: Fracture surface of sequential experiment $N°9$ ($F = +13/0\ kN$, $C = \pm 90\ Nm$) near the crack initiation hole. The scale is given by the 1 mm thickness of the samples.

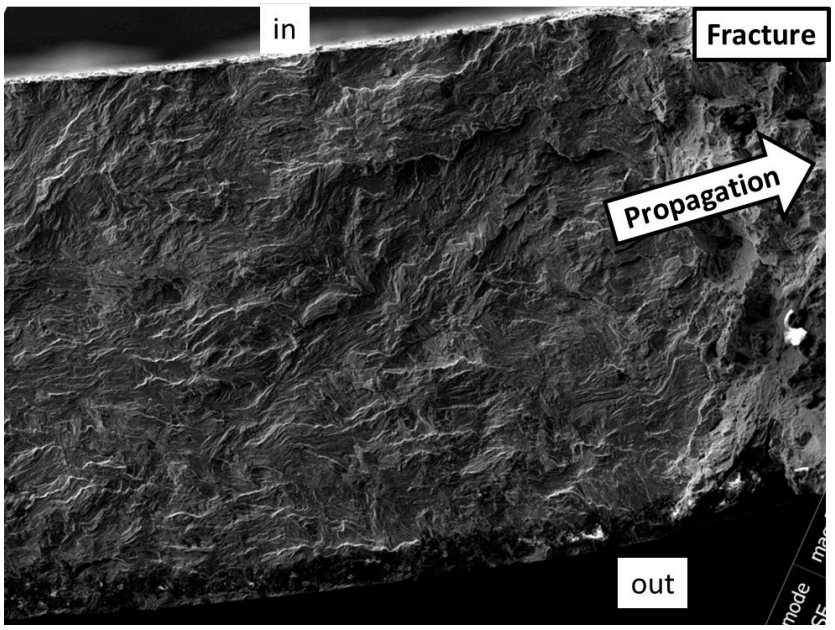

Figure 6.43: Fracture surface of sequential experiment $N°9$ ($F = +13/0\ kN$, $C = \pm 90\ Nm$) at the crack front.

Figure 6.44: Fracture surface of sequential experiment $N°9$ ($F = +13/0\ kN$, $C = \pm 90\ Nm$) obtained with an optical microscope.

The surface is not worn at all, in spite of a very high number of cycles ($1.64\ 10^6$) and a bending correction of -3.5 kN that should induce some compression during the shearing cycles. It actually looks similar to those observed in pure mode I, which is consistent with the fact that U_{II} was less than 0.1, and ΔK_{II}^{eff} stayed below 3 $MPa\sqrt{m}$ during the whole experiment (and $\Delta K_I^{eff}/\Delta K_{II}^{eff} < 0.28$). The crack front of the 6.3 mm-long crack is straight and normal to the inner and outer surfaces, this corresponding more or less to an iso K_I profile (as shown previously on figure 6.11). Most of the sequential experiments share a similar crack front shape and orientation.

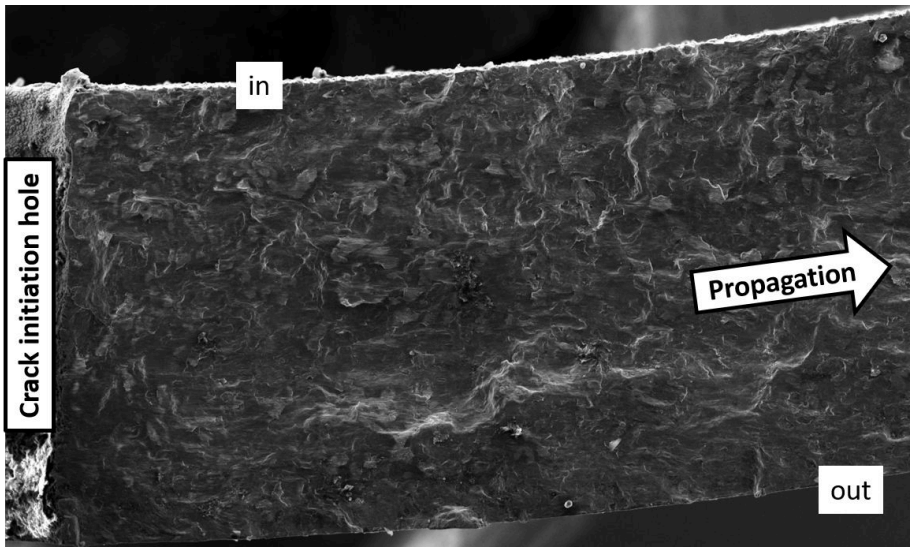

Figure 6.45: Fracture surface of sequential experiment $N°19$ ($F = +10/0\ kN$, $C = \pm 90\ Nm$) near the crack initiation hole.

For the same torque amplitude ($\pm 90\ Nm$, $10/0\ kN$) and in spite of a much smaller number of cycles (51 000) the fracture surface of test 19 for which U_{II} rose from 0.17 to 0.42 and ΔK_{II}^{eff} up to 28 $MPa\sqrt{m}$ during a long coplanar growth exhibits a gradient in wear (see figures 6.45 & 6.46): substantial near the center hole and progressively decreasing near the final crack front (the amplitude of the sliding displacements is larger near the hole ($[U_\theta] \propto \Delta K_{II}^{eff} * \sqrt{\text{distance to the tip}}$), as well as the number of wear cycles). Clusters of round, oxidized metal debris are present (see figure 6.47). Their formation in fatigue cracks grown in mode II was analysed in detail by [Smith and Smith, 1982]. Such debris, when they remain trapped inside the contact (which might become more frequent when static compression is applied while shearing), form what tribologists call a "third body layer" which separates the "first bodies" and tends to reduce their friction and to protect them from further wear. If, at

the contrary, these debris are ejected, wear becomes more severe. In this experiment, the effects of friction and asperities might be very dependent on the position along the crack.

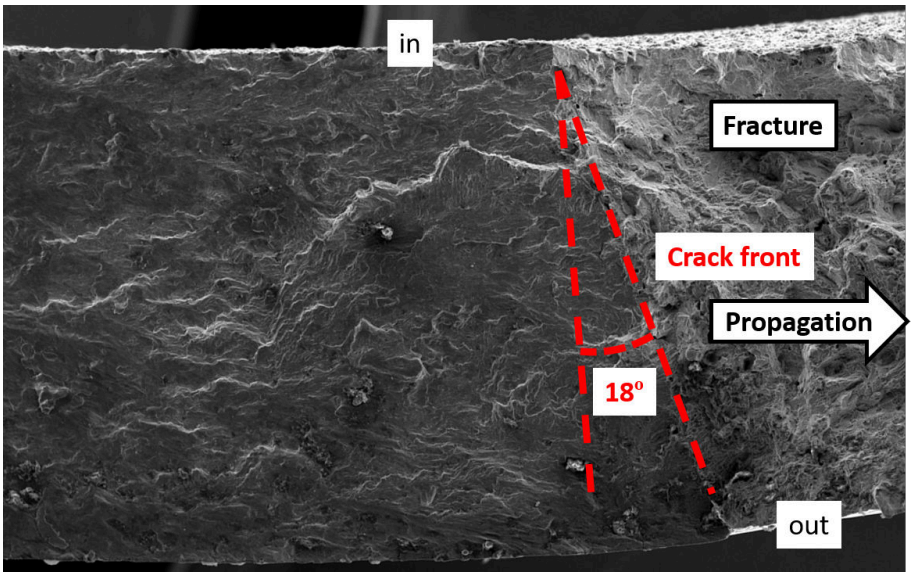

Figure 6.46: Fracture surface of sequential experiment $N°19$ ($F = +10/0\ kN$, $C = \pm 90\ Nm$) at the crack front.

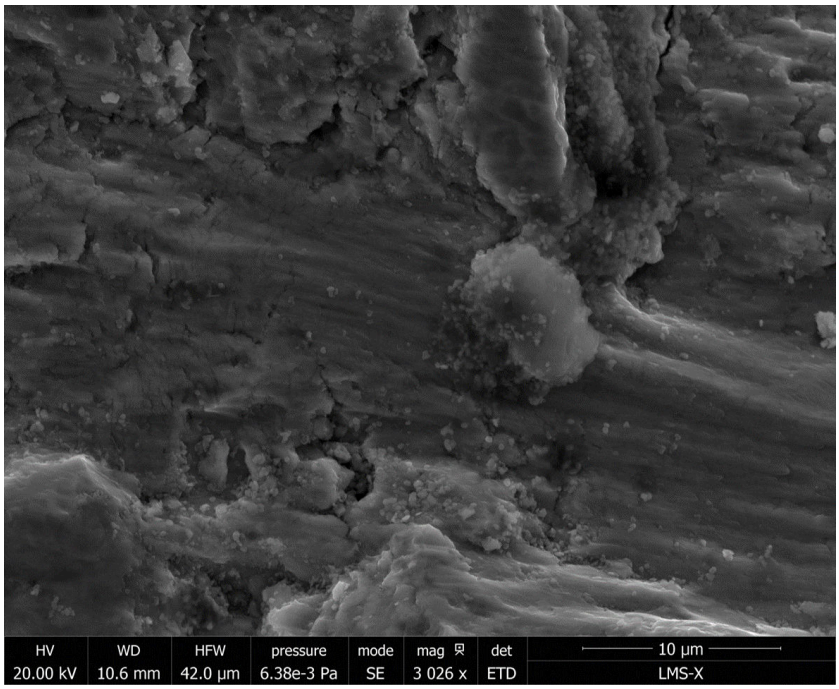

Figure 6.47: Oxidized metal debris, observed on the fracture surfaces of sequential experiment $N°19$ ($F = +10/0$ kN, $C = \pm 90\ Nm$).

The crack front is not normal to the inner and outer surfaces, but tilted by 18° towards the inner surface. For such crack front shape, the effective SIFs estimated using DIC and the FEM model supposing a crack front normal to the inner and outer surfaces might be wrong and should be used with caution in the analysis.

The evolution of the SIFs along such a front was computed using an XFEM model, and is plotted figure 6.48. This front inclination tends to make K_I slightly less uniform, but is slightly closer to an iso K_{II} & K_{III} contour, suggesting that both shear and opening SIFs drive the propagation.

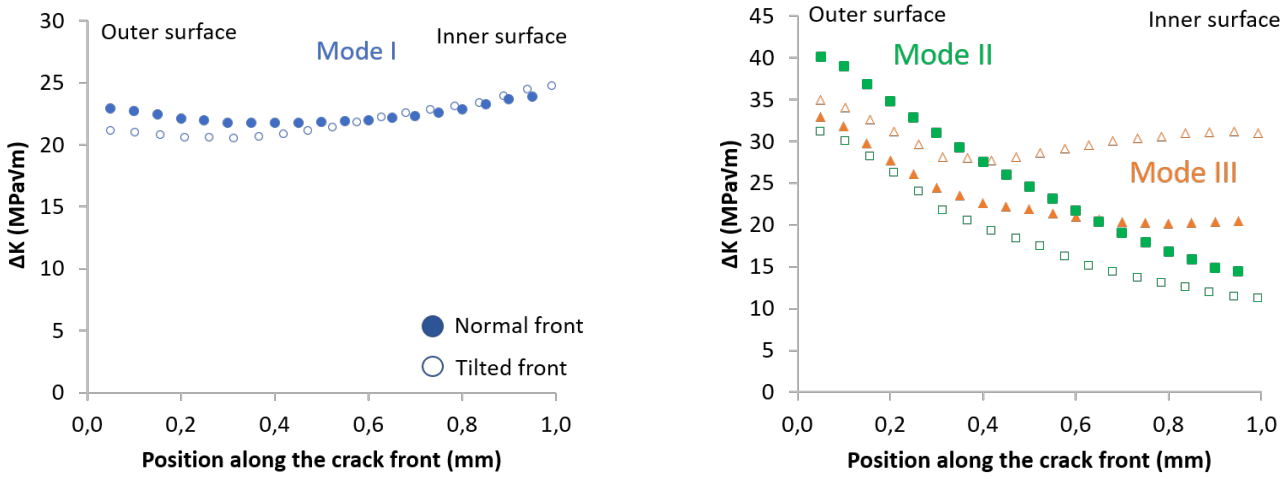

Figure 6.48: Evolution of the SIFs along the front for a straight front normal to the inner an outer surfaces (full symbols) and a straight front inclined by 18° (hollow symbols).

For an intermediate torque amplitude (test $N°4$, $\pm 110\ Nm$, $7/0\ kN$, 235 000 cycles, U_{II} larger than in most other cases and rising from 0.3 to 0.5 and ΔK_{II}^{eff} up to 14 $MPa\sqrt{m}$) the fracture surface is worn over its entire length and even more rounded debris are observed than in the previous case (fig. 6.49). At some places, these debris seem to be squeezed and compacted into a friable layer which flakes (fig. 6.50).

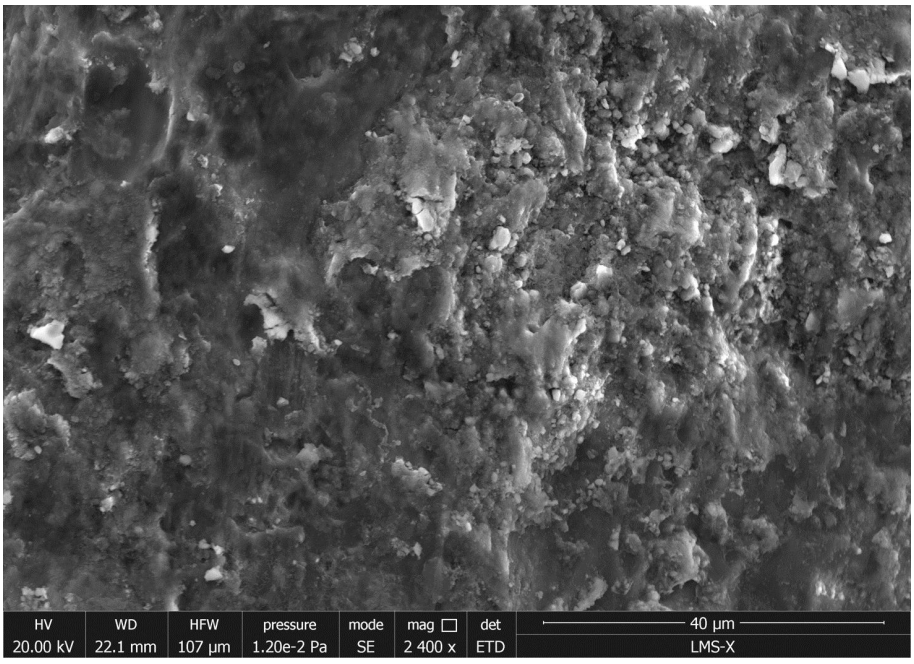

Figure 6.49: Rounded debris on the fracture surfaces of test $N°4$, $\pm 110\ Nm$, $7/0\ kN$.

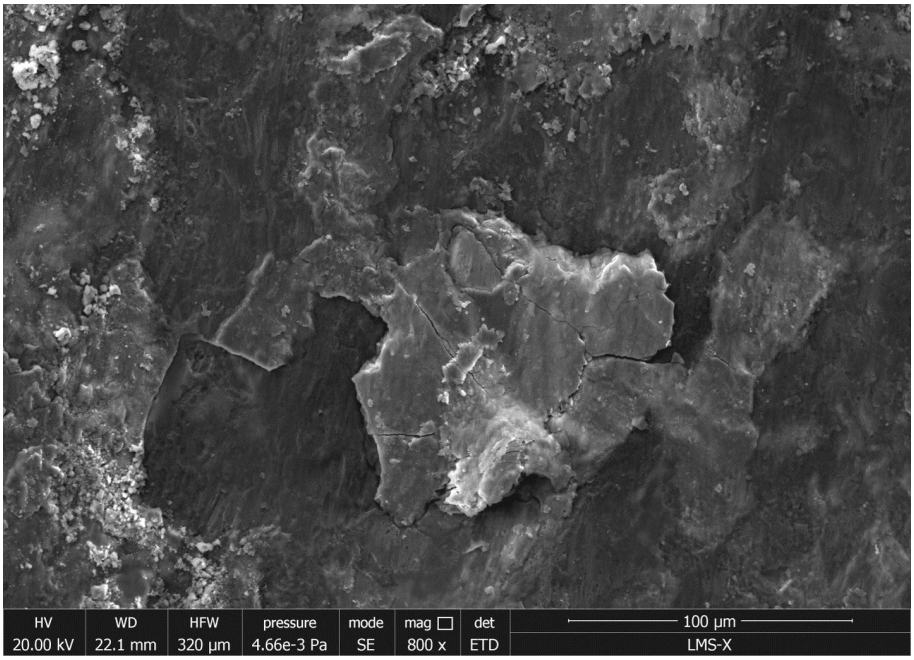

Figure 6.50: Squeezed and compacted debris on the fracture surfaces of test $N°4$, $\pm 110\ Nm$, $7/0\ kN$.

For the highest torque amplitude (test $N°11$, $\pm 160\ Nm$, $11/0\ kN$, U_{II} rising from 0.45 to 0.5, ΔK_{II}^{eff} rising up to 18 $MPa\sqrt{m}$) the fracture surface is surprisingly worn considering the very small number of cycles (6000) with a tendency to flaking (fig 6.51). The angle at which the crack front intercepts the outer surface is a typical result of shear-mode corner-point singularity.

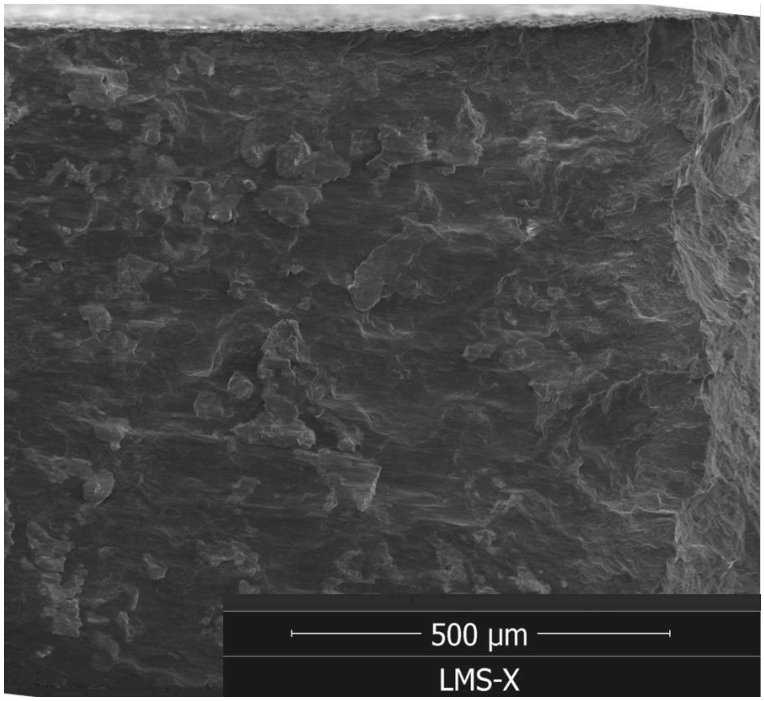

Figure 6.51: Highly worn fracture surface of test $N°11$, $\pm 160\ Nm$, $11/0\ kN$.

For the same torque amplitude and peak tensile load, but with compression while shearing (sequential experiment $N°10$, $F = +11/-5\ kN$, $C = \pm 160\ Nm$, U_{II} from 0.15 to 0.4), wear is even more severe, as shown on figure 6.52, maybe partly due to an enhancement of asperities progressive flattening by the biaxial ratchetting phenomenon proposed by Kapoor [Kapoor, 1997].

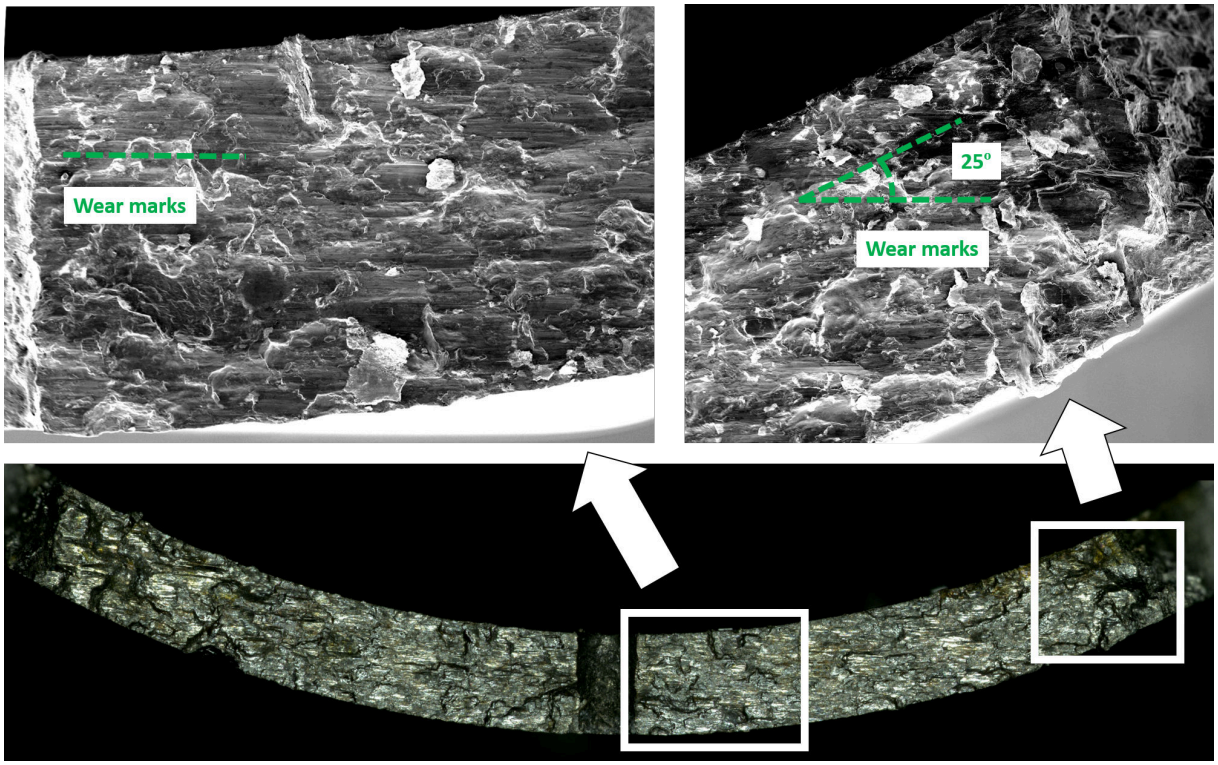

Figure 6.52: Fracture surface and wear marks of sequential experiment $N°10$ ($F = +11/-5\ kN$, $C = \pm 160\ Nm$) obtained with an optical microscope and SEM.

Some debris came out of the crack during the experiment, as shown on figure 6.53 (the same occurred for exp. $N°6$ with compression as well, and in a lesser extent during experiment $N°19$, without compression but with a longer crack growth).

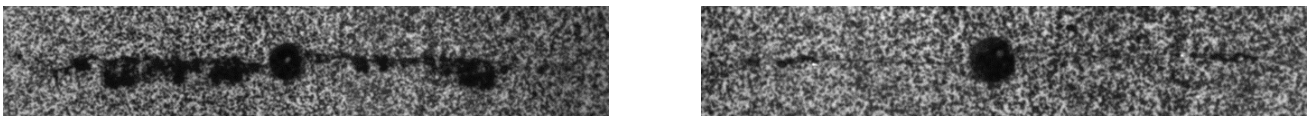

Figure 6.53: Wear debris coming out of the crack during experiment $N°10$ (left). DIC pattern after cleaning (right).

Some oxidized areas are present, as shown on the EDS and BSE image figure 6.54. This oxidation is present with or without compression, as shown on the BSE images figure 6.55 (where the oxidized areas appear darker, as shown on figure 6.54). EDS analysis shows similar peak oxygen content, but sample $N°11$, without compression, shows a more or less uniform oxidation. By contrast, sample $N°10$ exhibits long wear marks on bare metal, where friction is probably stronger (white areas), and a few zones of clustered debris (darker areas).

The effect of compression can be assessed using Archard's law:

$$V_{wear} = k * P * [u] \tag{6.10}$$

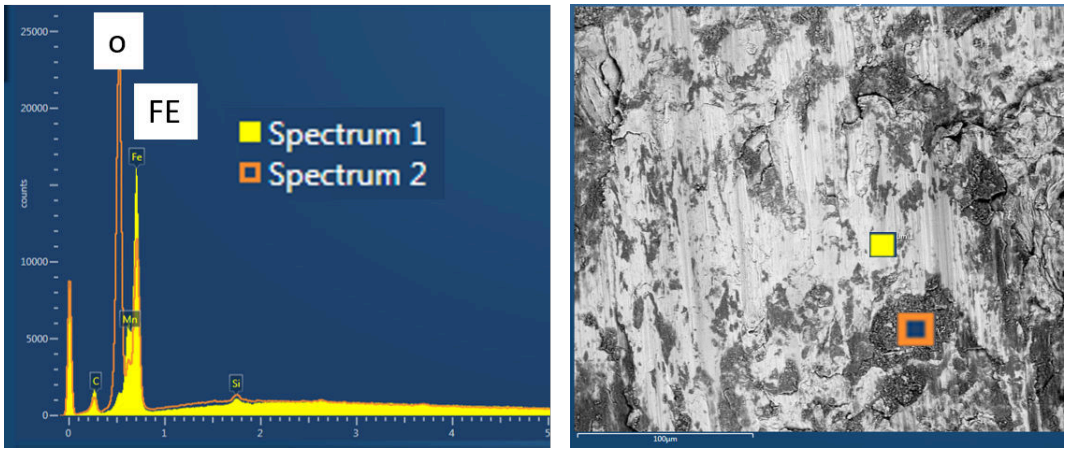

Figure 6.54: Oxidized areas on the fracture surface of test $N°10$ ($F = +11/-5\ kN$, $C = \pm 160\ Nm$). Right image: BSE.

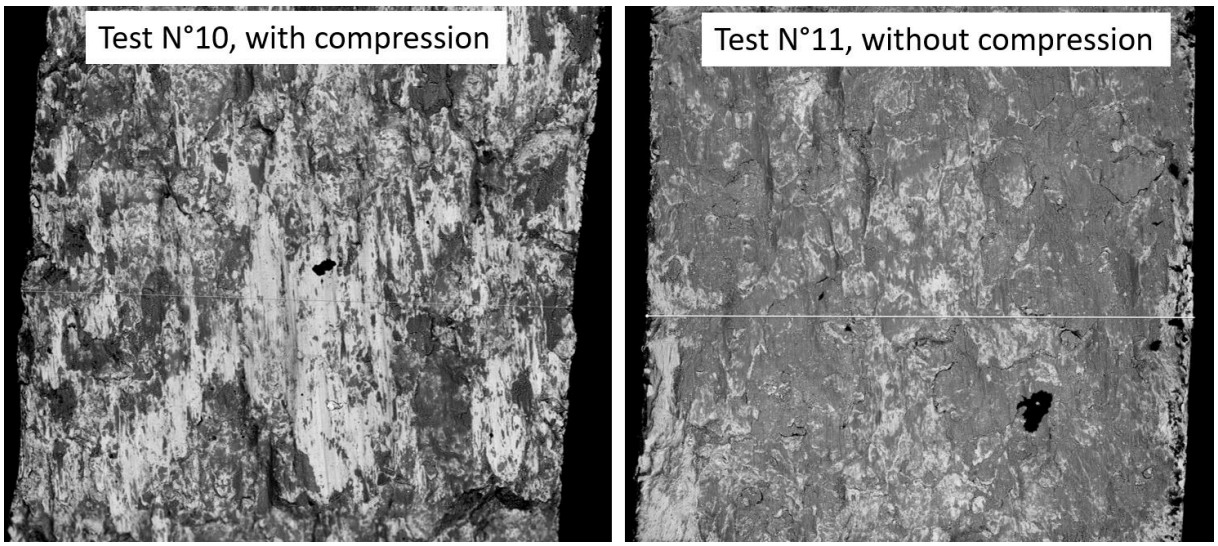

Figure 6.55: Oxidized areas on the fracture surface of test $N°10$ ($F = +11/-5\ kN$, $C = \pm 160\ Nm$) (left) and $N°11$ ($\pm 160\ Nm$, $11/0\ kN$) (right) with BSE.

With V_{wear} the volume of debris per unit of surfaces, k a constant, P the normal stress and $[u]$ the relative displacement of the surfaces: the higher the normal pressure and the relative crack face sliding, the more pronounced the wear. Since $[u] \propto \Delta K_{II}^{eff} * \sqrt{\text{distance to the tip}}$, we have, at a given position:

$$V_{wear} \propto P * \Delta K_{II}^{eff} \tag{6.11}$$

Assuming a uniform Coulomb friction: $\Delta K_{II}^{eff} = F_{II}(a) * (\sqrt{\pi a}) * (\Delta Tau - Tau^{friction}) = F_{II}(a) * (\sqrt{\pi a}) * (\Delta Tau - 2\mu P)$:

$$V_{wear} \propto P * (\Delta tau - 2\mu P) \tag{6.12}$$

$$\frac{\partial V_{wear}}{\partial P} \propto \Delta tau - 4\mu P \tag{6.13}$$

From this last equation, it appears that depending on the shear stress range compared to $4\mu * P$, a normal pressure

can either enhance of hinder crack face wear. If P is too high, it prevents the crack from sliding, thus suppressing wear. In the opposite, if P is too low (no compression), there is also no wear.

However, the influence of normal pressure is more complex than suggested by this equation, since Arnaud [Arnaud, 2018] has shown in Ti-6Al-4V that the energetic wear coefficient (parameter relating the worn volume to the energy dissipated in the contact) actually decreases as the pressure increases. So does the friction coefficient, because of changes in the tribological conditions (fraction of trapped/ejected debris, reduction of oxygen access, transition from abrasive to adhesive wear...).

Near the central hole, the wear marks are parallel to the inner and outer surfaces, while near the crack tip (5.8 mm long crack), those marks are inclined by 25° towards the outer surface, while the crack front is normal this surface (see figure 6.52). This means that the ratio of the out-of-plane over the in-plane relative crack face displacement is equal to:

$$\frac{[u_{III}]}{[u_{II}]} = tan(25) = 0.47 \tag{6.14}$$

and the effective shear SIFs ratio is equal to:

$$\frac{\Delta K_{III}^{eff}}{\Delta K_{II}^{eff}} = \frac{[u_{III}]}{[u_{II}] * (1+\nu)} = 0.36 \tag{6.15}$$

Which is between the 0.18 ratio measured by DIC and the 0.64 ratio predicted by XFEM computations (mean value on the whole front) shown on figure 6.40. The DIC measurement method might be inaccurate and underestimate ΔK_{III}^{eff}.

During 90 ° out-of-phase experiments, wear was also pronounced, in spite of a small torque amplitude ($N°14$, $F = +11/-5\ kN$, $C = \pm 70\ Nm$), as figure 6.56 suggests: compression was indeed present during part of the shearing cycle, along with high levels of ΔK_{II}^{eff}. For a higher shear amplitude ($N°12$, $F = +11/-5\ kN$, $C = \pm 160\ Nm$), round, detached wear debris accumulate near the final crack front, just before bifurcation (6.57).

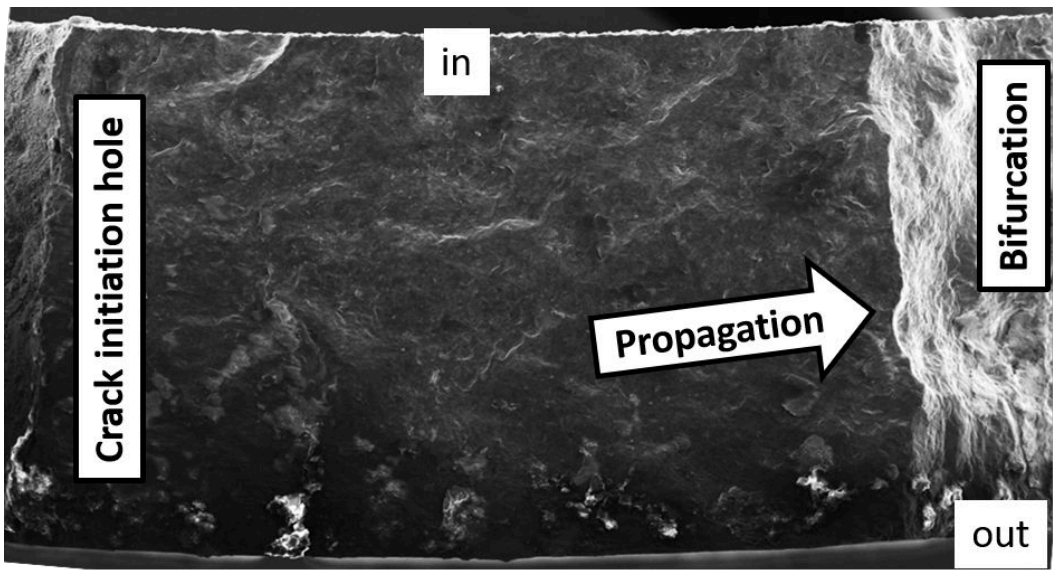

Figure 6.56: Fracture surface of 90 ° out-of-phase experiment $N°14$ ($F = +11/-5\ kN$, $C = \pm 70\ Nm$), near the crack initiation hole.

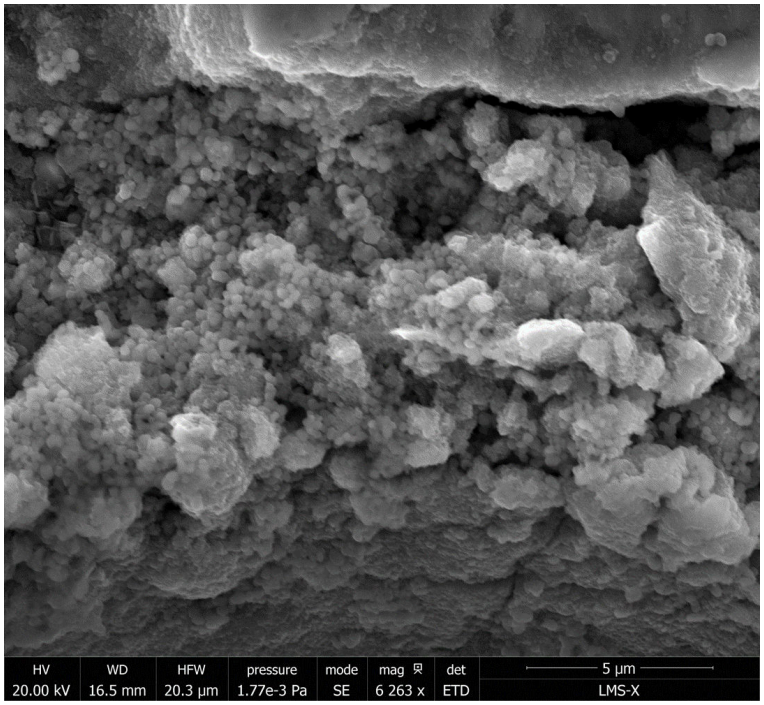

Figure 6.57: Wear debris near bifurcation of 90 ° out-of-phase experiment $N°14$ ($F = +11/-5\ kN$, $C = \pm 160\ Nm$).

The sequential experiment run on tilted precracks produce fracture surfaces that are much less worn, even when the applied number of cycles (136 000) as well as the shear loading range ($\Delta C = 45/-145$ vs $\pm 70\ Nm$) were higher, like for test $N°16$ ($10/0\ kN$) shown on figure 6.58.

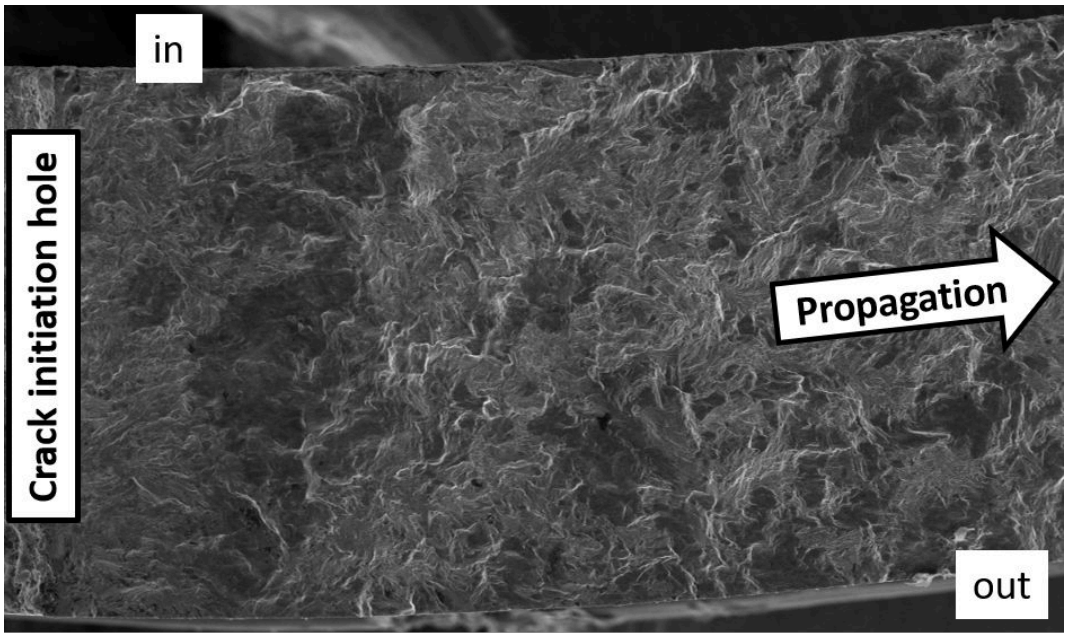

Figure 6.58: Fracture surface of tilted sequential experiment $N°16$ ($F = +10/0\ kN$, $C = +45/-145\ Nm$), near the crack initiation hole.

6.3.4 Analysis of crack growth rates

Crack growth rates were obtained by fitting a polynomial of order 1 to 5 to the a(N) curves (the order depending on the crack growth length), and then deriving it.

The obtained growth rates range from $1.9 * 10^{-9}$ to $1.3 * 10^{-6}$ $m/cycle$, which covers the range of the on field measured values. Paris-like equations (that is: power functions) correlating the measured growth rates with various combinations of nominal or effective SIFs described below were fitted, and the prefactor, C, exponent, n, and correlation coefficient, R^2, are reported in table 6.8. The width of the envelope containing 90 % or 100 % of the data points, defined as the ratio between the crack growth rates of the upper envelope over that of the lower envelope is also indicated (see figure 6.60).

Table 6.8: Coefficients of various kinetic laws fitted to the data.

Driving force	m	C $(m/cycle)$	R^2	Enveloppe 90%	Enveloppe 100%
ΔK_{eq}^{nom}	*confidential*	*confidential*	0.41	8.4	17.1
ΔK_{I}^{eff}	*confidential*	*confidential*	0.56	7.2	169.5
ΔK_{shear}^{eff}	*confidential*	*confidential*	0.47	8.8	210.3
ΔK_{eq}^{eff}	*confidential*	*confidential*	0.87	4.4	11.1
$\Delta K_{Wong,II}^{eff}$	*confidential*	*confidential*	0.89	4.0	14.7

The equivalent ΔK is defined as:

$$\Delta K_{eq} = \sqrt{(\Delta K_I)^2 + (\Delta K_{shear})^2} \tag{6.16}$$

with ΔK_{shear} as defined for mixed mode II & III experiments:

$$\Delta K_{shear} = \sqrt{(\Delta K_{II})^2 + \frac{1}{1-\nu}(\Delta K_{III})^2} \tag{6.17}$$

The crack growth rate does not correlate well with ΔK_{eq}^{nom}, nor with ΔK_{I}^{eff} or ΔK_{shear}^{eff} alone, as shown in figure 6.59 and table 6.8. Using these driving forces, the coefficients of correlation are low, and the envelopes are wide.

The crack growth rates correlates much better with ΔK_{eq}^{eff}, as shown in figure 6.60 and table 6.8. Such a simple driving force gives a coefficient of correlation of 0.87, still lower than that of pure mode I experiments ($R^2 = 0.961$), but not too bad considering the wide variety of loadings & growth rates, as well as the uncertainties on the effective SIFs. 90% of the data points are contained within a factor 4.4 in growth rate, and 100% within a factor 11.1. The curve is superimposed with that of mode I experiments, and not too far from that of mode mixed mode II & III experiments, which has a higher slope (3.25).

A slightly better fit can be obtained using a driving force inspired of that proposed by Wong [Wong et al., 1996]:

$$\Delta K_{Wong,II}^{eff} = \Delta K_{II}^{eff} * (1 + (\frac{\Delta K_{I}^{eff}}{\Delta K_{II}^{eff}})^w) \tag{6.18}$$

with $w = 1.05$ (1.3 in [Wong et al., 1996]). The improvement over ΔK_{eq}^{eff} being negligible (see table 6.8), the later driving force was kept, due to its energetical meaning.

The evolution of the crack growth rate as a function of ΔK_{eq}^{eff} is plotted on figure 6.61 with different colors and symbol depending on the testing conditions and crack path. While the data points of sequential experiments giving

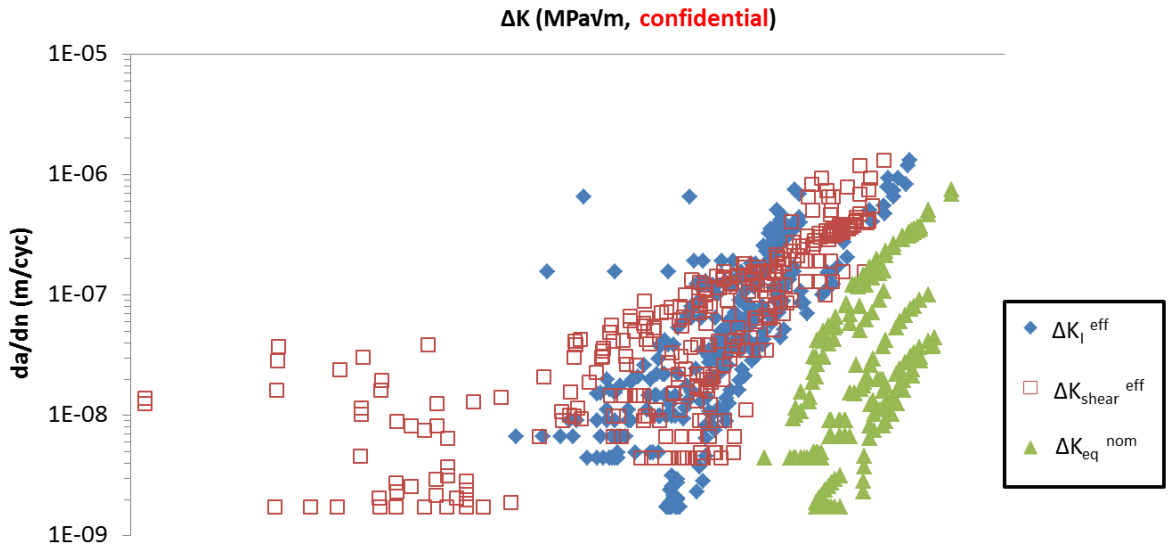

Figure 6.59: Crack growth rates for all the non-proportional mixed-mode I + II experiments, using three driving forces: ΔK_{eq}^{nom}, ΔK_I^{eff} & ΔK_{shear}^{eff}.

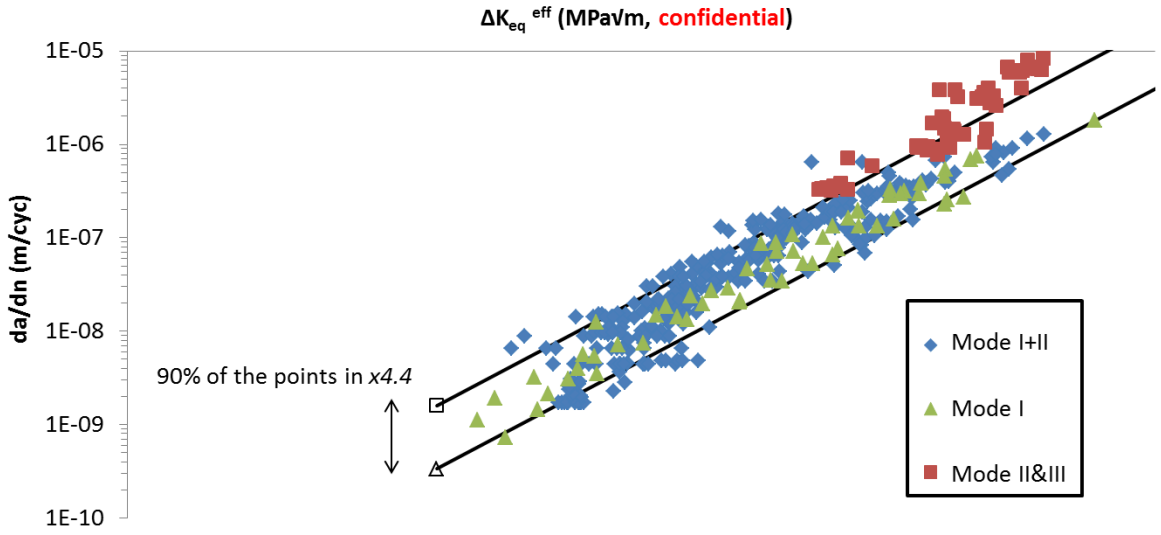

Figure 6.60: Crack growth rates for all the non-proportional mixed-mode I + II experiments as a function of ΔK_{eq}^{eff}, and corresponding 90% upper and lower envelopes. The pure mode I and non-proportional mixed-mode I + II data are superimposed.

rise to a long coplanar growth are relatively well clustered, those of sequential experiments leading to bifurcation after a short coplanar growth are more scattered. This is due to the fact that accurate crack growth rate measurements are difficult to perform during less than 1 mm growth, while ΔK_{II}^{eff} is however rapidly increasing due to wear, this leading to horizontal scattering of the data points.

The data of sequential experiments on tilted precracks are superimposed with those on normal precracks, before and after the bifurcation, which is consistent with the fact that the loading shape is quite similar.

The data from 90 ° out-of-phase experiments are a bit scattered before bifurcation, for the same reason as with the sequential experiments (inaccurate measurement of the rate during short coplanar growth), and more clustered after bifurcation (longer propagation). The crack growth rate seems to be lower than during the sequential experiments, for the same loading range, but no firm conclusion can be drawn given the scatter. High effective SIFs might be

overestimated due to crack-tip plastic flow couplings, as discussed in section 6.2.4, and this overestimation is higher for 90 ° out-of-phase loadings than for sequential ones, which can lead to apparently smaller growth rates.

Experiment $N°9$ witnessed different loading ranges: 10/-5 kN & ± 110 Nm (9_a), then 10/-5 kN & ± 140 Nm (9_b) and finally 13/0 kN & ± 90 Nm. For the first two loadings, the crack growth rates were small (a few 10^{-10} $m/cycle$) and measured only over a ≈ 0.1 mm crack growth (to avoid too long experiments), which is too small to have reliable results (using DIC with the aforementioned setup) and thus to be included in the previous graphs. These measured growth rates appear to be within a factor 3 of the ones predicted using ΔK_{eq}^{eff}.

In [Wong et al., 1996], [Wong et al., 2000b] & [Akama, 2003], the crack growth rates measured in non-proportional mixed-mode I + II on rail steels seemed to depend only on the effective SIFs range, and not on the loading path, which is consistent with the present results. By contrast, a difference in growth rate of a factor 2.46 was found for 316L stainless steel (softer material, which might have more plasticity couplings: $\sigma_{UTS} = 610$ MPa, $\sigma_Y = 320$ MPa, $A\% = 48$) in [Fremy et al., 2014b] between a square and a cross loading path of similar amplitudes. The experiments presented in this study cannot be as precise as those of [Fremy et al., 2014b], as closure effects and crack face friction are present here, which adds uncertainties on the estimated effective SIFs, while they were avoided by Fremy et al. by applying a positive R_I. Even if an intrinsic effect of the effective loading path on the crack growth rate cannot be excluded here, it would be of second order relative to the large influence of the nominal loading path on the effective one, and thus on the crack growth rate.

Here, the biggest effect of the loading paths does not seem to be intrinsic (that is, on the ΔK_{eq}^{eff} - da/dN relation), but extrinsic, that is: on the relation between nominal and effective SIFs (U_I and U_{II} ratios). Experiments $N°10$ & 12 with the same nominal ΔK, but with a sequential or 90° out-of-phase loading paths have very different different effective SIFs (factor ≈ 2 on ΔK_{eq}), and thus crack path and growth rates (4.5 mm coplanar growth versus 0.4 mm, and factor 5 on the crack growth rate).

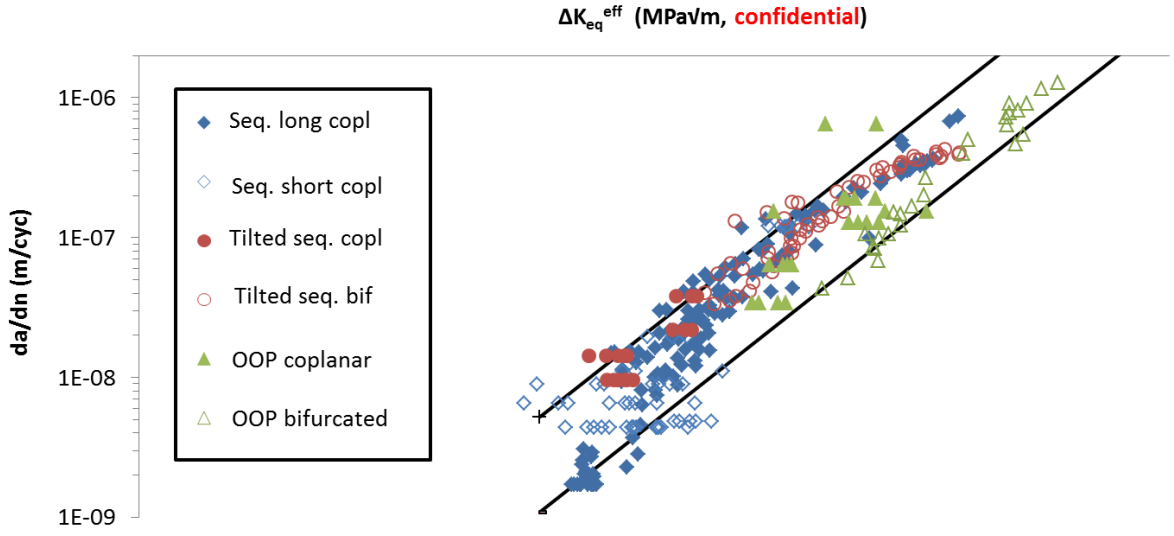

Figure 6.61: Crack growth rates for all the non-proportional mixed-mode I + II experiments as a function of ΔK_{eq}^{eff}, depending on the testing conditions and crack path. Seq. long/short copl: sequential experiments giving rise to a long/short coplanar growth. Tilted seq. copl/bif: tilted sequential experiments, before/after bifurcation. OOP coplanar/bifurcated: 90 ° out-of-phase experiments before/after bifurcation.

In order to highlight a possible synergetic effect between mode I and mode II loadings during sequential tests,

the crack growth rates obtained by cumulating the mode I and shear modes contributions are estimated as follow:

$$\frac{da}{dN}_{Cumulated} = C_I * (\Delta K_I^{eff})^{n_I} + C_{II\&III} * (\Delta K_{shear}^{eff})^{n_{II\&III}} \tag{6.19}$$

Where C_I, n_I, $C_{II\&III}$, $n_{II\&III}$ are the coefficients obtained from the pure mode I and mode II & III experiments respectively. As the range of ΔK_{shear} is smaller during mode I + II experiments than during mode II & III experiments, the Paris-type equation for shear mode is extrapolated here. This cumulated crack growth rate is plotted in figure 6.62 as a function of the measured crack growth rate, and compared to the crack growth rate estimated using ΔK_{eq}. On this figure, the closer to the line of slope 1, the better.

In average, the cumulated crack growth rate is not below the measured rate: the simple sum of mode I and shear modes crack growth rates alone does not systematically underestimate the measured one. This means that there are no apparent synergistic effects due to shear and tensile plastic flow couplings, in opposition to the observations of [Doquet and Pommier, 2004] on a ferritic-pearlitic steel, based on a much smaller number of tests. This estimation of crack growth rate is even surprisingly accurate considering that the coefficients in the Paris-like equations were taken from pure mode I and mode II & III experiments and not optimized in order to get the best fit. However, the correlation with measured crack growth rates is not as good as the results obtained with ΔK_{eq}: the points are gathered in an envelope of a factor 11.1 for ΔK_{eq}, and 12.5 for the cumulated growth rate. The mean relative square error, defined as:

$$Error = \frac{1}{k} * \Sigma_1^k \left(2 * \frac{\frac{da}{dN}_{estimated} - \frac{da}{dN}_{measured}}{\frac{da}{dN}_{estimated} + \frac{da}{dN}_{measured}} \right)^2 \tag{6.20}$$

is of 0.3 for ΔK_{eq} and 0.41 for the cumulated growth rate.

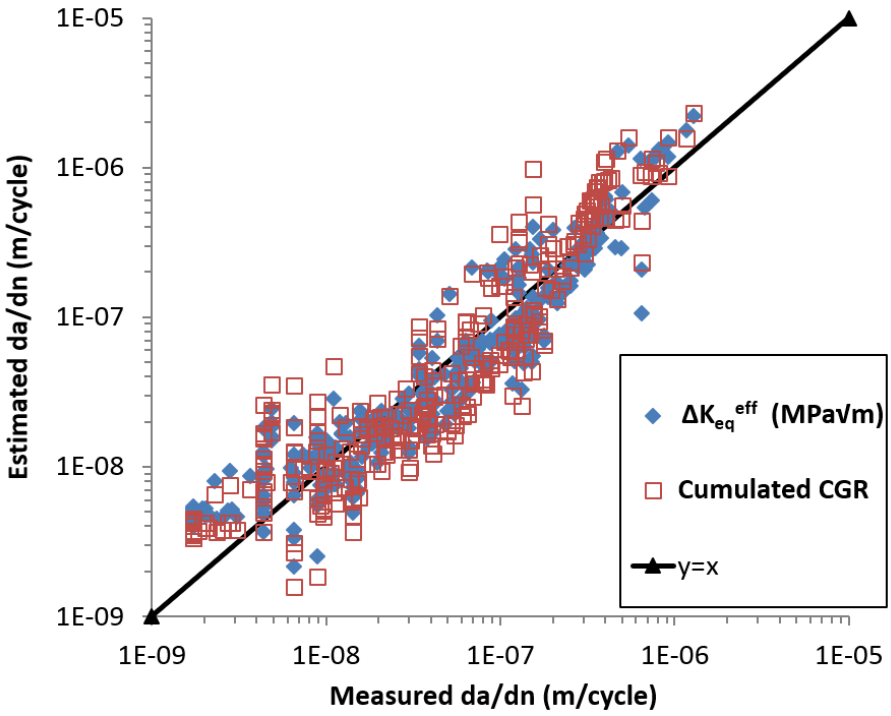

Figure 6.62: Predicted crack growth rates estimated by cumulating the mode I and shear mode contributions or using ΔK_{eq} as a function of the measured crack growth rate.

Experiment $N°18$, which was similar to experiment $N°19$, except that it was performed in water, led to similar

crack growth rates (see appendix D), meaning that water did not increase the crack growth rate due to corrosion or a reduction of the friction between the crack faces (which would increase ΔK_{II}^{eff}).

6.3.5 Analysis of crack paths

As shown in section 6.3.2, the range of the effective SIFs is no sufficient to predict bifurcation. The complete effective loading paths from various cycles are thus analyzed here, using various approaches. For each experiments and each of the two crack tips, 3 cycles are analyzed (when the measurements are available): one during coplanar growth, one at bifurcation, and one after bifurcation, making a total of 56 analyzed cases (see table 6.9). The predicted crack growth angles are compared with the measured ones. When double bifurcations at various angles were obtained, the longest branch was considered. Those 56 cases include 8 cases (14% of the data) for which the effective SIFs might be inaccurate (as discussed in 6.2.4).

Table 6.9: Test conditions and cycles analyzed for crack path prediction.

Exp. number	loading type	Max / Min axial force (kN)	Max / Min torque (N.m)	Nominal $\frac{\Delta K_{II}}{\Delta K_I}$	Cycle during coplanar growth	Cycle at bifurcation	Cycle after bifurcation
4	Sequential	7/0	± 110	2.7	160000	180000	/
5	Sequential	10/0	± 150	2.6	500	15000	/
6	Sequential	10/-5	± 150	2.6	70000	128000	/
7	Sequential	12/5	± 110	1.6	560000	610000	/
8	Sequential	10/0	± 90	1.6	50000	/	/
9	Sequential	13/0	± 90	1.2	1640000	/	/
10	Sequential	11/-5	± 160	2.5	18000	20500	/
11	Sequential	11/0	± 160	2.5	500	4000	/
19	Sequential	10/0	± 90	1.6	50000	/	/
12	90 ° out-of-phase	11/-5	± 16	2.5	/	500	2500
13	90 ° out-of-phase	11/-5	± 110	1.7	/	1000	15000
14	90 ° out-of-phase	11/-5	± 70	1.1	500	5000	80000
16	Tilted sequential	10/0	45/-145	0.8	500	20000	120000
17	Tilted sequential	10/0	80/-160	1.4	500	5000	37500

The dilatancy ΔK_I during sequential experiments (which was below 8% of ΔK_{II}^{eff}) was neglected, as it led to less than 4° difference in crack path prediction and 7% difference in the $\Delta K_{II}/\Delta K_I$ value corresponding to the transition from coplanar to bifurcation using the MTS criterion.

The bifurcation angles were measured over a few hundreds of micrometers, since on shorter distances the paths were sometimes tortuous and the bifurcation angle non uniform along the crack front, making reliable measurements impossible (this can be due to effects of the microstructure or to a bifurcation that did not occur simultaneously along the whole crack front). However, the bifurcation criteria applied in this section are used to predict the angle of an infinitesimally small branch, and not of a few hundreds of micrometers long one, which might induce some errors.

Another source of errors can be the determination of the cycle at which the crack bifurcated. This cycle was determined using the strain map obtained by DIC (where the branch can be seen if it is long enough) and by seeking for a change of slope in the da/dN curve (which corresponds to bifurcation), with a precision that is difficult to estimate.

Considering these various sources or experimental errors, the percentage of successful prediction of crack growth direction of various criteria are assessed within less than 10, 20 or 30° error.

Classical LEFM criteria, namely the maximum tensile stress criterion (MTS), maximum range of the tensile stress criterion (MTSR), maximum Δk_I^* ($\Delta k_I^* = max(k_I^*) - min(k_I^*, 0)$), maximum ΔG^* were tested first. The results in terms of percentage of successful prediction of crack growth direction are reported in table 6.10 for the 34 cases where the cracks continued to propagate straight ahead (that is: before or after bifurcation, as indicated in table 6.9) and the 22 cases where bifurcation occurred (table 6.11).

The max energy release rate criterion successfully predicts continued coplanar growth, but is very poor at predicting bifurcation. Since $\Delta G \propto (\Delta K_{eq})^2$, it means that the crack does not grow in the direction maximizing its growth rate if we assume that ΔK_{eq} is the crack driving force. The MTS criterion is much better than the MTSR criterion, and slightly better than the max Δk_I^* criterion, but is still not very good, since the predicted bifurcation angles (70°) are a bit different from the measured ones ($50 - 60°$), and bifurcations are predicted for almost half of the cases where the crack path actually remained straight.

Table 6.10: Percentage of accurate predictions when continued coplanar crack growth was observed.

≠ with measured angle (°)	% of good predictions for straight crack growths			
	max ΔG^*	max Δk_I^*	MTS	MTSR
<=10	85	53	53	6
<=20	88	59	59	9
<=30	91	62	62	15

Table 6.11: Percentage of accurate predictions for bifurcations.

≠ with measured angle (°)	% of good predictions for bifurcations			
	max ΔG^*	max Δk_I^*	MTS	MTSR
<=10	9	9	9	0
<=20	27	36	41	32
<=30	32	82	82	73

In order to improve these predictions, elastic-plastic FEM computations reproducing the effective loading path and measured crack length, without contact nor friction, were run. For simplification purposes, the cracks were modeled as coplanar, even when they were not, and the applied loads were set so as to reproduce the effective SIFs loading path. The obtained time evolution of the stress & strain fields were used to test various approaches, such as the MTSp, the MTSRp, the maximum of $\sigma_{\theta\theta} * \epsilon\theta\theta$, and the local approach (competition between SWT damage model in the direction of MTSp, and max of $F\&S * Findley's$ damage model) using the same coefficients as for mode I and mode II & III experiments. Each time, the stresses and strains were analyzed in all possible directions,

at 40 μm (as for mode II & III experiments) from the crack tip (4 elements ahead), except for the local approach where the results were averaged on a 40 μm line starting from the crack tip.

The results in terms of percentage of successful prediction of crack growth direction are reported in table 6.12 for cases where the cracks continued to propagate straight ahead (before or after a bifurcation) and in table 6.13 for cases were bifurcation occurred. The local approach gives the best results in case of straight crack growth, very close to the MTSp, as the tension driven damage mechanism, which was evaluated in the MTSp direction, was almost always predominant over the shear-driven damage mechanism. The MTSp criterion is slightly better than its LFEM version (MTS), but the predicted bifurcation angles are still a bit different from those measured experimentally: 86% good predictions within $\pm 30°$, meaning that bifurcation is indeed predicted to occur at the correct crack length, but only 14% within $\pm 10°$ due to the fact the predicted bifurcation angle is still $\approx 70°$, while the measured angles were at $50-60°$. The max of $\sigma_{\theta\theta} * \epsilon_{\theta\theta}$ criterion gives most accurate prediction of the bifurcation angles within $\pm 10°$, for cases where bifurcation actually occurred. However, it often predicts bifurcation when the crack remained straight: adding a strain component to the criterion helped getting better bifurcation angles, but bifurcation is predicted too early.

Table 6.12: Percentage of accurate predictions when continued coplanar crack growth was observed, taking into account crack tip plasticity.

$\neq$ with measured angle (°)	% of good predictions for straight crack growths			
	MTSp	MTSRp	max $\sigma_{\theta\theta} * \epsilon_{\theta\theta}$	Local approach
<=10	50	0	32	53
<=20	62	12	41	65
<=30	65	18	53	68

Table 6.13: Percentage of accurate predictions for bifurcations taking into account crack tip plasticity.

$\neq$ with measured angle (°)	% of good predictions for bifurcations			
	MTSp	MTSRp	max $\sigma_n * \epsilon_n$	Local approach
<=10	14	5	68	9
<=20	55	45	91	45
<=30	86	73	91	91

In order to improve those predictions for the sequential experiments, the influence of the non singular stresses was studied. The influence of the T-stress has been thoroughly studied in the literature, but other non singular stresses exists: that induced by compression/closure effects, and that induced by friction between the crack faces. The effect of such non-singular stresses was investigated by Frelat & Leblond [Leblond and Frelat, 2000] for an elastic material under monotonic loading. When compression is applied, the initial kink angle is found to be unchanged, with a further deviation of the crack from its original bifurcation angle as it propagates (using $k_{II}^* = 0$ criterion). Here, their effect is analyzed for an elastic-plastic behaviour and cyclic loading.

Elastic-plastic computations of a pseudo sequential loading path were performed at the same $\Delta K_I^{eff} = 8.1\ MPa\sqrt{m}$ & $\Delta K_{II}^{eff} = 16.1\ MPa\sqrt{m}$ for an $a = 2\ mm$ long central crack in a plate under plane stress. Various mode I load ratios ($R_I = 0$ & $R_{II} = -1$) and various friction coefficients (0 or 0.5, leading to $U_{II} = 1$ & $U_{II} = 0.5$) were studied. For each computation, the angular distribution of the peak value of the tangential stress over time

was extracted ($\sigma_{\theta\theta,\,max(t)}$), and reported on figure 6.63.

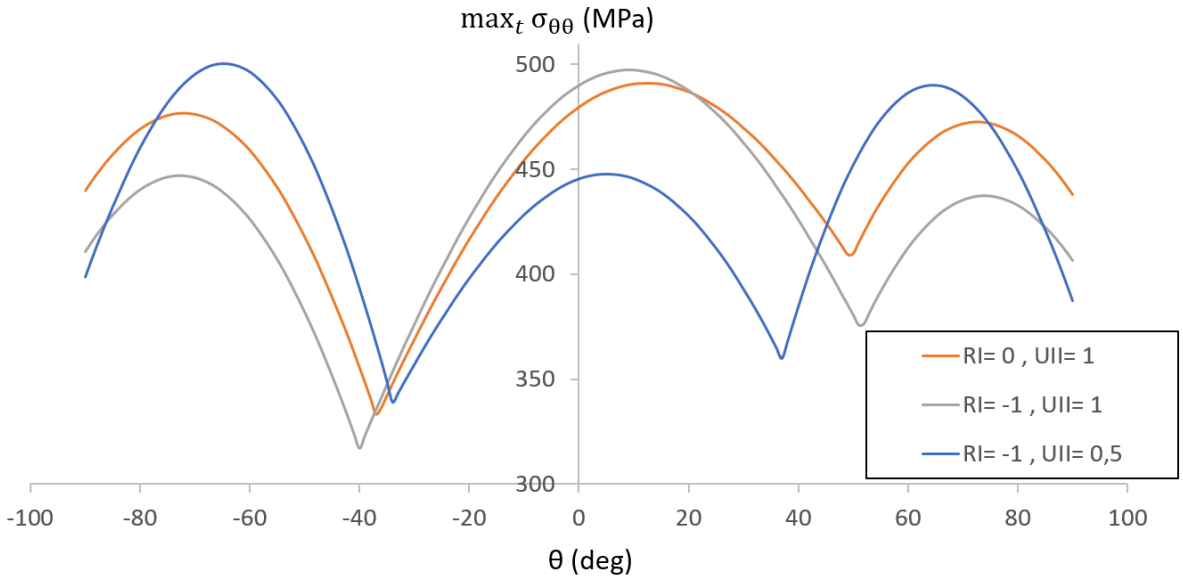

Figure 6.63: Evolution of the maximum of the tangential stress $\sigma_{\theta\theta}$ a function of the direction, at 40 μm from the crack tip for an **elastic plastic** behavior and pseudo sequential mode I + II loadings at $\Delta K_I^{eff} = 8.1\ MPa\sqrt{m}$ & $\Delta K_{II}^{eff} = 16.1\ MPa\sqrt{m}$.

Without compression nor friction, three maxima appears on the curve: at -72° (476 MPa) and 73° (474 MPa) due to the reversed mode II cycle, and at 13° (491 MPa) due to the mode I cycle. The maximum due to mode I loading is not exactly at 0° (as it would be without mode II loading) due to the coupling between shear and tensile plastic flows. The static compression while shearing ($R_I = -1$) slightly increases the peak $\sigma_{\theta\theta}$ near 0° (by less than 2 %), and tends to shift it back to 0°, but reduces the peaks near ±70° (by 8 %), making bifurcation even less probable if it is driven by the hoop stress. This means that the increased length of coplanar growth observed when compression was added while shearing might not only be due to a reduction of $\Delta K_{II}^{effective}/\Delta K_I^{effective}$, but also to the effect of compression on the stress distribution ahead of the crack tip. When friction is added ($R_I = -1$, $U_{II} = 0.5$, $\mu = 0.5$), the height of the peak near 0° is reduced by 10 % (compared to $R_I = 0$), which is due again to the coupling between shear and tensile plastic flows at the crack tip. At the same time, the height of the peaks near ±70° is increased by 5 %, and their angular position are shifted: ±65° instead of -72° & 73°. In fact, the friction stress adds a component to $\sigma_{\theta\theta}$ which is maximal at ±45° (depending on the loading direction), thus shifting the direction of the secondary maxima of hoop stress to a value closer to ±45° and increasing its height.

Those non singular stresses were added in the previous elastic-plastic simulations of the effective loading paths using the U_I and U_{II} ratios:

$$\tau_{friction} = (1 - U_{II}) * \tau_{applied} \tag{6.21}$$

$$\sigma^{contact} = \sigma^{compression} + \sigma^{closure} = \sigma^{compression} + (U_I - 1) * \Delta\sigma^{tension} \tag{6.22}$$

Those stresses are added to the loads applied at the edges of the specimen, and on the crack faces as two opposites loads, so that the effective SIFs remains unchanged. This method was only applied to sequential experiments, for whom all the effective SIFs are correctly estimated, and the U ratios are known. The MTS (elastic computations),

MTSp criteria and local approach were tested again in these conditions, at 40 μm from the crack tip.

The results for the various approaches are reported in table 6.14. Adding crack-face compression and friction does not improve the predictions of the MTS criterion, as bifurcations are still predicted too early. However, adding these effects highly improved the predictions of the MTSp criterion and local approach: 87% are now within 20° of the measured angle. The few wrong predictions correspond either to very high loading ranges, for which the material constitutive equations identified from cyclic tests up to 619 MPa at most had to be extrapolated (stresses up to 1 GPa at 40 μm from the crack tip), or to long cracks (more than 4 mm), for which mode III is present and was not considered in the approach. Adding dilantacy might slightly improve the results, as it would further reduce the predicted bifurcation angles, and make it closer to the $50-60°$ measured experimentally.

Table 6.14: Percentage of accurate predictions for pseudo sequential experiments (coplanar growth and bifurcation). Values estimated at 40 μm ahead of the crack tip.

$\neq$ with measured angle (°)	% of good predictions for sequential loadings				
	MTS	MTS with non singular stresses	MTSp	MTSp with non singular stresses	Local approach with non singular stresses
<=10	53	57	50	50	47
<=20	63	67	70	87	87
<=30	83	67	90	97	97

Even if the results are improved by taking into account crack tip plasticity, contact, and friction, predictions within 20° is still not good enough for incremental simulations in the industrial context for which errors would accumulate, and some ingredient seems to be missing: the direction might not be controlled by the maximum tangential stress, but by a more complex function involving the strain. Another explanation for the errors can be the formation of multiple branches, shielding each-other.

6.3.6 Estimation of friction and contact stresses

Because of crack roughness and plasticity-induced closure, contact and friction stresses exist between the crack faces and play an essential role on both crack paths and kinetics, even in the absence of any applied normal compression. However, in industrial simulations of rolling contact fatigue crack growth, smooth cracks are modeled, and contact/friction stresses exist only if a normal compression is applied and Coulomb's friction is assumed. To overcome this limitation, a simple, approximate way to capture these "intrinsic" contact/friction stresses in such industrial context is proposed in this section, based on their estimated evolutions during the sequential tests

The DIC-FEM coupling method with elastic-plastic computations (presented in 3.2.3) was used to obtain the friction and contact stresses profiles along the crack faces (see figures 6.64 & 6.65) for mode II loadings with various superimposed static tensile or compressive axial load (performed during experiment $N°$ 19). As expected, for mode II loading (figure 6.64), a static compression enhances crack face friction, which rises with the distance to the crack tip. The stress concentration due to the central hole does not seem to explain this tendency, because it drops much faster than the computed friction stress. Note that friction is still present without any far-field compression, and even when a slight opening stress is present ($K_I = 3.3\ MPa\sqrt{m}$), which is probably due to crack face roughness. As a consequence, the friction stresses (and ΔK_{II}^{eff}) cannot be predicted with a Coulomb's law.

For mode I loading at negative R ratio (figure 6.65), the computed contact stresses are higher than the minimal far-field stress, and even for $R = 0$, contact stresses are still present, which is certainly due to closure effects. Slightly positive "contact stresses", which have no physical meaning, are obtained for a 27 MPa minimal tensile load ($R = 0.2$). The reason for this artefact is yet unclear.

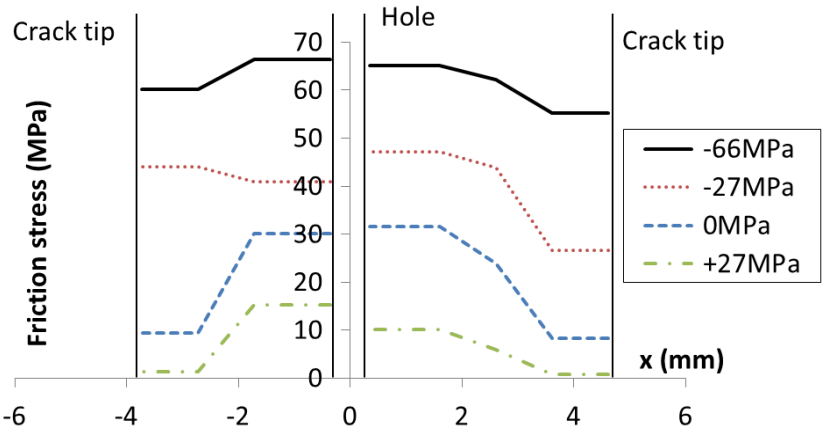

Figure 6.64: Estimated friction stress profile at fixed $\Delta\tau = 115\ MPa$ with various static tensile or compressive loads.

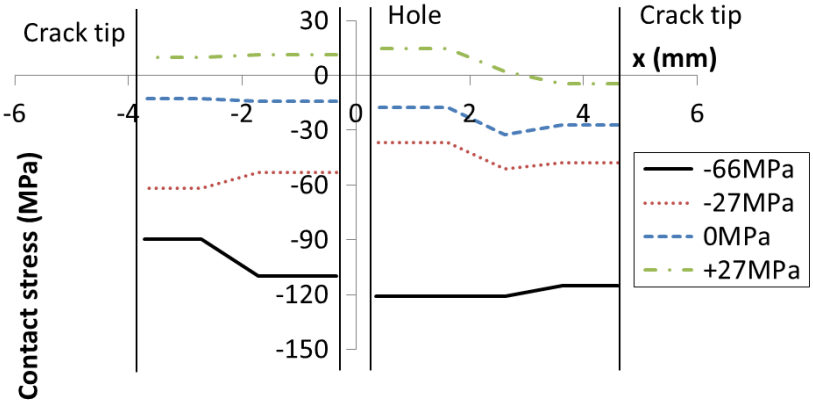

Figure 6.65: Estimated contact stress profile in mode I at fixed σ_{max} (133 MPa) for various σ_{min}

From those two friction and contact stress profiles, a direct relation between contact and friction stresses could be expected in the form of a Coulomb's-like friction law with an additional constant term accounting for crack face roughness:

$$\tau^{friction} = \mu * \sigma^{compression} + \tau^{roughness} \text{ for a sliding crack} \tag{6.23}$$

$$\tau^{friction} = \tau^{applied} \text{ for a locked crack} \tag{6.24}$$

However, under a static compression of $-26\ MPa$, the friction stress profile for mode II loadings at various $\Delta\tau$ is not constant, but depends on the amplitude of $\Delta\tau$, as shown on figure 6.66: the higher the applied shear stress, the higher friction stress. In each case, a non zero ΔK_{II}^{eff} is measured, meaning that the crack is not locked and a coulomb-like law would predict a constant friction stress.

From those results, the friction stress should be a function of both the compressive stress and applied shear stress. In addition, several other factors like the worn volume (reduction of roughness), wear mode (adhesive or

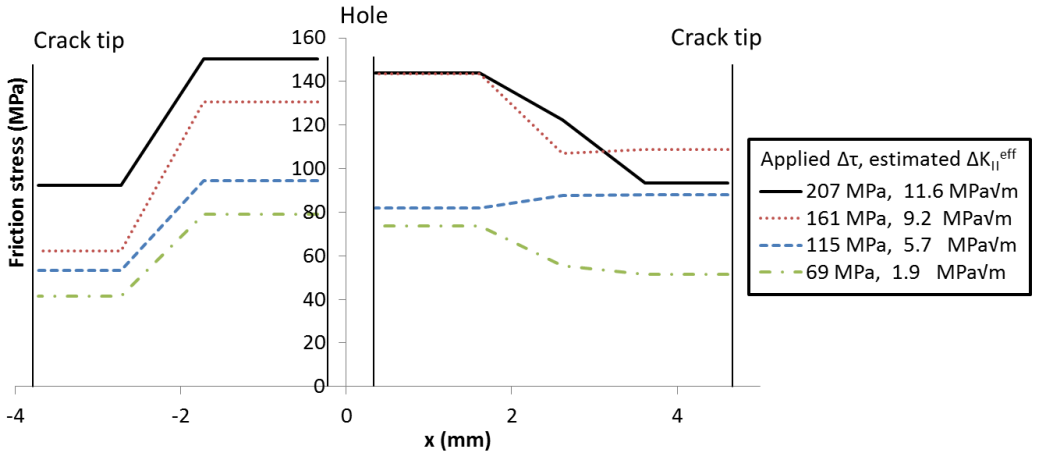

Figure 6.66: Estimated friction stress profile at fixed $-26\ MPa$ static compression with various $\Delta\tau$.

abrasive, which changes the friction & wear coefficient [Arnaud, 2018]), and the sliding amplitude compared to the wavelength of the asperities (for asperities climbing, as proposed by [Gross and Mendelsohn, 1988]) should play a role.

In order to get a simple (simplistic) model to use in the SNCF's computation scheme (which already account for Coulomb's friction), the evolution of the effective SIFs from various experiments was studied. From those effective SIFs, it is possible to define "equivalent" macroscopic contact and friction stresses:

$$\Delta\tau^{friction} = (1 - U_{II}) * \Delta\tau^{applied} \tag{6.25}$$

$$\sigma^{contact} = \sigma^{compression} + \sigma^{closure} = \sigma^{compression} + (U_I - 1) * \Delta\sigma^{tension} \tag{6.26}$$

If we suppose that the friction stress is an affine function of both the applied shear stress and the contact stress (for a non locked crack), we can propose the following empirical formula:

$$\tau^{friction} = (1 - \alpha) * \tau^{applied} + \mu * \sigma^{contact} + \tau^0 \tag{6.27}$$

With α a coefficient accounting for the reduction due to dilatancy (a part of the shear load is transformed into mode I, and is thus retrieved from shear modes), μ friction coefficient, and τ^0 a threshold accounting for asperities locking. During a cycle with $R_{II} = -1$:

$$\Delta\tau^{friction} = (1 - \alpha) * \Delta\tau^{applied} + 2 * \mu * \sigma^{contact} + 2 * \tau^0 \tag{6.28}$$

Which becomes, by multiplying by $Fm_{II}(a) = \Delta K_{II}^{nom}/\Delta\tau$:

$$\Delta K_{II}^{friction} = (1 - \alpha) * \Delta K_{II}^{nom} + 2 * \mu * \sigma^{contact} * Fm_{II} + 2 * K_{II}^0 \tag{6.29}$$

and:

$$\Delta K_{II}^{eff} = \Delta K_{II}^{nom} - \Delta K_{II}^{friction} = \alpha * \Delta K_{II}^{nom} - 2 * \mu * \sigma^{contact} * Fm_{II} - 2 * K_{II}^0 \tag{6.30}$$

In this equation, α represents the asymptotic value of U_{II}, as illustrated on figure 6.67, which is similar to figure 6.38 obtained from experimental data.

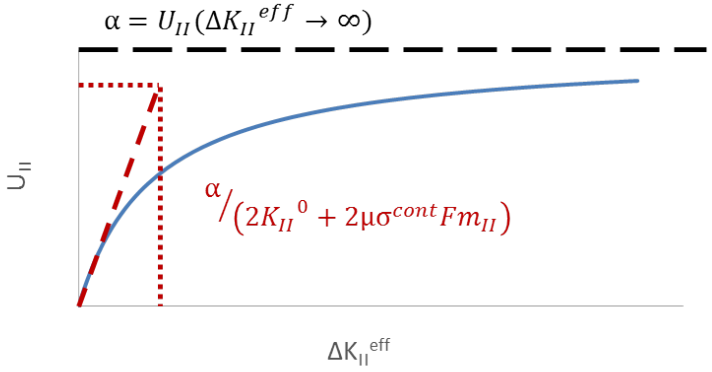

Figure 6.67: Illustration of U_{II} as a function of $\Delta K_{II}^{effective}$ predicted using equ. 6.30.

The evolution of $\Delta K_{II}^{eff} + 2 * \mu * \sigma^{contact} * Fm_{II}$ is plotted as a function of ΔK_{II}^{nom} on figure 6.68.a. The best fit is obtained for $\mu = 0.3$, and gives $K_{II}^0 =$ *confidential data* $MPa\sqrt{m}$ & $\alpha =$ *confidential data*. From this fit, it is then possible to predict the effective ΔK_{II}^{eff} (using eq. 6.30), which is plotted on figure 6.68.b. as a function of the measured one. The predictions are within $\pm 5\ MPa\sqrt{m}$, for ΔK_{II}^{nom} ranging from 12 to 55 $MPa\sqrt{m}$, U_{II} ratios from 0 to 0.44 and compressive stresses from 0 to $-66\ MPa$.

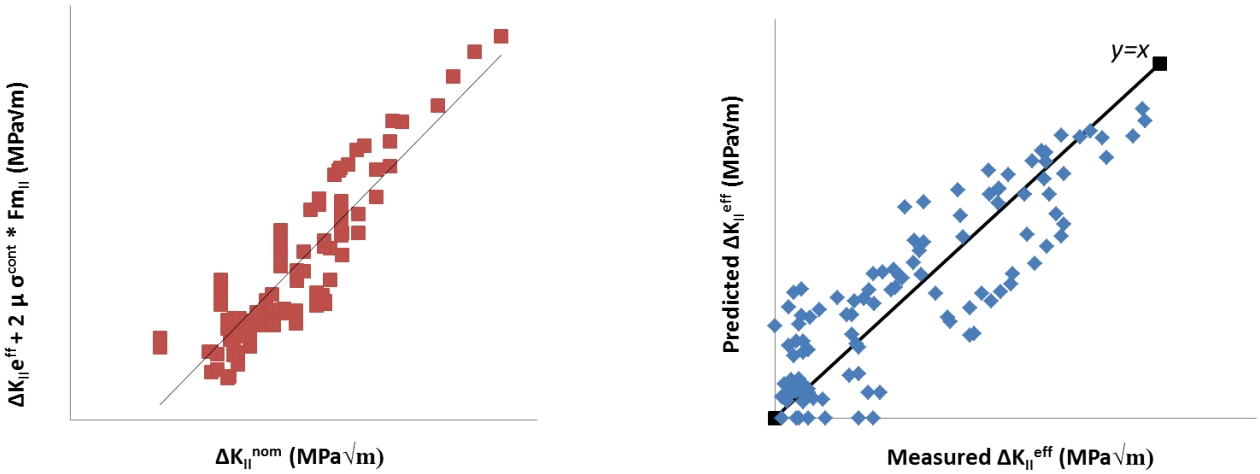

Figure 6.68: Influence of ΔK_{II}^{nom} on ΔK_{II}^{eff} when removing the effect of the contact stress (a) . Predicted (eq. 6.30) versus measured ΔK_{II}^{eff} (b). *No data for confidentiality reasons.*

Better results could certainly be obtained by taking wear into account (change of asperities size, debris, change of wear mode and friction coefficient...), which will change the values of α, μ and K_{II}^0 during the experiment: indeed, very different fracture surfaces were observed on the considered experiments, going from mode I type fracture surfaces (exp. $N°$ 9), with a high roughness, to highly worn (exp. $N°$ 6 & 10) fracture surfaces (see section 6.3.3).

Such wear model should account for the fact that at a given ΔK_{II}^{nom}, ΔK_I^{eff} has an influence on ΔK_{II}^{eff}: if ΔK_I is high, the crack will grow faster than the asperities are worn, the crack tip will remained locked and ΔK_{II}^{eff} will be small. However, if ΔK_I is small, the crack will grow slower than the asperities are worn, and ΔK_{II}^{eff} will be increased.

6.4 Conclusions on mixed mode I + II experiments

The crack paths and growth rates during non-proportional mixed-mode I + II tests were analyzed, based on the effective SIFs issued from stereo-DIC, fractographic observations and elastic-plastic FE simulations, leading to the following results:

- Plasticity and crack roughness lead to closure effects (U_I from 0.76 to 1) while friction and asperities interlocking reduce the effective shear mode singularity (U_{II} from 0 to 0.52). Depending on the loading path and amplitude, very different fracture surfaces are observed, going from mode I-like surfaces to highly worn surfaces.

- The effective SIFs are quite dependent on the shape of the nominal loading paths. For example, two experiments with the same ΔK^{nom}, but one sequential and the other 90° out-of-phase exhibited a factor 2 between their effective SIFs, a factor 5 on their crack growth rates and a factor 11 on the extend of coplanar growth. No correct prediction of mixed-mode fatigue crack growth can thus be made without a correct assessment of closure and friction effects.

- For pseudo sequential loadings, the effective mode mixity ratio, which controls the crack path, is often initially well below its nominal value, but rises progressively during coplanar growth, as crack face asperities get worn. Bifurcation finally occurs when $\Delta K_{II}^{eff}/\Delta K_I^{eff} \gtrapprox 2$ (in accordance with the MTSp criterion).

- A static compression while shearing reduces $\Delta K_{II}^{eff}/\Delta K_I^{eff}$ and makes its wear-induced rise slower. As a result, it increases the extent of coplanar growth, which is thus controlled by the wear process. Compression might also postpone bifurcation by reducing the the peak tangential stress at ±70°.

- For 90° out-of-phase loading and sequential loading on a tilted precrack, bifurcation does not correspond to any specific value of the effective mode-mixity ratio.

- The MTSp and local approach, applied to effective loading paths, allow an accurate prediction of crack bifurcation, but the predicted kink angle is ≈ 70°, while it is rather ≈ 50−60°. Taking into account the compression and friction non singular stresses improves the predictions.

- In the present study, after corrections of the SIFs for closure and contact/friction effects, no intrinsic influence of the effective loading path was found, and the effective ranges seemed sufficient to predict the crack growth rates.

- The crack growth rate can be relatively well predicted by an "effective" $\Delta K_{eq} = \sqrt{(\Delta K_I^{eff})^2 + (\Delta K_{II}^{eff})^2 + \frac{1}{1-\nu}(\Delta K_{III}^{eff})^2}$.

- Since the simulations run at SNCF consider smooth cracks that do not undergo friction unless normal compression is applied and Coulomb's friction implemented, a simple empirical formula is proposed to capture the existence of "intrinsic" contact/ friction effects on rough cracks and estimate the effective SIFs. It accounts in an approximate way for the effects of friction and asperities interlocking/sliding, and could be improved by taking into account the evolution of the crack faces morphology and wear mode.

Chapter 7

Proposition of an approach to predict the crack path and growth rate

Contents

In this chapter, an approach to be implemented in SNCF's computations scheme "PropaFiss3D" in order to predict the crack path and growth rate of Squat-type cracks will be proposed. Its relevance will be discussed by comparison of its predictions to the results of sequential mixed-mode experiments I + II & III.

7.1 Proposed approach

In order to be implemented in SNCF's computations scheme, the proposed approach should not include elastic-plastic computations, that are not yet compatible with the XFEM method, which does not incorporate cyclic plasticity. However, friction and contact between the crack faces in presence of a normal compression are already partly taken into account by a Coulomb's friction model.

The Following approach is thus proposed:

Closure effects are accounted for using the following equations:

$$K_I^{closure} = (1 - U_I) * K_I^{max} \tag{7.1}$$

$$K_I^{eff}(t) = max(K_I^{nom}(t) - K_I^{closure}; 0) \tag{7.2}$$

where U_I is a constant. This coefficient could be determined from the effective SIFs measurements performed using DIC during mode I or non-proportional mixed-mode I+II experiments. However, those measurements correspond to plane stress conditions (surface measurements), which lead to higher plasticity-induced closure effects than under plane strain conditions (see section 2.4), as it is the case in Squat-type cracks (in the bulk of rails). U_I should thus be chosen between 1 and the value obtained using DIC.

Such a simplified approach with a constant U_I does not account for the observed effects of the R ratio and of ΔK_I on U_I (which was found to vary between 0.4 and 1 in mode I (Fig. 4.23 of chapter 4) as well as in mixed-mode I + II (Fig 6.36). Anyway, note that the R ratio (defined as $K_{I\,min}/K_{I\,max}$, where $K_{I\,min}$ is computed without any unilateral condition and can thus be negative) varies along the front of a squat-type crack and with the operating temperature, so that the relevant mode I R ratio is not easy to define. This makes the choice of a constant U_I reasonable in an engineering approach.

In order to estimate the effective shear-mode SIFs, the equations 6.27 and 6.30 of chapter 6 are used:

$$\tau^{friction} = (1 - \alpha) * \tau^{applied} + \mu * \sigma^{contact} + \tau^0 \tag{7.3}$$

$$\Delta K_{II}^{eff} = \Delta K_{II}^{nom} - \Delta K_{II}^{friction} = \alpha * \Delta K_{II}^{nom} - 2 * \mu * \sigma^{contact} * Fm_{II} - 2 * K_{II}^0 \tag{7.4}$$

Crack face friction comes from two sources:

- A macroscopic source: the extrinsic friction stress (due to the far field compression), modeled by a Coulomb law, which is already included in PropaFiss. It is represented by the term multiplied by μ in equs. 7.3 & 7.4.
- A microscopic source: the intrinsic friction stress, due to crack face roughness, which is represented by α and K_{II}^0 in equs. 7.3 & 7.4.

From the SIFs corrected for Coulomb's friction, denoted as $K^{coulomb}$, K_{II}^{eff} for a sequential mixed-mode I + II

loading can be estimated as:

$$\Delta K_{II}^{eff} = max(\alpha * \Delta K_{II}^{Coulomb} - 2 * K_{friction}; 0) \tag{7.5}$$

With

$$K_{friction} = K_{II}^{0} + \mu * K_{I}^{closure} \tag{7.6}$$

Where $\mu * K_I^{closure}$ accounts for the fact that if the crack closes earlier, it will be under compression earlier (thus leading to Coulomb-type friction).

In order to access $K_{II}^{eff}(t)$ (and not only ΔK_{II}^{eff}), the following equation is proposed:

$$\begin{aligned} &\text{If } |K_{II}^{eff}(t) - \alpha K_{II}^{Coul}(t)| < K_{fr} \text{ then } \dot{K}_{II}^{eff}(t) = 0 \\ &\text{Else: } K_{II}^{eff}(t) = \alpha K_{II}^{Coul}(t) - sign(\dot{K}_{II}^{Coul}(t)) * K_{fr} \end{aligned} \tag{7.7}$$

If constant α and K_{fr} are assumed, friction still occurs when the crack is fully opened, as illustrated on figure 7.1 for a cyclic mode II with a static K_I, which is incorrect: for path (a), $K_{II}^{eff}(t)$ should be equal to $K_{II}^{nom}(t)$.

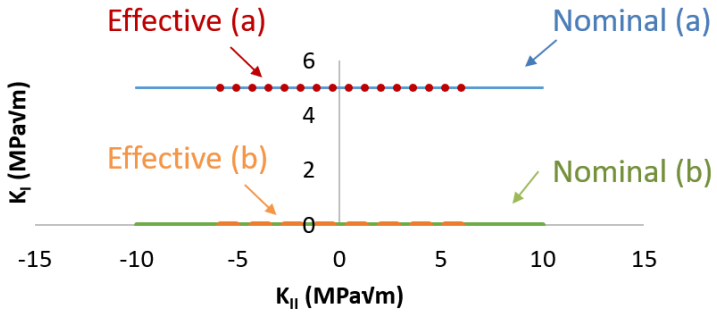

Figure 7.1: Nominal and effective loading path predicted using eq. 7.7 with constant α and K_{fr}, for (a) cyclic mode II with static mode I, and (b) cyclic mode II.

In order to account for the progressive reduction in asperity-induced friction as the crack opens, the evolution $\alpha(K_I^{eff})$ and $K_{fr}(K_I^{eff})$ described on figure 7.2 are proposed, with $K_I^{friction} =$ *confidential data* $MPa\sqrt{m}$, obtained from cyclic mode II experiments superimposed with various static mode I loadings.

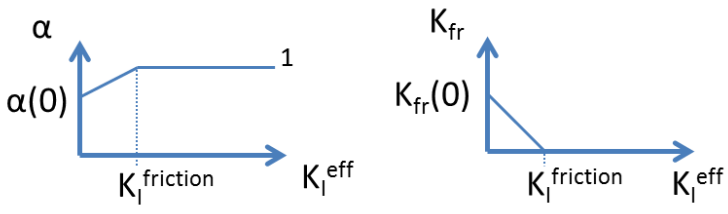

Figure 7.2: Proposed evolution of $\alpha(K_I^{eff})$ and $K_{fr}(K_I^{eff})$.

To generalize eq. 7.7 for mode II & III, a discrete time evolution of $K_{II}^{eff}(t)$, considered as a vector in the K_{II}

- K_{III} space is proposed:

$$\underline{K}^{eff}(t+1) = \alpha(t+1)\underline{K}^{Coul}(t+1) + \frac{\alpha(t+1)\underline{K}^{Coul}(t+1) - \underline{K}^{eff}(t)}{\|\alpha(t+1)\underline{K}^{Coul}(t+1) - \underline{K}^{eff}(t)\|} * min(K_{fr}(t+1); \|\alpha(t+1)\underline{K}^{Coul}(t+1) - \underline{K}^{eff}(t)\|) \tag{7.8}$$

This evolution of $\underline{K}^{eff}(t)$ is illustrated on figure 7.3. If $\|\alpha\underline{K}^{Coul}(t+1) - \underline{K}^{eff}(t)\| < K_{fr}(t+1)$ (fig. a.), then $\underline{K}^{eff} = constant$ (locked crack), and if $\|\alpha\underline{K}^{Coul}(t+1) - \underline{K}^{eff}(t)\| > K_{fr}(t+1)$, $\underline{K}^{eff}$ evolves.

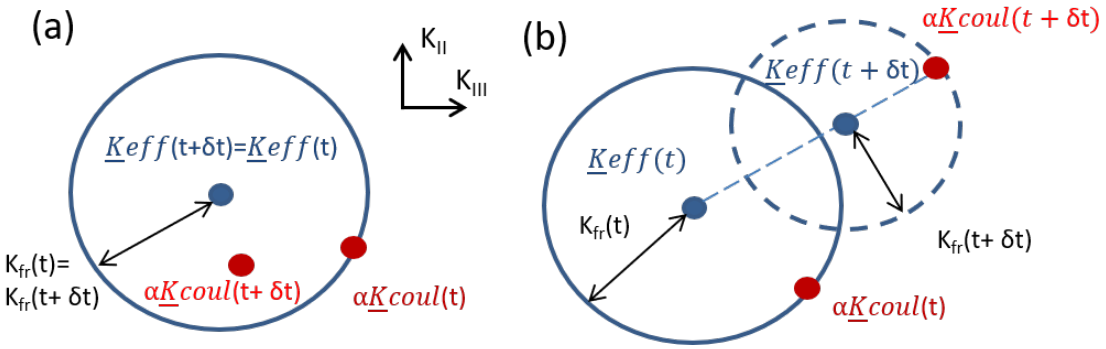

Figure 7.3: Illustration of the evolution of $\underline{K}^{eff}(t)$ (SIFs in the K_{II} - K_{III} space) using eq. 7.8. (a): $\|\alpha\underline{K}^{Coul}(t+1) - \underline{K}^{eff}(t)\| < K_{fr}(t+1)$, and (b): $\|\alpha\underline{K}^{Coul}(t+1) - \underline{K}^{eff}(t)\| > K_{fr}(t+1)$

For non-proportional loadings, such an approach will be dependent on the discretization pitch. It is an engineer approach, which does not account for the differences in crack face roughness parallel or normal to the front ($< Ra >= 8.8\ \mu m$ versus $< Ra >= 5.9\ \mu m$ respectively, measured during mixed-mode II & III experiments), which could lead to different α & K_{fr} for mode II or III. It also neglects the dilatancy effects. A model accounting for the reduction of friction due to wear should give better results, as it would be able to account for history effects induced by crack face roughness: friction at time t would be reduced if the previous cycles were performed at $\Delta K_{II}^{nom}(t-1) >> \Delta K_{II}^{nom}(t)$ instead of at $\Delta K_{II}^{nom}(t-1) = \Delta K_{II}^{nom}(t)$, thus leading to different $\Delta K_{II}^{eff}(t)$ for the same $\Delta K_{II}^{nom}(t)$.

Examples of effective paths obtained using this approach (Coulomb's friction with eqs. 7.2 & 7.8) are given on figure 7.4. The nominal and experimental effective loading paths are those of figures 6.30 (sequential and pseudo-sequential loadings) & 6.32 (90° out-of-phase loading). As mentioned earlier, the effects of dilatancy are not accounted for. The proposed approach does not either predict the observed asymmetry of the effective loading path ($R_{II}^{effective} > -1$, while $R_{II}^{nominal} = -1$), but the predicted shape and size of effective loading paths are in reasonable agreement with the measured ones.

From the effective loading path, the crack path can be predicted using the Maximum Tangential Stress criterion, even though this criterion is less accurate than the MTSp criterion, taking into account the non-singular contact stresses (but no cyclic elastic plastic computations can be performed). This criterion is only implemented for mode II (using equ. 2.11), and not mode III.

The crack growth rate can be predicted using a Paris-type equation with ΔK_{eq}^{eff} defined as:

$$\Delta K_{eq}^{eff} = \sqrt{(\Delta K_I^{eff})^2 + (\Delta K_{II}^{eff})^2 + \frac{1}{1-\nu}(\Delta K_{III}^{eff})^2} \tag{7.9}$$

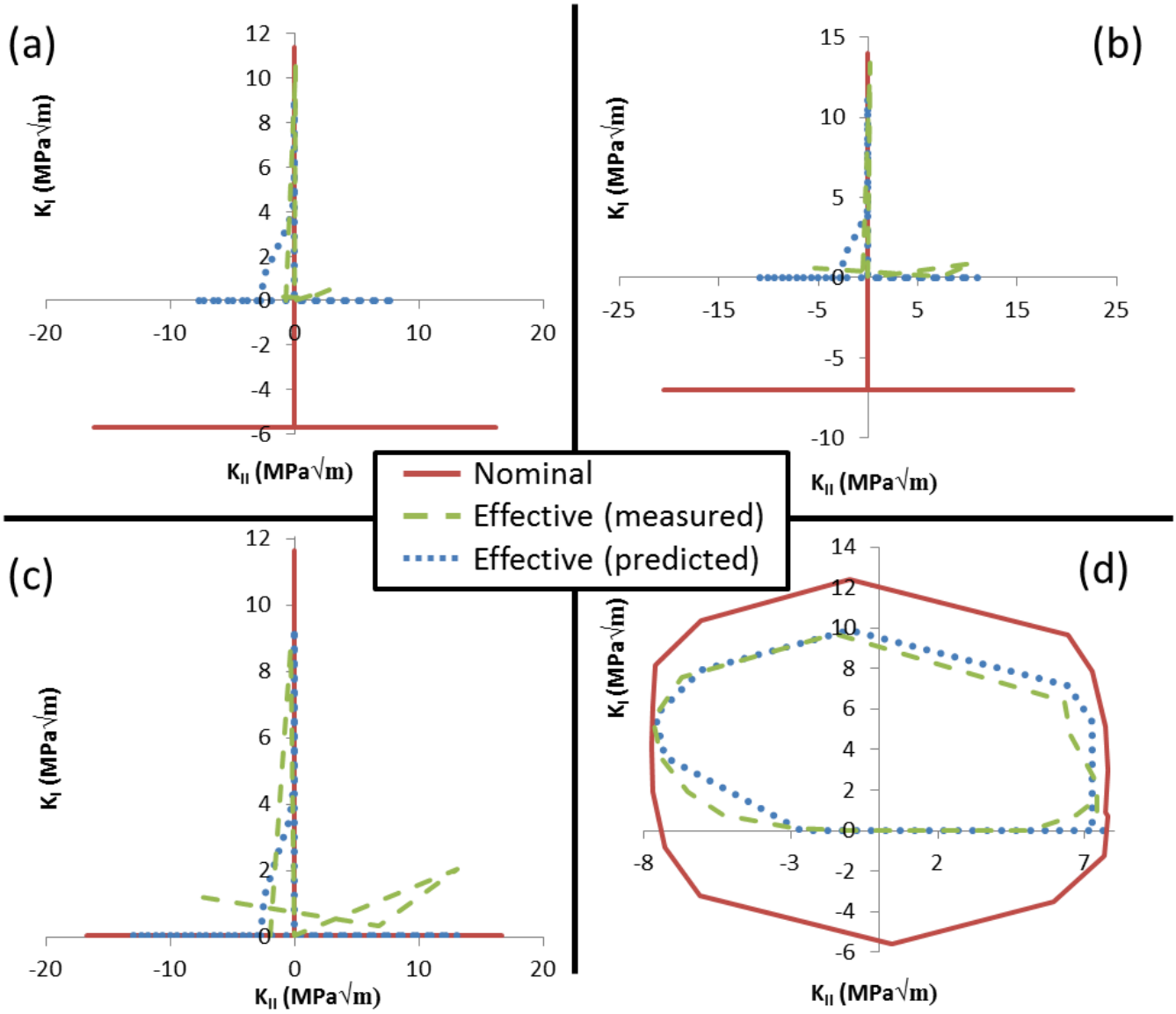

Figure 7.4: Evolution of K^{nom}, K^{eff} measured by DIC, and K^{eff} predicted using the proposed approach in the $K_I - K_{II}$ space, for various experiments: experiment $N°10$ ($F = +11/-5$, $C = \pm 160\ Nm$) at cycle 2000 (a) & 11 000 (b), experiment $N°11$ ($F = +11/0\ kN$, $C = \pm 160\ Nm$) at cycle 2000 (c) and 90 ° out-of-phase experiment $N°14$ ($F = +11/-5\ kN$, $C = \pm 70\ Nm$) at cycle 5000 (d).

And the C and m coefficients determined in section 6.3.4. This equation does not account for the intrinsic influence of the shape of the loading path, which was however not highlighted by non-proportional mixed-mode I + II experiments, and seems to be of second order relative to the large extrinsic influence of the shape of the nominal path on the effective SIFs (due to contact & friction).

Using a explicit approach, crack growth will finally be evaluated as illustrated on figure 7.5.

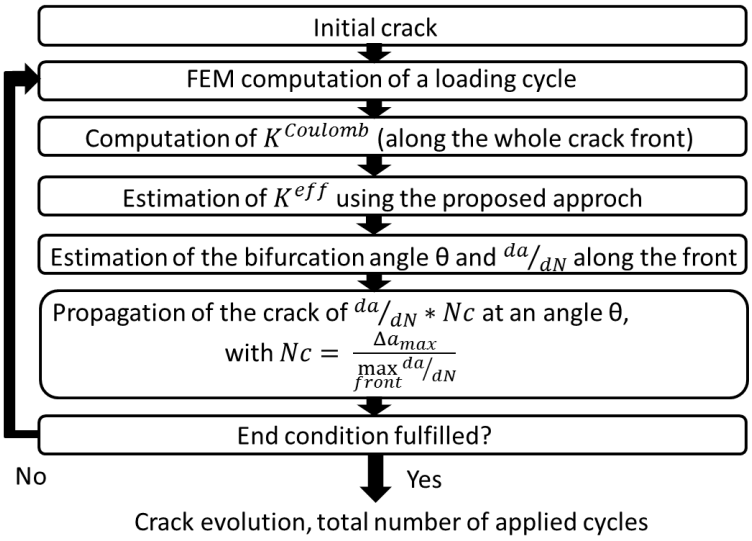

Figure 7.5: Principle of the crack growth simulations. Δa_{max} is the maximum crack growth increment (set by the user) at each step.

The relevance of the proposed approach will first be assessed, based on experimental observations of 3D crack growth in $R260$ steel under sequential or pseudo-sequential mode I + II + III loadings made by Xiqing Chang, student from ENSTA, during a 10 weeks internship. Nawfal Bouhout, a student from Ecole des Ponts, helped with the development of the numerical simulations during a 6 month internship.

7.2 Crack growth predictions for sequential mixed-mode I + II & III experiments

7.2.1 Experimental setup and results

Cylindrical samples, 12 mm in diameter, with a transverse 1.6 mm-deep notch, as illustrated on figure 7.6 were precracked in mode I (under a maximum tensile load of 17 kN, with $R = 0$), and then submitted to sequential tension ($R = 0$) + reversed torsion or tension-compression and reversed torsion, keeping compression constant while shearing (pseudo-sequential loading), until fracture. The force induces mode I along the crack, while the torque induces mostly mode III at the deepest point and mode II on the edges. The loading conditions are indicated in Table 7.1.

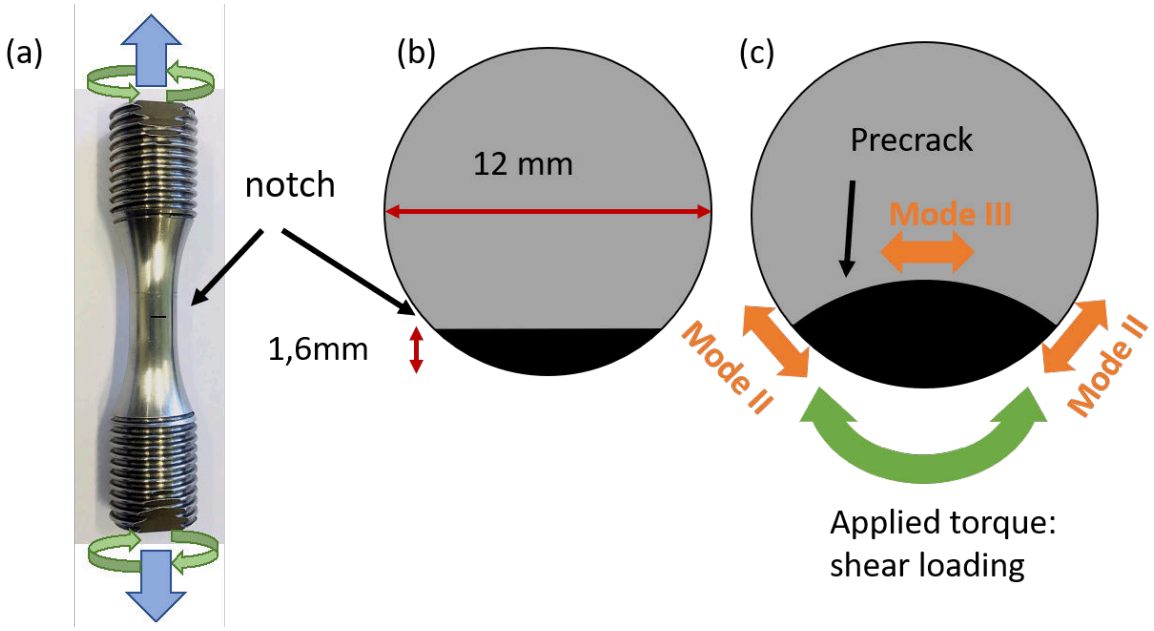

Figure 7.6: Notched sample for sequential mixed-mode I + II & III tests (a), initial notch geometry (b), semi-circular front after mode I precracking & schematic of the applied shear loading (c).

Table 7.1: Test conditions and resulting crack growth for sequential mixed mode I+ II & III experiments. N_{sequ} correspond to the number of applied mixed-mode cycles.

Test $N°$	N of pre-cracking cycles	Precrack depth (mm)	Fmax/Fmin (kN)	Cmax/Cmin (Nm)	N_{sequ}	Crack path
1	130000	4	17/-7	33/-31	8885	coplanar
2	112000	3	17/0	33/-31	15745	coplanar
3	135000	3.8	17/0	66/-62	9618	bifurcation

The precrack & final crack front can be seen on the fracture surfaces (see figures 7.7 & 7.8). After precracking, the crack front is approximately semi-circular (figure 7.7 later), while at the end of the mixed-mode experiment, just before unstable fracture, the front is rather straight (see figure 7.7 later). For that test $N°1$, the final front is somewhat asymmetric probably due to a misalignment of the sample axis and the axis of the rotative actuator.

The coordinates of points along the precrack front and final crack front were measured on fractographic images and 4^{th} order polynomials were fitted to be used in XFEM simulations, as shown below.

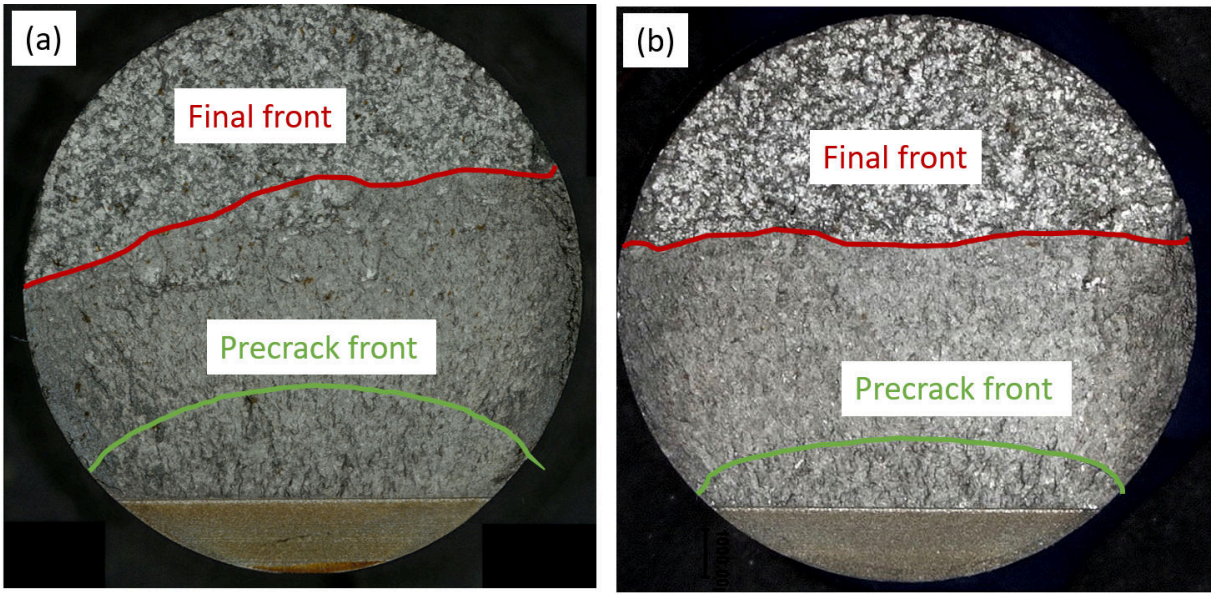

Figure 7.7: Precrack and final crack front of sequential mixed-mode I + II & III test $N°1$ ($F = 17/-7\ kN$, $C = 33/-31\ Nm$) (a) and test $N°2$ ($F = 17/0\ kN$, $C = 33/-31\ Nm$) (b).

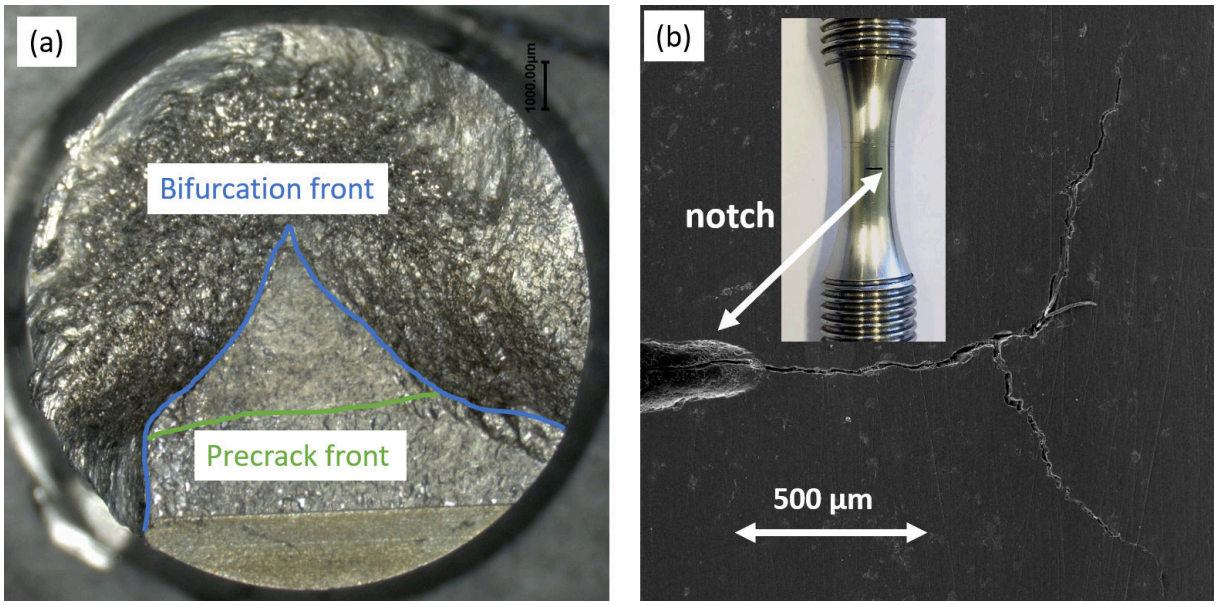

Figure 7.8: Precrack and final crack front of sequential mixed-mode I + II & III test $N°3$ ($F = 17/0\ kN$, $C = 66/-62$ Nm) (a), along with a side surface view of the bifurcation (obtained by SEM observation of a casted replica) (b).

Wear marks were observed on the fracture surfaces. During tests $N°1$ & 2 (coplanar growth), wear was more pronounced on the edges than in the center of the crack (see figure 7.9), which can be explained by the higher shear SIFs at the edges (see figures 7.11 & 7.12).

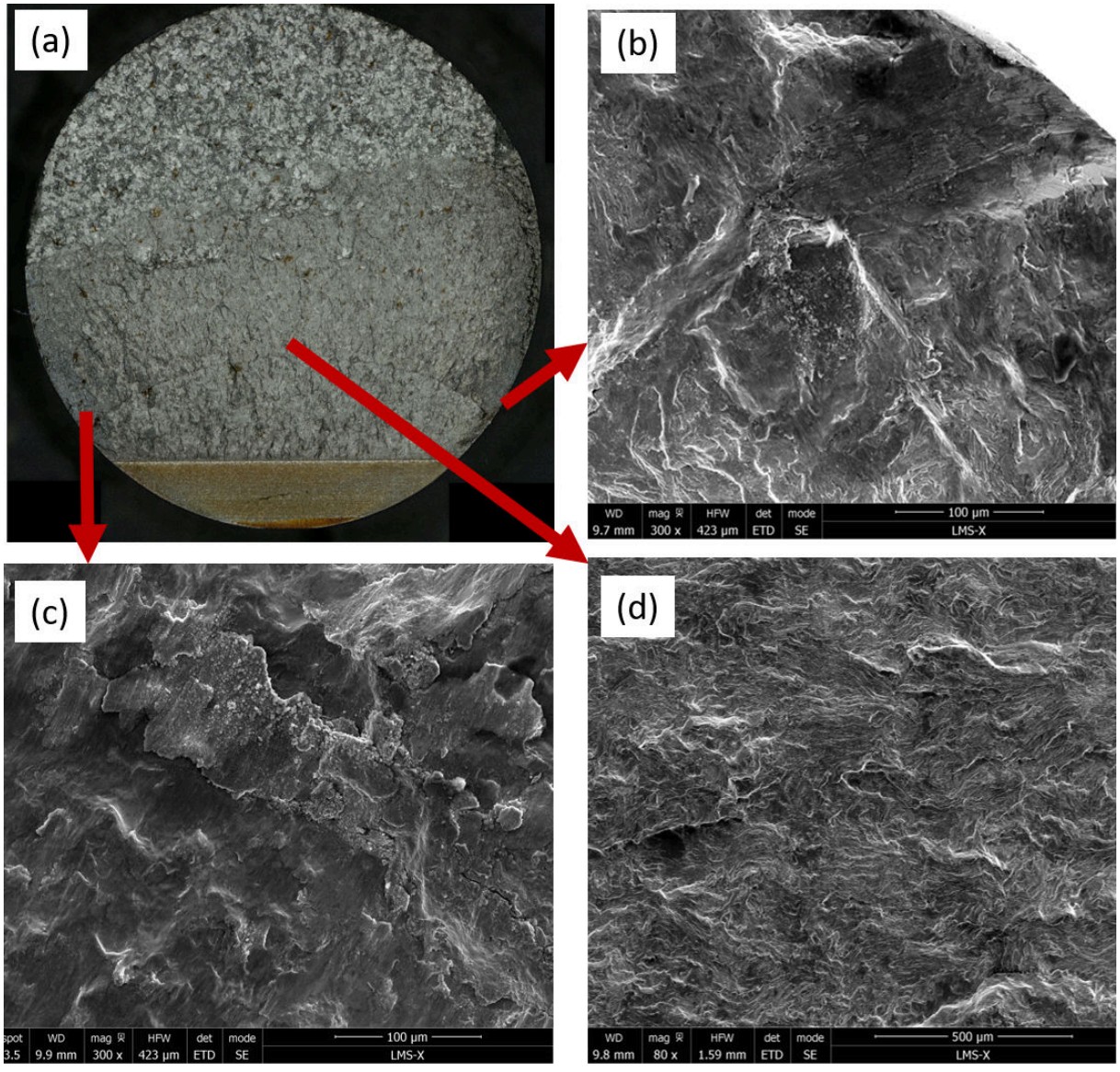

Figure 7.9: Wear at various positions on the crack of test $N°1$ ($F = 17/-7\ kN$, $C = 33/-31\ Nm$).

7.2.2 Numerical simulations of the tests

Since the initial notch, precrack, and final crack front shapes are known (see figure 7.7), along with the applied load, torque and number of cycles, FEM crack-propagation simulations using the aforementioned approach were run in order to asses its ability to predict crack growth:

- Simulations of precracking (mode I alone), with various values of U_I.
- Simulations of crack growth during the sequential experiment (starting from the experimental precrack front), with various values of α & U_I.

The friction coefficient μ and the sliding threshold K_{II}^0 were set to the values determined in section 6.3.6 ($\mu = 0.3$, $K_{II}^0 = \textit{confidential data}\ MPa\sqrt{m}$). K_{II}^0 was not changed, as its influence would be small for a such high shear SIFs amplitudes.

A 40 mm long elastic cylinder with 12 mm diameter is considered. The imposed boundary conditions are zero displacement on the bottom, and imposed force & torque at the top of the model (see figure 7.10). The initial crack front shape is given as an input for the simulation in the form of a 4^{th} order polynomial, along with the loading range and Δa_{max} (maximum allowed crack growth increment at each step over the whole front, fixed a 0.2 mm). The crack propagation is then simulated following the explicit scheme presented previously (see fig. 7.5). The mesh is given on figure 7.10. The distance between two nodes of the initial crack front is set at ≈ 0.1 mm. At each step, the SIFs are computed along the whole crack front, except at the nodes located too close to the external surface, in order to avoid corner point singularities.

Examples of SIFs profiles for an applied force (a) or torque (b) are given on figures 7.11 & 7.12 for the final precrack front and final crack front respectively. The force induces mode I along the crack, while the torque induces shear modes, mostly mode III at the centre and mode II on the edges. While Squat-type cracks also experience sequential mixed-mode I + II & III, in this case mode II is mostly found at the centre and mode III on the edges.

The SIFs are then fitted by a 4^{th} order polynomial to remove spurious oscillations, and used estimate the crack growth direction and rate on the whole crack front (yellow elements on figure 7.10), exception made of the points that are too close to the surface (black elements on figure 7.10.a & b), which are extrapolated by supposing that the crack front is straight near the surface. Nodes can be added on the side surface to keep the correct density (see figure 7.10.c).

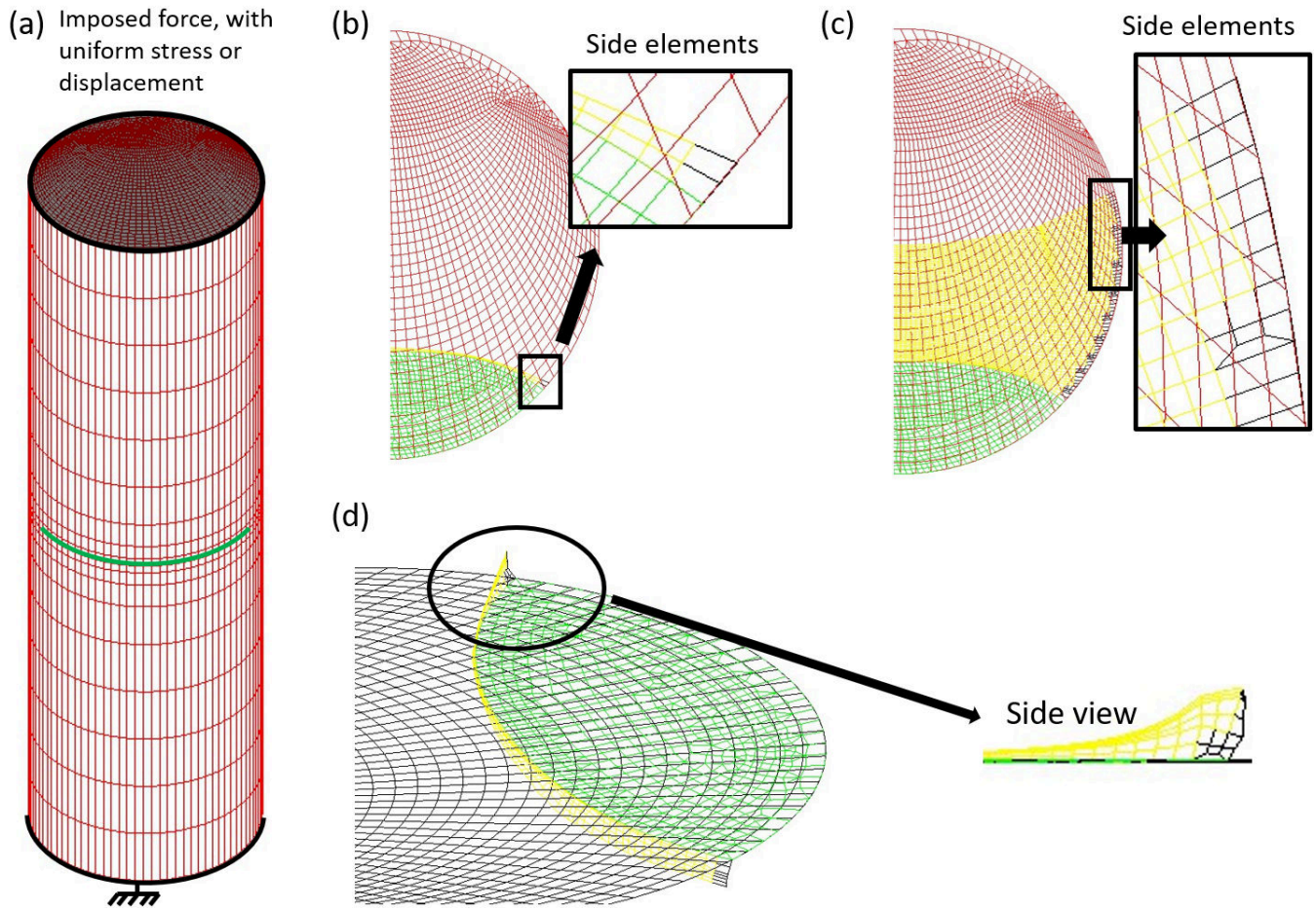

Figure 7.10: (a) mesh of the sample. (b) mesh of the initial crack (green), and propagation after 1 iteration (yellow & black). (c) example of crack mesh after 30 iterations. (d) Mesh of the crack after bifurcation.

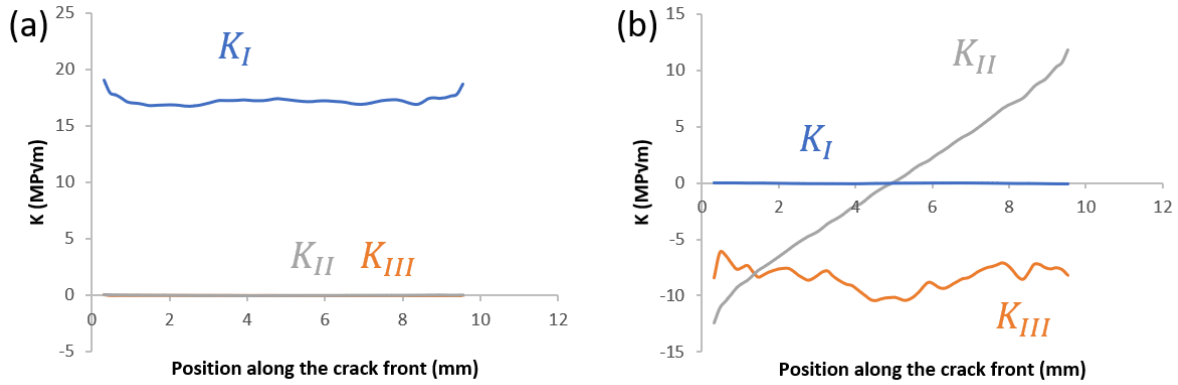

Figure 7.11: Evolution of the SIFs along the precrack front a) at peak tensile load and b) at maximum torque for the sequential mixed-mode I + II & III test $N°1$, for a 17 kN tensile load, and a 35 Nm torque.

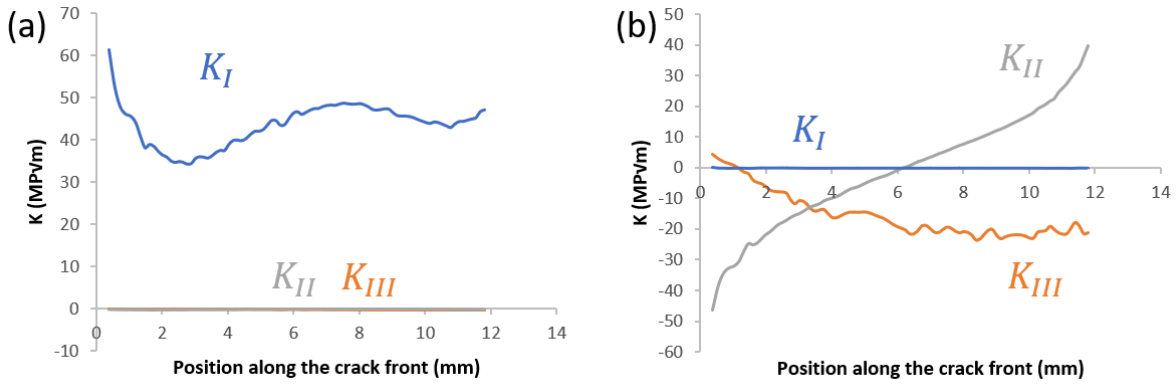

Figure 7.12: Evolution of the SIFs along the final crack front a) at peak tensile load and b) at maximum torque for the sequential mixed-mode I + II & III test $N°1$, for a 17 kN tensile load, and a 35 Nm torque.

Results of precracking simulations, in terms of number of cycles to retrieve the experimental precrack front, are reported in table 7.2, along with some examples of computed precrack fronts in figure 7.13. U_I = *confidential data* leads to a correct estimation of the number of cycles to get the precrack for both tests, while higher values of U_I underestimate it. However, crack initiation from the notch is certainly not immediate (as it is assumed in the simulation), meaning that higher values of U_I could be correct. If crack initiation is assumed to take 30 000 *cycles*, U_I = *confidential data* gives the best results.

Whatever the value of U_I, the crack front shape is incorrect near side surfaces (overestimated crack depth), which could be due either to the assumption of uniform U_I along the front (instead of a lower value near side surface to capture a locally stronger plasticity-induced closure, as successfully done by Newmann and Raju [Newman and Raju, 1981]), or to a non-uniform crack initiation starting from the center of the notch, or to the fact that XFEM assume a $1/\sqrt{r}$ singularity, which is wrong near side surfaces [Bazant and Estenssoro, 1979].

Table 7.2: Error between the computed and the measured numbers of cycles to get a precrack front corresponding to that of test $N°1$ or $N°2$, depending on U_I.

U_I	Error on $N_{cycles,\ precrack}$ for test $N°1$ (%)	Error on $N_{cycles,\ precrack}$ for test $N°2$ (%)
confidential data	4	0
confidential data	-26	-29
confidential data	-46	-48

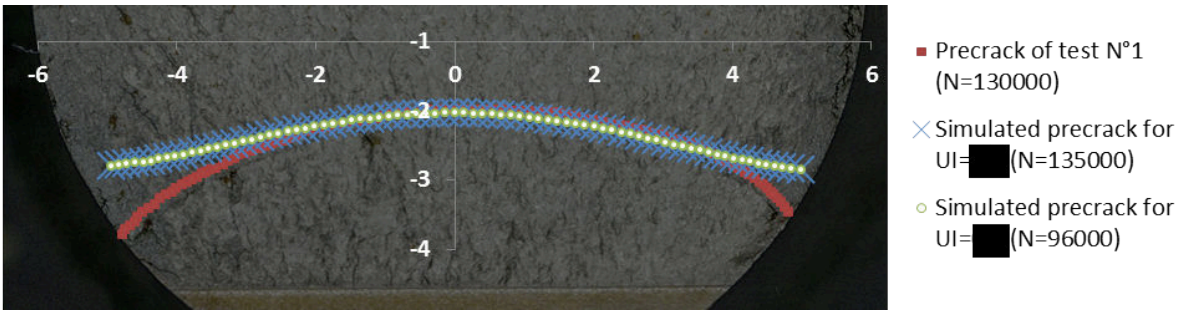

Figure 7.13: Predicted precrack front shape for various U_I, versus the experimental one.

Results of crack propagation simulations under a sequential loading, in terms of crack path and number of cycles to retrieve the experimental final crack front, are reported in table 7.3. Some examples of computed crack fronts are reported in figure 7.14. For test $N°1$ & 2, coplanar crack growth is predicted for all sets of parameters, which is consistent with the experimental results. The best results in terms of number of cycles to failure are obtained for U_I *confidential data* and α between *confidential data*. However, bifurcation is not predicted for test $N°3$ if $\alpha =$ *confidential data*, while it is for $\alpha =$ *confidential data* (as illustrated on figure 7.10.d). The second value should thus be preferred. This bifurcation is predicted to initiate immediately at 70° near the side surfaces, while the crack remains coplanar in its center, which is consistent with the experiment. At each iteration, a larger part of the front (from the side surfaces towards the center) is predicted to bifurcate, until the simulation stops due to crack meshing difficulties. $U_I =$ *confidential data* and $\alpha =$ *confidential data* also give reasonable predictions in terms of number of cycles to failure and crack path. It is likely that the presence of the notch, which reduces the contact surface (and is not accounted for in the simulations), reduces the effects of crack face friction, and thus artificially increases α.

The computed crack fronts, illustrated on figure 7.14, are concave near side surfaces instead of convex. This could be due to a locally overestimated ΔK_{shear} (locally stronger friction? corner point singularities, see section 2.2.4?). As expected, the crack concavity is reduced when α decreases (and the relative influence of mode I increases).

Table 7.3: Error between the computed and the measured numbers of cycles for sequential test $N°1$ or $N°2$, and prediction of crack bifurcation for test $N°3$, depending on U_I & α.

U_I	α	Error on N_{sequ} for test $N°1$ (%)	Error on N_{sequ} for test $N°2$ (%)	Prediction of bifurcation for test $N°3$
confidential data	*confidential data*	-5	-18	yes
confidential data	*confidential data*	19	16	no
confidential data	*confidential data*	37	16	yes
confidential data	*confidential data*	69	67	no
confidential data	*confidential data*	104	74	yes
confidential data	*confidential data*	144	152	no

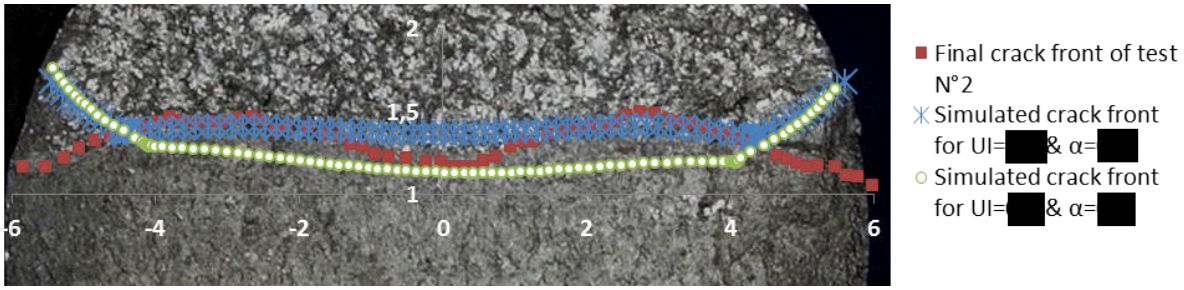

Figure 7.14: Predicted crack front shape for various U_I & α, versus the experimental one.

From the simulations of precracking and sequential loading, $U_I =$*confidential data* and $\alpha =$ *confidential data* are the best values to predict the crack paths and growth rates. Those value are quite close to those obtained from effective SIFs measurements during sequential mixed mode I+II ($U_I =$ *confidential data* and $\alpha =$ *confidential data*). The difference can partly be explained by the presence of the notch which reduces the contact surface, and by the thicker specimen (which reduces closure effects, see section 2.4). However, given the uncertainty on the crack growth rate prediction using ΔK_{equ}^{eff} (90% of the data within a factor 4 in crack growth, see figure 6.60), most of the tested combinations of U_I & α can be considered as reasonably good.

7.3 Conclusions & perspectives for the proposed approach

A simplified, engineer approach using only LEFM and the MTS criterion and thus compatible with SNCF's numerical tool was proposed to estimate the effective SIFs (taking crack face roughness into account), and predict the crack path and growth rate.

- The proposed approach allows a reasonable prediction of the effective SIFs for non-proportional mixed-mode I + II experiments, which a simple Coulomb friction model cannot do.
- It was applied to sequential mixed-mode I + II & III experiments, with a reasonable agreement in terms of crack path and growth rate. The parameters giving the best predictions were close to those determined for sequential mixed-mode I + II experiments. However, the shape of the crack near side surfaces was not entirely satisfying, which could be due to assumptions of uniform closure effects, or overestimated shear mode SIFs near side surfaces.
- This approach will now be implemented in SNCF's numerical tool and its prediction for squat-type cracks will be compared with on-field measured data.
- Crack propagation experiments on rails are currently performed at the Japanese Railway Technical Research Institute, with a simplified initial crack geometry and a simplified loading. The results of those experiments will also be compared to the predictions of the proposed approach.
- The fracture surfaces of Squat-type cracks taken from the field and opened in a three point bending hydraulic press will be compared to the fracture surfaces obtained during sequential mixed-mode I + II experiments, in order to qualitatively compare the amount of wear.

Chapter 8

Conclusion and perspectives

8.1 Conclusions

Typical loading paths undergone by Squat-type cracks have been estimated using SNCF's numerical tool "PropaFiss3D", for various track and temperature conditions, taking manufacturing residual stresses into account. The computed loading paths were nearly sequential mixed-mode I + II & III, including a compression phase. In order to investigate crack growth under such loadings, mode I, mixed-mode II & III and non-proportional mixed-mode I + II experiments were performed under representative loading paths. The goal was to assess the influence of each mode alone, as well as their combination, on crack growth.

In order to monitor such a large number of fatigue crack propagation experiments (more than 40), Digital Image Correlation (DIC) was extensively used. A numerical tool was developed to obtain the crack tip position and effective SIFs under non-proportional mixed-mode loading including compression phases from the measured displacement fields. Classical methods (that is: projection over William's expansion series) were shown to overestimate the effective SIFs and to yield an incorrect crack tip position in such cases. It could nonetheless be used to locate the crack tip position in mode I, by applying it to image pairs captured at maximum load and after a small elastic unloading.

In order to estimate the effective SIFs in the presence of substantial crack tip plasticity as well as contact & friction stresses between the crack faces, an inverse analysis of the measured relative displacement jump profiles, compared to the profile obtained from an elastic-plastic computation plus an offset, was proposed. Such method was found to yield satisfying results, as long as the couplings between shear and tensile plastic flows at the crack tip remained small. An approach coupling DIC and FEM computations was also proposed to evaluate the effective SIFs and the contact stresses along the crack faces, but was found to be much more time consuming and noise sensitive than the previous approach, which was thus preferred. Details about experimental procedures are given in chapter 3.2.

During some of these experiments, sand blasting was shown to be a simple and effective surface marking technique for DIC on casted replicas (impossible with a speckle painting), allowing in-plane displacement fields to be obtained, even when the specimen surface cannot be observed directly with a camera. The out-of-plane displacements were obtained from topographic measurement of the replicas, using either an Atomic Force Microscope or a digital optical microscope (depending on the displacement range).

Mode I experiments (presented in chapter 4) were performed at various load ratios, and the measured crack growth rates correlated well with ΔK_I^{eff}. The compressive stage of the cycles did not accelerate crack growth, as it was expected, but slowed it down. This was attributed to the compression-enhanced build up of an oxide layer, leading to oxide induced closure.

During proportional mixed-mode II & III experiments (presented in chapter 5), long coplanar fatigue crack growth (instead of bifurcation) was observed for a sufficiently high loading range. The crack growth rates for such coplanar growth correlated well with $\Delta K_{equ}^{eff} = \sqrt{\Delta K_{II}^{effective^2} + 1.25 \Delta K_{III}^{effective^2}}$. However, even when coplanar shear mode crack growth was witnessed, the crack eventually bifurcated, which was attributed to the shielding effects of multiple branch cracks more or less normal to the main crack plane.

Eventually, mode I alone was unable to explain the crack growth in rails, as the crack growth rates predicted for a realistic ΔK_I range (neglecting water trapping/pressurization effect) were too small compared to the on-field measured values. Neither were shear modes alone, as the observed crack path was not consistent with the one observed in rails at similar crack growth rate. It is most likely the combination of opening and shear modes in a complex loading path that explains the crack growth in rails.

Sequential mixed-mode I + II experiments (presented in chapter 6) were thus performed, with or without a static compression while shearing. During these experiments, the crack bifurcated when $\Delta K_{II}^{eff}/\Delta K_{I}^{eff}$ reached approximately 2. A normal compression while shearing led to substantially longer coplanar growth, as it slowed down crack face wear (mostly by reducing the sliding range) and the resulting rise of $\Delta K_{II}^{eff}/\Delta K_{I}^{eff}$.

For sequential, "tilted sequential" and 90° out-of-phase loadings, the crack growth rates correlated well with $\Delta K_{eq}^{eff} = \sqrt{(\Delta K_{I}^{eff})^2 + (\Delta K_{II}^{eff})^2 + \frac{1}{1-\nu}(\Delta K_{III}^{eff})^2}$. No significant intrinsic influence of the effective loading path on the crack growth rate was found. For sequential mode I + II, the simple sum of the growth rates for mode I alone & mode II alone also gave a satisfying estimate of the measured crack growth rates, which tends to rule out a synergistic effect due to plastic interactions.

The MTS criterion, applied to effective loading paths, underestimated the extent of coplanar growth, while the MTSp criterion (which takes into account plasticity-induced stress redistribution at the crack tip) provided better predictions of the crack length at bifurcation, but did not predict truly coplanar growth before ($\approx 10°$ angle). Taking contact and friction stresses into account in the MTSp was found to improve the predictions.

Friction and interlocking between the rough crack faces led to a strong reduction of the effective SIFs during mixed-mode II & III and non-proportional mixed-mode I + II experiments, even without any normal compression applied, while Coulomb's law applied to a smooth crack (the usual approach in industrial computations) does not predict any friction in such cases. The sliding of such rough crack faces also induced dilatancy effects: two mode I sub-cycles were observed within each reversed shear mode cycle.

Due to these friction effects, the shape of the nominal loading paths had a large influence on the effective SIFs during non-proportional mixed-mode experiments. A 90° out-of-phase loading path led to twice higher shear-mode SIFs than a sequential loading path at similar nominal SIFs ranges: in the first case, the crack was opened at maximum shear stress, while in the later case, the crack was closed while shearing, and underwent friction.

If friction and interlocking effects control the effective SIFs, the later, as well as the normal compression, control crack face wear, which plays a central role. Indeed, wear reduces the crack face roughness and thus friction between the crack faces, leading to increased effective shear SIFs. As a result, during sequential mixed-mode I + II tests, $\Delta K_{II}^{eff}/\Delta K_{I}^{eff}$ was often initially well below its nominal value, but raised progressively during coplanar growth due to crack face wear. Wear debris came out of the crack during some experiments. Depending on the loading path and amplitude, very different fracture surfaces were observed, going from unaltered mode I-like surfaces to highly worn surfaces. Intermediate cases were also obtained: highly worn surfaces away from the tip, in areas which underwent many cycles, and unaltered areas close to the tip, where the surfaces were more recently created and the relative sliding displacements smaller. A normal compression seemed to change the degree of crack faces oxidation and the proportion of trapped debris, thus certainly modifying both friction and wear rate.

In the end, effective SIFs, crack face roughness & wear are tightly linked. The challenge for structural applications is thus not just to choose the most appropriate bifurcation criterion and crack growth law, but also to take crack face roughness and wear into account in order to estimate the correct effective SIFS to use in these models.

In order to predict the effective loading path from the nominal one, a simple, engineering approach was proposed for SNCF's numerical scheme (presented in chapter 7). It uses a constant mode I load ratio U_I, and relies on the division of friction into two sources: an extrinsic one (due to the far field compression), and an intrinsic friction one (due to crack face roughness). It allowed a reasonable prediction of the effective SIFs from non-proportional mixed-mode I + II experiments, which a simple Coulomb's friction model could not do.

Coupled with simple LEFM criteria/models, it successfully predicted the crack path and growth rate for sequential mixed mode I + II & III experiments.

8.2 Perspectives

The proposed approach remains yet to be implemented in SNCF's numerical scheme to perform simulations at the structural scale. This will allow to validate the approach by comparing the crack path and mean crack growth rate over a year to SNCF's on field measured values.

This validation at the structural scale will also be performed using crack propagation experiments on rails, which are currently performed at the Japanese Railway Technical Research Institute, with a simplified initial crack geometry and a simplified loading.

Finally, the fracture surfaces of Squat-type cracks taken from the field will be compared to the fracture surfaces obtained during sequential mixed-mode I + II experiments. This will allow a qualitative comparison of the amount of wear, and thus of the range of the effective shear SIFs.

The proposed approach to estimate the effective SIFs is a simplified engineering approach, and could be improved by modeling wear in the FEM simulations. This has been done (for crack initiation and propagation) by Llavori et al. using an Archard's law [Llavori et al., 2019], or by Cardoso et al. [Cardoso et al., 2019] (for crack initiation) using the dissipated energy. The influence of a third body layer, which was witnessed during some sequential mixed-mode I + II experiments, may be non negligible and can also be modeled, as done by Arnaud [Arnaud et al., 2017].

Such wear modelling would not only provide a better estimation of the effective SIFs for a constant amplitude loading, but also account for wear-induced history effects: after several cycles at high shearing range, cycles at lower amplitude should give rise to reduced friction, due to the more pronounced wear induced by the previous loading cycles.

A proper modeling of oxide-induced closure, probably important for squat-type cracks submitted to large compressions and to moisture, would be advisable to improve the effective SIFs estimation. There is currently no such model available in the literature. This is not surprising, since such a model would have to consider complex, coupled mechanical, thermal and chemical mechanisms, and to capture the effects of crack width (distance from a free surface) and orientation (upwards/downwards growth) on the release of oxide debris (as shown by Maierhofer et al. [Maierhofer et al., 2018]).

Eventually, even if the effective SIFs are more accurately estimated, it may still be advisable to take crack tip plasticity into account (since it improves crack path predictions), but cyclic plasticity is not compatible with the XFEM method yet. Even if it was, those computations, coupled with the non-linear Coulomb's friction and the large model size would lead to prohibitive computation times. A solution would be to compute the effective SIFs and possibly non-singular stresses using the XFEM method, and use them as boundary conditions for FEM elastic-plastic computations at the crack tip scale (a few mm), for every node along the crack front.

From an industrial perspective, the improved SNCF's computation scheme will help understand crack propagation in rails and optimize maintenance intervals. It should allow to quantify the influence of various operating conditions, such as the type of train, train speed, wheel and rail geometry, track stiffness, etc... thus allowing to propose optimized conditions.

If the approach is proven successful, experiments could then be performed on other rail grades, such as $R200$, in order to help understand their advantages and drawbacks, and select the best grade depending on the operating conditions.

Bibliography

[cas, 2019] (2019). Cast3m (castem). http://www-cast3m.cea.fr/.

[Abanto-Bueno and Lambros, 2002] Abanto-Bueno, J. and Lambros, J. (2002). Investigation of crack growth in functionally graded materials using digital image correlation. *Eng Fract Mech*, 69(14-16):1695–1711.

[Akama, 2003] Akama, M. (2003). Fatigue crack growth under mixed loading of tensile and in-plane shear modes. *QR of RTRI*, 44:65–71.

[Akama and Kiuchi, 2012] Akama, M. and Kiuchi, A. (2012). Long co-planar mode III fatigue crack growth under non-proportional mixed mode loading in rail steel. *J rail and rapid transit*, 226:489–500.

[Amestoy et al., 1979] Amestoy, M., Bui, H., and Dan Van, K. (1979). Déviation infinitésimale d'une fissure dans une direction arbitraire. *C.R.A.S.*, 289:99–102.

[Ancellotti et al., 2017] Ancellotti, S., Benedetti, M., Dallago, M., and Fontanari, V. (2017). Fluid Pressurization and Entrapment Effects on the SIFs of Cracks produced under lubricated Rolling-Sliding Contact Fatigue. *Procedia structural integrity*, 2:3098–3108.

[Arnaud, 2018] Arnaud, P. (2018). *Etude expérimentale et numérique de l'usure et de son influence sur les mécanismes de fissuration en fretting et fretting fatigue*. PhD thesis, Ecole centrale de Lyon.

[Arnaud et al., 2017] Arnaud, P., Fouvry, S., and Garcin, S. (2017). A numerical simulation of fretting wear profile taking account of the evolution of third body layer. *WEAR*, 376-377:1475–1488.

[Barker et al., 1985] Barker, D. B., Sanford, R. J., and Chona, R. (1985). Determining K and related stress-field parameters from displacement fields. *Experimental Mechanics*, 25:399–407.

[Bazant and Estenssoro, 1979] Bazant, Z. P. and Estenssoro, L. F. (1979). Surface singularity and crack propagation. *Int J Solids Struct.*, 15:405–426.

[BEATT, 2006] BEATT (2006). Rapport d'enquête technique sur le déraillement du train 5941 survenu le 25 février 2006 à Saint Flour (15). Technical report, Bureau d'Enquêtes sur les Accidents de Transport Terrestre.

[BEATT, 2016] BEATT (2016). Rapport d'enquête technique sur la rupture multiple de rail, franchie en vitesse par des trains le 26 novembre 2013 à Carbonne (31). Technical report, Bureau d'Enquêtes sur les Accidents de Transport Terrestre.

[BEATT, 2017] BEATT (2017). Rapport d'enquête technique sur les multiples ruptures de rail au passage du train 72049 entre Pons et Jonzac (17) le 13 décembre 2016. Technical report, Bureau d'Enquêtes sur les Accidents de Transport Terrestre.

[Beretta et al., 2010] Beretta, S., Folett, S., and Valiullin, K. (2010). Fatigue crack propagation and threshold for shallow micro-cracks under out-of-phase multiaxial loading in a gear steel. *Eng Fract Mech*, 77:1835–1848.

[Bertolino and Doquet, 2009] Bertolino, G. and Doquet, V. (2009). Derivation of effective stress intensity factors from measured crack face displacements. *Eng Fract Mech*, 76:1574–1588.

[Blaysat et al., 2015] Blaysat, B., Hoefnagels, J. P. M., Lubineau, G., Alfano, M., and Geers, M. G. D. (2015). Interface debonding characterization by image correlation integrated with Double Cantilever Beam kinematics. *Int J Solids Struct.*, 55:79–91.

[Bogdanski and Lewicki, 2008] Bogdanski, S. and Lewicki, P. (2008). 3D model of liquid entrapment mechanism for rolling contact fatigue cracks in rails. *Wear*, 265:1356–1362.

[Bogdanski et al., 1998] Bogdanski, S., Olzak, M., and Stupnicki, J. (1998). Numerical modelling of a 3d rail rcf 'squat'-type crack under operating load. *FFEMS*, 21:923–935.

[Bold, 1990] Bold, P. (1990). *Multiaxial fatigue crack growth in rails.* PhD thesis, University of Sheffield.

[Bonniot et al., 2018] Bonniot, T., Doquet, V., and Mai, S. H. (2018). Mixed mode II and III fatigue crack growth in a rail steel. *Int J Fatigue*, 115(October 2018):42–52.

[Bonniot et al., 2019] Bonniot, T., Doquet, V., and Mai, S. H. (2019). Determination of effective stress intensity factors under mixed-mode from digital image correlation fields in presence of contact stresses and plasticity. *STRAIN*.

[Branco and Antunes, 2003] Branco, R. and Antunes, F. V. (2003). Fatigue crack growth under mixed loading of tensile and in-plane shear modes. *Eng Fract Mech*, 75.

[Branco et al., 2008] Branco, R., D.M., R., and Antunes, F. (2008). Influence of through-thickness crack shape on plasticity induced crack closure. *FFEMS*, 31:209–220.

[Brown et al., 1985] Brown, M. W., Hay, E., and Miller, K. J. (1985). Fatigue at notches subjected to reversed torsion and static axial loads. *FFEMS*, 8(3):243–258.

[C. Betegón Biempica et al., 2009] C. Betegón Biempica, C., del Coz Díaz, J., García Nieto, P., and Peñuelas Sánchez, I. (2009). Nonlinear analysis of residual stresses in a rail manufacturing process by FEM. *Applied Mathematical Modelling*, 33:34–53.

[Cardoso et al., 2019] Cardoso, R. A., Doca, T., Néron, D., Pommier, S., and Araújo, J. A. (2019). Wear numerical assessment for partial slip fretting fatigue conditions. *Tribology International*, 136:508–523.

[Carlson and Kardomateas, 1994] Carlson, R. and Kardomateas, G. (1994). Effects of compressive load excursions on fatigue crack growth. *Int J Fatigue*, 16:141–146.

[Christodoulou et al., 2016] Christodoulou, P. I., Kermanidis, A. T., and Haidemenopoulos, G. N. (2016). Fatigue and fracture behavior of pearlitic Grade 900A steel used in railway applications. *Theoretical and Applied Fracture Mechanics*, 83:51–59.

[Dahlin and Olsson, 2003] Dahlin, P. and Olsson, M. (2003). The effect of plasticity on incipient mixed-mode fatigue crack growth. *FFEMS*, 26:577–588.

[Dahlin and Olsson, 2004] Dahlin, P. and Olsson, M. (2004). Reduction of mode I fatigue crack growth rate due to occasional mode II loading. *Int J Fatigue*, 26:1083–1093.

[Dang Van, 1973] Dang Van, K. (1973). A comprehensive approach for modeling fatigue and fracture of rails. *Sciences Technique Armement*, page 47.

[Dang Van et al., 2009] Dang Van, K., Maitournam, M., Moumni, Z., and Roger, F. (2009). A comprehensive approach for modeling fatigue and fracture of rails. *Eng Fract Mech*, 76:2626–2636.

[de Matos and Nowell, 2007] de Matos, P. and Nowell, D. (2007). On the accurate assessment of crack opening and closing stresses in plasticity-induced fatigue crack closure problems. *Eng Fract Mech*, 74:1579–1601.

[de Matos and Nowell, 2008] de Matos, P. and Nowell, D. (2008). The influence of the Poisson's ratio and corner point singularities in three-dimensional plasticity-induced fatigue crack closure: A numerical study. *Int J Fatigue*, 30:1930–1943.

[de Matos and Nowell, 2009] de Matos, P. and Nowell, D. (2009). Experimental and numerical investigation of thickness effects in plasticity-induced fatigue crack closure. *Int J Fatigue*, 31:1795–1804.

[Decreuse et al., 2009] Decreuse, P. Y., Pommier, S., Gentot, L., and Pattofatto, S. (2009). History effect in fatigue crack growth under mixed-mode loading conditions. *Int J Fatigue*, 31:1733–1741.

[Decreuse et al., 2012] Decreuse, P. Y., Pommier, S., Poncelet, M., and Raka, B. (2012). A novel approach to model mixed mode plasticity at crack tip and crack growth. Experimental validations using velocity fields from digital image correlation. *Int J Fatigue*, 42:271–283.

[Destuynder et al., 1983] Destuynder, P., Lescure, S., and Djaoua, M. (1983). Some remarks on elastic fracture mechanics. *Journal de mécanique théorique et appliquée*, 2:113–135.

[Donzella et al., 2005] Donzella, G., Faccoli, M., Ghidini, A., Mazzù, A., and Roberti, R. (2005). The competitive role of wear and RCF in a rail steel. *Eng Fract Mech*, 72:287–308.

[Doquet et al., 2009] Doquet, V., Abbadi, M., Bui, Q. H., and Pons, A. (2009). Influence of the loading path on fatigue crack growth under mixed-mode loading. *Int J Fracture*, 159:219–232.

[Doquet and Bertolino, 2008a] Doquet, V. and Bertolino, G. (2008a). A material and environment-dependent criterion for the prediction of fatigue crack paths in metallic structures. *Eng Fract Mech*, 75:3399–3412.

[Doquet and Bertolino, 2008b] Doquet, V. and Bertolino, G. (2008b). Local approach to fatigue cracks bifurcation. *Int J Fatigue*, 30:942–950.

[Doquet et al., 2010a] Doquet, V., Bui, Q. H., Bertolino, G., Merhy, E., and Alves, L. (2010a). 3D shear-mode fatigue crack growth in maraging steel and Ti-6Al-4V. *Int J Fracture*, 165:61–76.

[Doquet et al., 2010b] Doquet, V., Bui, Q. H., and Constantinescu, A. (2010b). Plasticity and asperity-induced fatigue crack closure under mixed-mode loading. *Int J Fatigue*, 32:1612–1619.

[Doquet et al., 1994] Doquet, V., Caldemaison, D., and Bretheau, T. (1994). Combined tension and torsion cyclic tests inside a scanning electron microscope. *Proc. 4th Int. Conf. Biaxial/multiaxial Fatigue, Saint-Germain-en-Laye*, 2:19–26.

[Doquet and Frelat, 2001] Doquet, V. and Frelat, J. (2001). Branch crack development from the flank of a fatigue crack propagating in mode II. *FFEMS*, 24(3):207–214.

[Doquet and Pommier, 2004] Doquet, V. and Pommier, S. (2004). Fatigue crack growth under non-proportional mixed-mode loading in ferritic-pearlitic steel. *FFEMS*, 27:1051–1060.

[Dylewski et al., 2017] Dylewski, B., Risbet, M., and Bouvier, S. (2017). The tridimensional gradient of microstructure in worn rails – Experimental characterization of plastic deformation accumulated by RCF. *WEAR*, 392–393:50–59.

[Erdogan and Ratwani, 1972] Erdogan, F. and Ratwani, M. (1972). A circumferential crack in a cylindrical shell under torsion. *International Journal of Fracture Mechanics*, 8:87–95.

[Erdogan and Sih, 1963] Erdogan, F. and Sih, G. C. (1963). On the crack extension in plates under plane loading and transverse shear. *Basic engineering*, 85:519–525.

[Fletcher and Beynon, 1999] Fletcher, D. and Beynon, J. (1999). A simple method of stress intensity factor calculation for inclined fluid-filled surface-breaking cracks under contact rolling. *Proc Instn Mech Engrs*, 213:299–304.

[Fletcher et al., 2007] Fletcher, D. I., Hyde, P., and Kapoor, A. (2007). Investigating fluid penetration of rolling contact fatigue cracks in rails using a newly developed full-scale test facility. *Proceedings of the Institution of Mechanical Engineers, Part F: Journal of Rail and Rapid Transit*, 221(1):35–44.

[Fremy et al., 2014a] Fremy, F., Pommier, S., Galenne, E., Courtin, S., and Le Roux, J.-C. (2014a). Load path effect on fatigue crack propagation in I + II + III mixed mode conditions - Part 2: Finite element analyses. *Int J Fatigue*, 62:113–118.

[Fremy et al., 2014b] Fremy, F., Pommier, S., Poncelet, M., Raka, B., Galenne, E., Courtin, S., and Roux, J. C. L. (2014b). Load path effect on fatigue crack propagation in I + II + III mixed mode conditions - Part 1: Experimental investigations. *Int J Fatigue*, 62:104–112.

[Gray et al., 1983] Gray, G., Williams, J., and Thompson, A. (1983). Roughness-induced crack closure: An explanation for microstructurally sensitive fatigue crack growth. *Metallurgical transactions*, 14:421–433.

[Gross et al., 1964] Gross, B., Srawley, J., and Brown, W. (1964). Stress intensity factors for a single-edge-notch tension specimen by boundary collocation of a stress function. Technical report, NASA TN D-2395.

[Gross and Mendelsohn, 1988] Gross, T. S. and Mendelsohn, D. A. (1988). On the effect of crack face contact and friction due to fracture surface roughness in edge cracks subjected to external shear. *Eng Fract Mech*, 31:405–420.

[Gross and Mendelsohn, 1989] Gross, T. S. and Mendelsohn, D. A. (1989). Mode I stress intensity factors induced by fracture surface roughness under pure mode III loading: Application to the effect of loading modes on stress corrosion crack growth. *Metallurgical Transactions A*, 20(10):1989–1999.

[Gross et al., 1995] Gross, T. S., Zhang, Y., and Watt, D. W. (1995). Fracture Surface Interference in Shear-II. Experimental Measurements of Crack-Tip Displacement Field under Mode-II Loading in 7075-T6 A1. *Acta Metallurgica et Materialia*, 43:901–906.

[Hamam et al., 2007a] Hamam, R., Hild, F., and Roux, S. (2007a). Stress intensity factor gauging by digital image correlation: Application in cyclic fatigue. *Strain*, 43(October 2006):181–192.

[Hamam et al., 2007b] Hamam, R., Pommier, S., and Bumbieler, F. (2007b). Variable amplitude fatigue crack growth, experimental results and modeling. *Int J Fatigue*, 26:1634–1646.

[Harilal et al., 2015] Harilal, R., Vyasarayani, C. P., and Ramji, M. (2015). A linear least squares approach for evaluation of crack tip stress field parameters using DIC. *Optics and Lasers in Engineering*, 75:95–102.

[Hellier et al., 1987] Hellier, A. K., Corderoy, D. J. H., and McGirr, M. B. (1987). A practical mixed Mode II/III fatigue test rig. *Int J Fatigue*, 9:95–101.

[Hellier et al., 1991] Hellier, A. K., McGirr, M. B., and Corderoy, D. J. H. (1991). A finite element and fatigue threshold study of shelling in heavy haul rails. *Wear*, 144:289–306.

[Hellier et al., 2011] Hellier, A. K., Zarrabi, K., and Merati, A. A. (2011). On the mode II fatigue threshold for mild steel. *Int J Fract*, 167:267–272.

[Highsmith and Woodruff, 2009] Highsmith, S. and Woodruff, G. W. (2009). *Crack path determination for non-proportional mixed-mode fatigue*. PhD thesis, Georgia Institute of Technology.

[Hos et al., 2016] Hos, Y., Freire, J. L. F., and Vormwald, M. (2016). Measurements of strain fields around crack tips under proportional and non-proportional mixed-mode fatigue loading. *Int J Fatigue*.

[Hosdez et al., 2019] Hosdez, J., Langlois, M., Witz, J.-F., Limodin, N., Najjar, D., Charkaluk, E., Osmond, P., Forre, A., and Szmytka, F. (2019). Plastic zone evolution during fatigue crack growth: Digital image correlation coupled with finite elements method. *Int J Solids Struct.*, 171:92–102.

[Hourlier and Pineau, 1982] Hourlier, F. and Pineau, A. (1982). Propagation of fatigue cracks under polymodal loading. *FFEMS*, 5(4):287–302.

[Innotrack, 2009] Innotrack (2009). Definitive guidelines on the use of different rail grades. Technical report, Innotrack.

[Jägg and Scholtes, 2005] Jägg, S. and Scholtes, B. (2005). Crack-tip residual stresses and crack propagation in cyclically-loaded specimens under different loading modes. *Zeitschrift für Metallkunde*, 96:770–774.

[Jessop et al., 2016] Jessop, C., Ahlström, J., Hammar, L., Fæster, S., and Danielsen, H. K. (2016). 3D characterization of rolling contact fatigue crack networks. *Wear*, 366-367:392–400.

[Kalker, 1979] Kalker, J. (1979). The computation of three-dimensional rolling contact with dry friction. *Int. Journal for Numerical Methods in Engineering*, 14:1293–1307.

[Kaneta and Murakami, 1987] Kaneta, M. and Murakami, Y. (1987). Effects of oil hydraulic pressure onsurface crack growth in rolling/sliding contact. *Tribology International*, 20:210–217.

[Kapoor, 1997] Kapoor, A. (1997). Wear by plastic ratchetting. *WEAR*, 212:119–130.

[Kfouri, 1999] Kfouri, A. P. (1999). A crack in a linear-elastic material under mode II loading, revisited. *FFEMS*, 22(5):445–448.

[Kim and C.S., 2002] Kim, J. and C.S., K. (2002). Fatigue crack growth behavior of rail steel under mode I and mixed mode loadings. *Materials Science and Engineering*, A338:191–201.

[Lachambre et al., 2015] Lachambre, J., Réthoré, J., Weck, A., and Buffiere, J. Y. (2015). Extraction of stress intensity factors for 3D small fatigue cracks using digital volume correlation and X-ray tomography. *Int J Fatigue*, 71:3–10.

[Ladevèze, 1999] Ladevèze, P. (1999). *Nonlinear Computationnal Structural Mechanics - New Approaches and Non-Incremental Methods of Calculation*. Springer.

[Larijani et al., 2014] Larijani, N., Brouzoulis, J., Schilke, M., and Ekh, M. (2014). The effect of anisotropy on crack propagation in pearlitic rail steel. *WEAR*, 314:57–68.

[Leblond and Frelat, 2000] Leblond, J. and Frelat, J. (2000). Crack kinking from an initially closed crack. *IJSS*, 37:1595–1614.

[Lemaitre et al., 2009] Lemaitre, J., Chaboche, J., Benallal, A., and Desmorat, R. (2009). *Mécanique des matériaux solides*. DUNOD.

[Lemaitre and Chaboche, 1994] Lemaitre, J. and Chaboche, J.-L. (1994). *Mechanics of solid materials*. Cambridge university press.

[Lenkovs'kyi, 2015] Lenkovs'kyi, T. M. (2015). Influence of the Friction of Crack Faces on the Cyclic Crack-Growth Resistance of 65G Steel Under Mode II Loading. *Materials Science*, 50(5):682–686.

[Lin et al., 2019] Lin, B., Alshammrei, S., and Tong, J. (2019). Characterisation of fatigue crack tip field in the presence of significant plasticity. *Theor Appl Fract Mec.*, 103.

[Llavori et al., 2019] Llavori, I., Zabala, A. and. Urchegui, M. A., Tato, W., and Gómez, X. (2019). A coupled crack initiation and propagation numerical procedure for combined fretting wear and fretting fatigue lifetime assessment. *Theoretical and Applied Fracture Mechanics*, 101:294–305.

[Lopez-Crespo et al., 2008] Lopez-Crespo, P., Shterenlikht, A., Patterson, E. A., Yates, J. R., and Withers, P. J. (2008). The stress intensity of mixed mode cracks determined by digital image correlation. *The Journal of Strain Analysis for Engineering Design*, 43:769–780.

[Lopez-Crespo et al., 2009] Lopez-Crespo, P., Shterenlikht, A., Yates, J. R., Patterson, E. A., and Withers, P. J. (2009). Some experimental observations on crack closure and crack-tip plasticity. *FFEMS*, 32:418–429.

[Mai et al., 2017] Mai, S. H., Gravouil, A., Nguyen-Tajan, M. L., and Trolle, B. (2017). Numerical simulation of rolling contact fatigue crack growth in rails with the rail bending and the frictional contact. *Eng Fract Mech*, 174:196–206.

[Maierhofer et al., 2018] Maierhofer, J., Simunek, D., Gänser, H. P., and Pippan, R. (2018). Oxide induced crack closure in the near threshold regime: The effect of oxide debris release. *Int J. Fatigue*, 117:21–26.

[Maouche et al., 1997] Maouche, N., Maitournam, H., and Dang Van, K. (1997). On a new method of evaluation of the inelastic state due to moving contact. *WEAR*, 203-204:139–147.

[Mathieu et al., 2012] Mathieu, F., Hild, F., and Roux, S. (2012). Identication of a crack propagation law by digital image correlation. *Int J Fatigue*, 36:146–154.

[Maya-Johnson et al., 2015] Maya-Johnson, S., Ramirez, A. J., and Toro, A. (2015). Fatigue crack growth rate of two pearlitic rail steels. *Eng Fract Mech*, 138:63–72.

[Merati et al., 2012] Merati, A. A., Hellier, A. K., and Zarrabi, K. (2012). On the mixed Mode II/III fatigue threshold behaviour for aluminium alloys 2014-T6 and 7075-T6. *FFEMS*, 35:2–12.

[Newman, 1981] Newman, J. C. (1981). A Crack-Closure Model for Predicting Fatigue Crack Growth under Aircraft Spectrum Loading. Technical report, NASA.

[Newman and Raju, 1981] Newman, J. C. and Raju, I. S. (1981). An empirical stress-intensity factor equation for the surface crack. *Eng Fract Mech*, 15:185–192.

[Nguyen-Tajan and unfschilling, 2011] Nguyen-Tajan, T. M. L. and unfschilling, C. (2011). On a new method of evaluation of the inelastic state due to moving contact. *WCRR World congress of railway research*.

[ORR, 2006] ORR (2006). Train Derailment at Hatfield. Technical report, Office of Rail Regulation.

[Paris and Erdogan, 1963] Paris, P. and Erdogan, F. (1963). A critical analysis of crack propagation laws. *Basic engineering*, 85:528–533.

[Park and Bernstein, 1979] Park, Y. and Bernstein, I. (1979). The process of crack initiation and effective grain size for cleavage fracture in pearlitic eutectoid steel. *Metallurgical Transactions A*, 10:1653–1664.

[Paul and Tarafder, 2013] Paul, S. K. and Tarafder, S. (2013). Cyclic plastic deformation response at fatigue crack tips. *Int J Pressure Vessels and Piping*, 101:81–90.

[Pinna and Doquet, 1999] Pinna, C. and Doquet, V. (1999). Preferred fatigue crack propagation mode in a M250 maraging steel loaded in shear. *FFEMS*, 22(3):173–183.

[Plank and Kuhn, 1999] Plank, R. and Kuhn, G. (1999). Fatigue crack propagation under non-proportional mixed mode loading. *Eng Fract Mech*, 62:203–229.

[Pokluda and Pippan, 2008] Pokluda, J. and Pippan, R. (2008). Can pure mode III fatigue loading contribute to crack propagation in metallic materials? *FFEMS*, 28:179–185.

[Pokluda et al., 2014] Pokluda, J., Pippan, R., Vojtek, T., and Hohenwarter, A. (2014). Near-threshold behaviour of shear-mode fatigue cracks in metallic materials. *FFEMS*, 37:232–254.

[Pokluda et al., 2008] Pokluda, J., Trattnig, G., Martinschitz, C., and Pippan, R. (2008). Straightforward comparison of fatigue crack growth under modes II and III. *Int J Fatigue*, 30:1498–1506.

[Pokorný et al., 2017] Pokorný, P., Vojtek, T., Náhlík, L., and Hutař, P. (2017). Crack closure in near-threshold fatigue crack propagation in railway axle steel EA4T. *Eng Fract Mech*, 185:2–19.

[Pommier and Bompard, 2000] Pommier, S. and Bompard, P. (2000). Bauschinger effect of alloys and plasticity-induced crack closure: a finite element analysis. *FFEMS*, 23:129–139.

[Pommier and Hamam, 2007] Pommier, S. and Hamam, R. (2007). Incremental model for fatigue crack growth based on a displacement partitioning hypothesis of mode I elastic–plastic displacement fields. *FFEMS*, 30:582–598.

[Pommier et al., 1997] Pommier, S., Prioul, C., and Bompard, P. (1997). Influence of a negative R ratio on the creep-fatigue behaviour of the N18 nickel base superalloy. *FFEMS*, 20(1):93–107.

[Réthoré, 2010] Réthoré, J. (2010). A fully integrated noise robust strategy for the identification of constitutive laws from digital images. *Int J Numer Meth Eng*, 84:631–660.

[Réthoré et al., 2005] Réthoré, J., Gravouil, A., Morestin, F., and Combescure, A. (2005). Estimation of mixed-mode stress intensity factors using digital image correlation and an interaction integral. *Int J Fracture*, 132(1):65–79.

[Réthoré et al., 2013] Réthoré, J., Muhibullah, Elguedj, T., Coret, M., Chaudet, P., and Combescure, A. (2013). Robust identification of elasto-plastic constitutive law parameters from digital images using 3D kinematics. *Int J Solids Struct.*, 50:73–85.

[Réthoré et al., 2007] Réthoré, J., Roux, S., and Hild, F. (2007). Noise-robust stress intensity factor determination from kinematic field measurements. *Eng Fract Mech*, 75:3763–3781.

[Rodesch, 2013] Rodesch, P. (2013). Prise en compte de Contraintes Résiduelles dans la fatigue de composants ferroviaires. Master's thesis, Ecole des Ponts.

[Roux and Hild, 2006] Roux, S. and Hild, F. (2006). Stress intensity factor measurements from digital image correlation: Post-processing and integrated approaches. *Int J Fracture*, 140(1-4):141–157.

[Sander and Richard, 2005] Sander, M. and Richard, H. A. (2005). Finite element analysis of fatigue crack growth with interspersed mode I and mixed mode overloads. *Int J Fatigue*, 27:905–913.

[Sehitoglu, 1985] Sehitoglu, H. (1985). Crack opening and closure in fatigue. *Eng Fract Mech*, 21:329–339.

[SeverStal and Lucchini, 2009] SeverStal and Lucchini (2009). Rails et laminés pour superstructures de chemin de fer.

[Simon, 2014] Simon, S. (2014). *De la dynamique ferroviaire à l'accommodation microstructurale du rail*. PhD thesis, Institut national des sciences appliquées de Lyon.

[Simon et al., 2013] Simon, S., Saulot, A., Dayot, C., Quost, X., and Berthier, Y. (2013). Tribological characterization of rail squat defects. *Wear*, 297(1-2):926–942.

[Smith et al., 1970] Smith, K., Watson, P., and Topper, T. (1970). A stress-strain function for the fatigue of metals. *J Mater*, 5:767–778.

[Smith and Smith, 1982] Smith, M. and Smith, R. (1982). The formation of spherical wear debris in mode II fatigue cracks. *Wear*, 76:105–128.

[Smith and Smith, 1988] Smith, M. C. and Smith, R. A. (1988). Toward an understanding of mode II fatigue crack growth. *Basic Questions in Fatigue*, 1:260–280.

[Stanzl et al., 1989] Stanzl, S., Czegley, M., Mayer, H., and Tschegg, E. (1989). Fatigue crack growth under combined mode I and mode II loading. *In STP1020-EB Fracture Mechanics: Perspectives and Directions (Twentieth Symposium)*, ASTM STP 1020:479–496.

[Suresh and Ritchie, 1982] Suresh, S. and Ritchie, R. (1982). A Geometric Model for Fatigue Crack Closure Induced by Fracture Surface Roughness. *METALLURGICAL TRANSACTIONS A*, 13A:1627–1631.

[Suresh et al., 1981] Suresh, S., Zamiski, G., and Ritchie, R. (1981). Oxide-induced crack closure: an explanation for near-threshold corrosion fatigue crack growth behavior. *Metallurgical Transactions A*, 12A:1435–1443.

[Tabatabaei, 2014] Tabatabaei, A. M. (2014). *Fracture and fatigue crack growth characterization of conventional and head hardened railway rail steels*. PhD thesis, Middle East Technical University.

[Tada et al., 1973] Tada, H., Paris, P., and Irwin, G. (1973). The stress analysis of cracks.

[Tanaka, 1974] Tanaka, K. (1974). Fatigue crack propagation from a crack inclined to the cyclic tensile axis. *Eng Fract Mech*, 6:493–507.

[Tarantino, 2011] Tarantino, G. (2011). *Shear-mode propagation of short cracks under rolling contact fatigue*. PhD thesis, Politecnico Di Milano.

[Tarantino et al., 2011] Tarantino, M. G., Beretta, S., Foletti, S., and Lai, J. (2011). A comparison of Mode III threshold under simple shear and RCF conditions. *Eng Fract Mech*, 78(8):1742–1755.

[Tong et al., 2018] Tong, J., Alshammrei, S., Wigger, T., Lupton, C., and Yates, J. R. (2018). Full-field characterization of a fatigue crack: Crack closure revisited. *FFEMS*, 41:2130–2139.

[Tong et al., 1995a] Tong, J., Yates, J. R., and Brown, M. W. (1995a). A model for sliding mode crack closure part I: theory for pure mode II loading. *Eng Fract Mech*, 52(495):599–611.

[Tong et al., 1995b] Tong, J., Yates, J. R., and Brown, M. W. (1995b). A model for sliding mode crack closure part II: mixed mode I and II loading and application. *Eng Fract Mech*, 52(4):613–623.

[Topper and Yu, 1985] Topper, T. and Yu, M. (1985). The effect of overloads on threshold and crack closure. *Int J Fatigue*, 7:159–164.

[Trollé, 2014] Trollé, B. (2014). *Simulation multi-échelles de la propagation des fissures de fatigue dans les rails.* PhD thesis, Institut national des sciences appliquées de Lyon.

[Tschegg, 1983a] Tschegg, E. (1983a). Sliding mode crack closure and mode III fatigue crack growth in mild steel. *Acta Metallurgica*, 31(9):1323–1330.

[Tschegg and Stanzl, 1988] Tschegg, E. and Stanzl, S. (1988). The significance of sliding mode crack closure on mode iii fatigue crack growth. *Basic questions in fatigue*, 1:214–232.

[Tschegg, 1983b] Tschegg, E. K. (1983b). Mode III and Mode I fatigue crack propagation behaviour under torsional loading. *Journal of Materials Science*, 18(6):1604–1614.

[UIC, 2002] UIC (2002). Défauts de rails. Technical report, Union Internationale des Chemins de fer.

[Vojtek et al., 2016a] Vojtek, T., Hohenwarter, A., Pippan, R., and Pokluda, J. (2016a). Experimental evidence of a common local mode II growth mechanism of fatigue cracks loaded in modes II, III and II+III in niobium and titanium. *Int J Fatigue*, 92:470–477.

[Vojtek et al., 2013] Vojtek, T., Pippan, R., Hohenwarter, A., Holan, L., and Pokluda, J. (2013). Near-threshold propagation of mode II and mode III fatigue cracks in ferrite and austenite. *Acta Materialia*, 61:4625–4635.

[Vojtek et al., 2015a] Vojtek, T., Pokluda, J., Hohenwarter, A., and Pippan, R. (2015a). Progress in understanding of intrinsic resistance to shear-mode fatigue crack growth in metallic materials. *Int J Fatigue*, 89:36–42.

[Vojtek et al., 2016b] Vojtek, T., Pokluda, J., Hohenwarter, A., and Pippan, R. (2016b). Intrinsic Behaviour of Modes II, III and Mixed Mode II+III Fatigue Cracks in Metallic Materials. In *ICMFF 11*, Seville.

[Vojtek et al., 2015b] Vojtek, T., Pokluda, J., Šandera, P., Horníková, J., Hohenwarter, A., and Pippan, R. (2015b). Analysis of fatigue crack propagation under mixed mode II + III in ARMCO iron. *Int J Fatigue*, 76:47–52.

[Vojtek et al., 2019] Vojtek, T., Pokorný, P., Kuběna, I., Náhlík, L., Fajkoš, R., and Hutař, P. (2019). Quantitative dependence of oxide-induced crack closure on air humidity for railway axle steel. *Int J. Fatigue*, 123:213–224.

[Vormwald et al., 2018] Vormwald, M., Hos, Y., Freire, J. L., Gonzáles, G. L., and Díaz, J. G. (2018). Crack tip displacement fields measured by digital image correlation for evaluating variable mode-mixity during fatigue crack growth. *Int J Fatigue*, 115:53–66.

[Wong et al., 1996] Wong, S. L., Bold, P. E., Brown, M. W., and Allen, R. J. (1996). A branch criterion for shallow angled rolling contact fatigue cracks in rails. *Wear*, 191:45–53.

[Wong et al., 2000a] Wong, S. L., Bold, P. E., Brown, M. W., and Allen, R. J. (2000a). Fatigue crack growth rates under sequential mixed-mode I and II loading cycles. *FFEMS*, 23:667–674.

[Wong et al., 2000b] Wong, S. L., Bold, P. E., Brown, M. W., and Allen, R. J. (2000b). Two measurement techniques for determining effective stress intensity factors. *FFEMS*, 23:659–666.

[Yates et al., 2010] Yates, J. R., Zanganeh, M., and Tai, Y. H. (2010). Quantifying crack tip displacement fields with DIC. *Eng Fract Mech*, 77:2063–2076.

[Yoneyama et al., 2007] Yoneyama, S., Ogawa, T., and Kobayashi, Y. (2007). Evaluating mixed-mode stress intensity factors from full-field displacement fields obtained by optical methods. *Eng Fract Mech*, 74:1399–1412.

[Zanganeh et al., 2013] Zanganeh, M., Lopez-Crespo, P., Tai, Y. H., and Yates, J. R. (2013). Locating the crack tip using displacement field data: A comparative study. *Strain*, 49:102–115.

[Zhang et al., 2007] Zhang, J., He, X., and Du, S. (2007). Analysis of the effects of compressive stresses on fatigue crack propagation rate. *Int J Fatigue*, 29:1751–1756.

[Zhao, 2012] Zhao, X. (2012). *Dynamic wheel/rail contact at singular defects with application to Squats.* PhD thesis, Delft University of Technology.

Appendix A

Extraction of the samples from new rails

The samples were extracted from the head of 8 new rail 1-meter sections made of $R260$ low alloy rail steel, as described in figure A.1.

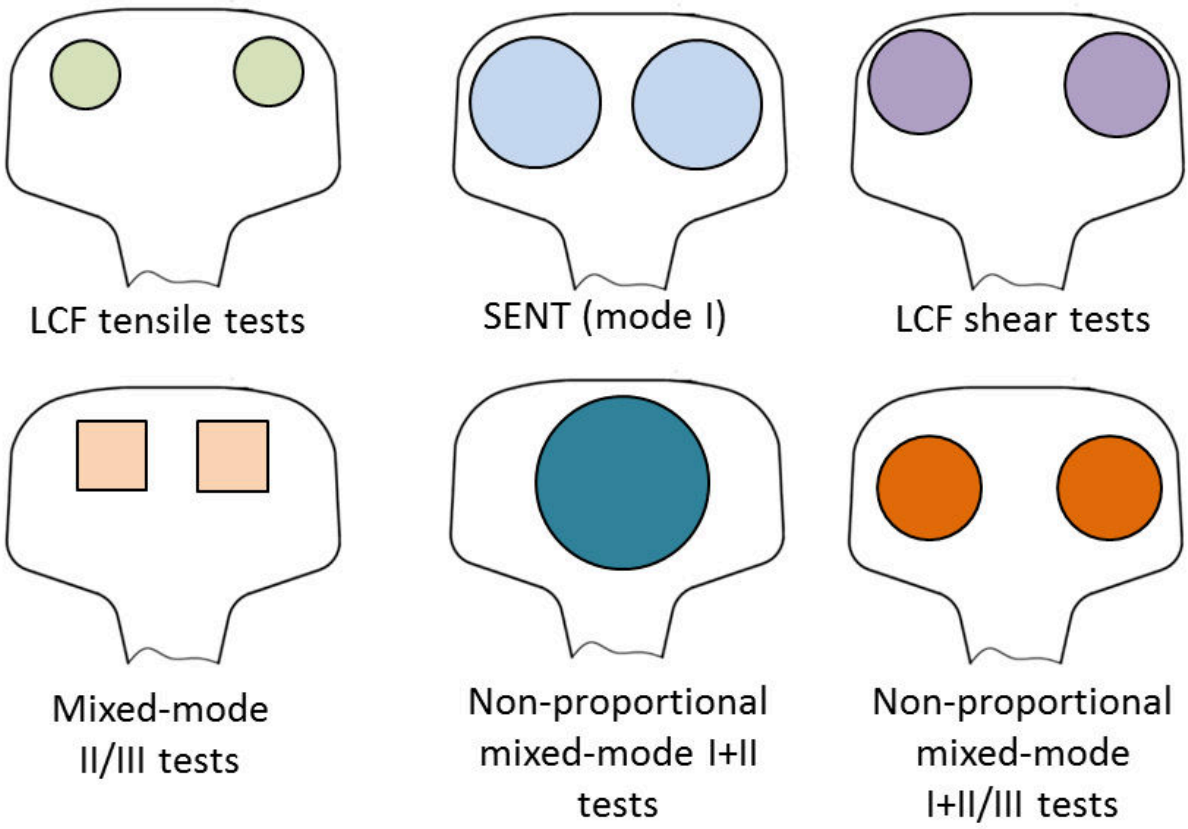

Figure A.1: Extraction areas.

Appendix B

PS algorithm with William's expansion

The algorithm used to determine the crack tip and effective SIFs using a projection over William's expansion is described in figure B.1. At each possible crack tip location, only a part of the DIC field is used, as shown on figure B.2. *Rint* is chosen sufficiently large to avoid DIC elements which are overlapping the crack and for which the correlation is wrong. The algorithm is a mix between the grid search of [Harilal et al., 2015] and the PS algorithm of [Zanganeh et al., 2013].

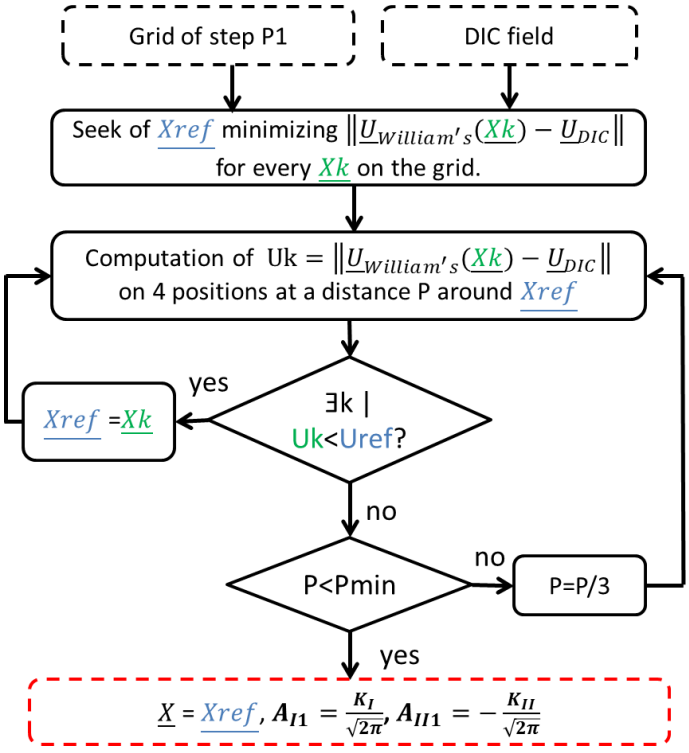

Figure B.1: PS algorithm with William's expansion. $\underline{Xref}$ represents the current supposed crack tip and $\underline{Xk}$ the tested crack tip positions

Noting the horizontal and vertical displacements u_x and u_y respectively, with G the shear modulus and $k =$

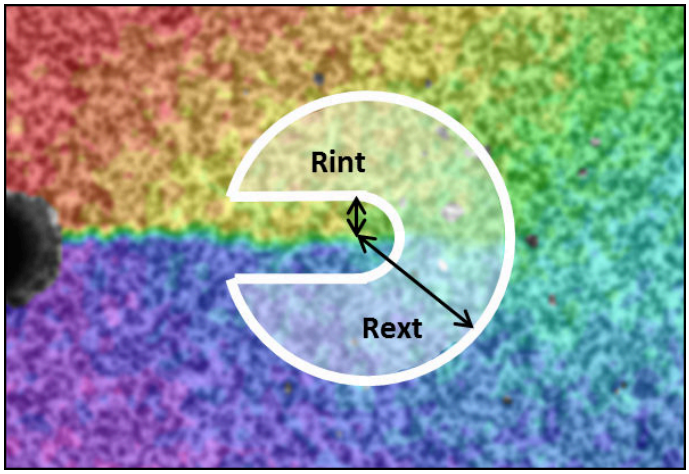

Figure B.2: Shape of the zone used in the PS algorithm. $Rext = 1.2\ mm$ and $Rint = 0.2\ mm$.

$(3-\nu)/(1+\nu)$ (plane stress hypothesis), William's expansion writes:

$$\begin{aligned} u_x = &\sum_{n=0}^{N} \frac{A_I^n}{2G} r^{\frac{n}{2}} \left((\kappa + \frac{n}{2} + (-1)^n) cos(\frac{n}{2}\theta) - \frac{n}{2} cos((\frac{n}{2} - 2)\theta) \right) \\ &+ \sum_{n=0}^{N} \frac{A_{II}^n}{2G} r^{\frac{n}{2}} \left((-\kappa - \frac{n}{2} + (-1)^n) sin(\frac{n}{2}\theta) + \frac{n}{2} sin((\frac{n}{2} - 2)\theta) \right) \end{aligned} \tag{B.1}$$

$$\begin{aligned} u_y = &\sum_{n=0}^{N} \frac{A_I^n}{2G} r^{\frac{n}{2}} \left((\kappa - \frac{n}{2} - (-1)^n) sin(\frac{n}{2}\theta) + \frac{n}{2} sin((\frac{n}{2} - 2)\theta) \right) \\ &+ \sum_{n=0}^{N} \frac{A_{II}^n}{2G} r^{\frac{n}{2}} \left((\kappa - \frac{n}{2} + (-1)^n) cos(\frac{n}{2}\theta) + \frac{n}{2} cos((\frac{n}{2} - 2)\theta) \right) \end{aligned} \tag{B.2}$$

The rigid body translations t_x and t_y are contained in the order 0 terms:

$$t_x = \frac{A_I^0}{2G}(\kappa + 1) = \frac{4A_I^0}{E} \tag{B.3}$$

$$t_y = \frac{A_{II}^0}{2G}(\kappa + 1) = \frac{4A_{II}^0}{E} \tag{B.4}$$

The stress intensity factors are contained in the order 1 terms:

$$K_I = \sqrt{2\pi} A_I^1 \tag{B.5}$$

$$K_{II} = -\sqrt{2\pi} A_{II}^1 \tag{B.6}$$

The rigiby body rotation Ω and the T-stress T are contained in the order 2 terms:

$$\Omega = \frac{A_{II}^2}{2G}(\kappa + 1) = \frac{4A_{II}^2}{E} \tag{B.7}$$

$$T = \frac{A_I^2}{2G}(\kappa + 1)E = 4A_I^2 \tag{B.8}$$

The parameters used in this study are: $R_{int} = 0.2\ mm$, $R_{ext} = 1.2\ mm$, grid step $P_1 = 0.1\ mm$, PS algorithm steps from $P = 0.033\ mm$ to $P = 0.0037$, order of the William's expansion terms: from 0 to 7. Using those parameters, the time to process one DIC field is about 5 to 10 seconds. Each projection over William's expansion is extremely fast since it only needs to invert a $16 * 16$ matrix and build/multiply some $n * n$ matrix, n being the number of points in the projection zone.

Appendix C

Influence of the crack initiation hole and crack asymmetry in mode I+II experiments

3D FEM computations (see figure C.1) were performed in order to verify that the hole could be neglected. The crack front was modeled as straight and radial with 12 nodes, and a uniform σ_{zz} was applied at the end of the specimen.

For a 1.5 mm long crack, the error between the abacus and the computation is below 3%. The effect of a dissymmetry in the crack length on the two sides of the hole was also investigated and was found to have little influence: less than 2.5 % error for a 250 % dissymmetry on a $2a = 3.5$ mm crack.

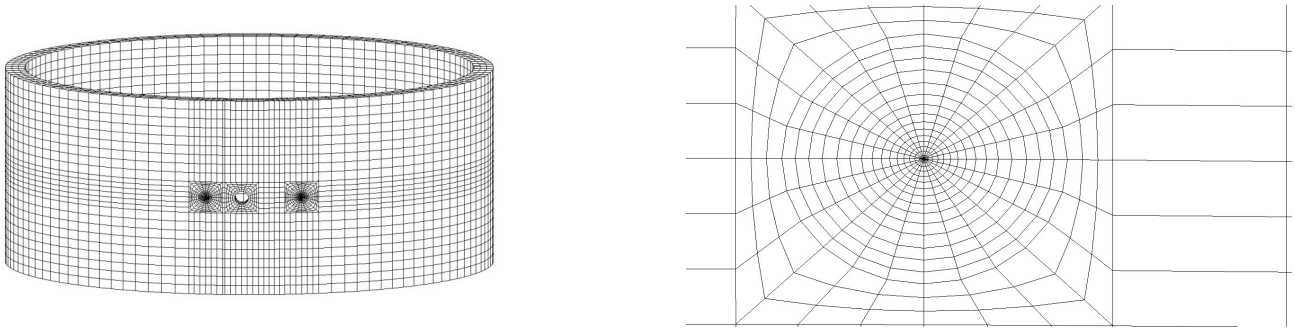

Figure C.1: 3D mesh of the sample with the hole, and zoom on the crack tip.

This model was not used for further analysis since K_{III} is wrongly estimated due to a bug in the $CAST3M$ software. XFEM computations were then preferred.

Appendix D

Non-proportional mixed-mode I+II experiment in water

A sequential mixed-mode I+II experiment (exp $N°18$ in table 6.4) using the samples and testing machine detailed in section 6.2 was performed in tap water at $F = 10/0\ kN$ and $C = \pm 90\ Nm$, which is similar to exp $N°19$ performed in air.

The crack was kept in water by sealing the inside of the sample with silicone, and using a silicone soft envelope, as shown on figure D.1.a. The envelope is filled with tap water or emptied using a squeeze bottle. In order to track crack propagation, the silicone envelope can be rolled up (as in figure D.1.b) in order to reveal the DIC pattern.

The presence of water led to paint swelling, making reliable effective SIFs measurements impossible, and crack tip position estimation difficult (but still possible since it uses a field that is away from the crack lips). The $a(N)$ evolution is plotted on figure D.2 for experiments with and without water.

Crack propagation kinetics is similar in water and in air, suggesting that neither corrosion-assisted crack growth nor corrosion products-induced closure, nor crack opening due to entrapped water, nor reduction of friction between the crack faces occurred (or those effects perfectly counterbalanced each other). The fracture surfaces are similar in water and in air (worn near the crack initiation hole, rough near the tip), with some oxides in both cases.

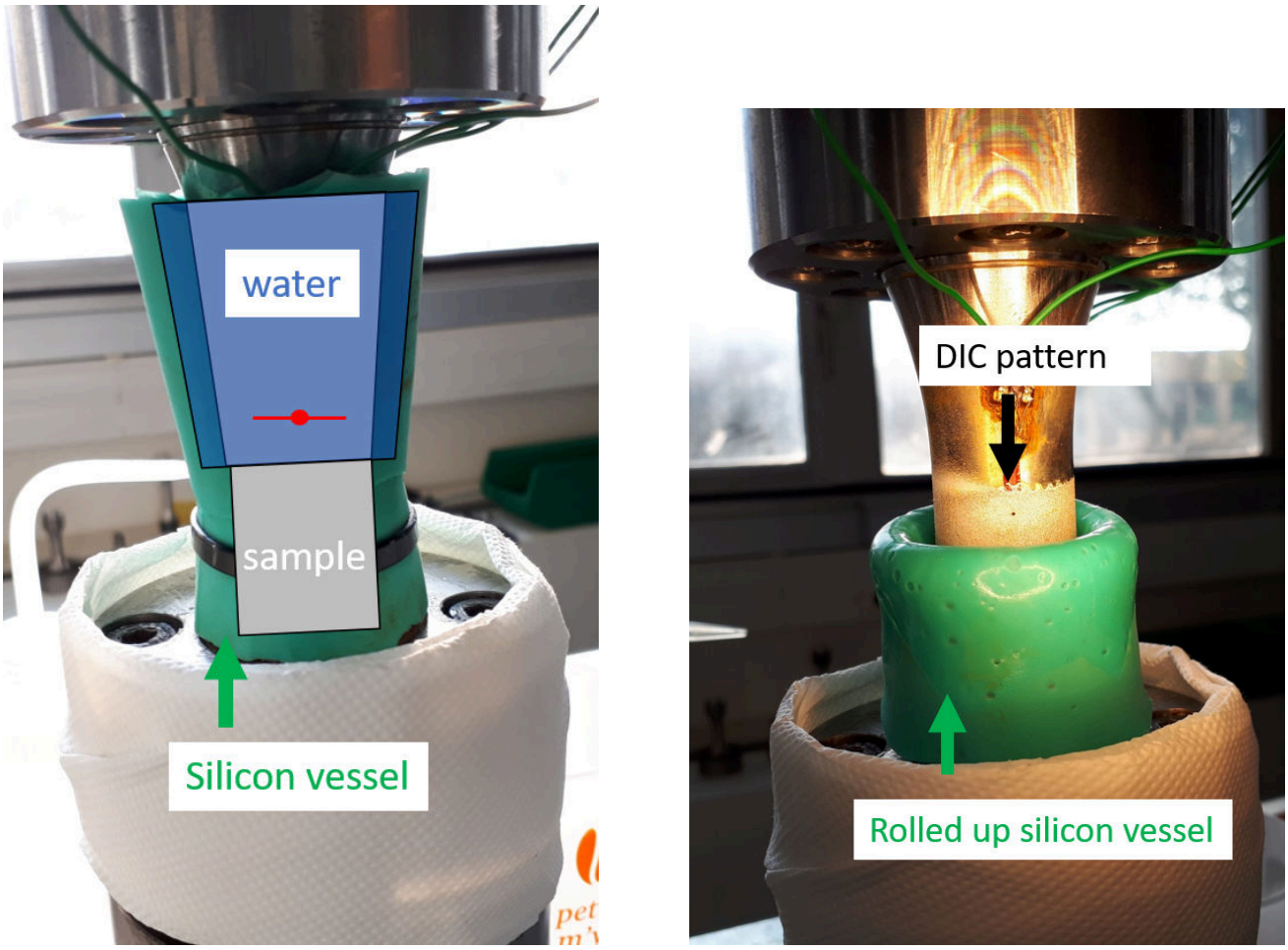

Figure D.1: Setup for experiments in water: during fatigue testing (a) and during image recording (b).

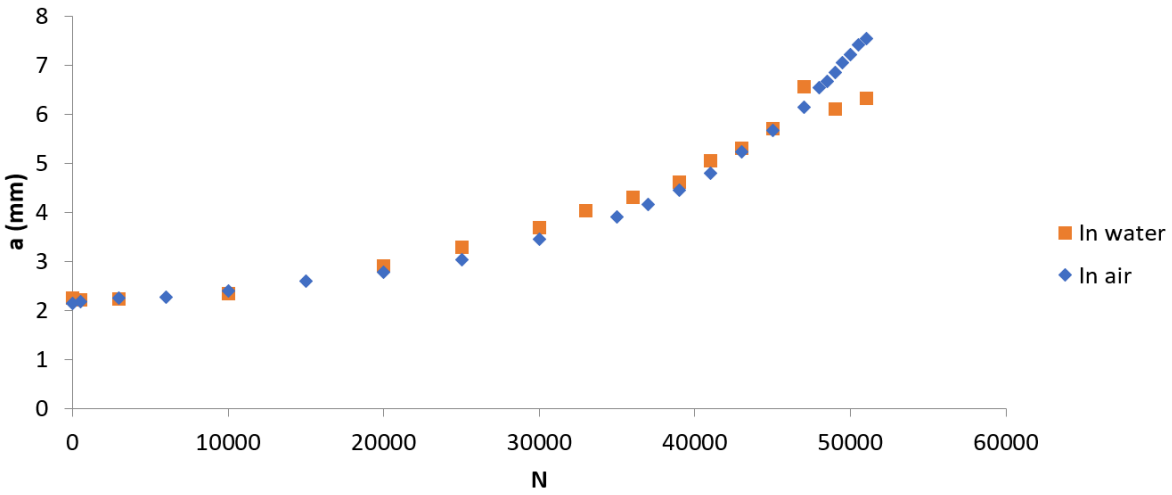

Figure D.2: Estimated crack length during experiments performed at the same loading amplitudes, in water or in air.

Appendix E

Non-proportional mixed-mode I+II *in situ* experiment in a SEM

Non-proportional mixed-mode I+II *in situ* SEM experiments were performed in order to have direct measurements of the relative crack face displacement jump. A XL40 SEM, equiped with a tension/compression/torsion testing machine, allowing $\pm 10\ kN$ axial force and $\pm 50\ Nm$ torque at a $\approx 0.1\ Hz$ frequency, was used [Doquet et al., 1994]. The samples are cylinders, with a 10.8 mm external diameter and a 0.9 mm thickness, containing a 0.7 mm hole for crack initiation. Those samples are precracked in a hydraulic testing machine, mechanically polished down to 1 μm diamond paste, and then covered with gold micro-grids of 5 μm pitch (as shown on figure E.1) using e-beam lithography, before *in situ* testing.

Mode II loadings at various amplitudes and with various static axial forces were applied. Images at two opposite torque values are given on figure E.1, where asperities interlocking can be seen. Those asperities can be plasticized and cracked (then detached, thus leading to wear), as illustrated on figure E.2.

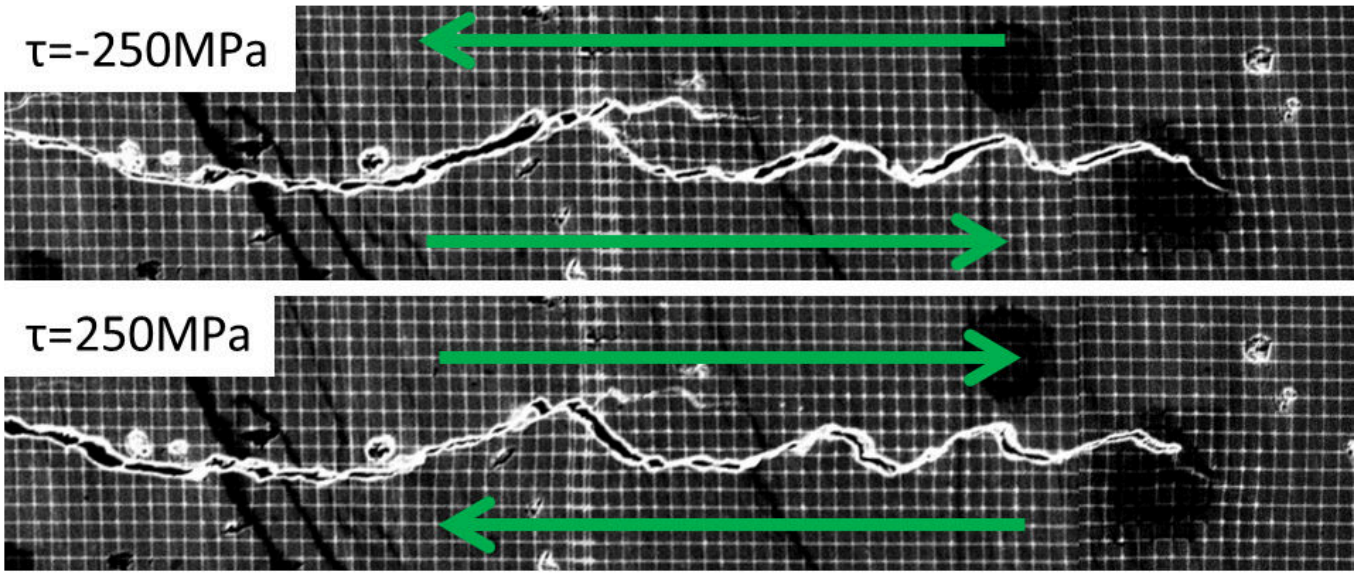

Figure E.1: Images taken at $\tau = \pm 250\ MPa$ and $\sigma = 0.\ 5\ \mu m$ grid pitch.

The relative crack face opening and sliding displacements were measured and compared to that obtained from

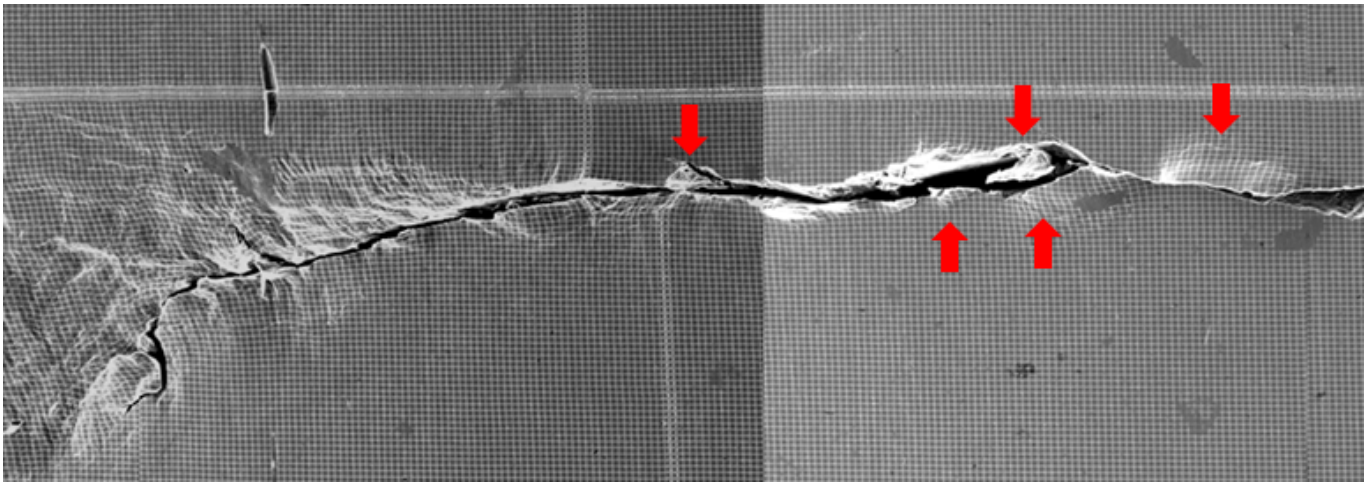

Figure E.2: Plasticized and cracked asperities after a torque overload.

elastic-plastic FEM computations, as illustrated on figure E.3. For $\tau = -172\ MPa$ and $\sigma = 0$, an opening displacement jump is observed, although $\Delta K_I^{nom} = 0$, due to dilatancy effects. The measured sliding displacement jump is much lower than that computed by FEM elastic-plastic computations due to friction and asperities interlocking between the crack faces.

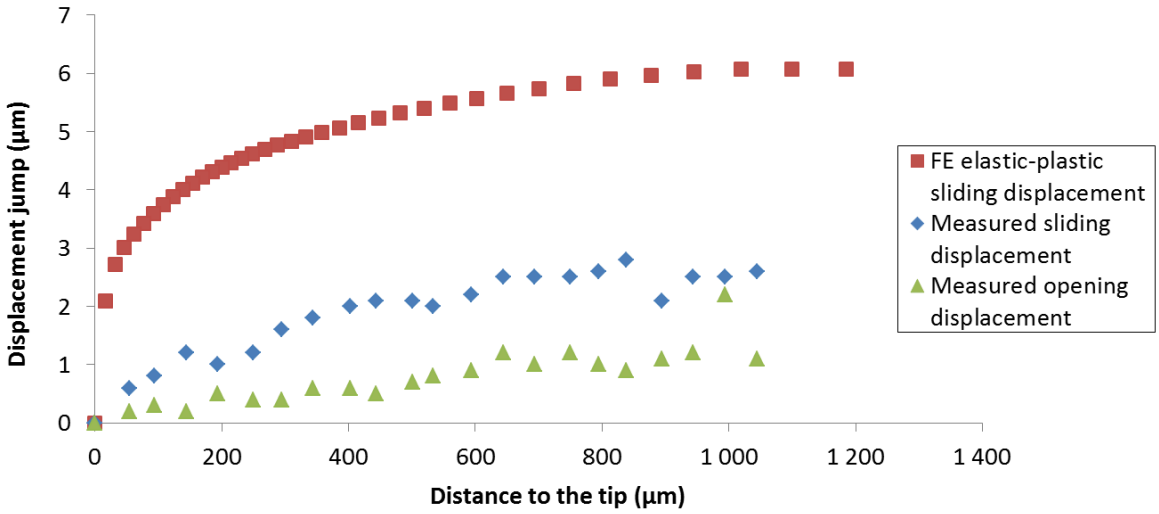

Figure E.3: Measured displacement jump at $\tau = -172\ MPa$ and $\sigma = 0$.

The measured ΔK^{eff} for various mode II loadings ($R_{II} = -1$) with static axial forces are given in table E.1. Without static compression, $U_{II} < 0.72$ and varies with the shear amplitude. The dilatancy ΔK_I^{eff} is $\approx 0.16 \Delta K_{II}^{eff}$ (since $R_{II} = -1$, there are two mode I cycle during a fully reversed mode II cycle, and $K_I^{eff} \approx 0.32 |K_{II}^{eff}|$). However, when compression was added, the crack remained locked so that $U_{II} = 0$ and $\Delta K_I^{eff} = 0$. No measurements were made at higher torque levels under compression due to a problem with the testing machine.

During these experiments, MnS inclusions, which are elongated along the specimen axis, were found to change the crack path locally. Ahead of the crack tip, they have an influence on the stress field, as showed on figure E.4, and may be detached and broken if the stresses are high enough ((a) on figure E.4). As the crack propagates, they can lead to a zig-zag crack propagation, as illustrated on figure E.5, which increases the roughness. These effects,

Table E.1: Measured ΔK^{eff} and U ratios for various mode II loadings with static axial forces.

$\sigma\ (MPa)$	$\Delta\tau\ (MPa)$	ΔK_I^{eff} $(MPa\sqrt{m})$	ΔK_{II}^{eff} $(MPa\sqrt{m})$	ΔK_I^{nom} $(MPa\sqrt{m})$	U_{II}	$\Delta K_I^{eff}/\Delta K_{II}^{eff}$
0	344	1.7	9.7	23.8	0.41	0.17
0	500	4.1	24.8	34.4	0.72	0.16
-240	344	0.0	0.0	23.8	0.00	/

observed on the surface of thin specimens (0.9 mm thick), may not be as influent on a crack in the bulk of the rail.

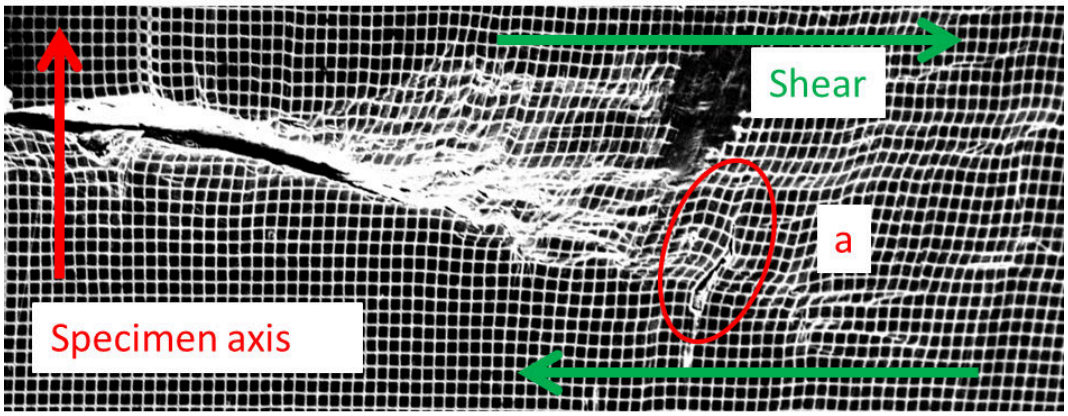

Figure E.4: Inclusion ahead of the crack tip under mode II loading, $\Delta K_{II}^{nom} = 66\ MPa\sqrt{m}$, $\tau = 360\ MPa$ (not LEFM conditions).

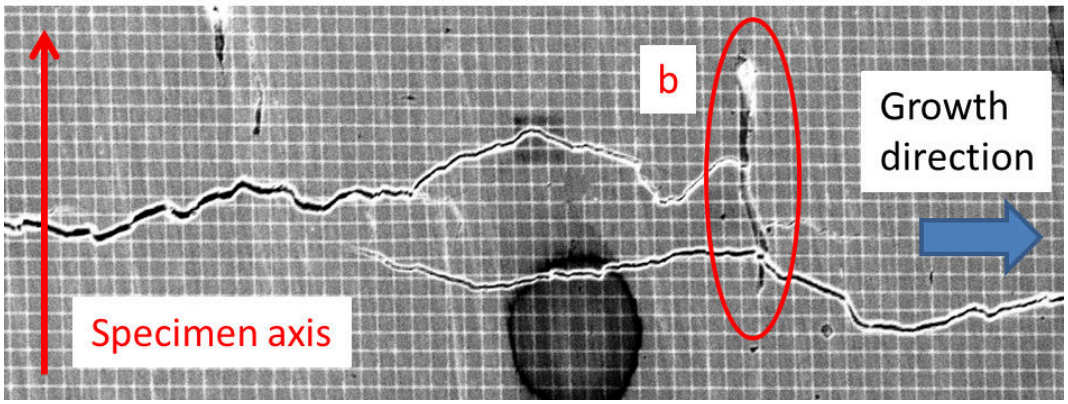

Figure E.5: Longitudinal crack induced by an inclusions during mode I precracking.

Appendix F

Résumé de la thèse en Français

Fissuration par fatigue en mode mixte non proportionnel des rails de chemins de fer. De l'étude expérimentale à la mise en œuvre d'un modèle: Résumé de la thèse en Français

Thomas Bonniot

Table des matières

1 Contexte

Les rails sont soumis à de la fatigue de roulement suite au passage répété des roues de trains. Ce phénomène peut engendrer plusieurs types de fissures, tels que les Squats, défauts amorcés en haut de la table de roulement suite aux fortes déformations plastiques de cisaillement induites par le passage des roues. Ces fissures (Figure 1) se propagent dans un plan fortement cisaillé, incliné de 20 degrés par rapport à l'axe vertical, pour des profondeurs bien au-delà de la zone plastifiée.

FIGURE 1 – Fissure de type Squat.

Afin d'améliorer notre compréhension des phénomènes responsables de la propagation de ces fissures, et d'améliorer les règles de maintenance, SNCF a développé un outil numérique permettant d'estimer l'évolution temporelle des facteurs d'intensité des contraintes (FIC) le long du front [Trollé, 2014, Mai et al., 2017]. Ces simulations prennent en compte le contact et le frottement entre les lèvres de la fissure sous la forme d'un modèle de Coulomb. Cependant, il manque encore un modèle fiable pour prédire le trajet et la vitesse de propagation de la fissure.

L'évolution temporelle des facteurs d'intensités des contraintes (FICs) a été calculée, à l'aide de l'outil numérique développé à la SNCF, pour une fissure de type squat de 20mm de profondeur inclinée de 20 degrés par rapport à l'axe vertical. Ces chargements on été utilisés pour piloter des essais en laboratoire. Les contraintes résiduelles ont été prises en compte, ainsi que diverses conditions de chargement (géométrie de la voie, température extérieure). L'évolution des FICs dans le plan K_I - K_{II} au point le plus profond de la fissure est donnée Figure 2. Les rails étant soudés à une température de $20°C$, et de longueur fixée, des contraintes thermiques longitudinales sont induites par les changements de température.

Des valeurs (virtuelles) négatives de K_I (obtenues par un autre calcul sans contact) sont tracées Figure 2 pour représenter le niveau de compression sur la fissure. Les trajets calculés correspondent à peu près à une séquence de mode I puis mode II & III sous compression, et sont approximés par les trajets séquentiels en pointillés. Pour une température de $20°C$, il y a peu de mode I et beaucoup de compression lors du cisaillement, ce qui réduit ΔK_{II}^{eff}, tandis que pour une température de -5$°C$, l'amplitude du mode I devient presque aussi grande que celle du mode II, et il y a moins de compression lors du cisaillement.

Il n'existe aucune approche communément acceptée pour prédire la vitesse et le trajet de propagation de fissure pour ce type de chargement. Cette prédiction est rendue encore plus complexe du fait des couplages entre les trois modes induits par la plasticité en pointe de fissure, ainsi que par le contact, frottement et usure des lèvres de fissures.

Le problème étant déjà assez complexe, les effets liés à l'amplitude variable du chargement (différents trains,

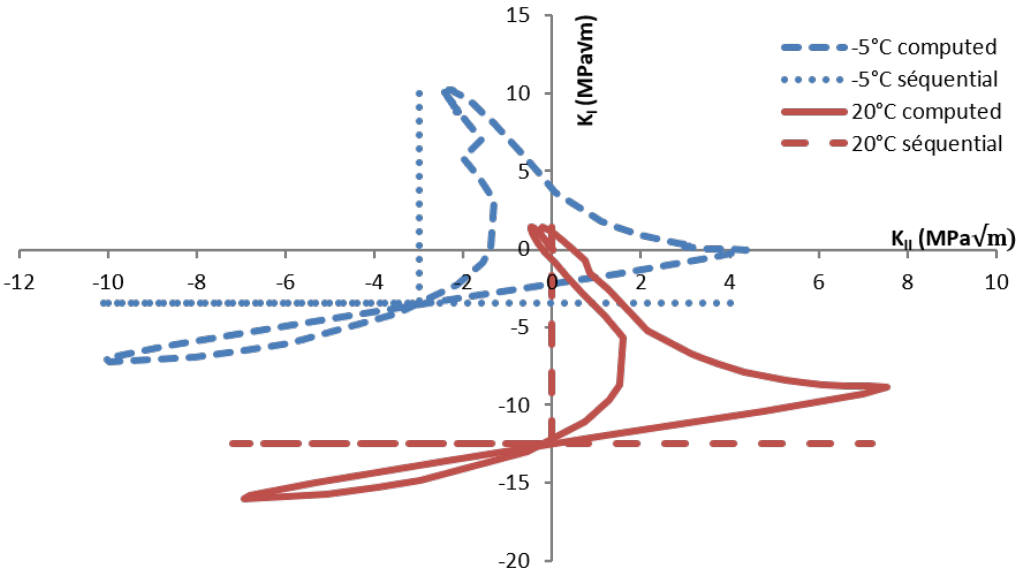

FIGURE 2 – évolution des FICs au fond d'un squat de 20mm de profondeur dans le plan K_I - K_{II} pour deux températures différentes et approximations séquentielles qui en sont faites.

efforts dynamiques dépendants de la vitesse, etc...) ainsi qu'à la pressurisation d'eau dans la fissure seront négligés pour le reste de l'étude.

Durant cette étude, des outils pour mesurer les FICs effectifs à partir de champs de déplacements obtenus par corrélation d'images ont été développés, permettant d'estimer l'influence du contact et frottement entre les lèvres de fissure.

Des essais de fissuration par fatigue en mode I, à différents rapports de charge (y compris négatifs) ont été menés afin d'obtenir des données cinétiques et étudier l'influence d'une compression. La possibilité que le mode I puisse à lui seul expliquer la fissuration des rails a été discutée.

Des essais de fissuration par fatigue en mode mixte II & III ont permis d'obtenir des données cinétiques pour divers taux de mixité K_{II}/K_{III}, et de discuter la possibilité d'une propagation coplanaire dans les rails due aux modes de cisaillement seuls.

Des chargements de mode mixte non-proportionnel I + II ont ensuite été étudiés, avec diverses formes de trajet, divers taux de mixité et la possibilité d'une compression lors du cisaillement. Plusieurs approches ont été testées afin de prédire le trajet et la vitesse de propagation des fissures.

Enfin, une approche permettant de prédire la fissuration des rails a été proposée, et validée sur des essais de mode mixte séquentiel I + II & III.

2 Développements expérimentaux

La corrélation d'images a été utilisée durant les essais afin de localiser la pointe de fissure et estimer les FICs effectifs. Un article [Bonniot et al., 2019] résume ces travaux. La méthode la plus "classique", qui consiste à projeter le champ expérimental sur la base des séries de William's [Abanto-Bueno and Lambros, 2002, Roux and Hild, 2006, Yoneyama et al., 2007], a été testée sur des champs issus de simulations éléments finis. Ces simulations, reproduisant des chargements de mode I ou II, prenaient en compte le comportement elasto-plastique du matériau, ainsi que du contact et frottement entre les lèvres de la fissure.

Il s'avère que dans le cas d'une zone plastique étendue devant la fissure (ce qui est surtout le cas en mode

II), cette méthode surestime la longueur de fissure ainsi que les FICs effectifs, tandis que dans le cas d'un fort frottement/compression entre les lèvres de la fissure, sa longueur est sous-estimée et les FICs effectifs surestimés. Ainsi, cette méthode n'est pas adaptée à la mesure des FICs effectifs lors d'essais représentatifs du chargement rencontré dans les rails. Elle permet cependant de localiser la pointe de fissure si elle est appliquée entre une image à ouverture maximale et une image prise après une petite décharge élastique.

Afin d'obtenir les FICs effectifs, une approche inverse a été proposée : le saut de déplacement relatif entre les lèvres de fissures est comparé à celui obtenu par des calculs éléments finis plus une constante. Cette méthode permet de capturer les effets de la plasticité en pointe de fissure, ainsi que du contact et frottement entre les lèvres de fissure pour des chargements de mode I ou mode II pur (ce que la méthode "classique" ne permet pas). Pour des chargements de mode mixe non-proportionnel, elle reste utilisable tant que les couplages entre les écoulements plastiques de mode I et II restent négligeables.

Enfin, une dernière méthode a été proposée, qui permet d'obtenir le profil des contraintes entre les lèvres de fissure en plus des FICs effectifs. Cette approches est basée sur un couplage entre DIC et calculs éléments finis : Sur des calculs élément finis (élastiques ou élasto-plastiques) pilotés aux bords par des conditions aux limites en déplacement issues de la DIC, on cherche le profil de contraintes entre les lèvres de fissure permettant d'avoir le champ de déplacement le plus proche du champ de DIC. Il suffit ensuite de calculer les FICs effectifs par un calcul avec les conditions aux limites issues de la DIC et les efforts entre les lèvres de fissure déterminés précédement.

Cette méthode s'étant révélée beaucoup plus gourmande en temps de calcul et plus sensible au bruit que la méthode des sauts de déplacements, c'est cette dernière qui a été utilisée dans la suite de l'étude.

3 Essais de mode I

Des essais de fissuration par fatigue en mode I ont été menés à divers rapports de charge sur des éprouvettes de type SENT. Le dispositif expérimental est décrit figure 3.

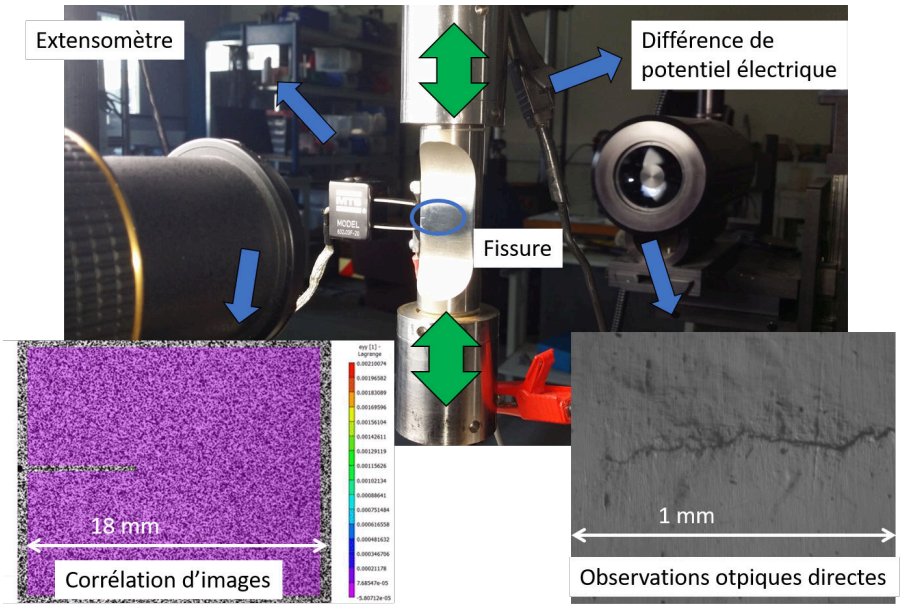

FIGURE 3 – Dispositif expérimental pour les essais de mode I.

L'échantillon est monté dans une presse hydraulique $\pm 100\ kN$, et sollicité à une fréquence de 10 à 20 Hz. Un

extensomètre est monté pour mesurer les effets de fermeture. La longueur de fissure est mesurée par différence de potentiel ou avec un microscope optique QUESTAR sur l'une de faces de l'échantillon (la surface ayant été préalablement polie). L'autre face est couverte d'un mouchetis en peinture afin d'obtenir le champ de déplacement proche de la pointe de fissure par DIC, et d'en déduire les FICs effectifs.

Du fait de la rigidité du montage, la contrainte aux bords de l'échantillon n'est pas uniforme, contrairement à ce que supposent les abaques de calcul de K_I [Tada et al., 1973]. Une abaque a donc été reconstruite à partir de mesures de $K_I^{nom}(a)$ par DIC.

Sept essais ont été réalisés, à rapport de charge R = 0.6, 0.3, -0.5, -1 et -2. L'évolution de la vitesse de propagation en fonction de ΔK_I^{nom} est tracée figure 4. Tous les points se situent dans une enveloppe d'un facteur 14.8 en vitesse, avec $R^2 = 0.928$.

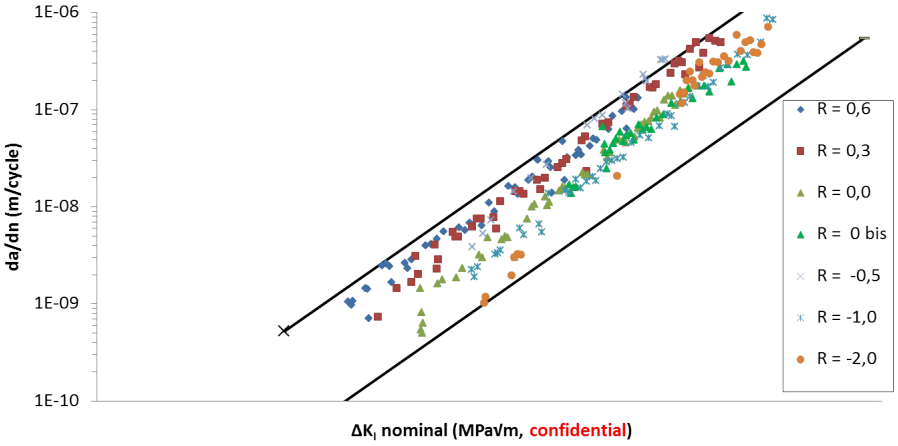

FIGURE 4 – Vitesse de propagation en fonction de $\Delta K_I^{nom} = K_I^{max} - min(K_I^{min}; 0)$ pour divers rapports de charge.

Contrairement à ce qui était attendu, la phase de compression ralentit la propagation. Cet effet a également été observé par Pokorný et al. [Pokorný et al., 2017] sur un acier à essieux ferroviaire, et a été attribué à la formation d'une couche d'oxyde sur les lèvres de fissure, favorisée par la compression, et induisant des effets de fermeture par oxydation. A rapport de charge positif, aucune trace de contact entre les lèvres de fissure n'est visible sur les faciès de rupture (fig. 5b&d), tandis qu'à rapport de charge négatif, des zones matées et oxydées apparaissent (fig. 5a&c).

La vitesse est prédite de manière satisfaisante avec ΔK_I^{eff}, comme illustré figure 6 : $R^2 = 0.964$, et tous les points se situent dans une enveloppe d'un facteur 5.6 en vitesse.

La vitesse de propagation prédite dans une gamme de ΔK_I^{nom} représentative des fissures dans les rails a été comparée à des mesures obtenues sur plus de 300 fissures présentes en voie. Il apparait que le mode I seul ne peut expliquer la fissuration des rails, car la vitesse prédite est plus de 5 fois inférieure à celle des fissures présentes dans les rails.

4 Essais de mode mixte II & III

Le mode I seul ne pouvant expliquer la fissuration des rails, des essais de mode mixte II & III ont été menés afin de vérifier si le cisaillement seul le pouvait.

Les échantillons sont des barres contenant une entaille en leur centre, servant à amorcer une préfissure par flexion 4 points. Une fois la préfissure obtenue, l'échantillon est sollicité en flexion 4 points dissymétrique, de sorte que son

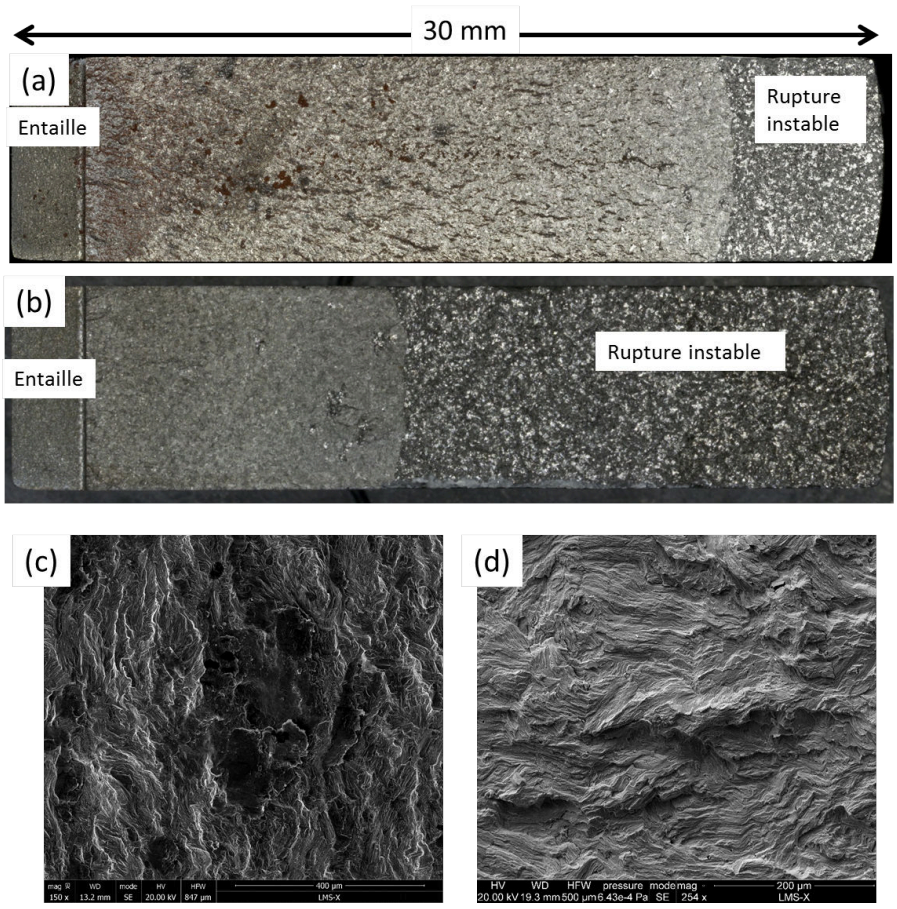

FIGURE 5 – Faciès de rupture : (a) essai à $R = -2$ et (b) essai à $R = 0.3$ au microscope optique, (c) essai à $R = -1$ et (d) $R = 0.3$ au MEB.

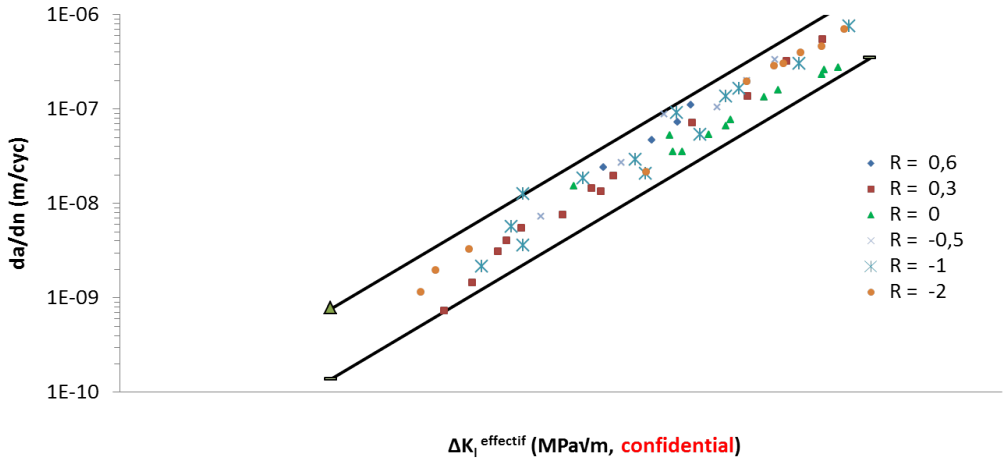

FIGURE 6 – Vitesse de propagation en fonction de ΔK_I^{eff} pour divers rapports de charge.

centre (avec l'entaille et la fissure) subisse uniquement un effort tranchant (et donc pas de moment fléchissant). Ainsi, la fissure est sollicitée uniquement en cisaillement. Le montage est illustré figure 7. L'échantillon peut être tourné autour de son axe afin de faire varier les proportions de mode II & III le long du front.

Une fois l'essai en cisaillement terminé, l'échantillon est rompu par rupture fragile à l'azote, ou par fatigue en mode I. Ceci permet d'accéder au faciès de rupture, et aux fronts de préfissure / fin d'essai de cisaillement, comme

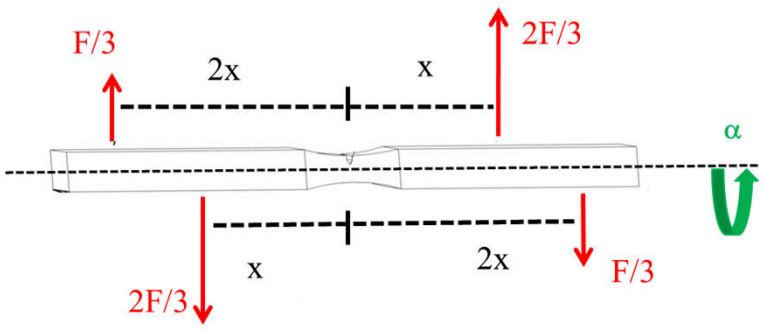

FIGURE 7 – Dispositif expérimental pour les essais de mode mixte II & III.

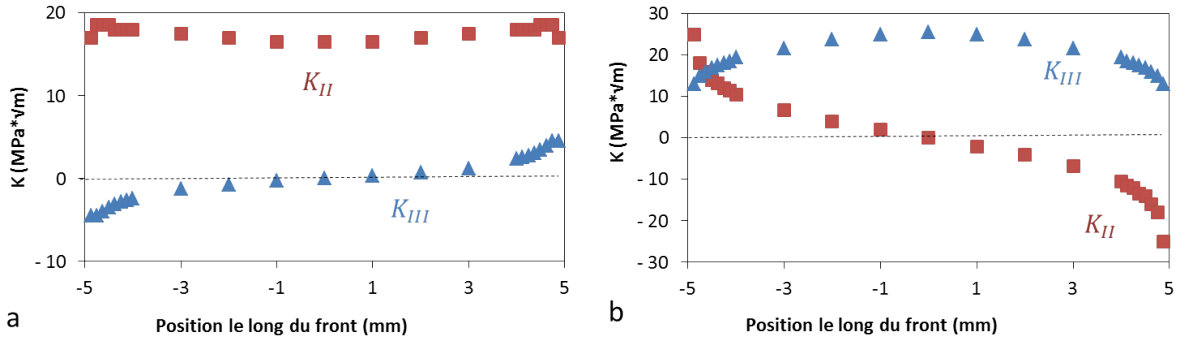

FIGURE 8 – Evolution des FICs le long du front.

illustré figure 9. Ceci permet d'accéder à la vitesse moyenne de propagation en tout point du front durant l'essai $\Delta a(z)/\Delta N$. L'objectif est ensuite de corréler cette vitesse et le trajet de la fissure aux FICs effectifs locaux.

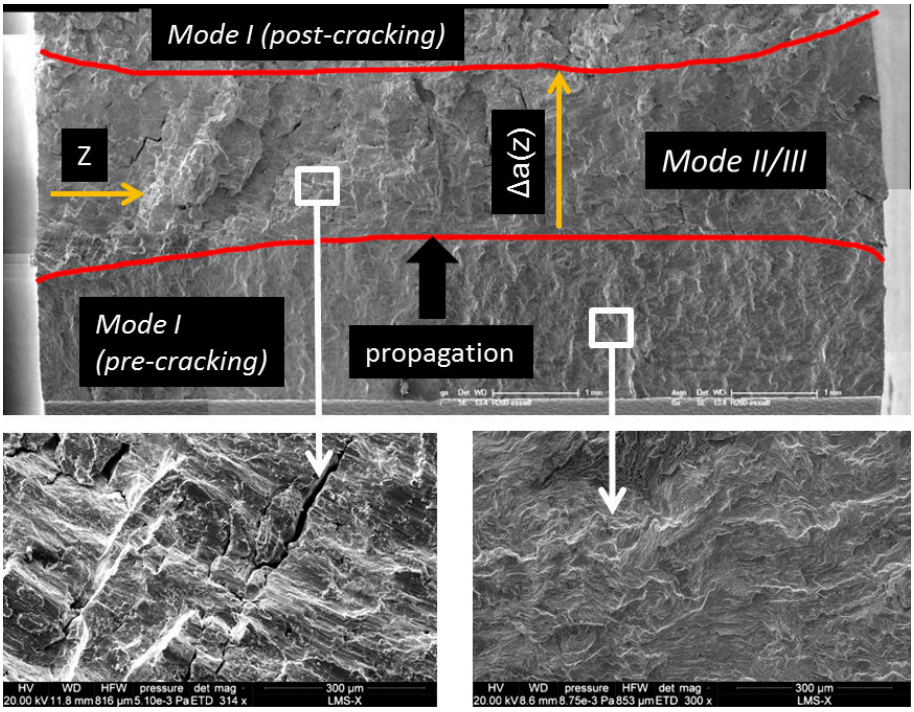

FIGURE 9 – Fronts finaux et initiaux de l'essai en cisaillement.

Afin d'estimer les FICs effectifs la méthode des sauts de déplacements proposée dans la partie 2 a été utilisée. Du fait de la position de l'échantillon dans la machine, ses surfaces latérales ne pouvaient être observées directement avec une caméra. Des répliques ont donc été prises à charges minimales, nulle et maximale. Un mouchetis topographique, obtenu par sablage et pouvant se transposer sur les répliques, a été utilisé pour obtenir les champs de déplacements plans (modes I et II) par DIC. Les champs de déplacements hors plan (mode III) ont été obtenus par mesure topographique, à l'aide d'un microscope à force atomique ou d'un microscope optique numérique (selon l'amplitude des débattements).

Du fait du frottement entre les lèvres de fissure, la fraction effective du chargement $U = \Delta K^{eff}/\Delta K^{nom}$ est réduite, comme illustré figure 10. Cette réduction est plus importante à $\alpha = 90°$, c'est à dire pour du mode III prédominant, ce qui s'explique par une rugosité plus importante parallèlement au front que orthogonalement au front ($Ra = 8.8\ \mu m$ vs $Ra = 5.9\ \mu m$). Le glissement des lèvres rugueuses induit une ouverture de la fissure (effet de dilatance), et donc deux cycles de mode I pour chaque cycle de cisaillement alterné.

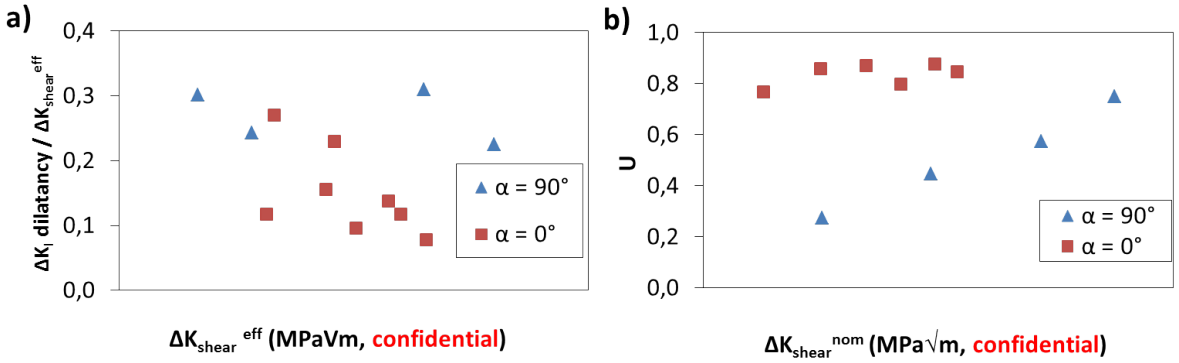

FIGURE 10 – Evolution de $U = \Delta K^{eff}/\Delta K^{nom}$ et $\Delta K_I^{eff}/\Delta K_{shear}^{eff}$.

De la propagation coplanaire sur des distances allant jusqu'à 2.8 mm a été observée pour des niveaux de chargements au-delà d'un certain seuil. Cependant, la fissure fini presque toujours par bifurquer (sauf pour des chargements très importants), ce qui peut s'expliquer par la formation de branches normales à la fissure, induisant des effets d'écran (et donc réduisant les FICs effectifs). Un exemple de telles branches est donnée figure 11.

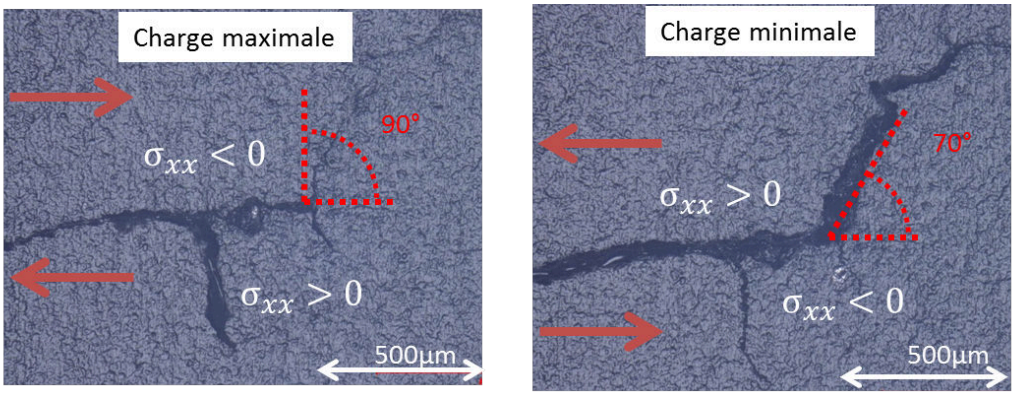

FIGURE 11 – Branche en arrière de la pointe lors d'un essai à $\alpha = 0$.

La vitesse moyenne de propagation coplanaire a été mesurée, et se corrèle raisonnablement bien avec $\Delta K_{equ}^{eff} =$

$\sqrt{\Delta K_{II}^{effective^2} + 1.25\Delta K_{III}^{effective^2}}$. Le facteur 1.25 signifie que le mode III est légèrement moins efficace que le mode III par rapport à ce qu'une approche énergétique prédirait (1.4). $\Delta K_{shear}^{eff} = \sqrt{E * \Delta G_{shear}^{eff}/(1-\nu^2)}$ fut cependant préféré comme force motrice, du fait de son sens physique, les prédictions étant proches de celles de ΔK_{equ}^{eff} (cf figure 12)

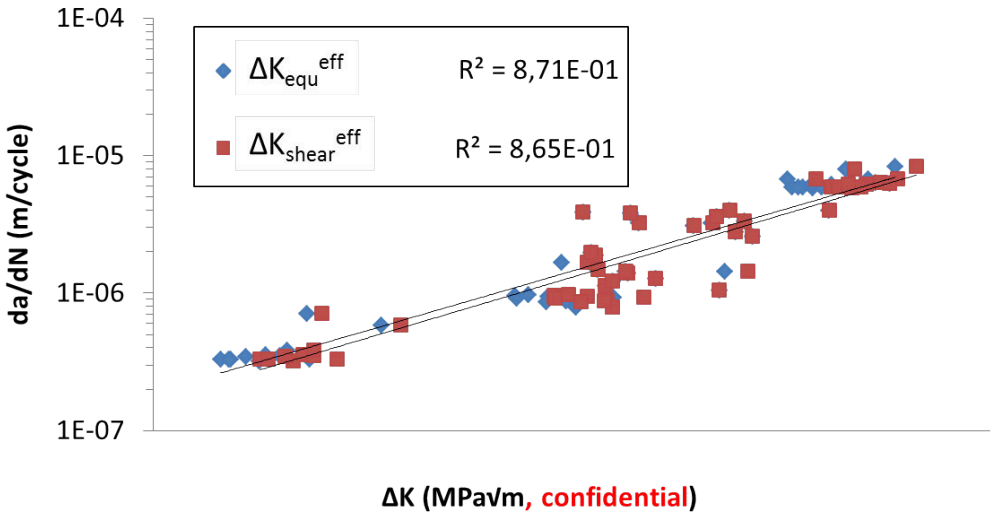

FIGURE 12 – Evolution de la vitesse de propagation coplanaire en fonction de $\Delta K_{equ}^{eff} = \sqrt{\Delta K_{II}^{effective^2} + 1.25\Delta K_{III}^{effective^2}}$ et $\Delta K_{shear}^{eff} = \sqrt{E * \Delta G_{shear}^{eff}/(1-\nu^2)}$.

Au vu de ces essais, il apparait qu'une fissure se propageant à la vitesse des fissures de type Squats dans les rails, et sollicitée uniquement en cisaillement, bifurquerait. Ainsi, les modes de cisaillement seuls ne permettent pas d'expliquer la fissuration des rails où les fissures restent coplanaires.

5 Essais de mode mixte non-proportionel I + II

Ni le mode I seul, ni les modes de cisaillement seuls ne peuvent expliquer la fissuration des rails, et il semble donc que ce soit la combinaison (non proportionnelle) des différents modes qui soit responsable de la propagation de ces fissures. Ces chargements ont été étudiés par des essais en mode mixte non proportionnels I + II.

Ces essais sont menés sur des tubes d'épaisseur 1 mm et de rayon externe 12.5 mm montés dans une machine de traction-torsion (deux actionneurs différents). Une préfissure d'environ 3 mm de long (demi-longueur 1.5 mm) est amorcée par un chargement de traction cyclique. L'échantillon est ensuite sollicité en traction-torsion : la traction induit du mode I, tandis que la torsion induit du mode II. Le dispositif expérimental est représenté Figure 13. Les échantillons sont recouverts d'un mouchetis en peinture afin d'effectuer un suivi par stéréo-corrélation d'images. La taille des subsets obtenus est d'environ 150 microns, avec un step de 20 microns. Les champs de déplacements issus de la corrélation d'images sont utilisés pour localiser la pointe de fissure et mesurer les FICs effectifs.

La liste des 15 essais réalisés est donnée Tableaux 1, 2, 3. Les chargements appliqués dans le plan K_I - K_{II} sont séquentiels, déphasés de 90 ° (forme elliptique) ou bien séquentiels inclinés (obtenus par un pilotage séquentiel des actionneurs de force et couple mais avec une préfissure inclinée), comme illustré Figure 14.

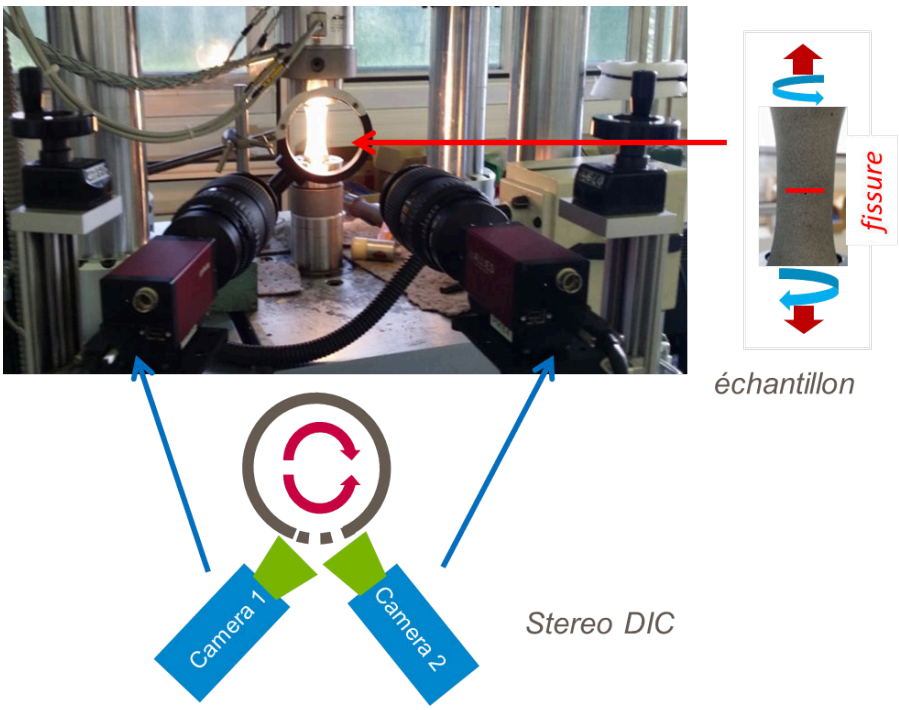

FIGURE 13 – Dispositif expérimental pour les essais en mode mixte non-proportionnel I + II.

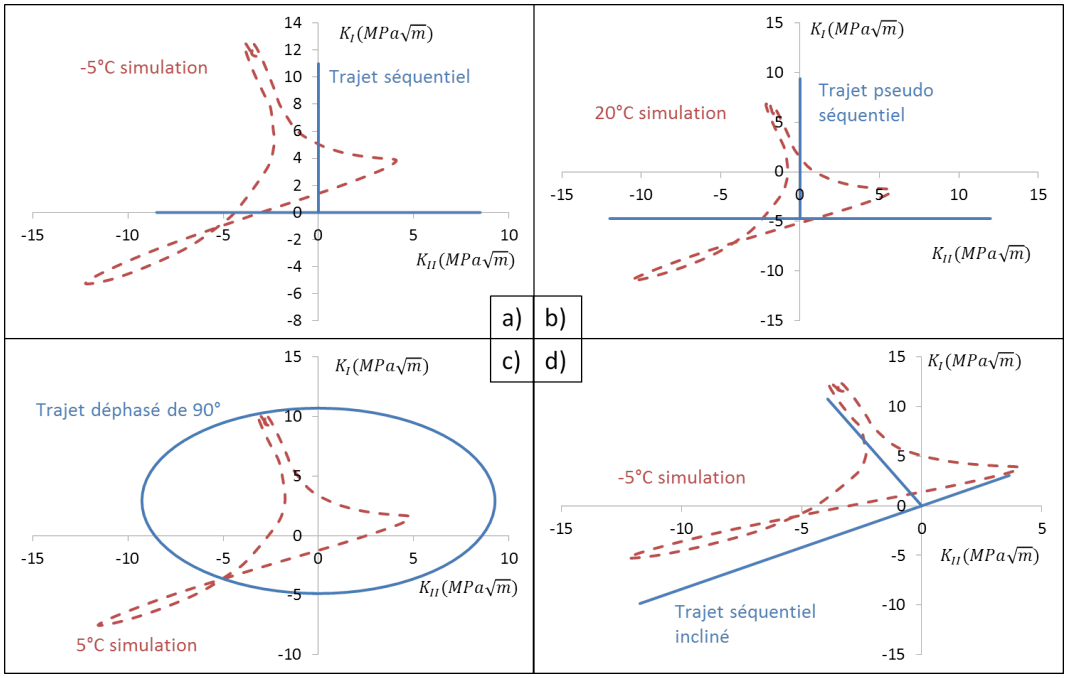

FIGURE 14 – Trajets de chargements testés.

5.1 Essais séquentiels

Dix essais avec un chargement pseudo-séquentiel ont été réalisés avec différents niveaux d'effort de traction, cisaillement et compression. Le chargement, nombre de cycle appliqué et résultat en terme de nombre de cycles à rupture et distance de propagation coplanaire sont donnés tableau 1. Lorsqu'il n'y a pas de compression pendant le cisaillement, la fissure bifurque après une courte propagation coplanaire (comme illustré Figure 15) lorsque

$\Delta K_{II}^{nom}/\Delta K_I^{nom} > 2$, comme observé par [Bold, 1990, Wong et al., 2000, Akama, 2003]. Cependant, lorsqu'une compression est ajoutée pendant le cycle de cisaillement, la fissure peut se propager de manière coplanaire pour $\Delta K_{II}^{nom}/\Delta K_I^{nom} > 2$. Ceci est dû à une augmentation du frottement, et une diminution de $\Delta K_{II}^{eff}/\Delta K_I^{eff}$: la propagation reste coplanaire tant que $\Delta K_{II}^{eff}/\Delta K_I^{eff} \lessapprox 2$. Ce ratio effectif est initialement inférieur au ratio nominal, mais croît du fait de l'usure des lèvres de fissure, et de la diminution du frottement en résultant. La Figure 16, représentant l'évolution de $\Delta K_{II}^{eff}/\Delta K_I^{eff}$ pour différentes conditions, illustre ce phénomène. L'ajout d'une compression lors du cycle de cisaillement réduit la valeur initiale de $\Delta K_{II}^{eff}/\Delta K_I^{eff}$, et ralentit sa croissance, tendant donc à favoriser une propagation coplanaire plus longue.

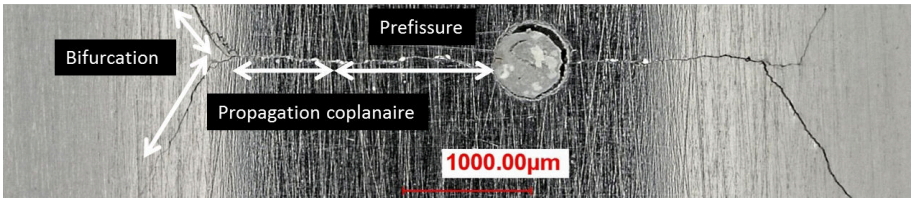

FIGURE 15 – Exemple de trajet de fissure.

TABLE 1 – Paramètres d'essais et résultats en termes de propagation coplanaire pour les essais pseudo-séquentiels.

Exp. N°	effort axial Max / Min (kN)	Couple (N.m)	$\frac{\Delta K_{II}}{\Delta K_I}$ nominal	Propagation coplanaire (mm)	N_{cycles} appliqués à un chargement donné (total si $\neq$)	N_{cycles} de propagation coplanaire	Jauge de déformation
9_a	10 / -5	± 110	1.9	≈ 0.1	400 000	400 000	non
9_b *	10 / -5	± 140	2.4	≈ 0.1	250 000 (1 050 000)	1 050 000	non
9 *	13 / 0	± 90	1.2	>4.3	240 000 (1 640 000)	1 640 000	non
8	10/0	± 90	1.6	>4	75 000	70 000	non
19	10/0	± 90	1.6	>6	51 000	51 000	oui
18 *w*	10/0	± 90	1.6	>6	51 000	51 000	oui
4	7/0	± 110	2.7	1	235 000	180 000	non
7 *	12/5	± 110	2.7	0.6	110 000 (630 000)	600 000	non
5	10/0	± 150	2.6	0.4	40 000	15 000	non
6	10/-5	± 150	2.6	3.8	133 000	128 000	non
11	11/0	± 160	2.5	0.6	6 000	3 000	oui
10	11/-5	± 160	2.5	4.5	23 000	20 000	oui

5.2 Essais avec chargements déphasés de 90°

Trois essais ont été menés avec un chargement déphase de 90° (comme illustré Figure 14.c). Tous ont donné lieu à une bifurcation après une courte propagation coplanaire. Le chargement, nombre de cycle appliqué et résultat en termes de nombre de cycles à rupture et distance de propagation coplanaire sont donnés tableau 2.

Des essais à $F = +11/-5\ kN$ et $C = \pm 160\ Nm$ ont été menés avec un chargement séquentiel et hors phase. Ces deux essais ont donc les mêmes amplitudes de ΔK_I^{nom} et ΔK_{II}^{nom}, mais avec des trajets dans le plan K_I - K_{II} différents. Néanmoins, les ΔK^{eff} obtenus sont très différents (dans un cas la fissure est comprimée lors du cisaillement, ce qui réduit ΔK_{II}^{eff}, alors que dans l'autre la fissure est ouverte lorsque le cisaillement est maximal). L'essai séquentiel a donné lieu à une propagation coplanaire, tandis que l'essai hors phase a donné lieu à une

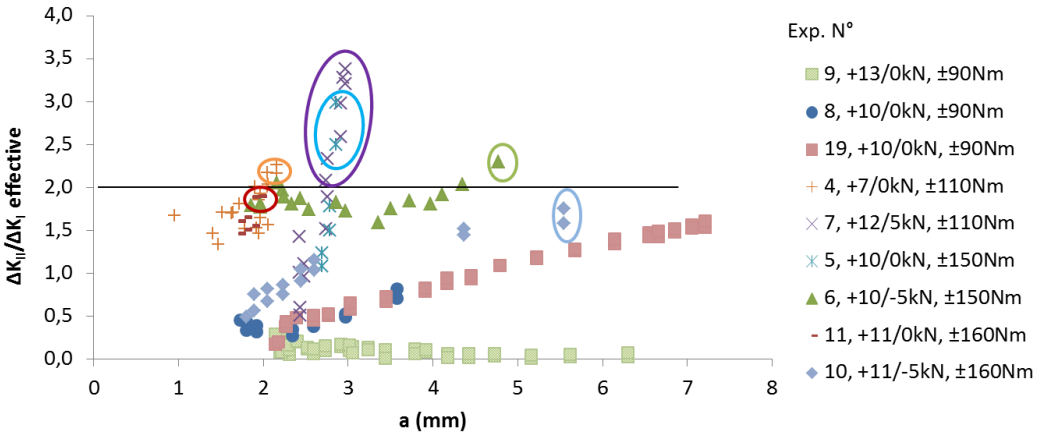

FIGURE 16 – Evolution de $\Delta K_{II}^{eff}/\Delta K_{I}^{eff}$ en fonction de la longueur de fissure lors des essais séquentiels.

bifurcation, avec une vitesse de propagation 10 fois plus grande.

TABLE 2 – Paramètres d'essais et résultats en termes de propagation coplanaire pour les essais avec un chargement séquentiel incliné.

Exp. N°	effort axial Max / Min (kN)	Couple (N.m)	$\frac{\Delta K_{II}}{\Delta K_I}$ nominal	Propagation coplanaire (mm)	N_{cycles} appliqués à un chargement donné (total si $\neq$)	N_{cycles} de propagation coplanaire	Jauge de déformation
12	11/-5	± 160	2.5	0.4	4000	500	oui
13	11/-5	± 110	1.7	0.6	23000	2000	oui
14	11/-5	± 70	1.1	0.3	105000	5000	oui

Ainsi, la donnée de la seule amplitude des FICs nominaux (ΔK_I^{nom}m et ΔK_{II}^{nom}) ne suffit pas à prédire le trajet et la vitesse de propagation. De même, la seule amplitude des FICs effectifs (ΔK_I^{eff} et ΔK_{II}^{eff}) ne suffit pas à prédire la bifurcation.

5.3 Essais avec chargement séquentiel incliné

Deux essais ont été menés avec un chargement séquentiel incliné (cf Figure 14.d), plus proche des chargements calculés. Ce trajet est obtenu par un pilotage séquentiel des actionneurs de couple et force, mais avec une préfissure inclinée. Le chargement, nombre de cycle appliqué et résultat en termes de nombre de cycles à rupture et distance de propagation coplanaire sont donnés tableau 3.

Pour les deux essais, la fissure a bifurqué après une courte propagation coplanaire, pour ensuite se remettre à l'horizontale et revenir à un chargement séquentiel. Ce chargement séquentiel incliné n'est donc vraisemblablement pas celui vu par les fissures dans les rails (qui ne bifurquent pas), ce qui pourrait être dû à une modélisation trop simpliste de l'effet des contraintes résiduelles, ou bien à l'hypothèse que la fissure dans le rail est semi-elliptique, alors que sa forme réelle est plus complexe (cf fig. 1).

5.4 Frottement et usure des lèvres de fissure.

Des exemples de trajets de chargement effectifs sont donnés figure 17. Les effets de fermeture dus à la plasticité et à la rugosité réduisent le rapport U_I (compris entre 0.76 à 1). Lors des essais séquentiels et pseudo-séquentiels, le frottement et l'enchevêtrement des aspérités le long des lèvres de fissure réduisent la singularité de mode II (U_{II}

TABLE 3 – Paramètres d'essais et résultats en termes de propagation coplanaire pour les essais avec un chargement déphase de 90°.

Exp. N°	effort axial Max / Min (kN)	Couple (N.m)	$\frac{\Delta K_{II}}{\Delta K_I}$ nominal	Propagation coplanaire (mm)	N_{cycles} appliqués à un chargement donné (total si $\neq$)	N_{cycles} de propagation coplanaire	Jauge de déformation
16	10/0	45/-145	1.6	0.4	136000	30000	oui
17	10/0	80/-160	2.1	0.3	44500	5000	oui

de 0 à 0.52, cf figure 18). Ceci ne peut être expliqué par un frottement de type Coulomb. Comme lors des essais de mode mixte II & III, de la dilatance est observée (graphe de gauche, figure 17).

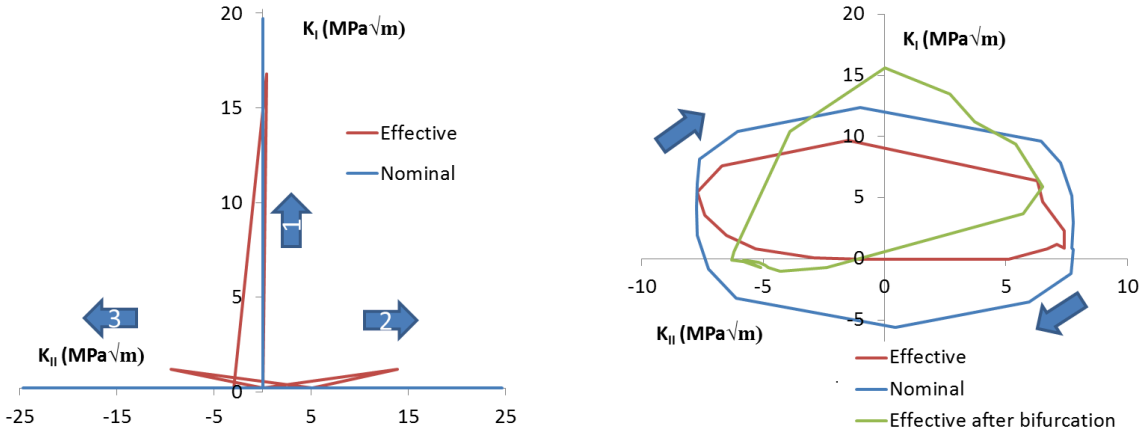

FIGURE 17 – Trajets de chargements pour l'essai séquentiel $N°19$ ($F = +10/0\ kN$, $C = \pm 90\ Nm$), au cycle 45000 (gauche), et l'essai déphasé de 90 ° $N°14$ ($F = +11/-5\ kN$, $C = \pm 70\ Nm$), au cycle 5000 (avant bifurcation) et 65000 (après bifurcation) (droite).

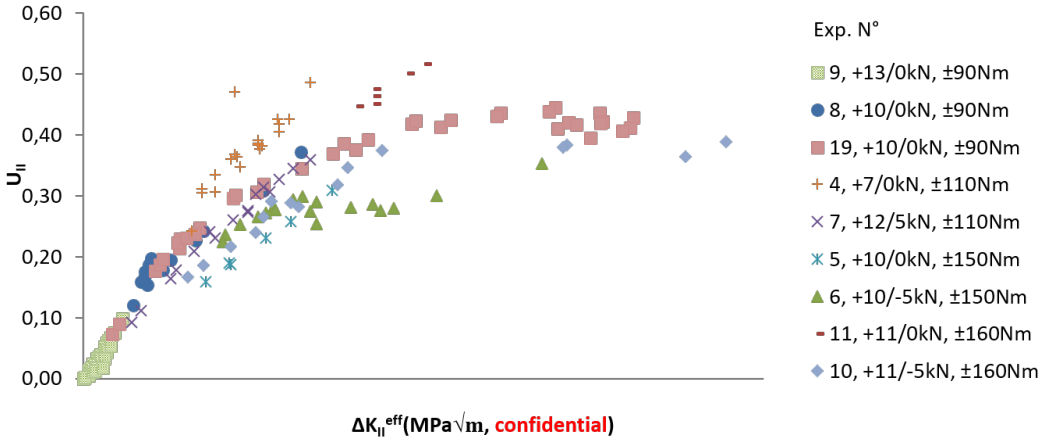

FIGURE 18 – Evolution de $U_{II} = \Delta K_{II}^{eff} / \Delta K_{II}^{nom}$ lors des essais pseudo-séquentiels.

La rugosité des lèvres de fissure, qui réduit fortement U_{II}, évolue lors des essais du fait de l'usure. Lors de l'essai N° 9, avec un faible niveau de couple ($\pm$ 90 Nm) la fissure apparente durant le cycle de mode II est plus courte que durant le cycle de mode I (cf figure 19.a), ce qui signifie que $\Delta K_{II}^{eff} = 0$. Dans ce cas, les lèvres ne sont pas usées, et le faciès de rupture est similaire à celui des essais de mode I. Pour l'essai N° 6, avec un couple plus important ($\pm$

150 Nm) et malgré la compression, les deux fissures apparentes ont la même longueur : $\Delta K_{II}^{eff} \neq 0$. Les faces de la fissure sont fortement usées, avec la présence d'oxydation et de débris. Ces derniers forment un troisième corps, qui influe sur l'usure et le frottement [Arnaud, 2018].

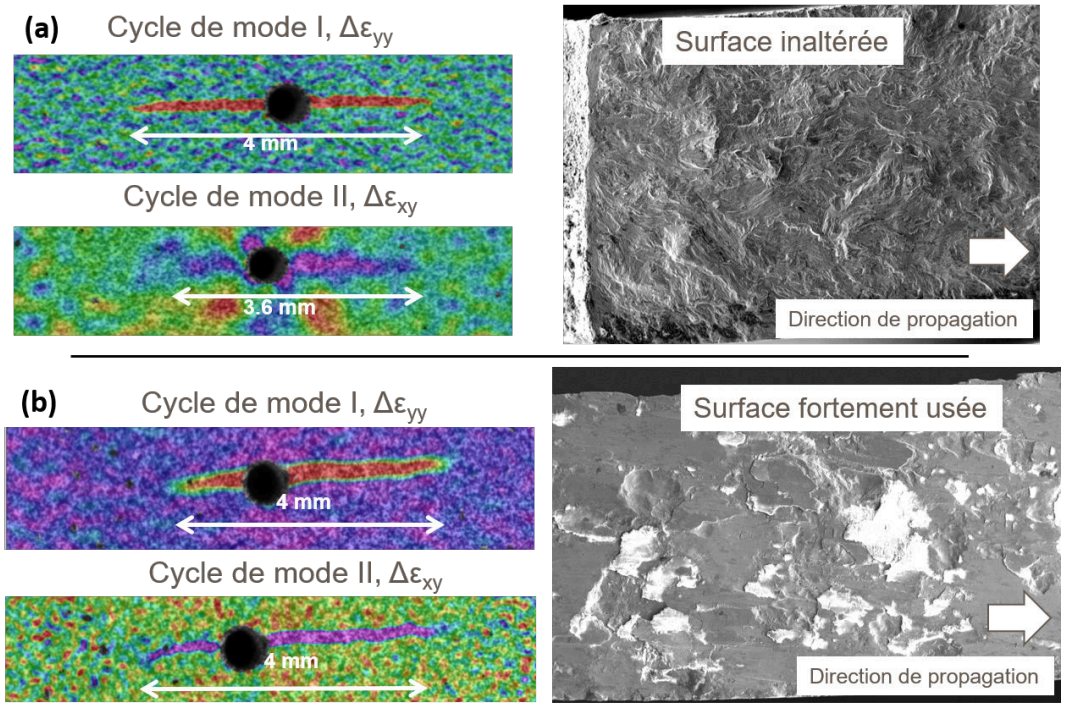

FIGURE 19 – (a) : fissure apparente durant les cycles de mode I et II, et faciès de rupture de l'essai N° 9 (13 / 0 kN, ± 90 Nm). (b) : fissure apparente durant les cycles de mode I et II, et faciès de rupture de l'essai N° 6 (10 / -5 kN, ± 150 Nm).

5.5 Vitesse de propagation

La vitesse de propagation se corrèle pour tous les essais (avec des chargements et trajets de fissures très différents !) avec $\Delta K_{eq}^{eff} = \sqrt{(\Delta K_I^{eff})^2 + (\Delta K_{II}^{eff})^2 + \frac{1}{1-\nu}(\Delta K_{III}^{eff})^2}$, comme illustré figure 20. 90% des points sont inclus dans une enveloppe d'un facteur 4 en vitesse, avec $R^2 = 0.87$. Ainsi, à l'opposé de Fremy et al. [Fremy et al., 2014], l'effet de la forme du trajet n'est pas observé. Du fait de la dispersion sur la courbe (le contact et frottement rendent l'estimation de la position de la pointe de fissure et des FICs effectifs difficiles), un tel effet ne peut être exclu, mais il semble être ici de second ordre par rapport à l'effet de la forme du trajet nominal sur les FICs effectifs (et donc sur la vitesse de propagation) via le contact et frottement.

Ainsi, il existe un critère simple pour prédire la vitesse de propagation, à condition de connaître les FICs effectifs (la vitesse ne se corrèle pas avec les FICs nominaux). Ceci nécessite donc d'avoir un moyen d'évaluer précisément ces FICs effectifs dans les calculs dans le rail, c'est-à-dire d'avoir une meilleure compréhension de l'évolution du frottement et des effets de fermeture entre les lèvres de la fissure.

5.6 Prédiction du trajet de fissuration

Comme expliqué précédemment, la donnée de la seule amplitude des FICs nominaux ou effectifs ne suffit pas à prédire le trajet de la fissure. L'approche employée a consisté à mesurer les évolutions temporelles $K_I^{eff}(t)$ et $K_{II}^{eff}(t)$ durant un cycle complet, pour différents cycles « remarquables » (avant et après bifurcation) des essais

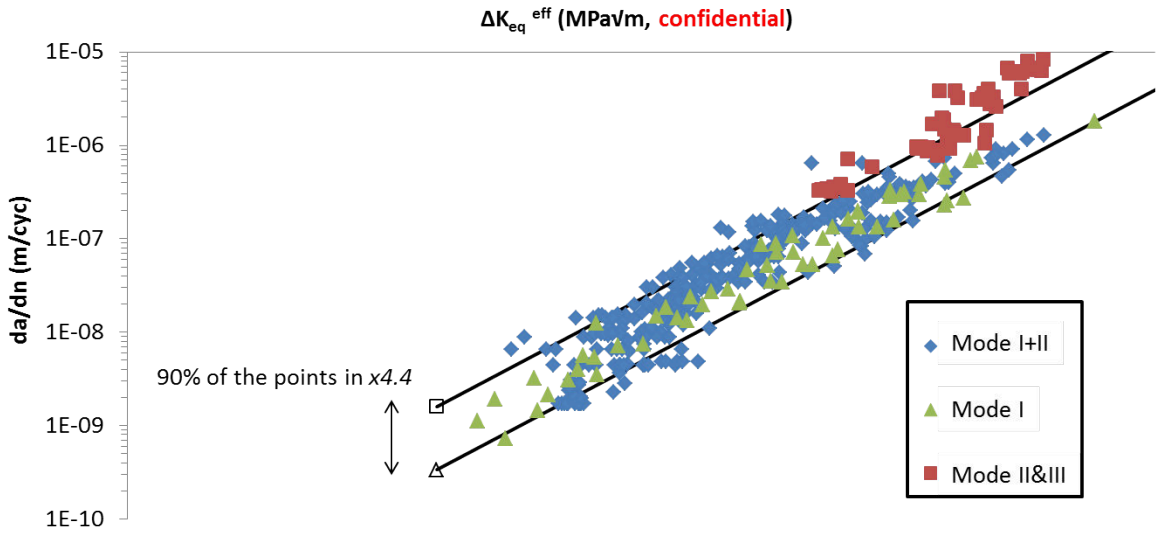

FIGURE 20 – Evolution de la vitesse de propagation pour les essais de mode I, mode mixte II & III et mode mixte non-proportionnel I + II en fonction de $\Delta K_{eq}^{eff} = \sqrt{(\Delta K_I^{eff})^2 + (\Delta K_{II}^{eff})^2 + \frac{1}{1-\nu}(\Delta K_{III}^{eff})^2}$.

pseudo-séquentiels. Pour chacune de ces évolutions, le trajet prédit par divers critères a été calculé et le pourcentage de prédictions « correctes » a été reporté dans le Tableau 4.

TABLE 4 – Pourcentage de trajets prédits avec une précision donnée pour les critères MTS, MTSp et MTSp avec prise en compte du contact et frottement.

Ecart inférieur à	% de succès		
	MTS	MTSp	MTSp avec contact & frottement
15 °	60	53 %	73 %
30 °	83	90 %	97 %

Le critère de la contrainte tangentielle maximale prenant en compte la redistribution des contraintes due à la plasticité en pointe de fissure (MTSp, [Dahlin and Olsson, 2003]) capte mieux la bifurcation que son équivalent élastique (MTS). La prise en compte du contact et frottement améliore les prédictions.

En effet, la prise en compte de la plasticité tend a diminuer les maximas de la contrainte tangentielle à $\approx \pm 70°$ (voir figure 21), ce qui augmente la distance de propagation coplanaire prévue. Cependant, la propagation coplanaire n'est jamais vraiment prédite, car le maximum à $\approx 0°$ est déplacé vers $\approx 15°$ du fait des contraintes résiduelles de cisaillement laissées par le cycle de mode II précédent. De plus, la bifurcation, lorsqu'elle a lieu, est toujours prévue à $\approx \pm 70°$, tandis qu'elle était comprise entre 40 et 60° lors des essais : ces deux effets expliquent les mauvais résultats de ce critère (MTSp) à moins de 15° dans le tableau 4.

Ajouter les contraintes de contact et frottement tend à rapprocher les maximas à $\approx \pm 70°$ vers $\approx \pm 45°$ (direction de contrainte tangentielle maximale si la fissure est bloquée), et rapproche le maxima correspondant à la propagation coplanaire vers $\approx 0°$, ce qui améliore les prévisions.

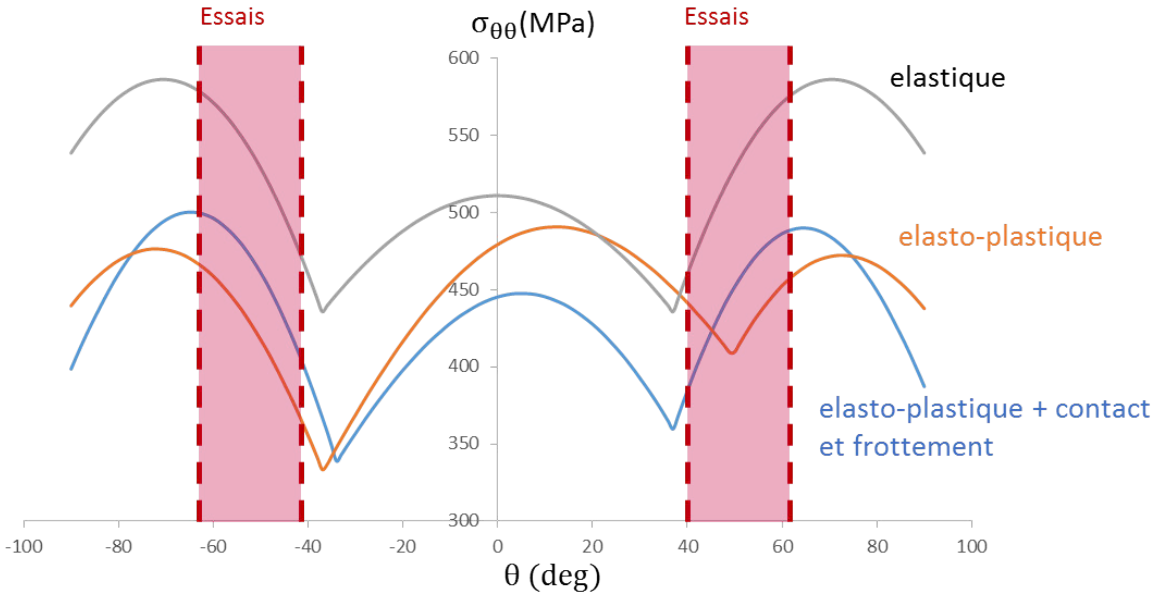

FIGURE 21 – Evolution du maximum temporel de la contrainte tangentielle devant la pointe, en fonction de l'angle. Calcul élément fini avec $\Delta K_{II}^{eff}/\Delta K_{I}^{eff} = 2$, $R_I = -1$ et $U_{II} = 0.5$.

6 Proposition d'une approche pour prédire la propagation des fissures

Le trajet et la vitesse de propagation peuvent être prédits de manière satisfaisante à partir de l'évolution temporelle des FICs effectifs (par exemple avec une loi de type Paris & ΔK_{eq}^{eff}, et le critère MTS). Cependant, la détermination des FICs effectifs à partir des valeurs nominales ne peut être faite avec une simple loi de type Coulomb, qui ingore l'effet de la rugosité des fissures. Une approche simple a donc été proposée afin d'être implémentée dans la chaine de calcul SNCF utilisant les éléments finis étendus. Cette approche repose sur l'hypothèse que le frottement peut se diviser en deux sources : une source extrinsèque (frottement de type Coulomb, lié à la compression lointaine) et une source intrinsèque (rugosité).

En mode I + II séquentiel, on calcule l'amplitude des FICs effectifs comme :

$$\Delta K_{I}^{eff} = U_I * K_{I}^{nom} \tag{1}$$

$$\Delta K_{II}^{eff} = \alpha * \Delta K_{II}^{coulomb} - 2 * K_{II}^{0} \tag{2}$$

Avec U_I une constante représentant les effets de fermeture par plasticité, K_{II}^{0} un seuil en dessous duquel la fissure est bloquée, et α la valeur asymptotique de U_{II} lorsque ΔK_{II}^{eff} est élevé. $\Delta K_{II}^{coulomb}$ représente la valeur de ΔK_{II} obtenue après prise en compte du frottement de type Coulomb.

Cette approche peut être généralisée à des cas de chargements quelconques en mode mixte non-proportionnel I + II + III.

Une validation de l'approche a été effectuée sur les des essais de mode mixte séquentiel et pseudo séquentiels I + II & III, avec des résultats satisfaisants.

7 Conclusions

Des trajets de chargement subis par les fissures de type Squats ont été simulés en utilisant une chaine de calcul développée par SNCF. Ces trajets sont de mode I + II + III quasi séquentiels, avec une phase de compression lors du cisaillement.

Un outil de post-traitement de champs de déplacements a été développé afin de suivre des essais représentatifs du chargement subis par ces fissures.

Ni le mode I seul, ni les modes de cisaillement seuls n'ont permis d'expliquer la fissuration dans les rails.

Des essais de mode mixte non-proportionnels I + II ont été effectués, dont le trajet et la vitesse de propagation ont pu être prédits avec des critères simples basés sur les FICs effectifs (loi de type Paris & ΔK_{eq}^{eff}, et le critère MTS)

Cependant, la détermination de ces FICs effectifs à partir des valeurs nominales s'est révélée complexe. Le challenge pour les applications industrielles n'est donc pas seulement de trouver le critère de bifurcation et la loi de propagation les plus adéquates, mais également de prendre en compte le frottement (lié aux aspérités), voire l'usure, dans les simulations afin d'estimer les FICs effectifs.

Afin d'estimer ces FICs effectifs, une approche simplifiée a été proposée et validée sur des essais de mode I + II & III séquentiels.

Cette approche reste cependant à valider par rapport au retour d'expérience de SNCF, et des essais menés sur un rail (à l'échelle 1 : 1).

Une modélisation de l'usure et du troisième corps, comme fait par [Arnaud and Fouvry, 2018], pourrait certainement améliorer les prédictions des FICs effectifs. La prise en compte des effets de fermeture induits par l'oxydation pourrait également s'avérer utile.

D'un point de vue industriel, la chaine de calcul finalisée permettra d'optimiser les intervalles de maintenance, de quantifier l'influence des conditions de circulation (géométrie du rail, raideur de la voie, météo, type de train...) sur la propagation des fissures et de proposer des conditions optimisées. Si elle s'avère fructueuse, cette approche pourra également être appliquée à d'autres nuances de rails, afin de déterminer leurs avantages et inconvénients.

Références

[Abanto-Bueno and Lambros, 2002] Abanto-Bueno, J. and Lambros, J. (2002). Investigation of crack growth in functionally graded materials using digital image correlation. *Eng Fract Mech*, 69(14-16) :1695–1711.

[Akama, 2003] Akama, M. (2003). Fatigue crack growth under mixed loading of tensile and in-plane shear modes. *QR of RTRI*, 44 :65–71.

[Arnaud, 2018] Arnaud, P. (2018). *Etude expérimentale et numérique de l'usure et de son influence sur les mécanismes de fissuration en fretting et fretting fatigue*. PhD thesis, Ecole centrale de Lyon.

[Arnaud and Fouvry, 2018] Arnaud, P. and Fouvry, S. (2018). A dynamical FEA fretting wear modeling taking into account the evolution of debris layer. *WEAR*, 412 :92–108.

[Bold, 1990] Bold, P. (1990). *Multiaxial fatigue crack growth in rails*. PhD thesis, University of Sheffield.

[Bonniot et al., 2019] Bonniot, T., Doquet, V., and Mai, S. H. (2019). Determination of effective Stress Intensity Factors under mixed-mode from DIC fields in presence of contact stresses and plasticity. *to appear in Strain*.

[Dahlin and Olsson, 2003] Dahlin, P. and Olsson, M. (2003). The effect of plasticity on incipient mixed-mode fatigue crack growth. *FFEMS*, 26 :577–588.

[Fremy et al., 2014] Fremy, F., Pommier, S., Poncelet, M., Raka, B., Galenne, E., Courtin, S., and Roux, J. C. L. (2014). Load path effect on fatigue crack propagation in I + II + III mixed mode conditions - Part 1 : Experimental investigations. *Int J Fatigue*, 62 :104–112.

[Mai et al., 2017] Mai, S. H., Gravouil, A., Nguyen-Tajan, M. L., and Trolle, B. (2017). Numerical simulation of rolling contact fatigue crack growth in rails with the rail bending and the frictional contact. *Eng Fract Mech*, 174 :196–206.

[Pokorný et al., 2017] Pokorný, P., Vojtek, T., Náhlík, L., and Hutař, P. (2017). Crack closure in near-threshold fatigue crack propagation in railway axle steel EA4T. *Eng Fract Mech*, 185 :2–19.

[Roux and Hild, 2006] Roux, S. and Hild, F. (2006). Stress intensity factor measurements from digital image correlation : Post-processing and integrated approaches. *Int J Fracture*, 140(1-4) :141–157.

[Tada et al., 1973] Tada, H., Paris, P., and Irwin, G. (1973). The stress analysis of cracks.

[Trollé, 2014] Trollé, B. (2014). *Simulation multi-échelles de la propagation des fissures de fatigue dans les rails.* PhD thesis, Institut national des sciences appliquées de Lyon.

[Wong et al., 2000] Wong, S. L., Bold, P. E., Brown, M. W., and Allen, R. J. (2000). Fatigue crack growth rates under sequential mixed-mode I and II loading cycles. *FFEMS*, 23 :667–674.

[Yoneyama et al., 2007] Yoneyama, S., Ogawa, T., and Kobayashi, Y. (2007). Evaluating mixed-mode stress intensity factors from full-field displacement fields obtained by optical methods. *Eng Fract Mech*, 74 :1399–1412.

université PARIS-SACLAY
ÉCOLE DOCTORALE
Sciences mécaniques et énergétiques, matériaux et géosciences (SMEMAG)

Titre : Fissuration par fatigue en mode mixte non-proportionnel des rails de chemin de fer. De l'étude expérimentale à la mise en oeuvre d'un modèle.

Mots clés : fatigue de roulement ; fissuration ; mode mixte ; corrélation d'images ; chargement non-proportionnel ; frottement

Résumé : Les rails de Chemins de fer sont soumis à de la fatigue de roulement due au passage répété des roues de train, ce qui induit différents types de fissures, telles que les Squats. Ces fissures sont soumises à un chargement de mode mixte non-proportionnel I + II + III, dans des proportions variables le long du front, avec des phases de compression, ce qui rend la prédiction de leur trajet et de leur vitesse délicate.
La cinétique de fissuration en mode I a été déterminée dans de l'acier à rail R260, pour des rapports R positifs et négatifs, ainsi que la cinétique de mode mixte II & III corrigée des effets de frottement. Les Facteurs d'Intensité des Contraintes (FICs) effectifs ont été obtenus à partir des sauts de déplacements dans le plan et hors plan mesurés en surface, le long de la fissure. De ces lois cinétiques, il ressort que ni le mode I seul, ni les modes de cisaillement seuls ne peuvent expliquer la fissuration des rails. C'est donc la combinaison des trois modes, suivant des trajets de chargement complexes, qui en est responsable.
Des essais de fissuration par fatigue en mode mixte non-proportionnel I + II ont ensuite été réalisés, suivant des trajets de chargement représentatifs. La stéréo corrélation d'images a été utilisée pour obtenir les champs de déplacements en pointe de fissure. Les méthodes classiques de mesure des FICs à partir de champs de déplacements n'étant pas adaptées, du fait des efforts de contact et frottement entre les lèvres de fissure, de nouvelles méthodes ont été développées. Les trajets et vitesses de fissuration ont été étudiés au regard de ces FICs effectifs. Le critère de la contrainte tangentielle maximale n'a pas permis de prédire le trajet de manière fiable, mais peut être améliorée par la prise en compte de la plasticité en pointe de fissure ainsi que des efforts de contact/frottement entre les lèvres de fissure. Les vitesses de propagation obtenues se corrélèrent bien avec une combinaison des trois FICs effectifs dans une loi de type ≪ Paris ≫.
De ces essais, il ressort que du fait de la rugosité de la fissure, l'enchevêtrement d'aspérités et le frottement réduisent considérablement les FICs effectifs. Et cela même en l'absence de compression normale, ce qui ne peut être modélisé par une simple loi de Coulomb. De plus, l'usure des lèvres de fissure a aussi une forte influence sur les FICs effectifs. Le challenge pour les applications structurelles est donc non seulement de choisir le critère de bifurcation et la loi cinétique les plus appropriés, mais également de prendre en compte la rugosité et l'usure des lèvres de fissure, afin d'estimer correctement les FICs effectifs à utiliser dans ces modèles.
Pour les applications industrielles, une approche d'ingénieur, simplifiée, a été proposée afin de prendre en compte le frottement induit par la rugosité dans l'estimation des trajets de chargements effectifs à partir des trajets nominaux. Cette approche a été validée sur des essais de mode mixte séquentiel I + II & III.

Title : Fatigue crack growth under non-proportional mixed-mode loading in rail steel. From experiment to simulation.

Keywords : rolling-contact fatigue ; crack growth ; mixed-mode ; digital image correlation ; non-proportional loading ; friction

Abstract : Rails are submitted to Rolling Contact Fatigue due to repeated passages of train wheels, which induces several types of cracks, such as Squat-type cracks. Those cracks undergo non-proportional mixed-mode I + II + III loading, including compression phases, in variable proportions along the crack front, making the prediction of their paths and growth rates a challenge.
Mode I crack growth kinetics, for positive and negative R ratios, were first determined in R260 steel, as well as friction-corrected crack growth kinetics for fully-reversed combined mode II and III. The effective Stress Intensity Factors (SIFs) were deduced from the measured in-plane and out-of-plane crack face sliding displacements. From those kinetic laws, it was deduced that neither pure mode I, nor pure shear mode loadings can explain the crack growth rates observed in rails. A combination of those three loading modes, according to complex loading paths had thus to be prospected.
Non-proportional mixed-mode I + II fatigue crack growth tests were then performed, following representative loading paths. Stereo digital image correlation was used to measure the near-tip displacement field. Post-treatment methods generally used to deduce the effective SIFs from these fields were inappropriate because of contact and friction stresses along the crack face. New methods were thus developed. The crack paths and growth rates were analyzed, using the effective SIFs. Crack path prediction by the maximum tangential stress criterion was found not to be very reliable, but substantially improved when crack tip plasticity and the presence of contact and friction stresses along the crack faces were taken into account. The measured crack growth rates correlated well with a combination of the three effective SIFs in a Paris-type law.
From these experiments, it appears that due to crack face roughness, asperities interlocking and friction substantially reduce the effective SIFs, even without any normal compression, which cannot be captured by a simple Coulomb's law. Besides, crack faces wear also has a large influence on the effective SIFs. The challenge for structural applications is thus not only to choose the most appropriate bifurcation criterion and crack growth law, but also to take crack face roughness and wear into account, in order to estimate the correct effective SIFS to use in these models.
For industrial applications, a simple engineering approach was proposed to integrate roughness-induced friction in the estimation of the effective loading path from the nominal one. This approach was validated on sequential mixed-mode I + II & III experiments.

Université Paris-Saclay
Espace Technologique / Immeuble Discovery
Route de l'Orme aux Merisiers RD 128 / 91190 Saint-Aubin, France